ÉCOLE POLYTECHNIQUE FÉDÉRALE DE LAUSANNE

Laboratoire de Physique des Accélérateurs de Particules

Performance evaluation of a crystal-enhanced collimation system for the LHC

Thèse de Doctorat

N° ????

présentée à la Section de Physique de la Faculté des Sciences de Base de l'École Polytechnique Fédérale de Lausanne pour l'obtention du grade de Docteur ès Sciences

par

Valentina Previtali

Physicienne diplômé de l'Universitá degli Studi di Milano, Italie.

Président du jury:	**Prof. Olivier Schneider**
Directeur de thèse:	**Prof. Leonid Rivkin**
Expert Interne:	**Dr. Minh Tam Tran**
Expert Externe:	**Dr. Ralph Assmann**
Expert Externe:	**Dr. Mike Seidel**

Lausanne 2010

Contents

List of Figures

List of Tables

Summary

The Large Hadron Collider (LHC) has been constructed at CERN (Conseil Européen pour la Recherche Nucléaire, Geneva, Switzerland), and recently started up. The LHC beams, currently accelerated to 3.5 TeV, are meant to reach the nominal energy of 7 TeV, and a total stored energy, in nominal conditions, of 360 MJ per beam [1, 2]. The contrast between the huge stored power and the delicate cryogenic environment calls for a sophisticated collimation system [3].

For overcoming the limitations of the actual collimation system, different upgrade solutions have been considered [4, 5, 6]; this Ph.D. work gives a first performance evaluation of a crystal-enhanced collimation system by analytical, experimental and simulation investigations.

In this work, two crystal collimation experiments are described: the T980 (Tevatron, Chicago, U.S.) and the UA9 (SPS, CERN, Geneva, Switzerland). The data are analyzed and actual crystal performances are measured. These experimental results and their cross-check with dedicated simulations constitute the foundations of a weighted, critical prediction for the LHC. Different scenarios for a possible LHC crystal-enhanced collimation system have been simulated. Here the results are described and optimal parameters for a possible crystal collimator are proposed.

Key words: LHC, Collimation, Crystal, Channeling, T980, UA9, Collimator scan, Multi-turn efficiency

1

Riassunto

Il "Large Hadron Collider" (LHC) e' stato costruito al CERN (Conseil Européen pour la Recherche Nucléaire, Ginevra, Svizzera), e recentemente messo in funzione. I fasci di LHC, al momento accelerati a 3.5 TeV, sono previsti raggiungere un'energia nominale di 7 TeV, corrispondendte a un'energia accumulata totale di 360 MJ per fascio [1, 2]. Il contrasto tra l'imponente energia eccumulata e il delicato ambiente criogenico rende necessario un sofisticato sistema di collimazione [3].

Per ovviare alle limitazioni del presente sistema di collimazione, differenti opzioni per l'upgrade sono state considerate [4, 5, 6]: questa tesi di dottorato fornisce una prima valutazione delle performances per un sistema di collimazione che utilizzi cristalli curvi, mediante studi ti tipo analitico, sperimentale e simulazioni.

In questo lavoro due esperimenti di "collimazione a cristallo" vengono descritti: l'esperimento T980 (Fermilab, Chicago, U.S.) e l'esperimento UA9 (SPS, CERN). I dati sperimentali sono qui analizzati e le reali prestazioni dei cristalli sono misurate. Su tali dati sperimentali, e sul loro confronto con simulazioni dedicate, vengono ponderate le successive predizioni per LHC. Scenari differenti per un sistema di collimazione a cristallo, da installare eventualmente nell'LHC, sono stati simulati. I risultati delle simulazioni vengono descritti e uno studio di ottimizzazione dei parametri di un eventuale cristallo e' discusso.

Key words: LHC, collimazione, cristallo, channeling, T980, UA9, scan del collimatore, efficienza su giri multipli

Introduction

The Large Hadron Collider (LHC) has been constructed at CERN, and recently started up. The LHC beams, currently accelerated to 3.5 TeV, are meant to reach the nominal energy of 7 TeV. In nominal conditions there will be 2808 bunches per beam, $1.15 \cdot 10^{11}$ protons per bunch, corresponding to an intensity of $3.2 \cdot 10^{14}$ protons and a total stored energy of 360 MJ per beam [1, 2].

These parameters make the LHC beam very powerful and highly destructive if lost in an uncontrolled way. Moreover the superconducting magnets of the LHC are highly sensitive to even tiny amount of energy deposition: direct beam losses in the super-conducting aperture could provoke a quench in the magnet or even irreversible damages to the machine [7, 8]. The contrast between the huge stored power and the delicate cryogenic environment calls for a sophisticated collimation system, able to intercept and control the unavoidable losses from the beam. This is the reason why the collimation system is a vital organ for the correct functioning of the LHC, and why its task is so hard to accomplish.

In order to gradually attack the problem, the LHC collimation system is being implemented in a phased approach [3]. The Phase 1 of the collimation system is designed to maximize the robustness of the system and guarantees $\sim 40\%$ of the nominal intensity during the first few years of LHC operation [9]. This phase is however expected to be limited in intensity reach by two factors: the achievable cleaning efficiency and the collimator-induced increase of the LHC impedance.
For overcoming these limitations a Phase 2 of the collimation system is being studied, with the goal to reach nominal and possibly ultimate intensities for the LHC. The Phase 2 design has not been finalized yet. Among the possible concepts are metallic secondary collimators that would complement Phase 1 collimators and would be used during stable physics operation. Beyond Phase 2 secondary collimators it is also being envisaged to implement other solutions, like dedicated absorber in cryogenic regions (cryo-collimators) [4], crystal-enhanced collimation [5], e-beam lens based beam scraping [6] and other advanced schemes.

The LHC collimation system is structured as a "multi stage system": short primary collimators intercept and disperse the primary halo beam, which is successively collected by a second, longer stage. At present the Phase 1 system is composed by graphite collimators. Particle showers generated by the secondary collimator are

collected by metallic absorber at the end of the collimation insertion, while tertiary collimators positioned in strategic locations protect particularly delicate and exposed equipment. The role of a primary collimator is to give a kick to the primary particles in order to increase their amplitude at the secondary collimator location. While an amorphous material would scatter the primary halo in all possible directions, a crystal could act as a "smart" scatterer of the beam: coherent effects like channeling [10] and Volume Reflection [11] can in principle deviate the beam halo in a controlled fashion, possibly improving the performance of a collimation system. My Ph.D. work aims at testing and evaluating the option of crystal-enhanced collimation for the LHC, both by experimental and simulation investigations. This thesis summarizes the work performed in the three years of my Ph.D. work.

The thesis is structured in six chapters.

The first part of **Chapter 1** is an introduction to the crystal theory: the crystal formalism is given and the approach used to describe the crystal structure is presented. Subsequently the possible coherent interactions between a positive charged particle and the crystal lattice are treated. In the second half of the Chapter 1, an overview about past experiments and the recent results in extraction line experiments give an historical perspective of the issue, and describe the ground from whom my Ph.D. thesis work moved.

Starting from **Chapter 2** the focus moves from the sole crystal object to the possible implementation of such an object in the multi turn dynamics of a circular accelerator. After a short introduction of accelerator physics and collimation theory, specific aspects of crystal collimation are discussed. In particular a new optical function (the grazing function g) is defined and used to characterize optimal crystal collimator locations [12]. The possible impact of crystal manufacturing imperfections (e.g. miscut) is also analyzed.

In **Chapter 3** the computational and analytical tools used during this Ph.D. work are described. Since both the simulations and the experimental data analysis constitute important parts of my work, the chapter is naturally divided in two parts: the first part treats the general description and the new features introduced in the tracking code used for collimation studies (`SixTrack` software[13, 14]), while the second part describes the experimental techniques and the analytical tools employed for the data analysis. Particular attention is given to the collimator scan method, a new tool developed for channeling efficiency calculation in a circular machine.

The last three chapters are dedicated to the three machines which have been studied during this Ph.D work: the Tevatron (FNAL,Batavia, USA), the SPS (CERN, Geneva, Switzerland) and the LHC (CERN, Geneva, Switzerland) .

The crystal experiment in Tevatron (T-980) is a crystal collimation experiment with the aim of improving the performance of the actual two-stage collimation system, and reducing the background at the experiments. A bent crystal is intended to deflect the beam halo to a downstream secondary collimator. The loss rate at the collimator location is recorded by a set of scintillators and by an ionization chamber: the detector signals are compared, and both sets of data are analyzed. The results include the channeling kick, the channeling efficiency estimation and their dependence on the crystal orientation. In **Chapter 4** the results of beam tests performed in winter 2008-2009 are presented, when an "old" o-shaped crystal, previously tested with unsatisfactory results at Brookaven (BNL, USA), was tested [15].

During the summer 2009 in the SPS the UA9 Crystal Collimation experiment began, designed to verify the usability and the possible advantages of using a crystal for collimation purposes in a circular machine [16]. In UA9 two new-generation crystals were inserted in the SPS and alternatively used as primary elements of a two stage collimation system: the beam halo was first intercepted by one crystal and then deviated on a downstream secondary collimator. The losses were recorded both in the region immediately downstream the crystal and in the rest of the ring. In **Chapter 5** the main results of the beam tests performed last summer are presented. A full set of simulations has been carried out, and the results are compared with the experimental ones.

The beam tests conducted in Tevatron (Chapter 4) and SPS (Chapter 5) contributed to finalize the scenario foreseen by the simulations of a possible crystal collimation-enhanced collimation system for the LHC, presented in **Chapter 6**. Different crystal geometries are considered, in a first attempt to optimize the system performances, yet maintaining a design compatible with the actual layout of the collimation insertion. The studies are performed with the same state-of-the-art code used for the design of the conventional LHC collimation system. The numerical models are described and the performance predictions are presented for the nominal 7 TeV energy. Open issues and further work towards a crystal collimation design for the LHC are discussed.

Chapter 1

Crystal Physics and Theory

In this chapter the basics of the crystal theory are given. After a short introduction on crystal structure, the different possible interactions between crystal and positively charged particles are presented. Some highlights of the physics of the processes will help us understanding the main processes (channeling, volume reflection, dechanneling and volume capture) both for straight and for mechanically bent crystals. The main parameters which characterize these effects are derived and discussed (e.g. critical angle, dechanneling probability).

The last part of the chapter is dedicated to a short review of the past experimental results. After giving an overview of the possible efficiency definitions, the "state of the art" for crystal single pass experiments is presented, showing the experimental results regarding the previously introduced processes. A last section introduces the past crystal experiments in circular machines, giving an historical overview and introduction to the work presented in the following of this thesis.

1.1 Crystal structure

A crystal is a solid with an high degree of order in its internal structure. The atoms which constitute the crystal are organized in a geometrical arrangement which is called lattice. The lattice is usually represented as a grid of lines in the space, and each interception of these lines is called node. In each node one or more atoms can be placed. It is possible to find a minimum volume of space in the shape of a 3D parallelepiped, called the crystal cell, whose infinite repetition by translation constitutes the solid structure of the entire crystal. This requires that a linear base **i**, **j** ,**k** can be chosen such that the translational operation **T**

$$\mathbf{T} = n_1\mathbf{i} + n_2\mathbf{j} + n_3\mathbf{k} \tag{1.1}$$

(where n_1, n_2 and n_3 are three arbitrary integers) connects two locations in the crystal having identical atomic enviroments. The lattice directions are then given in units of the linear base.
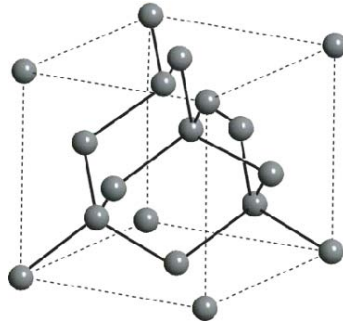
Figure 1.1: The diamond cubic lattice cell. This is the elementary cell for the Si crystal structure, after [17].

In crystallography many different lattice types are classified, however it is beyond the purpose of this thesis to describe the structure and symmetries of all the possible crystal structures (see a complete description, for example, in [17]). We briefly remind that the silicon (Si), which is of particular interest for our study, is arranged in a diamond lattice: a sketch of the diamond cell, which has been described as a "two interpenetrating face-centered cubic lattices" primitive lattices [18], is shown in Figure 1.1. The lattice constant of Si (edge of the cubic unitary cell) is $a = 5.430$ Å. The crystal orientation is critical for determining the kind of interactions between particles and the lattice. The two orientations which are most commonly used in the experiments treated in this thesis work are, in units of the linear base $(n_1 n_2 n_3)$, (110) and (111).

1.2 Particle interactions with crystals.

When a particle crosses a material which does not present strong symmetries (e.g. amorphous) it experiences a large number of uncorrelated interactions with the atoms compounding the material. Depending on the impact parameter and energy of the particle, a large variety of interactions, both elastic and inelastic, are possible: multiple Coulomb scattering, Rutherford scattering, ionization, elastic, quasi elastic and inelastic point-like interactions. A complete description of these effects, which are dominating in standard collimation materials, can be found in [19].

Even if these interactions occur also in a misaligned crystal, the following sections will be focused on the effects which take place when the impinging particle is well oriented along the main symmetry axes/planes of the crystal lattice structure. These interactions are called coherent interactions, because the particles interact with a subset of atoms arranged in a specific geometrical layout (e.g. a plane or an axis of the lattice) instead of interacting separately with each individual atom. The kind of coherent effect which takes place depends on the relative orientation between the particle velocity and the crystal lattice.

In case of orientation with respect to a plane (e.g. 110), we have planar channeling both for straight and bent crystals(section 1.2.1 and 1.2.2.1) or volume reflection (section 1.2.2.2) only for bent crystals. Secondary effects are dechanneling and volume capture, which are briefly treated in Section 1.2.3

In case of a crystal axis (e.g. 111), we will have axial channeling (section 1.2.4).

1.2.1 Planar channeling in straight crystals

In this section the coherent interaction of a charged particle with the planes of a straight crystal is studied. We pass from the potential energy for the particle-single atom interaction to the potential energy for the single crystal plane. It is then considered the interaction between a particle and the two adiacent crystal planes (section 1.2.1.1), and the motion of a particle and the critical parameters for the channeling effect (section 1.2.1.2) are derived. A full detailed analysis can be found in [10]. Finally, in section 1.2.1.3, two approximations for the crystal planar potential are presented: the square well and the harmonic potential.

1.2.1.1 Planar potential

If a particle (charge $Z_i e$) interacts with a single atom (atomic number Z), the potential energy associated with the interaction is (Thomas-Fermi model):

$$V(r) = \frac{Z_i Z e^2}{r} \Phi\left(\frac{r}{a_{TF}}\right) \tag{1.2}$$

where r is the distance between the particle and the atom, a_{TF} is the screening distance and it value is $0.8853 \, a_B \, Z^{-1/3}$, with $a_B = 0.529$ Å.

$\Phi\left(\frac{r}{a_{TF}}\right)$ is called screening function and takes into account the charge distribution of the atom. One of the most common analytical approximation for the screening function was given by Moliere [20]:

$$\Phi\left(\frac{r}{a_{TF}}\right) = \sum_{i=1}^{3} \alpha_i \exp\left(-\frac{\beta_i\, r}{a_{TF}}\right) \tag{1.3}$$

where $\alpha = (0.1, 0.55, 0.35)$, $\beta = (6.0, 1.2, 0.3)$. When the particle orientation is almost parallel to one of the main axes of symmetry of the crystal lattice, then the particle does not see anymore the potential from a single atom, but an averaged continuous potential U_{pl} from all the atoms aligned with its direction:

$$U_{pl} = N\, d_p \int_{-\infty}^{+\infty} \int_{-\infty}^{+\infty} V(x, y, z)\, dy\; dz \tag{1.4}$$

where $V(x, y, z)$ is specified in equation 1.2 (but expressed in cartesian coordinates), d_p is the inter-planar distance and N the volume density of the atoms. Considering also the thermal vibration (by averaging the atom positions over a Gaussian whose width depends on the temperature) it is possible to obtain a global equation for the planar potential U_{pl}. A plot for the potential energy associated with a single plane of Si crystal (orientation 110) is shown in Figure 1.2.
It is clear that the total particle potential energy $U(x)$ will depend on all the crystal
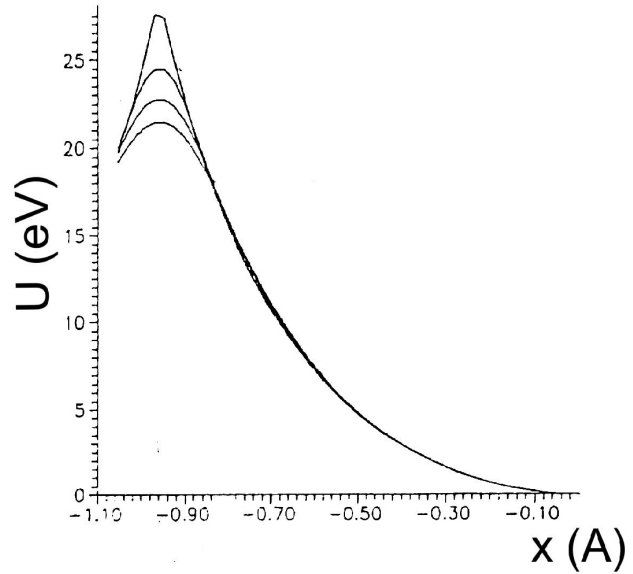
Figure 1.2: Planar potential energy (for a proton) for a single Si 110 crystal plane. The potential with the highest value refers to the static case (no Temperature dependence). The other lines (from top to bottom) refer to 77K, 300K and 500K. Image from [10].

planes, but in first approximation only the two planes that are closest to the particle are considered. By defining $x = 0$ the position in the middle between the atomic layers it follows:

$$U(x) = U_{pl}\left(\frac{d_p}{2} - x\right) + U_{pl}\left(\frac{d_p}{2} + x\right) - 2\, U_{pl}(d_p/2) \tag{1.5}$$
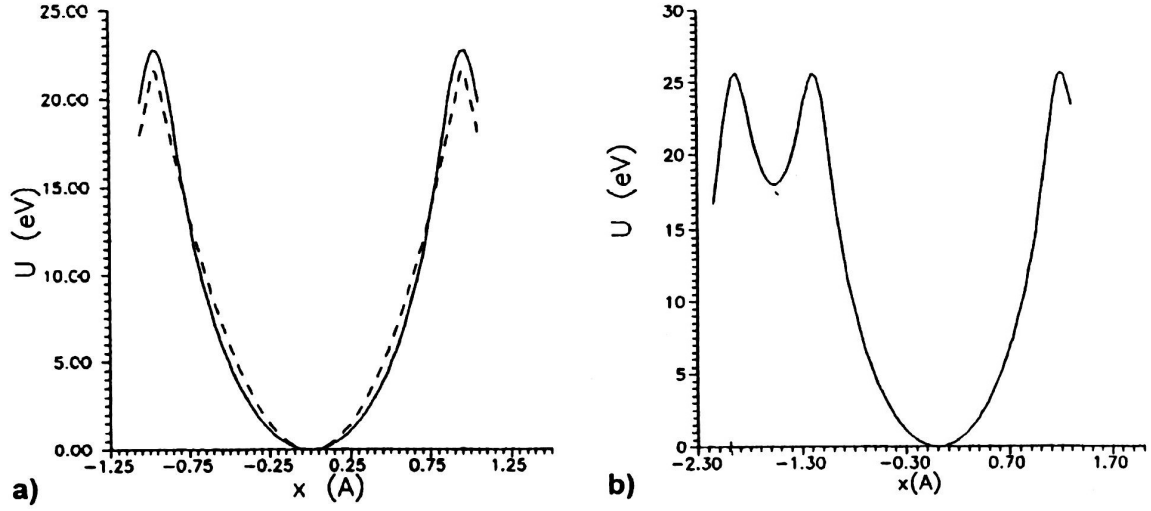
Figure 1.3: Planar potential energy for a proton, orientations (110) (case a., on the left hand side) and (111) (case b., on the right hand side) of Si crystal. In dashed line the harmonic approximation ($U \sim x^2$) is shown for the case (110). Image from [10].

where $U(0) = 0$ was imposed. Examples of the planar potential for the orientations (110) and (111) are shown in Figure 1.3 . It is possible to see in the picture that the planar potential rises to about 20-25 V at a ≈ 1Å distance, that means an average electric field of more than $2 \cdot 10^{11}$ V/m.

1.2.1.2 Transverse energy conservation and channeling critical angle

In this section the channeling effect is introduced, i.e. the motion of the particles which are trapped inside the potential well in between two atomic planes. By decoupling the Hamiltonian for transverse and longitudinal motion, the energy conservation law for the transverse motion is derived. The critical angle parameter, that is the maximum allowed angle for channeled particles, is defined and its dependence on the total energy is commented.

We showed in the last section the shape of the potential well in between two atomic planes. It is known from quantum mechanics that the permitted energy levels in a potential well are discrete, but in our case, for heavy particles like protons, the energetic states are so dense that the problem can be treated with a classical treatment (see [10] for details). Let's consider a particle with total relativistic energy

$$E_{tot} = \sqrt{p^2c^2 + m_0^2c^4} + U_{pl}(x) \tag{1.6}$$

where p is the momentum of the particle, c the speed of light and m_0 the rest mass. Obviously this quantity must be conserved. If the particle is moving in the x-z plane, and $p_x \ll p_z \approx p$, it is possible to rewrite the last equation like:

$$E_{tot} = \sqrt{p_z^2 c^2 + m_0^2 c^4} + \frac{p_x^2 c^2}{2\sqrt{p_z^2 c^2 + m_0^2 c^4}} + U(x) \tag{1.7}$$

Since $U(x)$ is a purely transverse potential, the longitudinal energy $E_z = \sqrt{p_z^2 c^2 + m_0^2 c^4}$ must be conserved. This implies the conservation also of the transverse energy $E_T = \frac{p_x^2 c^2}{2E_z} + U(x)$. Defining the angle $\theta = \frac{p_x}{p_z} = \frac{dx}{dz}$, and using the approximation $p_z \approx p$, $E_z \approx E$, it is finally obtained

$$E_T = \frac{pv}{2}\theta^2 + U(x) = \text{const} \tag{1.8}$$

that is the final conservation equation for crystal planar channeling, from which the critical parameters of channeling can be derived. Therefore a particle is confined in the potential well if its transverse energy is smaller than the maximum potential energy:

$$\frac{pv}{2}\theta^2 + U(x) < U_0 \tag{1.9}$$

In this case the particle is said to be in *channeling* mode. Assuming the initial coordinate $x_0 = 0$ (the particle enters in the middle between two planes), and using a potential where $U(0) = 0$ (like the one described by equation 1.5), then *the critical angle* for straight crystals θ_{C0} is obtained:

$$\theta_{C0} = \sqrt{\frac{2U_0}{pv}} \tag{1.10}$$

which in literature is also referred to as Lindhardt angle [21].The critical angle depends on the maximum of the planar potential energy U_0 (i.e. on the orientation and on the temperature), and decreases with momentum and the velocity of the particle. For relativistic particles, having $v \simeq c$ and using $E = mc^2$, it is obtained

$$\theta_{C0} = \sqrt{\frac{2U_0}{pv}} = \sqrt{\frac{2U_0}{E}} \tag{1.11}$$

where it is worth to notice the energy dependence. The cricital angle may then be defined as the maximum angle that a particle of energy E can have with respect to the selected crystallography direction for being trapped in channeling mode.

1.2.1.3 Planar potential approximations: harmonic potential

In this section the trajectory of the particle inside the crystal in the simplified harmonic potential approximation is studied.

The shape of the planar potential calculated with Moliere's approximation for the atomic potential is shown in Figure 1.3. A quite realistic, yet much more practical
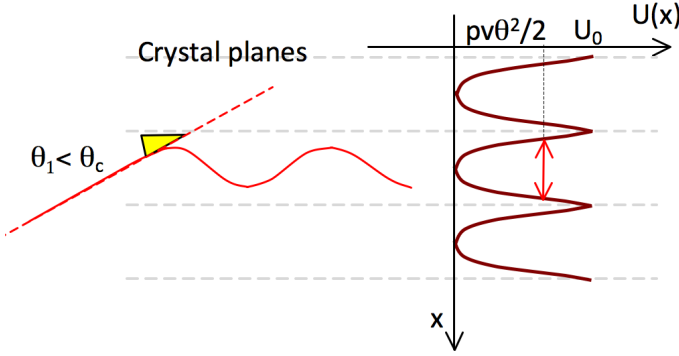
Figure 1.4: Harmonic approximation of the planar potential in a straight crystal, and particle trajectory in channeling mode.

approximation for the potential is the harmonic potential $U_h(x) = U_0 \left(\frac{2x}{d_p} \right)^2$. The difference between the harmonic potential and the Moliere approximation is shown in Figure 1.3. It can be shown that in this case the equation 1.8 is equivalent to the standard equation for a harmonic oscillator in the x direction. Keeping in mind that $\theta = \frac{dx}{dz}$ and deriving equation 1.8 with respect to z it is obtained:

$$\frac{pv}{2} \frac{d^2x}{dz^2} + \frac{dU(x)}{dx} = 0 \qquad (1.12)$$

Using $U(x) = U_h(x)$ and solving the differential equation, the solution[10] results

$$x = \frac{d_p}{2} \sqrt{E_T U_0} \sin \left(\frac{2\pi}{\lambda} + \phi \right) \qquad (1.13)$$

where the oscillation period λ is:

$$\lambda = \pi d_p \sqrt{\frac{pv}{2U_0}} = \pi \frac{d_p}{\theta_{c0}} \qquad (1.14)$$

with θ_{c0} as defined in equation 1.11. Our simulation code is based on this harmonic approximation model, implemented in the standard collimation tracking code, and extensively used in this thesis work.

1.2.2   Bent crystals

In the previous sections we have presented the channeling effect in a straight crystal, whose dynamics is determined by the conservation law for the transverse energy (equation 1.8). In this section similar effects for bent crystals are studied. In particular the two effects for which the transverse energy conservation law is still valid[1] are presented: the channeling (Section 1.2.2.1) and the volume reflection effect (Section 1.2.2.2).

1.2.2.1   Planar channeling in bent crystals

In this section an overview of the differences between the channeling in bent and straight crystals is given. We define a new coordinate system for a bent crystal, where it is still possible to define an effective transverse potential. In perfect analogy with the case of a straight crystal, a conservation law for the transverse energy is found. The critical parameters for channeling in bent crystals (critical radius, energy and angle) are then derived.

For the treatment of the dynamics in bent crystals it is useful to choose a reference system where the longitudinal coordinate z follows the curvature of the crystal. Since a centripetal force $F_{\bar{c}} = -pv/R(z)$ is needed to follow the curvature of the crystal (and then the new coodinate z), the particles in the new reference system experience an equal and opposite centrifugal force $F_c = pv/R(z)$. This is a fictitious force, because the new reference system is not inertial. For this reason, if computing the potential energy for the plane which is transverse to z in each point, a picture totally different from the one in a straight crystal [2] is obtained: this is due to the contribution of F_c. If the curvature radius $R(z)$ is constant over the length of the crystal ($R(z) = \text{const}$), then the transverse energy conservation equation 1.8 in the new reference system can be rewritten as:

$$E_T = \frac{pv}{2}\theta^2 + U_{eff}(x) = \text{const} \tag{1.15}$$

where

$$U_{eff}(x) = U(x) + \frac{pv}{R}x \tag{1.16}$$

U_{eff} is called the *effective planar potential* for bent crystals, and it is the sum of the planar potential $U(x)$ for straight crystals (see Section 1.2.1.1) and the centrifugal potential $F_c \cdot x$. An example of the different effective potentials for straight and bent

---

[1]It is worth to stress the passage from an inertial reference system for straight crystals to a non-inertial one for bent crystals (see details in Section 1.2.2.1).

[2]It is a fact that, given the curvature of a bent crystal, the planes associated with a smaller curvature radius have an higher nuclear density N. Since the planar potential $U(x)$ is proportional to N (equation 1.4), one could think that this is the reason for a change in the planar potential shape, which would cause a different channeling dynamics. Anyway, for typical crystal geometry, the relative difference in density between two adjacent planes is of the order of 10^{-10}, that can be considered negligible.

crystals is shown in Figure 1.5.
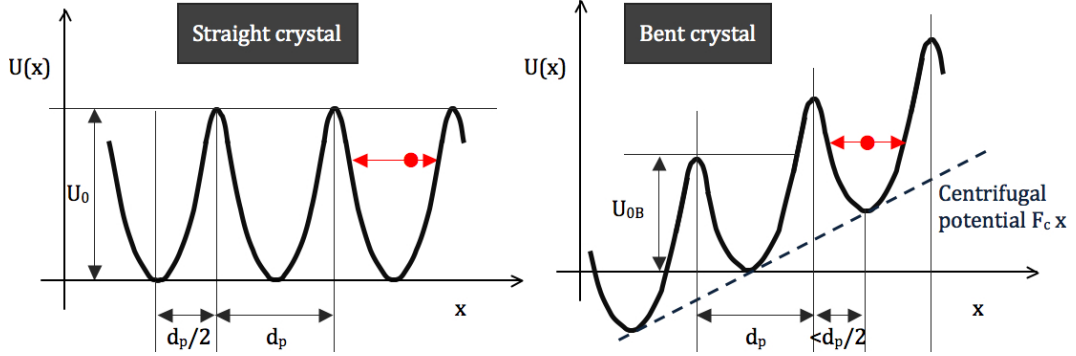
Figure 1.5: Effective potential for straight and bent crystals. The potential well depth is indicated in the two cases. In red a particle in trapped mode (channeling) is drawn.

The effect of the centrifugal force is to decrease the potential well depth for each potential well in between two atomic planes, and to shift its minimum. Obviously there is a value of the force F_c for which the potential well depth goes to zero, and the particles cannot be trapped anymore. Given a fixed particle energy, the bending radius for which the channeling disappears can be found by pairing the centrifugal force with the maximum electric force in straight crystal $U'_{max} = \left(\frac{dU(x)}{dx}\right)_{max}$. The formula for the critical radius R_c is immediately obtained:

$$R_c = \frac{pv}{U'_{max}(x)} \tag{1.17}$$

that can then be defined as the minimum bending radius for which the channeling mode well is still possible. Using the harmonic potential approximation (see Section 1.2.1.3) in equation the depth of the potential well $U_{0B}(\frac{R_c}{R})$ is:

$$U_{0B}\left(\frac{R_c}{R}\right) = U_0\left(1 - \frac{R_c}{R}\right)^2 \tag{1.18}$$

where U_0 is the potential well depth for a straight crystal. Analogously, the maximum acceptance angle for trapping a particle is:

$$\theta_c\left(\frac{R_c}{R}\right) = \theta_{c0}\left(1 - \frac{R_c}{R}\right) \tag{1.19}$$

where θ_{c0} is the critical angle for straight crystals.

1.2.2.2   Volume reflection

Beside the channeling effect, there is another effect which takes place in bent crystals and conserves the total transverse energy: the volume reflection. It consists of a single reflection of the particle by the crystal planes. In this section the physics of volume reflection is explained by using two models: at first the purely geometrical approximation, and then the more refined model with the harmonic approximation.

Figure 1.6: Volume reflection effect interpreted with a purely geometrical model.
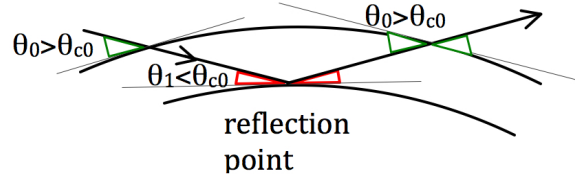
For understanding the principle let's first consider a simple geometrical model, where the particles is reflected by the atomic plane only if its impacting angle is smaller than the critical angle θ_{c0} for straight crystals. Let's consider a particle with initial impacting angle higher than θ_{c0}, going toward the center of the curvature (from now a negative sign is associated to this orientation). For effect of the curvature, at each new crystal plane the particle impacting angle decreases (see Figure 1.6). For this initial configuration there are then two possibilities:

1. Up to the end of the total crystal length ($z = z_{max}$) the absolute value of the impacting angle is still higher than $-\theta_{c0}$. In this case the particle crosses the whole length of the crystal without changing its initial direction.

2. there is a plane at $0 < z < z_{max}$ for which the impacting angle θ_1 is smaller than θ_{c0}: here the particle must be reflected. When coming back to the previous atomic plane the impacting angle is again higher than the critical one[3] (for symmetry reasons, see Figure 1.7). Going outward, the impacting angle with the new crystal planes crossed is going to increase. In this case the particle crosses back all the atomic planes up to the end of the crystal.

It is clear that, in our simplified model, the volume reflection effect occurs only if the impacting angle at the first crystal plane is, in absolute value, higher or equal than the critical angle defined in equation 1.19, but smaller or equal than the critical angle at the last plane of the crystal. Since the last crystal plane has an inclination $-\theta_b$ with respect to the first plane, the absolute value of the initial impacting angle must be smaller than $\theta_b + \theta_{c0}$, where θ_b is the total bending angle of the crystal . Using this geometrical approximation a summary table of all the processes that are expected in a bent crystal can be built, for different impacting angles θ_i (Table 1.1).

---

[3]this is exactly the reason why the critical angle for channeling in bent crystals must be smaller than the critical angle for the straight case.

Table 1.1: Different effects in a bent crystal as a function of the initial impacting angle (θ_i) of the particle, and the kick θ_k associated with each case. With θ_{c0} we refer to the critical angle for the straight crystal, while θ_c is the critical angle for bent crystals. Only the effects that satisfy the conservation of transverse energy (equation 1.15) are listed. The angle in this table are calculated based on the purely geometrical model described in the text.

Impacting angle	Effect	Kick
$\theta_i > \theta_c$	no change in angle	$\theta_k = 0$
$\|\theta_i\| < \theta_c$	channeling	$\theta_k \approx \theta_b$
$-\theta_{c0} > \theta_i > -\theta_c$	Reflection on the first atomic plane	$2\theta_c < \theta_k < 2\theta_{c0}$
$-\theta_b - \theta_{c0} > \theta_i > -\theta_{c0}$	Volume Reflection	$2\theta_c < \theta_k < 2\theta_{c0}$
$\theta_i < -\theta_b - \theta_{c0}$	no change in angle	$\theta_k = 0$

It must be stressed that in this table *only the effects that satisfy the conservation of transverse energy* are listed.

The explanation of the volume reflection effect using the conservation of the total transverse energy is analogous. For understanding the analogy it is important to remember that, if the total energy of the particle is fixed, its transverse kinetic energy is proportional to the square of the impacting angle θ_i (see equation 1.15). A
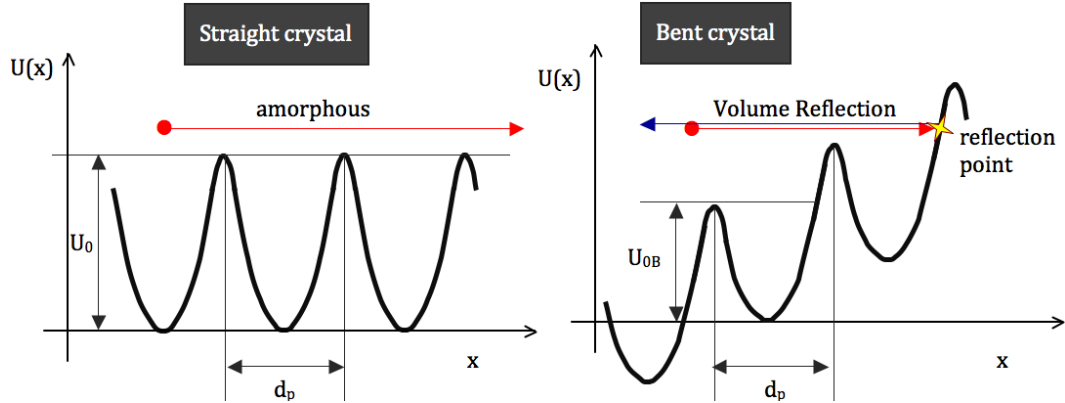
Figure 1.7: Effective potential for straight and bent crystals. The red point is the initial condition of the particle. Volume reflection for bent crystals is shown.

picture of the particle in the "transverse energy-transverse position" space is shown in Figure 1.7. The initial conditions of the particle are indicated by the red point, and the red arrow indicates the initial direction of the motion toward the interior of

the curvature. In the bent crystal, as crossing the atomic planes, the kinetic energy of the particle decreases: this is because the relative angle with respect to the atomic plane direction decreases. If the crystal is long enough, the particle arrives up to a plane where the particle is reflected back by the potential barrier.

1.2.3   Inelastic processes: volume capture and dechanneling

All the effects presented up to now are compatible with the conservation of the total transverse energy, as defined in equation 1.8 for straight crystals and equation 1.15 for bent crystals. However, there is a probability larger than zero that, when transversing the length of the crystal, the particle undergoes one or more interactions that change its total energy or its direction. If this happens, the transverse energy of the particle is not conserved anymore. In this section a qualitative introduction to two effects that can arise from a change in transverse energy of the particle is given: the volume capture and the dechanneling effect. A detailed description of these effects is beyond the scope of this thesis: a exhaustive overview can be found in [10].

In this section we use the formalism introduced in Section 1.2.2.1, where the reference system for bent crystals is introduced and the effective potential is derived. Both volume capture (Figure 1.8) and dechanneling effects (1.9) require a change in the transverse energy of the particle. Since a change in transverse energy is associated not only with a total energy variation, but may be to a mere change in the orientation of the particle, then both negative and positive changes of the energy are possible.
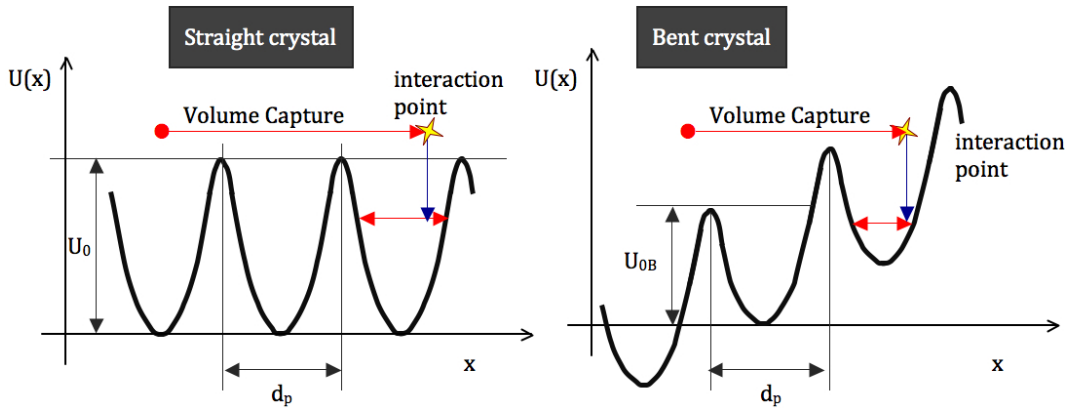
Figure 1.8: "Transverse energy - transverse position" space for straight and bent crystals. The red point indicates the initial conditions of the particle. The blue arrow indicates a change in the transverse energy of the crystal. The volume capture effect is illustrated.
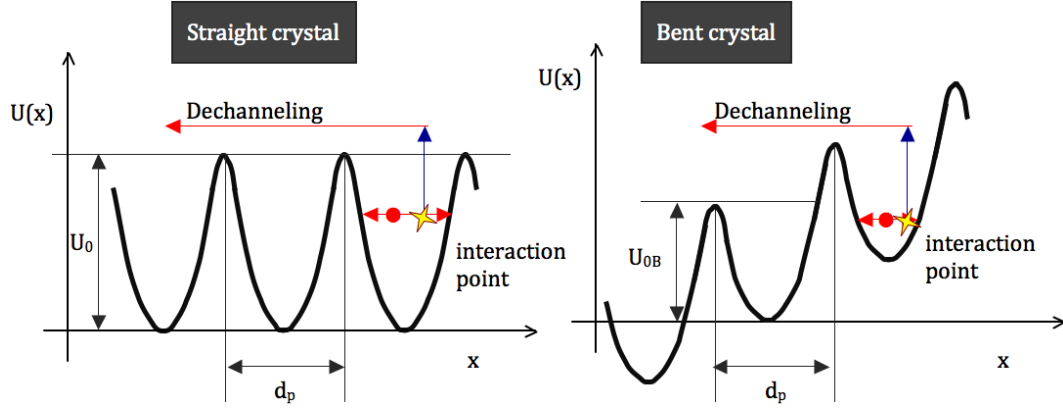
Figure 1.9: "Transverse energy - transverse position" space for straight and bent crystals. The red point indicates the initial conditions of the particle. The blue arrow indicates a change in the transverse energy of the crystal. The dechanneling effect is illustrated.

- *Negative transverse energy change: Volume capture*
  The volume capture of feed-in effect is presented in Figure 1.8: the initial state of the particle in the "transverse energy - transverse position" space is indicated by the red point, for both straight and bent crystals. If the particle loses some transverse energy (in one ore more collisions), it could be trapped in a potential well, and then follow the crystal curvature: this effect is called volume capture. The collisions are most likely to happen when the particle is close to an atomic plane (because the density of electrons is higher). The probability of being trapped is higher if the energy required to be trapped is smaller, that is if the particle is almost aligned with an atomic plane: for this reason the volume capture is a competitor to the volume reflection effect.

- *Positive transverse energy change: Dechanneling*
  The dechanneling or feed-out effect (in Figure 1.9) is the opposite of the volume capture effect. It is possible that a particle in channeled mode gains some transverse energy in one or more collisions with the electrons. Obviously, in total analogy with volume capture, the collisions are more likely to happen where the electron density is higher, therefore close to the atomic planes. If the energy gain is large enough, the particle can exit the channeling mode.
  It can be shown [10] that, in a straight crystal, the number of channeled particles decreases exponentially with the length of the crystal:

$$N = N_0\, e^{-z/L_D} \tag{1.20}$$

where L_{D0} is the dechanneling length (for Si crystals, of the order of centimeters in the GeV-TeV energy range). Using the harmonic potential described in

section 1.2.1.3, it can be proven [10] that the dechanneling length for a bent crystal with bending radius R is:

$$L_D(pv, R) = L_{D0}(pv) \left(1 - \frac{R_c(pv)}{R}\right)^2 \tag{1.21}$$

where R_c is the critical radius defined in equation 1.17.

1.2.4   Axial and quasi-axial channeling

Up to now the interaction between the particles and the crystal planar potential has been studied, and the different physics effects that can arise from this interaction. However, if the particle is aligned with one of the main crystal axis, then its motion is governed by the potential of the lattice of atomic strings averaged along the axis. Since the axial channeling depends on the shape of the potential islands in the axial direction, it is a very complex phenomenon, whose complete investigation is beyond the scope of this work. In this section the basic definitions are given to the reader. More details can be found in [22]. An example of experimental measurements can be found in Section 1.4.

Two types of coherent interactions with crystal axes exist:

1. the "hyperchanneling", where the particles are bounded to the axial potential of a single axis. In complete analogy with the planar case, for each energy and bending radius a critical angle exists, that is a limit impacting angle wherethe particle cannot be trapped anymore in the channeling state. However the maximum potential energy which confines the potential well is quite low (eg, in Si, between 1 and 6 eV in comparison with the $\approx$25 eV for planar channeling). Only a small fraction of particles is captured in hyperchanneling state.

2. the "doughnut scattering", which arises from many coherent interactions with the atomic strings. It is essentially a multiple scattering with the axes of the crystal.

What is special in axial dynamics is that, even if the particle impacting angle is higher that the critical angle for hyperchanneling, the axial deflection is still possible. This is because the doughnut scattering does not smear the transverse trajectories of the particles, so the particles can continue following the axis curvature. This kind of axial channeling is called "unbounded", in contrast to "bounded" state of hyperchanneling. This has been observed, both in the UA9 experiment (see Section 5.3.1) and in the H8-RD22 (Section 1.4), when the crystal is almost aligned in both horizontal and vertical direction. In Section 1.4 some results from deflection through doughnut scattering are shown.

1.3 Possible definitions of efficiency

In general, when considering different possible particle-crystal interactions, the idea of efficiency of a certain process is intuitively linked to the probability of observing that specific interaction under some well defined initial conditions. In principle, if N_{Tot} is a set of impinging particles and N_i is the number of particles which undergo the effect of interest, the "ideal" efficiency of the process can be defined as:

$$\eta_{ideal} = \frac{N_i}{N_{Tot}} \qquad (1.22)$$

However the initial requirements on the set of impinging particles, and the possibilities/methods to measure their total number, change with respect to the experimental settings (extraction line or circular machine) and on the available instrumentation. Here we try to give an exhaustive summary of the possible efficiency definitions which have been given in the past, and the methods used to calculate them: in particular, from now on, the channeling efficiency is examined, even though the same considerations are valid for other processes such as volume reflection, volume capture or dechanneling.

1.3.1 Single-pass efficiency

In single pass experiments like H8RD22 [23, 24, 25, 26] (see Section 1.4), the crystal is mounted on an extraction line and the particles can interact with the crystal only once. A telescopic system can reconstruct the tracks of the single particles before and after the crystal [27]. The angle of the particle before and after the interaction are measured, and therefore it is possible to measure how many particles receive the kick associated to the channeling process. In this case, a different channeling efficiency is usually associated to each crystal-particle orientation: when speaking of "single-pass" efficiency it is usually usually referred to the maximum channeling efficiency, obtained with the optimal alignment.

1.3.2 Multiturn efficiency

When inserting a crystal in a circular machine, for deviating the beam halo in a parasitic way (e.g. for extraction or collimation purposes), each particle in the halo could pass through the crystal, and interact with it, more than once (multi turn process). In this environment it is important to define what the quantity N_{Tot} is. Two choices are possibile:

- N_{Tot} is the total rate of interactions at the crystal, when the crystal is oriented in amorphous position: the efficiency is called "single-pass efficiency in multi-turn environment".

- N_{Tot} is the total number of particles in the halo: the obtained efficiency is called "multi-turn efficiency".

Single-pass efficiency in a multi-turn enviroment:

When N_{Tot} corresponds to the total rate of interactions at the crystal, each particle can be counted more than once. In past experiments conducted at Tevatron [28, 29, 30, 31] and RHIC [?, 32] (see Section 1.5 for details), the single pass channeling efficiency is calculated using a detector downstream the crystal, whose signal q is proportional to the rate of amorphous interactions at the crystal. Two different crystal-particle orientations are considered: in the first one only the amorphous interaction is possible, while the second one is the optimal channeling orientation; in the following we will refer to this two orientations, respectively, with the subscripts 1,2. It follows that:

$$q_1 = k \cdot N_{am,1} = k \cdot N_{Tot,1} \cdot \eta_{am,1} \tag{1.23}$$

$$q_2 = k \cdot N_{am,2} = k \cdot N_{Tot,2} \cdot \eta_{am,2} \tag{1.24}$$

where k is a proportionality factor which depends on the detector (efficiency / position / area...), N_{am} is the number of particles undergoing an amorphous interaction, N_{Tot} is the total number of interactions at the crystal and η_{am} the probability of amorphous interaction for the particles impinging the crystal surface. By definition it is:

$$\eta_{am,1} = 1 \tag{1.25}$$

It was also assumed:

$$\eta_{am,2} = 1 - \eta_{ch} \tag{1.26}$$

i.e. the channeling efficiency η_{ch} was considered the only alternative to the amorphous interactions. Considering the quantity:

$$\frac{q_1 - q_2}{q_1} = \frac{N_{Tot1} \cdot \eta_{am,1} - N_{Tot,2} \cdot \eta_{am,2}}{N_{Tot,1} \cdot \eta_{am,1}} = \frac{N_{Tot,1} - N_{Tot,2} \cdot (1 - \eta_{ch})}{N_{Tot,1}} \tag{1.27}$$

if $N_{Tot1} = N_{Tot2}$ then the equation becomes

$$\frac{q_1 - q_2}{q_1} = \eta_{ch} \tag{1.28}$$

that, in hypothesis of zero-divergence of the impinging beam, would correspond to the single passage probability. In reality, being the multi turn process more likely with the amorphous than with the channeling orientation, in general $N_{Tot,1} > N_{Tot,2}$, that implies an under-estimation of q_2 and therefore an over-estimation of η_{ch}. On the other hand, the multi turn process tends to smear the particle impacting angle, so that the divergence of the impacting particles is larger than zero, and therefore $= \eta_{ch}$ is lower than the single pass channeling efficiency.

All this effects have been considered negligible in the past.

Multi-turn efficiency:

Another possibility is to normalize the number of channeled particles N_i with respect to the total number of particles in the halo N_{Tot}, thus measuring the so-called "multi-turn" channeling efficiency, which expresses the probability for each particle to be channeled[4]. This efficiency was calculated in the past (RD22 experiment [33, 34, 35, 36]) by measuring the number of extracted particles N_i, and calculating the total rate of lost particles using beam lifetime measurements: this method, however, suffered from large uncertainties which derived by the estimation of N_{tot}. In this thesis a new method is proposed, which allows to measure the multi turn efficiency using a basic instrumentation, like a beam loss monitor located near a movable collimator downstream the crystal. All the details are given in Section 3.2.2.4.

It follows that the two efficiency measurements cannot be directly compared: the multi turn efficiency is expected to be larger that the single pass one.

1.4 State of the art for single pass crystal experiments: H8-RD22

While the rest of the thesis wilI be focused on the application of bent crystals in high energy circular accelerator, in this section an overview of the main experimental results for single pass experiments with high energy particles is presented. The reason for presenting a single pass experiment is to highlight the crystal effects presented in the theoretical introduction. In particular a short description of the H8-RD22 experiment[23, 24, 25, 26] is given, experiment which tested many different kind of crystals and configurations.

In 2006, the CERN management approved an experimental campaign with bent crystals in the North Area of the SPS. An international collaboration called H8-RD22, including CERN, INFN, PNPI, IHEP and JINP supported this activity. The experiment is still ongoing.

Many different kind of crystals were tested, both for materials and configurations. Si crystals seem to be the best performing one. For Si crystals, two different geometries were tested:

1. Strip crystal [37]: a strip of mechanically bent crystal. Bending principle: the main radius of curvature along the strip axis, impart an anticlastic radius of

---

[4]in the past this was also called "extraction" efficiency [30]

Figure 1.10: A pictorial view of the bending principle for strip crystals. A suitably cut crystal is mechanically bent at its extremities, by a C-shaped mechanical support. The curvature used in the experiments is the anticlastic one (crystal direction (111) in the picture). From [26].
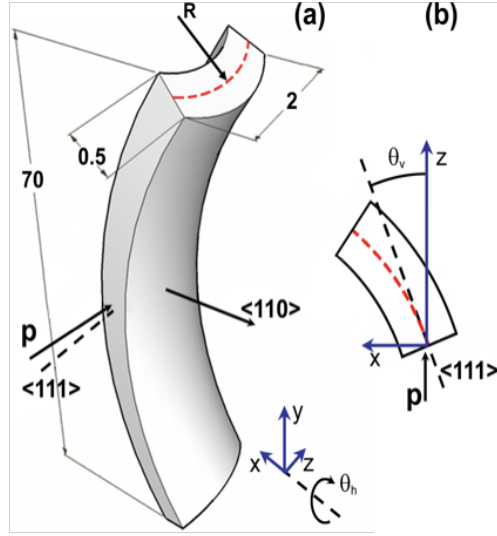
curvature to the face exposed to the beam. The bending principle is shown in Figure 1.10.

2. Quasi-mosaic crystal [38]. Bending principle: a crystal holder gives the principal curvature to the crystal axis. This generates an anticlastic curvature of the larger face, and, at the same time, the quasi-mosaic curvature of the (111) planes parallel to the thinner face. This is due to the anisotropy of the elastic tensor force, therefore it depends on the cut of the crystal. The bending principle is shown in Figure 1.11.

Figure 1.11: A pictorial view of the bending principle for quasi-mosaic crystals. A suitably cut crystal is mechanically bent at its extremities, by a C-shaped mechanical support (other kind of mechanical supports are possible). The curvature used in the experiments is the anticlastic one (crystal direction (111) in the picture). From [26].
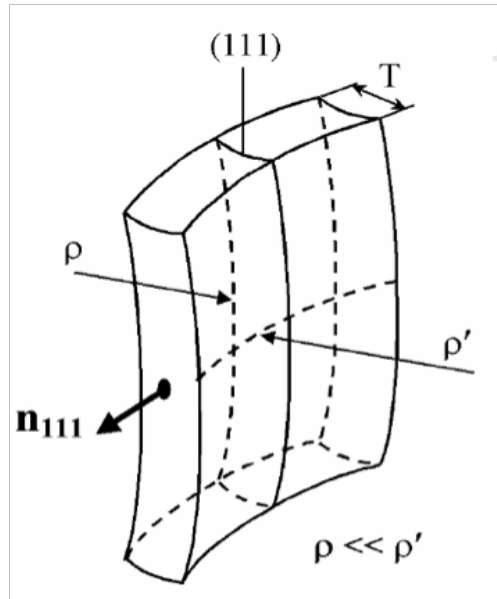
In this section only results for single crystals are presented, but it is worth to notice

that multi crystal configurations have been tested as well: assembly of many crystals mechanically aligned to each other were used to produce a cascade of multiple reflections and to measure the multi-process probability [39].
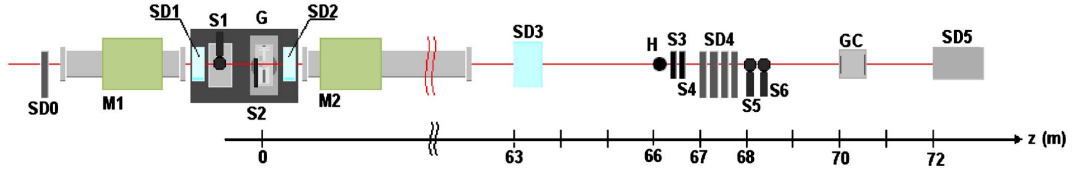
Figure 1.12: The detector of the H8-RD22 Collaboration. A goniometer (G) is used to align the crystal planes with the direction of incoming beams. A set of high-resolution Si microstrip detectors placed in the crystal zone (SD0-SD2) and about 70 m downstream (SD3-SD5), a high-rate gas chamber GC, and a scintillator trigger system (S1-S6) constitute the detector. From [27].

The layout of the experiment is shown in Figure 1.12 [27]. The crystal is mounted on a high precision goniometer which allows to orient it with respect to the beam with a precision of 1 μrad. The detector is based on Si strips and scintillator counters. Single particle trajectories are identified in the two detector arms, by which the incoming and outgoing angles are reconstructed. The measured difference in angle gives the effective crystal kick. The single particle counter capability of the telescopic system allowed to precisely calculate the fraction of particles for each deflection angle, and then to give an estimate of the efficiency for the channeling and the volume reflection effects.

In the framework of the H8-RD22 experiment, both primary protons from SPS and secondary emitted particles (mainly leptons) have been used during the tests. Here the focus is on the results obtained with the high energy proton beam (400 GeV). The divergence of the beam is of about 8 μrad.

The measured deflection angle induced by a Si strip crystal is shown in Figure 1.13 as a function of the crystal-beam orientation. The crystal has (110) channeling planes with a bending angle of 162 μrad. Its length in the beam direction is of 3 mm. The planar potential for (110) planes is $U_0 =$ 22.7 eV and corresponds to a critical angle of 10.6 μrad. The multiple scattering angle of 400 GeV protons in this crystal is equal to 5.3 μrad (i.e. small with respect to the critical angle). The results for quasi-mosaic crystals are qualitatively similar, though the calculated efficiencies are different.

The colour code in Figure 1.13 identifies the fraction of deflected particles. Six
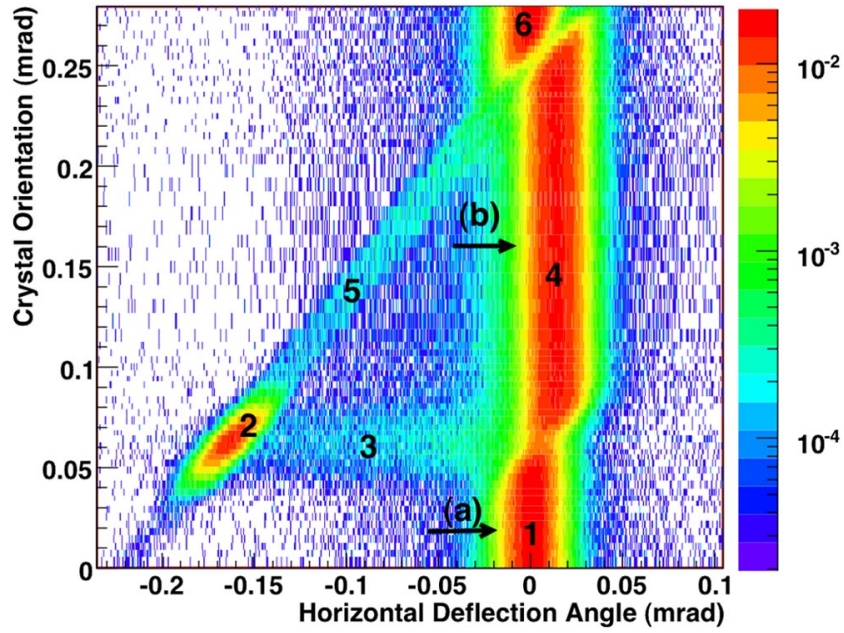
Figure 1.13: Beam intensity recorded by the Si microstrip detectors as a function of the horizontal deflection angle (x axis) and the crystal orientation (y axis). Six regions can be distinguished: (1) and (6) nonchanneling mode; (2) channeling; (3) dechanneling; (4) volume reflection; (5) volume capture. The angular acceptance for volume reflection and for channeling are clearly visible in the figure. From [23].

different interaction regimes are clearly visible; each one of these correspond to the crystal effects which have been explained in the first part of this chapter:

1. Region 1 (and Region 6): the beam is misaligned with respect to the crystal (110) direction. The angular spread of the particles is compatible with the multiple Coulomb scattering expected kick ($\approx 5\mu$rad). The average kick is zero.

2. Region 2: the beam is aligned for channeling. The particles in region 2 have received the full channeling kick ($\approx 160\mu$rad). The width of the channeling peak is ≈ 20 μrad, ie $\approx 2\theta_c$ (as expected, see Table 1.1).

3. Region 3: the beam is aligned for channeling, but the particles in region 3 have not received the full channeling kick: they exited the channeling mode before crossing the full crystal length. This region corresponds to the dechanneling effect.

4. Region 4: the beam is not aligned anymore for channeling, but the average kick is not zero. The average deflection is slightly larger than the critical angle ($\approx 1.5\theta_c$), and its sign is opposite to the channeling one. The angular acceptance of this region is equal to the total bending angle of the crystal θ_b (as expected, see Table 1.1). This is the volume reflection region.

5. Region 5: the angular range for this region is the same as Region 4. The particles receive a kick in the direction of the channeling kick, but with a smaller total kick. The total kick depends on the beam orientation: if the beam is misaligned of an angle $0 < \Delta\theta < \theta_b$ with respect to the crystal planes, than the average deflection associated to this region is $\theta_b - \Delta\theta$. This is the volume capture region.

The measured fractions of deflected particles with respect to the total number of particles impacting on the crystal were of about 50 % for channelling and more than 97 % for volume reflection[23]. Thorough all this thesis we will refer to this quantity as to the "single pass" efficiency of the associated process.

An example of quasi-axial channeling, already explained in Section 1.2.4 and measured during the H8-RD22 experiment, is presented in Figure 1.14 [24]. This is a measurement in axial channeling for a Si crystal, axis (111). A fraction of the initial axially channeled particles leaks into skew planar channels because the axis is also the intersection of several planes. Coherent scattering with the (111) atomic strings may accidentally direct a particle parallel to one of the skew planes; then the crystal bending strengthens the stability of this planar motion. Deflection of particles due to channeling by the strongest (110) skew channels was clearly observed as two tails departing from the axial spot.
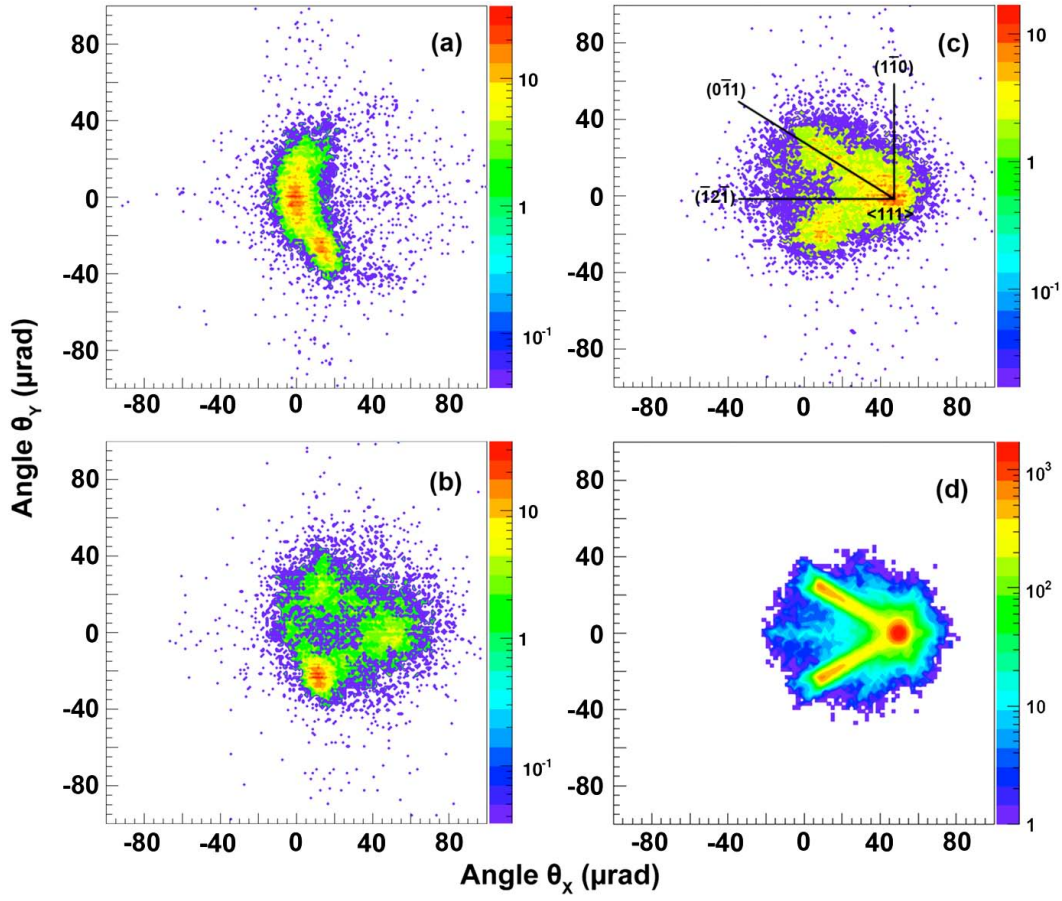
Figure 1.14: Beam intensity distribution as a function of the horizontal and vertical deflections at some orientation angles (θ_v) of the (111) axis with respect to the incident beam direction: (a) $\theta_v = -40\mu$rad, (b) $\theta_v = -15\mu$rad, and (c) $\theta_v = 0\mu$rad. (d) Simulation of experimental conditions in case of perfect alignment of the (111) axis with the beam direction, for comparison with the experimental case (c). From [24].

1.5 Past experiences in circular machines: an historical perspective

In the early 1990's, following the construction/proposal of circular accelerators in the TeV-energy range, the use of bent crystals was suggested to parasitically extract or to collimate the beam halo. In 1990 the RD22 experimental program was started in the SPS (CERN) for demonstrating the possibility to extract the beam halo with an efficiency larger than 10%[33, 34, 35, 36]. A large number of crystals, with different lengths, thicknesses and bending techniques were tested. The experiment was successful, and efficiencies of more than 10% were readily obtained [33]. It also supplied the first direct proof of multi turn channeling [36]: in order to directly observe the contribution of multi turn channeling, an artificial amorphous layer of 30μm was added to the crystal surface exposed to the beam, so that the impinging particles would need multiple passages through the crystal to overcome the amorphous layer and reach the channeling-active region. It was shown that channeling is still possible (but with lower efficiency). The RD22 experiment helped in focusing and understanding some important features of the multi turn channeling: in particular the unexpected large channeling acceptance of the crystal was attributed to the scattering of the incoming particles in the multi turn process, and to the consequent spread in angular divergence.

On the American side, a proposal for crystal collimation at SSC [40] triggered the interest in crystal experiments, and the experimental program E583 [28, 29, 30, 31] was approved at the Fermilab, US (FNAL) in 1992, just after the first successful results of RD22. The goal was proving the compatibility of a luminosity-driven crystal extraction with the delicate requirements of a cryogenic machine, without affecting the background in the experimental insertion. The experiment was successful: a record single-pass efficiency of $(38\pm11)\%$ was measured with a moderate increase of the background in the experiments [28, 31]. The E583 demonstrated the possibility of safely using crystals in a cryogenic environment.

At the end of the 1990's the first crystal collimation experiment was approved at Brookaven, US (BNL)[?, 32]. A bent crystal was installed in 2001 as a primary collimator with the aim of reducing background in the RHIC detectors. The experiment however gave controversial and unexpected results. The channeling acceptance was about 3-4 times larger than predicted by theory and simulations, and the measured single pass efficiencies (about 25%) were lower than expected: discrepancies that have been only partially explained by the unfavorable optics at the crystal location and by the multi turn effect. Most importantly, the effect on background reduction was not successful: most of the experiments had no benefits, and in some cases the use of crystal even worsened the background with respect to the one obtained with a 450-mm long copper scraper. The unsatisfactory performances were ascribed to the poor channeling efficiency of the crystal, and to the unfortunate optical parameters [32]. The experiment was dismounted while the interest in crystals was fading,

also for reasons related to the economical context and new priorities in high-energy physics.

In 2006, the successful results of the H8-RD22 single pass experiment (described in Section 1.4), the availability of new generation crystals and the insights coming from the new experimental results revived the worldwide interest about the possible use of crystals in circular accelerators/colliders. Nowadays two experiments on high energy circular machines are ongoing: the the T980 experiment at FNAL (see Chapter 4) and UA9 experiment in the SPS (see Chapter 5). Both experiments are presented in this thesis, their results constituting the core of the experimental results.

Chapter 2

Collimation and Crystal Cleaning Theory

In this Chapter the necessary theory for this thesis is given: at first we recall the basics of accelerator physics, then we present the main concepts of collimation theory. In particular the last section is dedicated to two important aspects of crystal collimation theory:

- the angular spread of the off momentum particles impinging on the crystal edge, treated with the grazing function formalism;

- the effect of a crystal miscut on the particle-crystal interaction.

33

2.1   Basics of accelerator physics

It is beyond the purpose of this thesis to give an exhaustive overview of the physics of high energy accelerators. For a complete introduction we refer to accelerator physics books like [41, 42]. In this section the fundamental concepts which will be used in this thesis are briefly recalled.

If we imagine that a circulating particle in a circular accelerator experiences only linear magnetic fields (i.e. only dipoles and quadrupoles), and that there is no coupling between vertical, horizontal and longitudinal planes, we can decouple the equations of motion for the different planes and solve them independently. This is assumed in the following. In this section we refer to the s coordinate as to the longitudinal direction and to the z coordinate for the transverse one (which remains valid both for horizontal and vertical case).

In the assumed approximation, the total transverse displacement z_T of a particle is the sum of its betatron z_β displacements and the transverse displacement z_s associated to the dispersion:

$$z_T \ = \ z_\beta + z_s \tag{2.1}$$

The betatron displacement and angle oscillate according to

$$z_\beta \ = \ a_z \, \sin(\phi_z) \tag{2.2}$$

$$z_\beta' \ = \ \frac{a_z}{\beta} \left(\cos(\phi_z) - \alpha \sin(\phi_z) \right) \tag{2.3}$$

thus describing an ellipse in the $z - z'$ phase space (see Figure 2.1). Here β (betatron function) and $\alpha = -\frac{1}{2}\frac{d\beta}{ds}$ are the Courant-Snider optical functions (also called Twiss parameters) for the z direction at the s coordinate[1] and a_z is the amplitude of the betatron oscillation. The betatron phase ϕ_z in equation 2.2 advances with turn number t according to

$$\phi_z(t) \ = \ 2\pi Q_z t + \phi_{z0} \tag{2.4}$$

where Q_z is the number of betatron oscillations in one turn (betatron tune) and ϕ_{z0} is the initial phase.

For each particle, a constant of motion $\bar{\varepsilon}_z$ can be defined, proportional to the action of the particle in the transverse phase-space $z - z'$: this is the single-particle emittance, which satisfies the equation:

$$\bar{\varepsilon}_z = \gamma \, z^2 + 2\alpha \, zz' + \beta \, z'^2 \tag{2.5}$$

where the quantity $\gamma = \frac{1+\alpha^2}{\beta}$ has been introduced, which completes the set of the Twiss parameters. For the full set of particles composing the beam, a statistical

---

[1]They can be derived from the solutions of the equation of motion in the transverse plane.
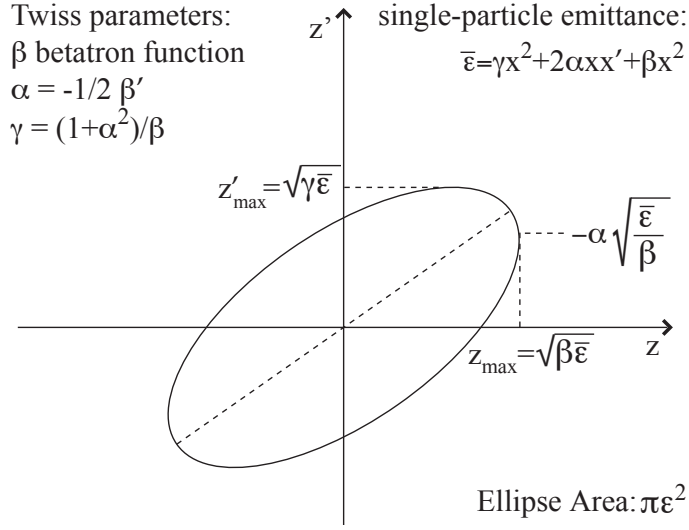
Figure 2.1: Transverse z-z' phase space. The orbit shown for a particle with the design momentum $(p_i - p_0 = 0)$. The definition and meaning of the Twiss parameters and of the single particle emittance are shown. The primed quantities stand for the derivatives with respect to the longitudinal coordinate s.

quantity ε_z can be defined: the so-called beam emittance, i.e. the rms value of the single-particle emittances. Using the emittance, the rms beam size σ_z and the rms divergence σ'_z can be defined:

$$\sigma_z = \sqrt{\varepsilon \beta} \tag{2.6}$$

$$\sigma'_z = \sqrt{\gamma \varepsilon} \tag{2.7}$$

In the following it will be convenient to express the particle betatron amplitude a_z as a function of the rms beam size:

$$a_z = n_z \cdot \sqrt{\varepsilon \beta} \tag{2.8}$$

where n_z is the normalized betatron amplitude of the particle.

Similarly, the synchrotron displacement and angle are

$$z_s = D\,\delta \tag{2.9}$$
$$z'_s = D'\,\delta \tag{2.10}$$

Here D (dispersion) and $D' = \frac{\partial D}{\partial s}$ (dispersion prime) are optical quantities, i.e. they depend only by the magnetic layout of the machine, and not on the particle characteristics. The quantity $\delta = \Delta p / p$ is the relative momentum offset, which

performs synchrotron oscillations according to

$$
\begin{aligned}
\delta &= a_s \sin(\phi_s(t)) & (2.11) \\
&= a_s \sin(2\pi Q_s t + \phi_{s0}) & (2.12)
\end{aligned}
$$

where a_s is the synchrotron amplitude, Q_s is the synchrotron tune and ϕ_{s0} the initial synchrotron phase. The RF cavities used to accelerate the beam are responsible for this oscillation. If considering the momentum distribution of the beam, we can use the rms momentum offset from the design momentum p_0:

$$
\sigma_p^2 = \frac{1}{N} \sum_{i=1}^{N} (p_i - p_0)^2 \tag{2.13}
$$

to express the synchrotron amplitude as:

$$
a_s = n_s \frac{\sigma_p}{p} \tag{2.14}
$$

where n_s is the normalized synchrotron amplitude of the particle.
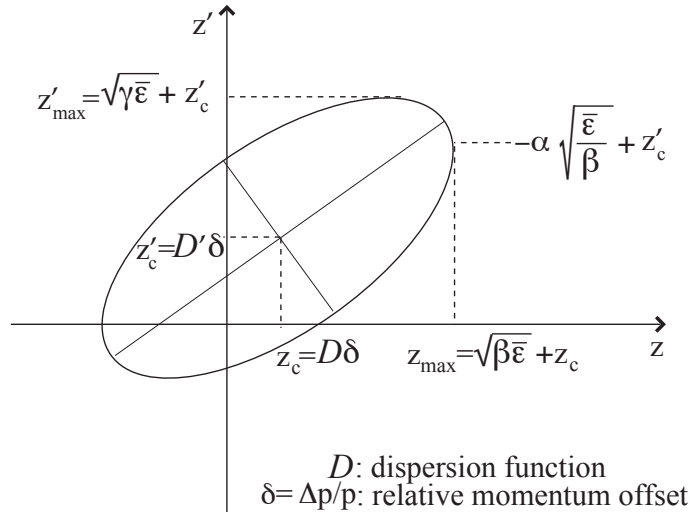
Figure 2.2: Transverse z-z' phase space. The orbit shown for a particle with a relative momentum offset $\delta = \Delta p/p$. The prime quantities are the derivatives with respect to the longitudinal coordinate s.

The transverse displacement at the s position (equation 2.1) is then:

$$
z_T = n_z \sqrt{\varepsilon \beta} \cos(\phi_z) + D \cdot n_s \frac{\sigma_p}{p} \sin(\phi_s(t)) \tag{2.15}
$$

Taking the derivative with respect to s we get the total angle $z'_T = \frac{\partial z}{\partial s}$ of a particle, that is written in general as:

$$z'_T = n_z \sqrt{\frac{\varepsilon}{\beta}} \left[\cos(\phi_z) - \alpha \sin(\phi_z) \right] + D' \cdot n_s \frac{\sigma_p}{p} \sin(\phi_s) \qquad (2.16)$$

The knowledge of the particle orientation is extremely important in case of a crystal collimator: for controlling the crystal operational mode (e.g. channeling vs amorphous), it is necessary to know the impacting angle of the particle with respect to the crystal planes, and to quantify the impact of an eventual angular spread on the crystal usability. More details about this issue are given in Section 2.3.1.

2.1.1 Floquet's transformations and normalized phase space

In this section the effect of a kick $\Delta\theta$ on the betatron motion is studied. This case is of particular importance for collimation studies: the case of a particle receiving a kick at the maximum of its betatron extension[2] is considered here. Under the specified conditions the kick takes the particle to an higher amplitude orbit in the phase-space, and it also generates a shift in phase. The sketch of the amplitude and phase variation for the channeling case is shown in Figure 2.3.
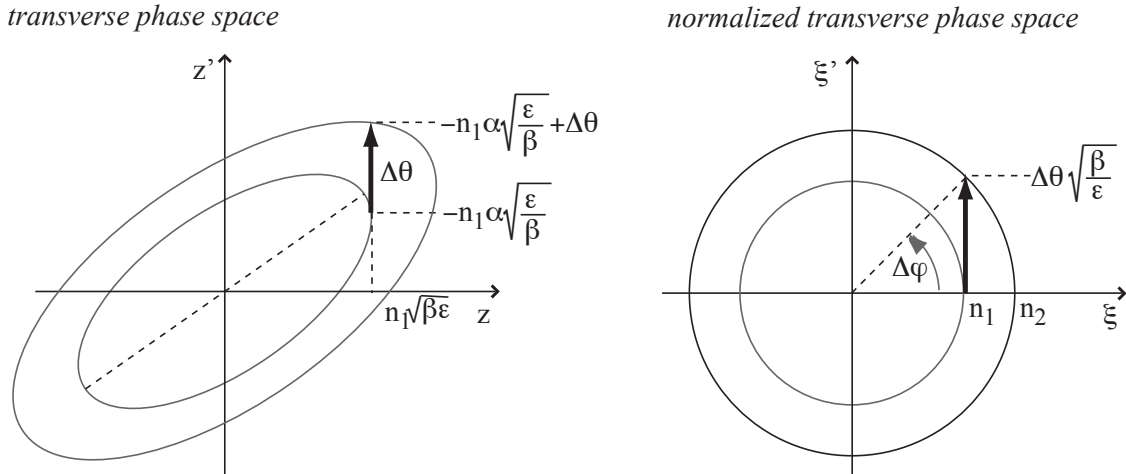
Figure 2.3: Particle receiving a kick at the maximum of its betatron extension. The case of initial phase $\phi_0 = 0$ is shown. The process is shown both in the normal and in the normalized transverse phase space.

---

[2]which is compatible with the case of particle impacting on a primary collimator, for continuous slow diffusion of the halo outwards.

The process becomes clearer if represented in the normalized phase space, where the Floquet transformations are applied to the canonical coordinates:

$$z \quad \rightarrow \quad \xi = \frac{z}{\sqrt{\beta \cdot \varepsilon}} \tag{2.17}$$

$$z' \quad \rightarrow \quad \xi' = \frac{z \cdot \alpha + z' \cdot \beta}{\sqrt{\beta \cdot \varepsilon}} \tag{2.18}$$

Here α, β are the Twiss parameters and ε is the rms emittance. In this representation the usual equations describing the particle trajectory (an ellipse in the phase space $z - z'$):

$$z_\beta \quad = \quad n_1 \sqrt{\varepsilon \beta} \, \sin(\phi_z) \tag{2.19}$$

$$z'_\beta \quad = \quad n_1 \sqrt{\frac{\varepsilon}{\beta}} \, (\cos(\phi_z) - \alpha \sin(\phi_z)) \tag{2.20}$$

become the simpler equations of a point moving on a circle, with the radius equal to the betatron amplitude n_1:

$$\xi_\beta \quad = \quad n_1 \sin(\phi_z) \tag{2.21}$$
$$\xi'_\beta \quad = \quad n_1 \cos(\phi_z) \tag{2.22}$$

Taking into account that, in the same space, the kick $\Delta\theta$ becomes $\Delta\theta \cdot \sqrt{\frac{\beta}{\varepsilon}}$, we can derive the expression to estimate the new amplitude n_k after a kick and the phase shift $\Delta\phi$:

$$n_k \quad = \quad \sqrt{n_1^2 + \Delta\theta^2 \cdot \frac{\beta}{\varepsilon}} \tag{2.23}$$

$$\Delta\phi \quad = \quad -\mathrm{sgn}(\Delta\theta) \cdot \arccos\left(\frac{n_k}{n_1}\right) \tag{2.24}$$

Ideally the optical functions do not depend on the particle momentum or amplitude.

The kick $\Delta\theta$ is considered positive when it is directed outward, and gives a negative phase shift, as shown in Figure 2.3 (remember that the phase advance in phase space is always clockwise).

2.2   Principles of standard collimation

In this section the motivations for collimation in a circular machine (Section 2.2.1) and the standard techniques for betatron and momentum cleaning (Section 2.2.2) are described. At last, in Section 2.2.3, the quantities generally used to qualify the effectiveness of a collimation system are defined.

The theory presented is valid for any collimation system, and therefore it is also applied in case of crystal collimation.

2.2.1   Motivation for collimation

In a perfectly linear machine, with infinite aperture and no energy losses, there would be no need for a halo cleaning system. The halo would not be generated, and anyway could not be lost. However in the reality two facts must be taken into account:

- - The beam particles generally drift outwards, generating the halo. Even if we usually assume that the transverse emittance is a constant of motion, in reality a series of processes slowly vary the amplitude of the betatronic oscillation (see Section 3.1.3). Moreover, for large distances from the geometrical center, the non linearities of the magnetic fields become more and more important, thus defining a maximum region A_{dyn} (dynamic aperture) in the phase space over which the motion is not stable, and the emittance is not conserved anymore. In highly non-linear machines the dynamic aperture can be even smaller than the available physical space (geometric aperture).

- - the geometric aperture A_{geom} of the machine is limited, defined by the beam pipe and by the aperture settings of the movable elements. If considering the real beam size in the transverse direction z, i.e.

$$\sigma_z^{real} = \sqrt{\beta\,\varepsilon + (D\,\sigma_p/p)^2} \qquad (2.25)$$

the measure of the available space for the beam is called beam acceptance A_z, and is defined as the maximum emittance that can fit in the machine geometrical aperture, considering the maximum allowed energy spread Δp_{buck}:

$$\varepsilon_x^{max} = \min_{0 \le s \le L} \left[\frac{A_{geom}^2 - (D \cdot \Delta p_{buck}/p)^2}{\beta(s)} \right] \qquad (2.26)$$

In addition one needs to avoid large radiation deposits along the ring (and in the detectors) . The requirements become obviously more stringent in case of superconducting machines, whose correct functioning could be hindered by energy losses in superconducting elements.

2.2.2   Betatron and momentum collimation: the multi-stage cleaning

As discussed in Section 2.1, for a linear machine and in absence of coupling between different planes, the transverse motion can be considered as the superposition of two independent motions, i.e. the transverse betatron motion and the synchrotron one. Since in a machine we are generally interested in cleaning both the particles with high betatron amplitude and the particles with high momentum deviation, it is possible to exploit the linearity of equation 2.1 for separating the two tasks. This has been done, for example, in LHC [9], where two different insertions are dedicated to collimation:

- an insertion characterized by low dispersion value, where the particles with largest distance from the beam center are characterized by high betatronic amplitude, regardless their momentum offset: this is an example of betatron cleaning.

- an insertion characterized by high dispersion value, so that the particles with largest distance from the beam center are mainly characterized by a high momentum offset, and not only by their betatronic amplitude: this is an example of momentum cleaning.

For high energy machines, where the halo has a highly destructive power, a multi-stage collimation system is mandatory, i.e. a series of collimators set with different aperture settings. The primary collimators, which are set to be the closest elements to the beam center, are intended to intercept the primary halo and to spray it downstream. The so-generated secondary halo is intercepted by the secondary collimators, whose normalized aperture n_2 (i.e. distance from the beam center in σ units) and phase advance with respect to the beam center must be optimized to maximize the efficiency of the system.[3] In this section the basic principles of multi-stage cleaning for both betatron and momentum cleaning are explained.

2.2.2.1 Betatron multi-stage cleaning theory

The pure betatron cleaning process is first considered, i.e. the cleaning of the particle with respect to their normalized betatron amplitude n_z. A region of zero dispersion and, in first approximation, only the scattering in the same plane of the analyzed halo is considered. In the following it is also assumed that the particles hit the primary collimator at the maximum of their betatron extension[4], and a kick $\pm\Delta\theta$ is given to the particle. The particles are first intercepted by the primary collimator, whose normalized aperture n_1 is the smallest one in the collimation system. The secondary collimators are set to a normalized aperture $n_2 > n_1$.

If the normalized apertures n_1, n_2 are fixed, the system is optimized if the secondary collimators can collect all the particles directly scattered by the primary collimator which have a normalized betatron amplitude higher than n_2. This is achieved when:

- the normalized amplitude of the scattered particle n_k is equal or larger to n_2. From equation 2.23 we get the expression for the minimum kick to get the required amplitude:

$$\Delta\theta_{opt} = \pm\sqrt{\frac{\varepsilon}{\beta}} \cdot \sqrt{n_2^2 - n_1^2} \qquad (2.27)$$

---

[3]For a rigorous definition of efficiency of a collimation system we refer to the concepts described in Section 2.2.3.
[4]which is reasonable for continuous slow drift of the halo outwards

positive kick/negative phase shift:
optimal phase advance: -Δφ_p

negative kick/positive phase shift:
optimal phase advance: π–Δφ_n
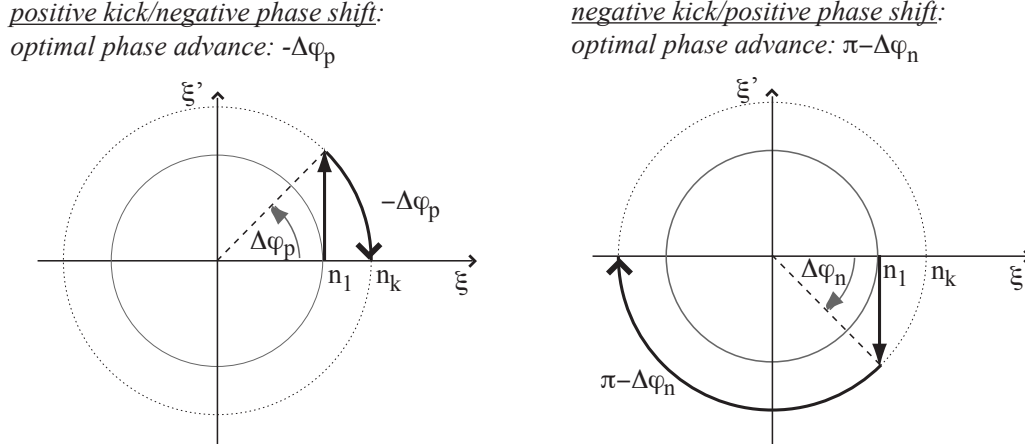
Figure 2.4: Negative and positive kick - and optimal phase advances for catching.

- the phase advance between the primary and secondary collimators $\Delta\phi^{coll}$ is such that the particle which received the kick $\Delta\theta_{opt}$ is at its maximum excursion at the collimator location.

As it is stated by equation 2.27, both positive and negative kicks can take the particle to the desired normalized amplitude n_2, and in principle both can result from the particle-collimator interaction. The value of the corresponding optimal phase advance depends on the sign of the kick $\Delta\theta_{opt}$: for this reason two different secondary collimator, covering both phase advances, are need for each primary collimator jaw. For positive (i.e. outwards) kicks the phase shift $\Delta\phi$ is negative, and the optimal phase advance $\Delta\phi^{coll}_{opt+}$ must be equal and opposite, as shown in Figure 2.4. Using equation 2.24, we get:

$$\Delta\phi^{coll}_{opt+} = \arccos\left(\frac{n_2}{n_1}\right) \tag{2.28}$$

For negative kick the optimal phase advance is:

$$\Delta\phi^{coll}_{opt-} = \pi - \arccos\left(\frac{n_2}{n_1}\right) = \pi - \Delta\phi^{coll}_{opt+} \tag{2.29}$$

For a detailed discussion on the optimization of a two stage collimation system with a two dimensional treatment, please see [43].

2.2.2.2 Momentum multi-stage cleaning theory

The betatron collimation theory must be complemented with momentum cleaning considerations: while in a zero dispersion region only the betatron motion determines the particle position, everywhere else the particles are sorted with respect to

their momentum offset $\delta = \Delta p / p_0$ (equation 2.9). A maximum acceptable value of $\Delta p / p_0$ exists, called the energy acceptance of the machine, which is determined by the RF cavities: particles with momentum within the energy acceptance limit are inside a stability region (RF bucket) in the longitudinal phase space $\Delta p - s$, and their momentum oscillates periodically around the design momentum p_0(equation 2.11). It is therefore not necessary or even desirable to remove the stable particles. However, if a particles falls out of the RF bucket before the ramp, the particles cannot be accelerated and they are lost at the beginning of the ramp. On the other hand if a particle is not in the RF bucket in a storage ring its momentum is fated to decrease indefinitely for synchrotron radiation, and so its distance from the beam center. For this reason this off momentum halo is particularly likely to hit the aperture, and must be removed by the collimation system.

Figure 2.5: Off momentum particles grazing the collimator edge, in the normalized ξ-ξ' phase space. The circle centered with the axis corresponds to the on-momentum particle trajectory.
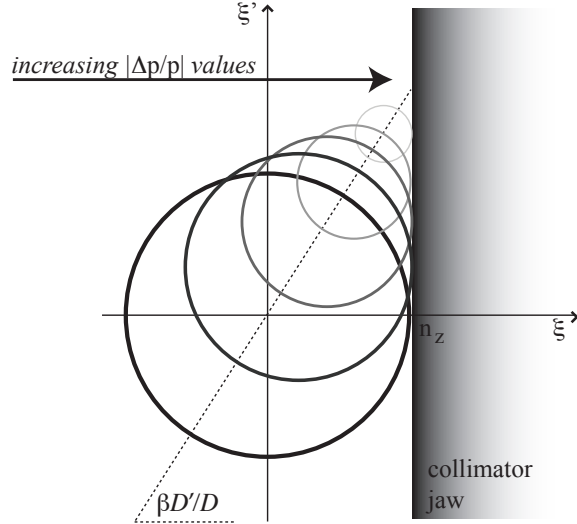
For cleaning the off momentum particles without touching the stable particles in the RF bucket, a large dispersion value is needed. As shown in Figure 2.5, a collimator located in dispersive region with normalized aperture n_z, would cut different off momentum particles to different starting betatron amplitudes $n_0(\delta)$, according to the equation:

$$n_0 \cdot \sqrt{\varepsilon_z \beta_z} + \delta D_z = n_z \cdot \varepsilon_z \beta_z \qquad (2.30)$$

where we again assume grazing particles on primary collimators. Ideally there should be no dependence of the optical functions on the particle momentum: in this case the equation 2.30 describes a line in the $n_0 - \delta$ plane [44]. This is generally true for particles in the RF bucket.

As shown in Figure 2.5, generally in case of off momentum particles also the impacting angle on the collimator edge changes. : this is particularly important for

crystal collimators, whose angular acceptance in channeling mode is of the order of few μrad. This aspect is analyzed in Section 2.3.1 with the grazing function formalism.

2.2.3   Global and local cleaning inefficiency

When performing tracking simulations for collimation studies, the quantity that is generally used to characterize a collimation system is called the inefficiency of the system. It is possible to evaluate both a global parameter (global inefficiency) or a local one (local inefficiency):

- The global inefficiency η_{ineff}^{gl} is a function of the betatron amplitude n_z, and it is defined as the number of particles which escape the collimation system with an amplitude higher than n_z over the total number of particle absorbed.

$$\eta_{ineff}^{gl}(n_z) = \frac{N_{abs}(n > n_z)}{N_{Tot}} \tag{2.31}$$

- It can be defined separately for the horizontal and vertical normalized amplitude, or for the radial amplitude $n = \sqrt{n_x^2 + n_y^2}$. The local cleaning inefficiency η_{ineff}^{loc} is defined as:

$$\eta_{ineff}^{loc} = \frac{N_{abs}(dl)}{N_{Tot} \cdot dl} \tag{2.32}$$

  e.g. the number of particles N_{abs} hitting the aperture in the longitudinal interval dl over the total number of particles absorbed by the collimation system N_{Tot}, normalized over the length. The plot of the local cleaning inefficiency along the ring is called loss map.

Whenever possible it is more meaningful to evaluate the local losses: what usually matters, e.g. for the safety of the superconducting magnets, is the local release of energy. It is therefore common to qualify a collimation system by using the local cleaning inefficiency.

2.3   Crystal cleaning theory

In this section aspect of the collimation theory, particularly important in case of crystal collimation, are treated:

- The grazing function g is introduced in section 2.3.1– a synchrobetatron optical quantity that is analogous (and closely connected) to the Twiss and dispersion functions β, α, D and D'. It parametrizes the rate of change of total angle with respect to synchrotron amplitude for grazing particles, which just touch the surface of an aperture when their synchrotron and betatron oscillations are

simultaneously (in time) at their extreme displacements. The grazing function can be important in case of crystal collimation operation – especially for the channeling mode, since the angular acceptance of the channeling process is a few μrad for impinging particles with energies of the order of TeV.

- The crystal collimation option relies on the knowledge of the bending angle of the crystal, and therefore on the expected channeling kick. A manufacturing inaccuracy such as a miscut of the crystal, however, can affect the channeling angle perceived by the particles grazing the crystal surface. The miscut angle effects are discussed in section 2.3.2.

2.3.1   Grazing function for crystals

Generally the betatron and synchrotron amplitudes a_z and a_s vary with time if any diffusion mechanisms are present. Here, in the limit of zero diffusion, the typical fractional change in a_z or a_s is assumed to be very much less than one in one betatron or synchrotron period. After an extremely long time these amplitudes will have evolved so that the aperture can only just be touched when its betatron and synchrotron displacements are simultaneously in time at their extrema – either maxima or minima, such that:

$$a_z + \mid D \mid a_s \ = \ \mid z_c \mid \tag{2.33}$$

This equation correlates the betatron and synchrotron amplitudes of the particles which are just grazing the collimator edge (displaced of z_c), i.e. particles with a vanishing impact parameter. Simultaneous betatron and synchrotron oscillation extrema are achieved on turn number t when the phases are

$$\phi_x(t) \ = \ \mathrm{sgn}(z_c) \quad \pi/2 \tag{2.34}$$
$$\phi_s(t) \ = \ \mathrm{sgn}(z_c)\,\mathrm{sgn}(D) \quad \pi/2 \tag{2.35}$$

where the possibilities of negative displacement x_c and negative dispersion D are explicitly taken into account. The *grazing angle* z'_G – the total angle of a grazing particle – is found by substituting these phases into Equation 2.16 and by using Equation 2.33 to eliminate a_z. It is

$$z'_G \ = \ -\frac{\alpha}{\beta} z_c \ + \ \mathrm{sgn}(z_c)\,\mathrm{sgn}(D) \left(\frac{\alpha}{\beta} D \ + \ D' \right) a_s \tag{2.36}$$

Thus the grazing angle depends linearly on the synchrotron amplitude a_s, and the linear slope of grazing angle with respect to synchrotron amplitude is

$$\frac{dz'_G}{da_s} \ = \ \mathrm{sgn}(x_c)\,\mathrm{sgn}(D) \left(\frac{\alpha}{\beta} D \ + \ D' \right) \tag{2.37}$$

We define the grazing function g as the dimensionless optical function:

$$g \equiv \left(\frac{\alpha}{\beta} D + D' \right) \qquad (2.38)$$

The grazing function g parametrizes the rate of change of total angle with synchrotron amplitude for grazing particles – those that just touch the surface of a collimator or other aperture when their synchrotron and betatron oscillations are simultaneously (in time) at their extreme displacements.
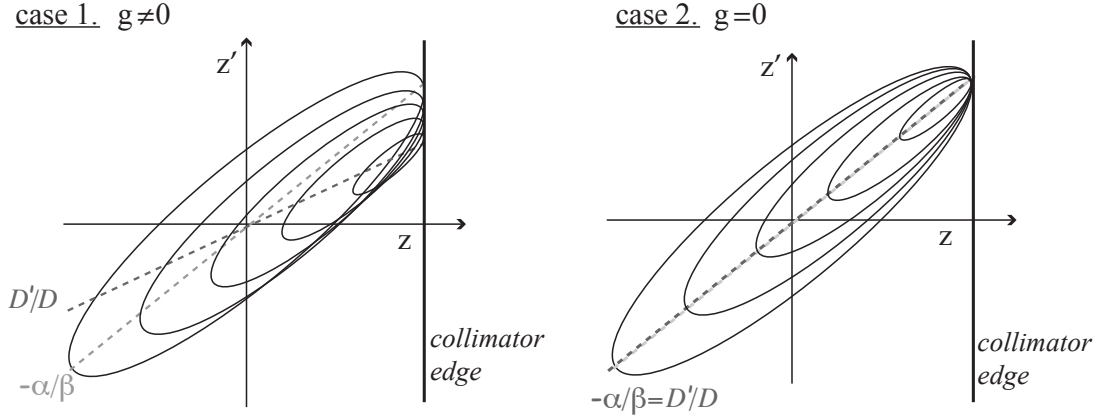
Figure 2.6: Grazing condition in the z-z' phase space: on the left hand side, the general case of off momentum particles grazing the crystal face, where the spread in z' is shown. On the right hand side the configuration of the off momentum particle orbits when the grazing function value is zero.

Any linear dependence of the grazing angle on the synchrotron amplitude is undesirable, since it may cause particles with some synchrotron amplitudes to fall outside the limited angular acceptance of a crystal.

The rigorous synchrobetatron condition for constant grazing angle is

$$g = \frac{\alpha}{\beta} D + D' = \sqrt{\beta}\, D'_N = 0 \qquad (2.39)$$

This is a condition on the optics, independent of the emittance and the energy spread of the beam. Since β is positive-definite, a collimator is ideally placed at a location where normalized dispersion is at a local maximum or minimum. This condition has already been noted in the literature [45, 46, 47, 43]. A pictorial view of the phase space $z - z'$ for off momentum particles grazing on the crystal edge is shown in Figure 2.6, both in case of grazing function different or equal to zero. In Figure 2.6 it is illustrated the meaning of the condition:

$$\frac{D'}{D} = -\frac{\alpha}{\beta} \qquad (2.40)$$

which is equivalent to Equation 2.39.

Two particular trivial solutions to the rigorous condition expressed in equation 2.39 are immediately obvious:

1. $D = D' = 0$: anywhere in a dispersion-free straight.

2. $\alpha = D' = 0$: simultaneous extrema of β and D, such as (logically) in the middle of a quadrupole at the boundary of a matched half-cell.

General solutions to the rigorous condition can be found at more practical locations in magnet-free straights which are *not* dispersion free. Further, it is sufficient for g to be "small enough" – complete rigor is not required. A complete description of the grazing function features can be found in [12], including the propagation of the grazing function through drifts, dipoles, and quadrupoles, and analytic expressions for g in perfectly matched periodic FODO cells, and in the presence of β or D error waves.

Table 2.1: Nominal optics, grazing functions, and other values at primary collimators in four accelerators. The last column records the grazing angle spread across the RF bucket.

	α	β [m]	D [m]	D' [10^{-3}]	g [10^{-3}]	E [TeV]	a_{Bucket} [10^{-3}]	σ_p/p [10^{-3}]	$\Delta x'_{TB}$ [μrad]
RHIC	-26.5	1155.0	-0.864	-16.2	3.6	0.10	1.50	0.50	5.40
SPS	-2.21	96.1	-0.880	-19.0	1.2	0.12	1.10	0.40	1.32
Tevatron	-0.425	67.5	1.925	15.0	2.9	0.98	0.45	0.14	1.31
LHC (IR3)	1.72	131.2	2.100	-30.1	-2.5	0.45	0.97	0.31	2.43
						7.0	0.35	0.11	0.88
LHC (IR7)	2.06	152.0	0.36	-5.6	-0.7	0.45	0.97	0.31	0.68
						7.0	0.35	0.11	0.25
LHC (crystal)	1.93	136.1	0.341	-5.6	-0.8	0.45	0.97	0.31	0.78
						7.0	0.35	0.11	0.28

Here we give some practical results on the influence of g on primary collimators in four hadron colliders – RHIC, SPS, Tevatron and LHC. Table 2.1 shows that in the considered cases the primary collimators have nominal grazing functions in the range from -0.0025 to $+0.0036$, in the absence of optical errors [9, 32, ?, 48, 49, 50]. The rigorous condition $g = 0$ has not been attained in these realistic (or proposed) implementations of amorphous and crystal primary collimators. This is in part because ideal locations have not been sought, and in part because they are not available.

The crystal acceptance angle σ'_A can be compared with the grazing angle spread from the center to the edge of the RF bucket (from synchrotron amplitude $a_s = 0$
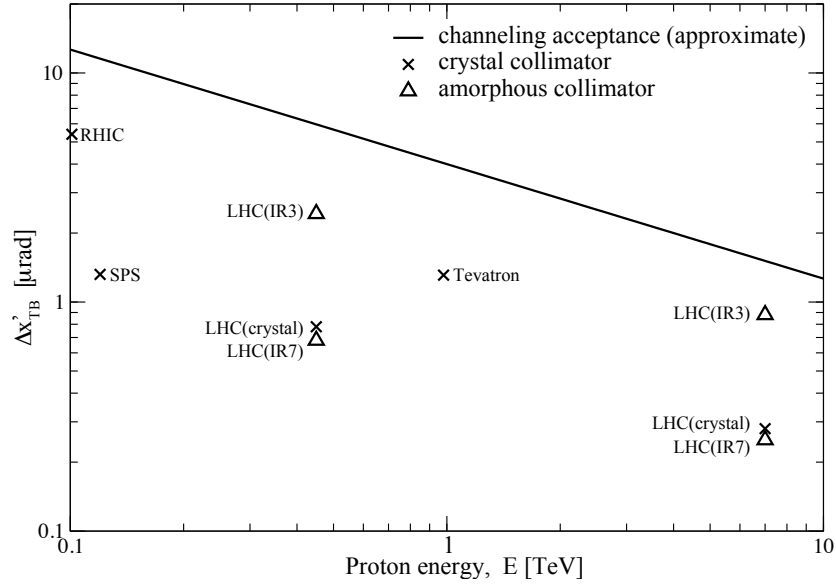
Figure 2.7: Variation of the grazing angle spread across the RF bucket as function of energy for amorphous and crystal primary collimators according to the data in Table 2.1 for RHIC, SPS, Tevatron, and LHC.

to $a_s = a_{Bucket}$). The grazing angle spread across the bucket,

$$\Delta x'_{TB} = \mid g \mid a_{Bucket} \qquad (2.41)$$

is especially relevant if a collimator is being used to intercept beam escaping from the RF bucket. Uncaptured beam is a major concern for the Tevatron and the LHC, because such beam migrates into the abort gap and can quench superconducting magnets – or even do irreversible damage – during an emergency abort [51].

The grazing angle spread across the bucket is recorded in the last column of Table 2.1. In general (avoiding scenario-specific details) it is desirable for this spread to be much less than the collimator acceptance angle,

$$\Delta x'_{TB} \ll \sigma'_A \qquad (2.42)$$

Thus the relaxed condition on the grazing function for efficient collimation is

$$\mid g \mid \ll \frac{\sigma'_A}{a_{Bucket}} \qquad (2.43)$$

Figure 2.7 shows how the grazing angle spread across the RF bucket Δ'_{TB} compares with the (approximate) channeling acceptance angle σ'_A, across two orders of magnitude in beam energy E. Both amorphous and crystal primary collimator locations are shown, with different symbols. The grazing function values g lead to

total angular spreads that are "safe" in all cases for nominal optics without errors, but by as little as a factor of two.

The grazing function is naturally small in well-matched optics with no (or small) dispersion and betatron waves. Although g is identically zero across a dispersion-free straight, it is not in general necessary to make dispersion (and the dispersion slope) zero at the collimator.

2.3.2   Crystals with miscut angle

The simulation usually considers a perfect crystal, i.e. a solid with a perfect crystalline structure and a perfect cut. While dislocations or defects in the crystal structure are expected to decrease the probability of channeling, the presence of a miscut angle affects the alignment of the crystal planes with respect to the incoming beam and, even more important, can give origin to a series of edge effects especially important when dealing with particles which have a small impact parameter. For this reason the presence of a miscut angle can seriously hinder the functioning of the designed collimation system.
In this section we give the basic definition of miscut angle, the analytical treatment of the problem, and deduce the expected edge effects.

2.3.2.1   Definition and orientation of the miscut angle

Let's first consider a straight crystal and give some definitions: we define "entrance face" the face of the crystal where the incoming beam is impacting, while we refer to the face tangent to the beam direction as "lateral face", as shown in Figure 2.8. Ideally the crystal should be cut such that the crystalline planes are perfectly aligned
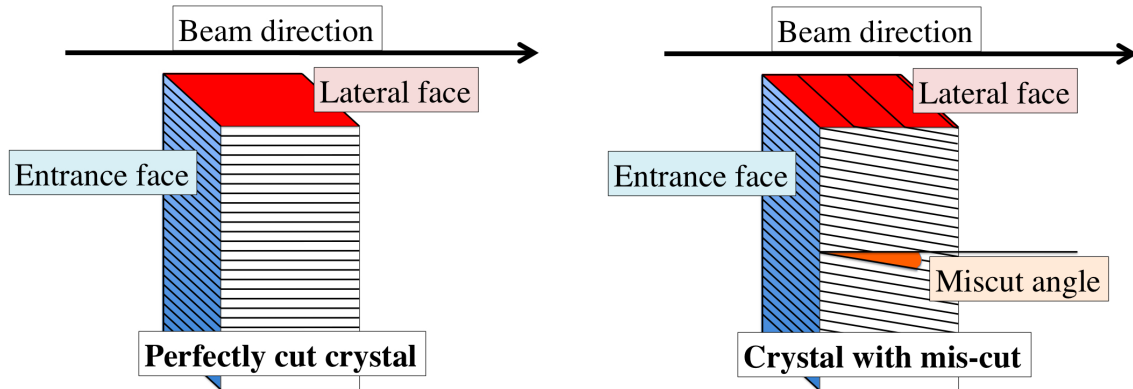
Figure 2.8: Perfectly cut crystal (on the left) and crystal with miscut angle (on the right). The entrance and lateral face of the crystal are indicated.

with the lateral face of the crystal, as indicated in Figure 2.8, image on the left hand side. In reality a non-zero angle between the lateral face and the planes is unavoidable (Figure 2.8, right): this angle is called miscut angle. In complete analogy, for bent crystals the miscut angle is the angle between the crystal plane and the tangent to the lateral face, in each point of the whole crystal length.
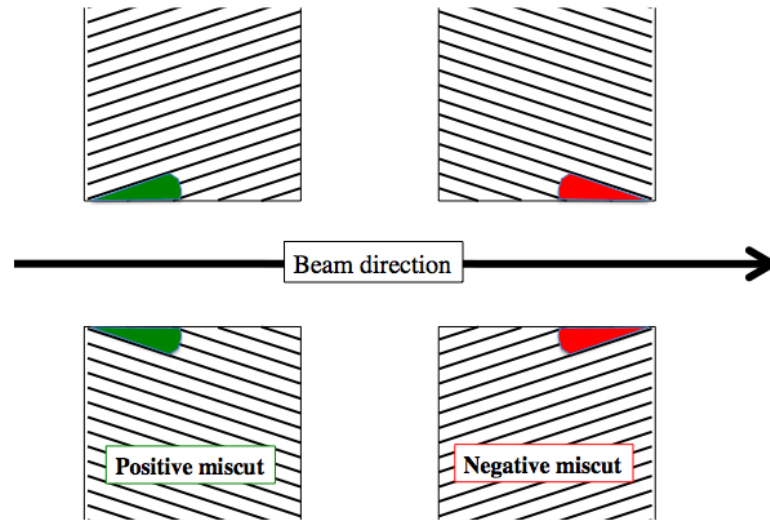
Figure 2.9: Positive and negative miscut angle in a straight crystal.

The sign assigned to the miscut angle in a certain configuration depends on the orientation of the angle itself with respect to the beam direction. The definition of positive or negative miscut angle is illustrated Picture 2.9: s being the longitudinal coordinate of the beam and assuming the crystal lateral face parallel to s, then

- Positive mis-cut angle (Picture 2.9, image on the left hand side): the absolute value of the angle between s and the crystal planes is smaller than $\pi/2$.

- Negative mis-cut angle (Picture 2.9, image on the right hand side): the absolute value of the angle between s and the crystal planes is larger than $\pi/2$.

Obviously the sign ("positive" or "negative") of the miscut angle depends on the orientation of the crystal planes with respect to the incoming beam: in order to switch the polarity of a crystal miscut angle it is enough to flip the crystal.

2.3.2.2 Edge effects in a crystal with miscut

Let's consider a zero divergence beam impacting on the crystal entrance face with a perpendicular angle. With no miscut angle (Figure 2.10, case 1), the beam is
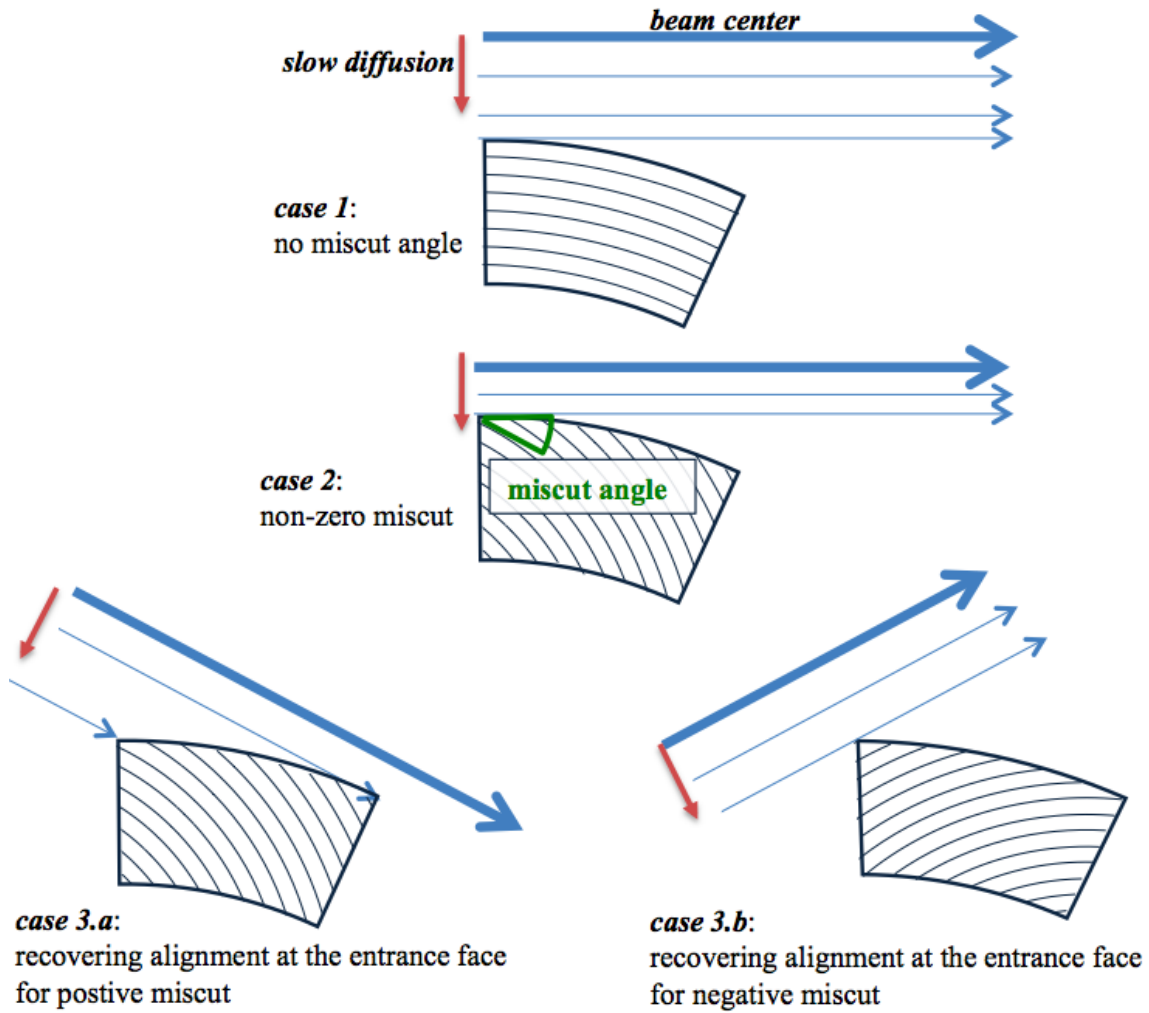
Figure 2.10: Case 1: crystal without miscut angle, with the incoming beam perpendicular to the entrance face. The particles are aligned with the crystalline planes at the entrance face. Case 2: crystal with miscut angle different from zero, with the incoming beam perpendicular to the entrance face; the particles are not aligned with the crystalline planes at the entrance face. Case 3.a: crystal with miscut angle larger than zero, with the incoming beam parallel to the crystalline planes at the entrance face. Case 3.b: crystal with miscut angle smaller than zero, with the incoming beam parallel to the crystalline planes at the entrance face.

naturally parallel to the crystalline planes at the entrance face, i.e. the crystal is in channeling orientation. However, keeping the same configuration but considering a miscut crystal (Figure 2.10, case 2), we have that the impacting particles are misaligned with respect to the crystalline planes and misalignment is equal to the miscut angle itself (by definition of miscut angle). As might be expected, it is possible to recover the channeling alignment by changing the relative orientation between the entrance face and the incoming particle, as illustrated in Figure 2.10, case 3.a (for positive miscut angles) and case 3.b (for negative miscut angles).

In a very first approximation, the only effect of the miscut angle is to change the crystal-particle relative alignment. In this section the side effect of changing the crystal orientation are investigated, and the edge effects due to the miscut angle are analyzed in details. The edge effects are particularly important in case of slow diffusion regime, i.e. when the beam halo slowly diffuses from the beam center toward the beam edge. Positive and negative miscut angles are treated separately.

2.3.2.3 Positive miscut angle

In this section the influence of a positive miscut angle on the particle-crystal interaction is analyzed. It will be demonstrated that the channeling mode is not limited to a specific particle-crystal orientation, but it is possible to have channeling in an angular range which correspond to the bending angle of the crystal. In this section, for simplicity, we shall consider only the case where the miscut angle is larger than the full crystal bending angle, which is the worst possible case, and the one true for the crystal used in the T980 experiment (see section 4.2.1). The full analytical treatment covering all the possible cases is presented in Appendix A.

In the following we consider a crystal with length l_{cry}, curvature radius R_{cry} and positive miscut angle θ_{mc}. The resulting bending angle θ_b is $\theta_b = l_{cry}/R_{cry}$. As shown in Figure 2.11, with the coordinate s_{cry} we refer to the curvilinear coordinate which follows the lateral face of the crystal, while the direction perpendicular to the entrance face is t. The relative angle between the direction t and the particle direction is called θ (see Figure 2.11).

For treating the positive miscut angle it is important to keep in mind few basic considerations:

- In the assumed zero divergence beam in zero-limit diffusion regime, the particles would first hit the point of the crystal which is closer to the beam center. For any impacting point along the whole crystal length, the particle relative angle θ remains unchanged;

- Even fixing the incoming particle angle, the relative alignment with the crystal
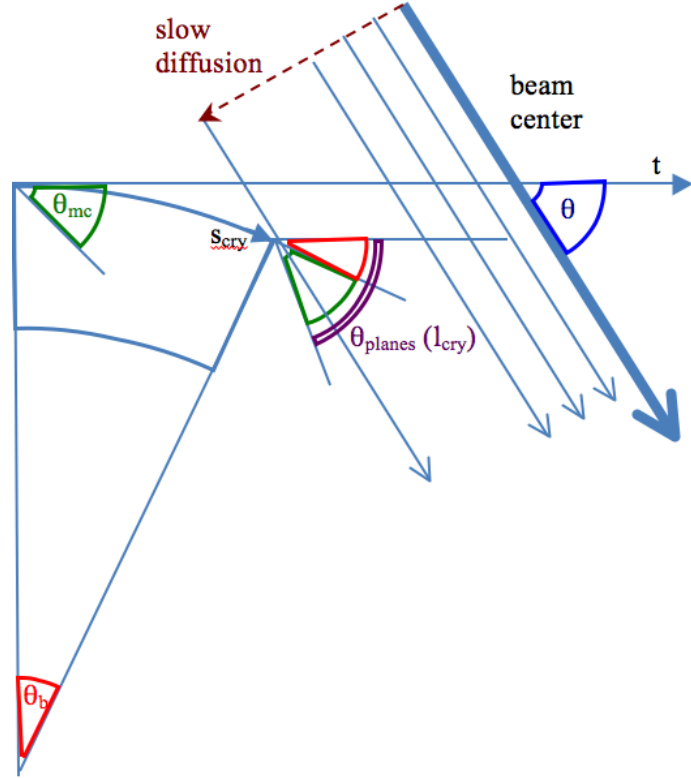
Figure 2.11:   Zero divergence beam impacting on the crystal surface. The bending angle θ_b, the miscut angle θ_{mc} and the impacting angle θ are shown. With θ_{pl} the angle between the direction t and the crystalline planes is shown.

planes changes for different crystal regions (because of the bending of the crystal). See in Figure 2.11 how the crystal planes alignment θ_{pl} changes from the entrance face ($\theta_{pl} = \theta_{mc}$) to the crystal end ($\theta_{pl} = \theta_{mc} + \theta_b$)

As already shown in Figure 2.10, in case of miscut angle, the crystal must be opportunely rotated in order to realign the incoming particle beam with the crystal planes. By definition of miscut angle, a particle angle of $\theta = \theta_{mc}$ would ensure a perfect channeling alignment (i.e. a zero angle between the crystal planes and the incoming particles) at the entrance face of the crystal. However the particle would first hit the end of the crystal, where the relative angle with the crystalline planes is lower, and the only possible interaction is the amorphous one. In order to reach the region suitable for channeling, a large amorphous region must be overcome. This would lower the channeling efficiency in a circular machine, as already noted in literature [34].

On the other hand, for $\theta = \theta_{mc} + \theta_b$, the particle would still hit first the end of the crystal and, in this case, they would be aligned with the crystal planes at that point. However the associated channeling kick is zero, because the remaining crystal length is zero. If coming back with a larger impact parameter, the relative angle with the crystal planes would increase, thus entering in the domain of the volume reflection effect.

Also in the intermediate, general case ($\theta_{mc} < \theta < \theta_{mc} + \theta_b$), the particles would first

hit the end of the crystal. They would neither be perfectly aligned for channeling at the end nor at the entrance face of the crystal, but in a region which is somewhere in between. It is demonstrated in Appendix A that, in terms of curvilinear coordinates s starting from the entrance face, the perfect alignment point s_{align} depends linearly on the angle θ:

$$s_{align}(\theta) = \frac{(\theta - \theta_{mc})}{\theta_b} \cdot l_{cry} \tag{2.44}$$

and the width of the channeling region is found to be:

$$\Delta s = \frac{2\theta_{crit}}{\theta_b} \cdot l_{cry} \tag{2.45}$$

where θ_{crit} is the crystal critical angle at the considered energy. Again, since the relative alignment in the region between the end of the crystal and the channeling region is suitable only for the amorphous interaction, the particle would have to overcome an amorphous layer whose thickness depends on θ (Appendix A):

$$x_{am} = (l_{cry} - s_{align}(\theta)) \cdot \sin\left(\frac{\theta + \theta_{mc} - \theta_b}{2}\right) \tag{2.46}$$

which, being θ_{mc}, θ_b and $\theta \ll 1$, in first approximation becomes:

$$x_{am} = l_{cry} \cdot \frac{\theta_{mc}^2 - (\theta - \theta_b)^2}{2\theta_b} \tag{2.47}$$

This shows that for large positive miscut angles the channeling effect is possible for a wide range of angles, i.e. for particle-crystal relative orientations $\theta_{mc} < \theta < \theta_{mc} + \theta_b$. For each orientations a different channeling kick is associated: this depends linearly by θ and reaches its maximum for $\theta = \theta_{mc}$, when the particles are aligned with the crystal planes at the entrance face and the full channeling angle can be achieved. To each orientation a different equivalent amorphous layer is also associated. The maximum amorphous layer thickness depends quadratically on θ and, again, reaches its maximum for $\theta = \theta_{mc}$: this means that for this orientation the largest kick is possible, but also the largest effective amorphous layer. As already noted in literature, and amorphous layer reduces the channeling efficiency in circular machines.

The model proposed here has been verified with simulations (section 3.1.2.3) and with experimental data (section 4.3.2.5).

2.3.2.4 Negative miscut angle

In this section the effect of a negative miscut angle is considered. It will be demonstrated that a minimum distance from the crystal edge (impact parameter) exists for the particles to receive the full channeling peak. The linear dependency of the

channeling angle on the impact parameter is derived.

In the following we consider a crystal with length l_{cry}, curvature radius R_{curv}, bending angle θ_b and negative miscut angle θ_{mc}. The coordinate s_{cry} refers to the curvilinear coordinate which follows the lateral face of the crystal, while the line perpendicular to the entrance face and tangent to the lateral face is t. The particle's angle θ is calculated with respect to the direction t. If a particle impacts on the entrance face, the distance between t and the impacting point is denominated as impact parameter b.

When having a negative miscut angle, the particle is aligned with the crystal planes only if $\theta = \theta_{mc}$: in the usual approximation of slowly diffusing beam, the first point s_0 hit by the beam halo is the edge of the crystal, i.e. $s_0 = 0$. However, even if the impacting particles enter channeling, particles with an impact parameter $b \simeq 0$ would cross a negligible length of the crystal: this implies a channeling kick $\theta_{chan} \simeq 0$. A critical impact parameter b_c defines the limit for the full and the partial channeling region:
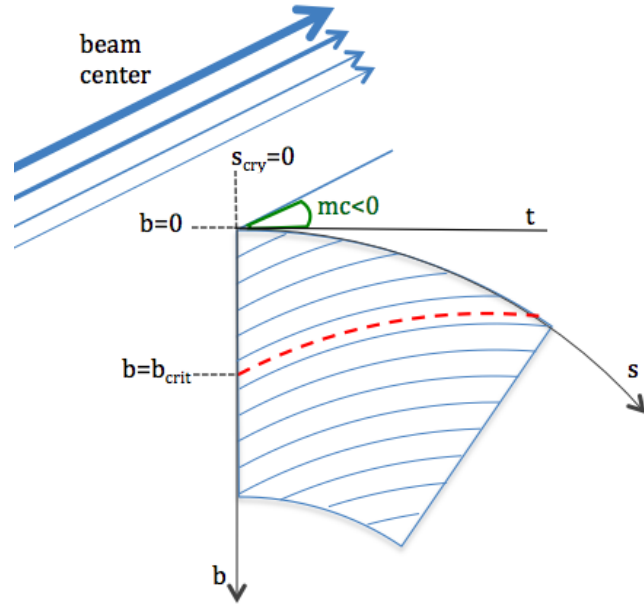
Figure 2.12: Negative miscut angle

- *Full channeling region:*
  if a properly aligned particle ($\theta = \theta_{mc}$) hits the entrance face with an impact parameter $b > b_c$, it can follow the crystal planes for the whole crystal length. It would then perceive the full channeling length of the crystal θ_b.

- *Partial channeling region:*
  if a properly aligned particle ($\theta = \theta_{mc}$) hits the entrance face with $0 > b > b_c$, it would enter in a channel whose length $\tilde{l}$ is shorter than the total crystal

length l_{cry}. For this reason it would perceive a reduced channeling lenght, described by the equation:

$$\theta_{chan} = \frac{\widetilde{l}}{l_{cry}} \cdot \theta_b = \frac{\widetilde{b}}{b_{cry}} \cdot \theta_b \tag{2.48}$$

Being the partial lenght $\widetilde{l} = b/\tan(\theta_{mc})$ and the bending angle $\theta_b = l_{cry}/R_{curv}$, we can get the expression for the channeling kick:

$$\theta_{chan} = \frac{b}{\tan(\theta_{mc}) \cdot R_{curv}} \tag{2.49}$$

whose validity is demonstrated with a dedicated simulation presented in Section 3.1.2.3.

2.4   Conclusions

After giving a short introduction of accelerator physics and collimation theory, more specific features of crystal collimation theory have been presented. In particular we studied the expected angular spread on the crystal collimator, and the impact of the miscut angle on the crystal-particle interaction.

The expected angular spread on the crystal edge was studied by defining a new optical function, g, which parametrizes the rate of change of total angle with synchrotron amplitude for grazing particles. It can be used for qualifying possible locations for crystal collimators: suitable locations are attained by choosing g values so that all particles over the relevant synchrotron amplitude range (for example, across an RF bucket) remain within the collimator acceptance angle. Past and future installations have been analyzed, revealing that the nominal realistic values of g are acceptably small, although they are not negligible.

The miscut angle has been defined and its impact analyzed, with particular focus on the edge effects which are remarkably important in case of circular machines. The orientation with respect to the beam defines the polarity of the miscut angle (positive or negative), and therefore defines the resulting edge effects. With positive miscut angle, partial channeling is possible for any crystal orientation within the volume reflection acceptance, with a partial channeling angle which depends on the crystal orientation. For a negative miscut angle, on the other hand, the channeling acceptance remains unchanged, but there is a superposition of different channeling kicks: it is demonstrated that the given channeling kick linearly depends on the particle impact parameter b, up to a critical value b_{crit} over which the full channeling kick is possible.

Chapter 3

Methods and Tools

In this chapter we present the main tools used during this thesis work. The chapter is divided in two parts:

- Simulation tools: the description of the codes used for the beam dynamics simulations. Particular focus is given to the new features introduced for the beam-crystal interaction treatment.

- Experimental methods: the assumptions and logic used to analyze the experimental data. In particular the collimator scan method is described, and the details for channeling angle calculation and efficiency estimation from collimator scan data are given.

3.1   Simulations

This section is dedicated to the main simulation tool which has been used for beam dynamics studies: `SixTrack`. In the next section (Section 3.1.1) the `SixTrack` code is briefly introduced, describing the required inputs (Section 3.1.1.1), the outputs and a set of secondary programs used to post process the data (Section 3.1.1.2). Then the focus is on the routine which is used to treat the crystal-particle interaction, describing its implementation in the pre-existing `SixTrack` code (Section 3.1.2.1), the main features of the original crystal routine (Section 3.1.2.2) and the modifications required to correctly treat the miscut angle effect (Section 3.1.2.3).
A last section is dedicated to the beam impact distribution studies (spatial and angular distribution). This studies have been carried out with a dedicated routine described in Section 3.1.3.

3.1.1   `SixTrack` - collimation version

`SixTrack` is a full six dimensional tracking code [52] in Fortran 77. The original purpose of `SixTrack` was to study non linearities and dynamic aperture in circular machines: for this reason the code was optimized to carry two particles through an accelerator structure over a large number of turns. Later the code was extended for tracking large ensemble of halo particles, and a collimation routine was implemented [13], thus generating the collimation version of `SixTrack`, i.e. the standard tool for collimation studies at CERN [53]. The collimation routine treats the interaction of the particles with standard collimators [54]. The Monte Carlo scattering routines in the collimation code are based on the older `K2` code [55].

3.1.1.1   `SixTrack` inputs

Three input files are required for `SixTrack`: a file specifying the machine optics, another for the beam and machine settings, and a third one containing all the collimator parameters. In this section we give a short description of each input file.

   The optics file specifies the layout of the machine. The collimation version of `SixTrack` requires that the optics is in thin lens approximation, i.e. the elements have no longitudinal extension and the effect of a magnetic element on the beam is represented by an impulse (kick) at the thin element location. One or more thin elements can be defined to represent each real element.

   All the parameters of the beam halo are defined in the tracking input file: energy, emittance, momentum spread, initial distributions in both transverse and longitudinal planes. The total number of particles and number of turns are defined here as well. Different halo distributions can be specified (see [9] for a detailed description).

The list and description of the collimators are included in the collimator database: here the collimator material, geometry and operational settings are defined. For a detailed description of the database entries, both standard collimator and a crystal collimator elements, please refer to Appendix B.

3.1.1.2 `SixTrack` outputs and post processing

Once provided with the required input files, `SixTrack` computes the trajectories of the halo particles along the machine, performing a fully chromatic, fully coupled tracking. In this section we describe what are the main output files of `SixTrack`, how they are processed by secondary codes/scripts, the final outputs of our simulations and their meaning.
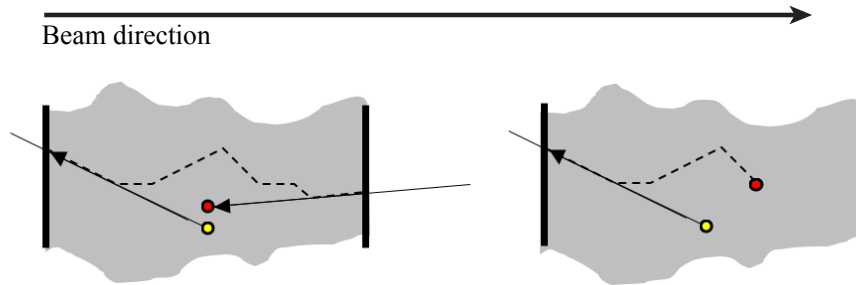
Figure 3.1: Example of elastic (left hand side) and inelastic (right hand side) interactions in `SixTrack`. In both cased, the collimation routine receives the coordinate of the particles at the center of the collimation (yellow point). The particle is then tracked backward of half collimator length, and the Monte Carlo routine calculates the interactions inside the collimator material (dotted line). If the interactions are elastic or quasi elastic, the coordinates of the outgoing particles are calculated, tracked backwards at the center of the collimator length (red point, picture on the left), and the tracking continues. If the interaction is inelastic, the interaction coordinates (red point, picture on the right) are saved, and the particle is removed from the tracking.

When a particle interacts with a collimator, many different kinds of interactions can happen. For a detailed description of the different interactions we refer to [19]. Depending on the interaction type, the code will give different outputs (see Figure 3.1):

1. Elastic and quasi-elastic interactions. In this category we include multiple Coulomb scattering, single diffractive scattering [56] and elastic point-like interactions. In this case `SixTrack` calculates the new 6-D coordinates of the particle, and continues with the tracking (Figure 3.1, left hand side). Starting

from the first elastic interaction with a collimator, the trajectory is saved at each element of the optics, until an inelastic interaction occurs or the code executes the total number of turns specified in the input file.

2. Inelastic interactions, e.g. ionization, excitation of the jaw material [57] and inelastic point-like interactions. This shower, however, is not calculated by In this case `SixTrack` considers the original particle as "absorbed" and removes it from the tracking. The 6-D coordinates of the particle at the inelastic interaction point are stored in a dedicated output file.
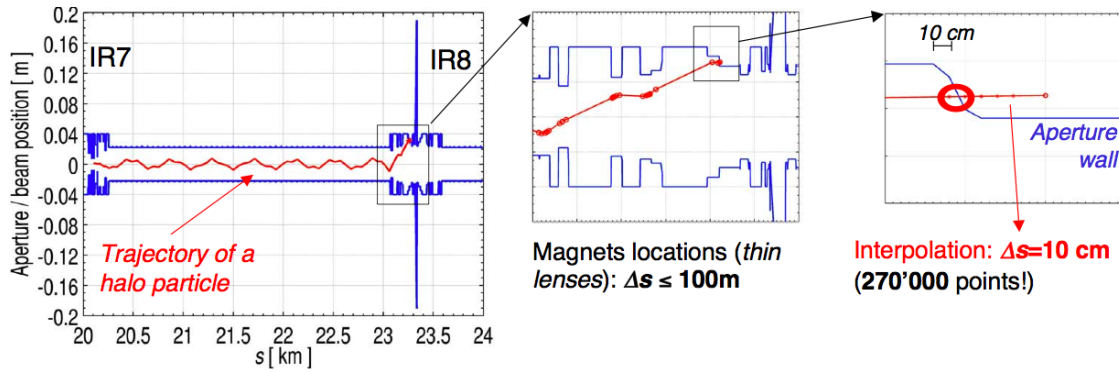
Figure 3.2: Example of a trajectory of a particle lost in the mechanical aperture, as calculated by the `BeamLossPattern` program, from [58].

Since `SixTrack` does not have an aperture model embedded in the code (due to CPU limits), a post processing of the data is necessary to find the particles which are eventually lost in the mechanical aperture of the machine. The comparison between the particle trajectories and the aperture model is performed by the `BeamLossPattern` code [58]. Both in case of the LHC and the SPS a detailed aperture model of the whole machine, not including collimators and protection elements, is available. For the aperture loss locations, a precision of 10 cm along the longitudinal coordinate can be achieved (Figure 3.2 [58]).

After a series of secondary codes and scripts used to process the `SixTrack` data, the final outputs of our simulations are:

1. The coordinates of the inelastic interactions, which are used as an input for shower calculations and energy deposition studies. These can be performed by any particle physics Monte-Carlo simulation code (at CERN for collimation studies `FLUKA` [59, 60] is used). For the standard collimation cases it is a common procedure to estimate with `FLUKA` the energy deposition at the collimator

itself and at the downstream elements. However for the simulations of a crystal collimation system the shower calculation has not been performed yet[1].

2. The loss locations along the ring and at the collimators. These data are used to get the most important result of our simulations, i.e. **loss map** along the ring. What is represented in a loss map is the local cleaning inefficiency of the collimation system (see definition in Section 2.2.3) versus the longitudinal coordinate.

3.1.2 Crystal routine in `SixTrack`

One of the main contributions of this thesis work on the simulation side is the implementation of an existing crystal routine into the `SixTrack` code, and the inclusion of the miscut angle effect. In this section the implementation of the routine in `SixTrack` (Section 3.1.2.1), the details of the crystal routine (Section 3.1.2.2) and finally the main modification done to the crystal routine (Section 3.1.2.3) are described.

3.1.2.1 The crystal routine implementation: from the beam reference system to the crystal reference system

During the implementation of the crystal routine, attention was paid in order to leave the structure of the tracking routine unchanged. The crystal is simply defined as a new type of collimator. Whenever a crystal element is found in the element sequence, the code calls a intermediate subroutine which adapts the reference system for the crystal routine, and then calls the crystal routine. The intermediate routine is described in this section.

When a particle reaches the longitudinal position of the crystal, the coordinate reference system must be changed according to the crystal orientation and to the impact point. The transformation can be described in six passages:

1. Let's consider a rectangular box containing the crystal, with the longitudinal face parallel to the beam orbit (image 1 in Figure 3.3). The beam reference system is rotated in order to have the x_{coll}-s_{coll} plane passing through the middle plane of the crystal. Please notice that no tilt of the entrance face has been foreseen in the code [2]. The transformation matrix is the rotation matrix:

$$(x_{coll}, z_{coll}) = \begin{pmatrix} \cos(\theta_{coll}) & -\sin(\theta_{coll}) \\ \sin(\theta_{coll}) & \cos(\theta_{coll}) \end{pmatrix} \begin{pmatrix} x_{beam} \\ y_{beam} \end{pmatrix} \qquad (3.1)$$

where θ_{coll} is the orientation of the crystal with respect to the x axis (image 1 in Figure 3.3).

---

[1]a model for the crystal, required for calculating the secondary emitted particle showers, is not yet available in `FLUKA`

[2]As a consequence no skew crystal collimator has been simulated. Details in Appendix C

1.

y_beam

θ_coll

x_beam   s_beam

Beam
Reference
Frame

2.

x_coll

s_coll

z_coll

Collimator
Reference
Frame

3.

x_coll

s_coll

Collimator reference
frame:
Lateral view

4.

x_coll

s_coll

Shift of the s axis

5.

θ_tilt   x_cry

s_cry

Crystal
reference
frame

6.

Total crystal length

x_cry

x_0

s_0   s_cry

Impact point (s_0, x_0)

7.

x_cry

s_cry

Shift the axes

8.

x_Rcry

s_Rcry

θ_int

Rotation

9.

Reduced crystal
length

x_Rcry

s_Rcry

Reduced
crystal
reference system

Figure 3.3: Reference frame transformation from the tracking routine in `SixTrack` to the crystal routine.

2. The s_{beam} axis is shifted towards the crystal in order to touch the lateral face of the bounding box (images 2 and 3 in picture 3.3). It is worth noticing that these first two passages are identical for the standard collimator routine: for this reason we refer to the resulting reference system as to the "collimator reference frame". Please note that a crystal, in the actual version of the routine, is always treated as a "one-sided" element, while usually the collimators have two jaws.

3. The origin of the reference system is shifted in order to lay on the bottom corner between the lateral and the entrance face of the crystal (image 4 in Figure 3.3).

4. The axes are rotated by an angle θ_{tilt}. Since the tilt of the crystal is defined to be zero when the crystal is aligned with the divergence of the beam at that longitudinal location, the angle θ_{tilt} is the sum of the divergence of the beam in that point and the tilt specified in the database (image 5 and 6 in Figure 3.3). This is the standard crystal reference frame.

5. The particle impacting point is calculated. If the particle impacts on the entrance face of the crystal, the crystal routine is immediately called for the total length of the crystal. If the particle does not hit the crystal at all, a simple drift is considered. If the particle hits the lateral face of the crystal, then the impacting point (s_0, x_0) is calculated (image 6 in Figure 3.3)), and the origin of the reference frame is shifted in (s_0, x_0) (image 7 in Figure 3.3).

6. The reference system is rotated one last time by the angle θ_{int}, so that the s axis is tangent to the crystal lateral face in the origin (image 8 in Figure 3.3). This reference system is called "reduce crystal reference system" (image 9 in Figure 3.3).

After this series of transformations, the reference system is now suitable for the crystal routine, which is applied and returns the 6-D coordinate vector of the particle in the same reference frame. The transformation which has been described in this section is then applied backwards, and the `SixTrack` tracking routine continues.

3.1.2.2 Description of the Monte-Carlo crystal routine

The crystal routine is a Monte Carlo routine written in Fortran 77 by a colleague from IHEP (Igor Yazynin), who worked for the CERN collimation collaboration to finalize and test his routine before the final implementation in `SixTrack`. The routine models the physics of the crystal-proton interaction via a Monte-Carlo simulation based on theoretical formulas (presented in Chapter 1). In this section we present the crystal geometry in the routine reference frame and the logic of the original crystal routine.

The reference system of the crystal routine is shown in Figure 3.4, and the (x, z, s) reference system corresponds, in the intermediate routine, to the reduced crystal reference system $(x_{Rcry}, z_{Rcry}, z_{Rcry})$ described in Section 3.1.2.1. The front
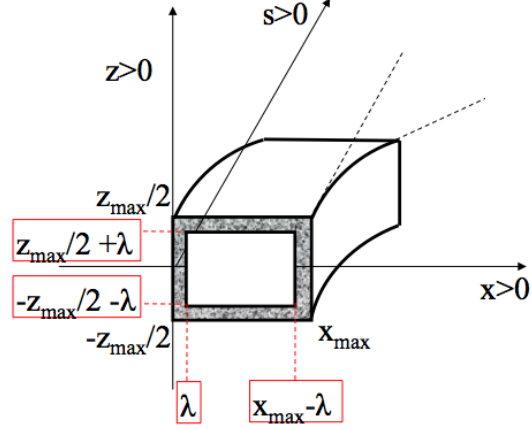
Figure 3.4: Crystal reference system as in the original crystal subroutine. An amorphous layer of thickness λ is considered.

face of the crystal lays on the s=0 plane, and its transverse dimensions are:

$$
\begin{aligned}
0 &< x < x_{max} \\
\frac{-z_{max}}{2} &< z < \frac{z_{max}}{2}
\end{aligned}
$$

where x_{max} and z_{max} are specified in the collimator database. The bulk of the crystal lays in the s > 0 volume, and the kick is given in the x direction towards positive x. (x' increasing) . The particle initial longitudinal position is always s=0. It is also possible to define an amorphous layer of thickness $\lambda > 0$; in this case the crystal edge is surrounded by a frame where the crystal planes are considered damaged, and cannot interact coherently. The only possible interaction in this region is the amorphous interaction.

When a particle hits the crystal, different processes can take place, depending on the particle energy, orientation with respect to the crystal planes, and on the crystal material. For an introduction to the different possible effects, it is referred to the Chapter 1 of this thesis. Here we briefly summarize the effects which are considered in the routine.

- **out**: the particle does not hit the crystal, a drift in space is considered.

- **amorphous**: the particle is not aligned with the crystal planes, or it hits the amorphous layer. In this case the particle interacts with the crystal as an amorphous material.

- **planar channeling**: the particle is trapped in the potential hole between two crystalline planes, and follows their orientation.
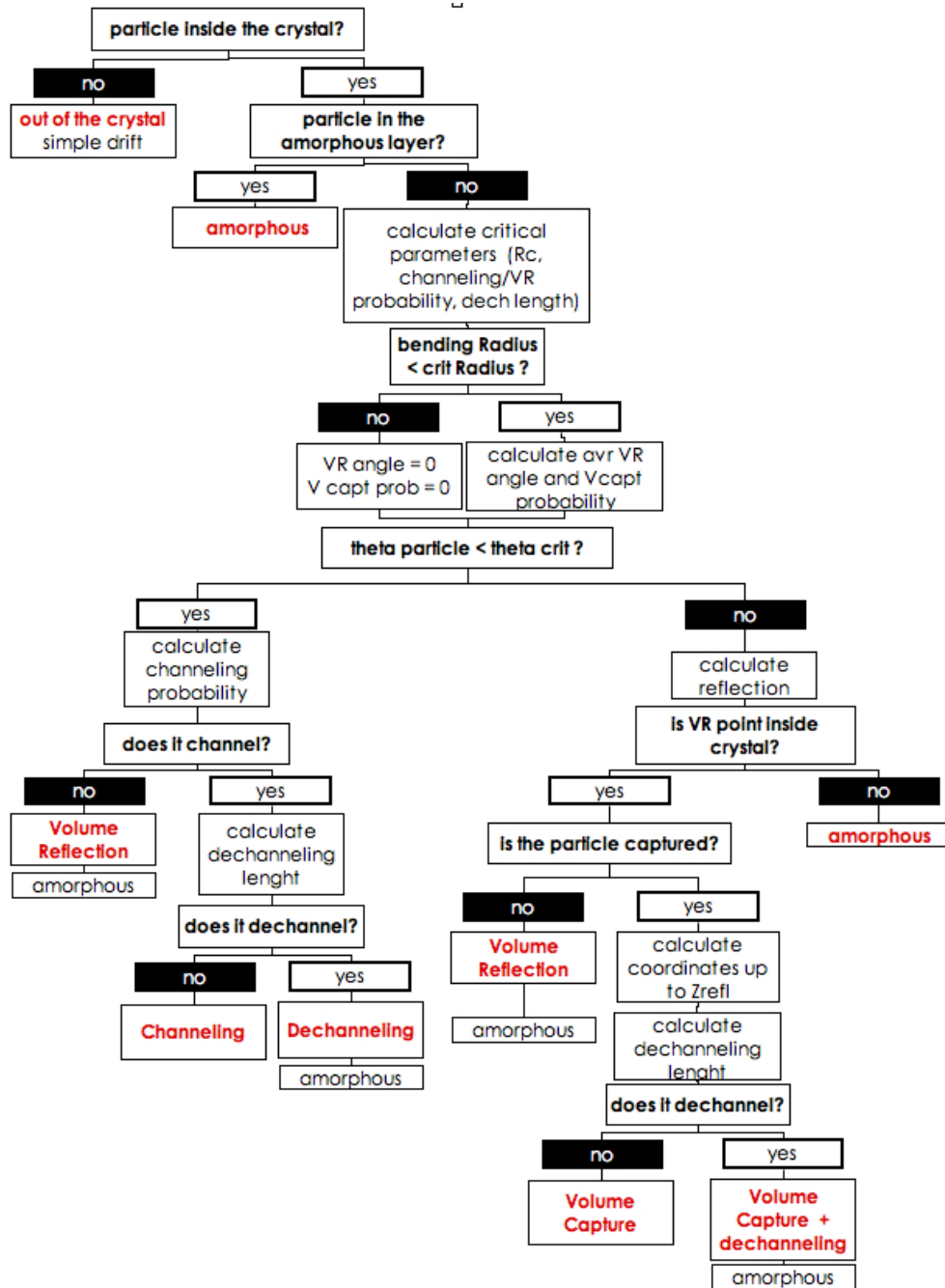
Figure 3.5: Crystal routine logic flow. The crystal effects considered in the routine (out / amorphous / channeling / volume reflection / volume capture / dechanneling) are indicated in red.

- **volume reflection** (VR): a single reflection of the particle in the bulk of the crystal changes the particle momentum by about $1.5\,\theta_c$, where θ_c is the critical angle for the bent crystal (see equation 1.19).

- **volume capture** (VC): crossing the bulk of the crystal, the particle can loose some energy, thus entering the planar potential hole. In this case, from the interaction point onward, the particle is trapped in channeling mode.

- **dechanneling**: while in channeling, the particle can have an inelastic interaction and its transverse energy could overcome the crystal planar potential. From the interaction point onward, the particle interacts with the crystal as an amorphous material.

It is important to remember the limitations of the model:

- the axial channeling is not treated;

- the curvature along the z direction (see Figure 3.4) is considered constant;

- the torsion effect cannot be simulated;

- the crystal holder geometry is not implemented.

- in case of inelastic interaction, the shower of secondary emitted particles in not calculated.

In order to calculate the probability for each particle to undergo a specific physical process, the crystal routine must know the crystal parameters and the particle coordinates. All these quantities are either defined as input variables of the routine itself, either passed as variables of the routine, or read as global (common) parameters from parent routines (tracking routine in `SixTrack`). The logic of the crystal routine is shown in the functional flow block diagram in Figure 3.5.

3.1.2.3   Miscut implementation in the routine

The main change from the original crystal routine is the implementation of the miscut angle (for definition and theory see Section 2.3.2). In order to simulate it correctly, two factors must be taken into account:

1. the inclination between the particle transverse momentum and the crystalline planes is different from the case of a perfectly cut crystal;

2. the geometry at the edges of a miscut crystal can generate edge effects which do not exist in case of a perfectly cut crystal.
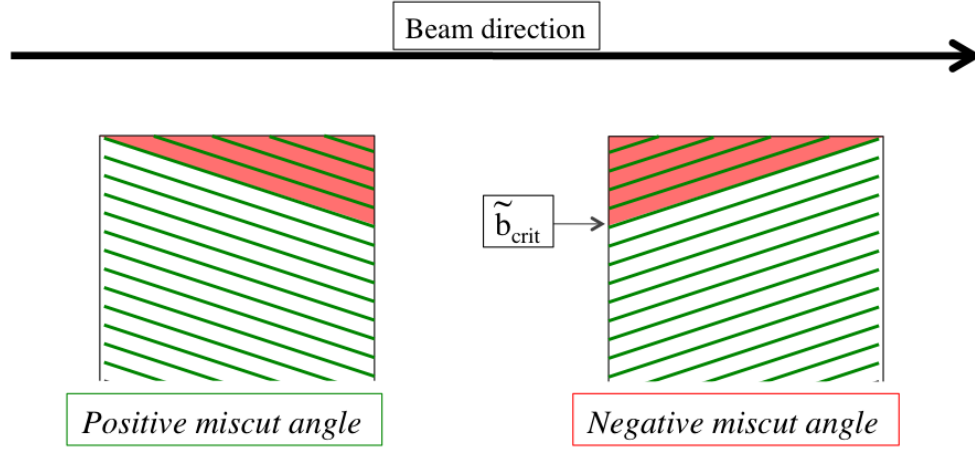
Figure 3.6: Positive and negative miscut angle orientations. The crystal, for simplicity and clearness, is represented as straight.

To correct the relative angle between the particle and the crystalline plane, the value of the miscut angle must be added to the transverse direction of the particle, both in case of positive and negative angle. This is enough for treating the interactions of the particles with the bulk of the crystal (green region in Figure 3.6). Regarding the edge geometry (red region in Figure 3.6), the positive and negative orientations must be treated differently.

It is important to remember that, given the reference frame transformations applied before calling the crystal routine (Section 3.1.2.1), the particle hits always the crystal at the longitudinal coordinate $s = 0$. This means that, in case of positive miscut angle, it is always enough to add the miscut angle value to the impacting angle of the particle.

For negative miscut angles, on the other hand, a "reduced" critical impact parameter $\widetilde{b}_c$ is defined (Figure 3.6), as the transverse distance between the crystal edge and the particle impact in the reduced crystal reference system. In this case:

- if the particle hits the entrance face with a reduced impact parameter $\widetilde{b} > \widetilde{b}_c$ (green region), it is sufficient to add the miscut angle value to the particle transverse momentum.

- if the particle hits the entrance face with $0 > \widetilde{b} > \widetilde{b}_c$, the miscut angle is still added to the particle transverse momentum and the total channeling angle is reduced to:

$$\theta_{chan} = -\widetilde{b}/\tan(\theta_{mc})/R_{curv} \qquad (3.2)$$

where θ_{mc} is the miscut angle value and R_{curv} is the curvature radius.

The value of $\widetilde{b}_c$ can be found with simple trigonometric considerations:

$$\widetilde{b}_c = -l \cdot \tan(\theta_{mc}) \qquad (3.3)$$

where l is the length of the crystal in the reduced reference system.

These simple transformations succeed in describing the miscut angle effects treated analytically in Section 2.3.2. Figure 3.7 and Figure 3.8 show the results of two simulations for a crystal with large miscut angle inserted in the LHC, at the collision energy of 7 TeV. The crystal is a 10 mm-long silicon crystal with curvature radius of 100 m and a miscut angle of 1 mrad. The design channeling angle for this crystal is 100μrad. At the LHC collision energy the critical angle for this crystal is about 2.1μrad. The impact coordinate in the collimator reference system (see Figure 3.3, image 3) is here called total impact parameter b, as usually done for standard collimators.
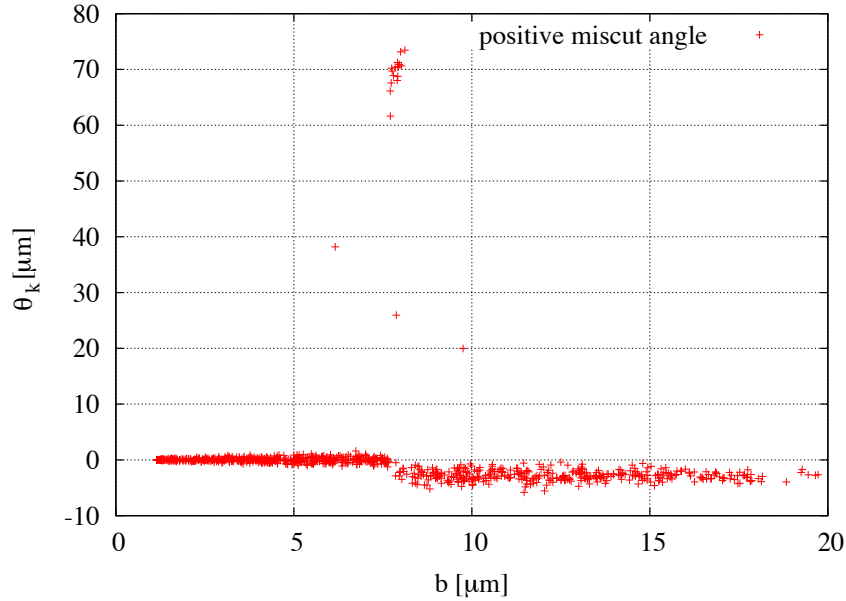
Figure 3.7: Crystal kick versus impact coordinate in the collimator reference system, for a crystal with positive miscut angle.

Figure 3.7 corresponds to the positive miscut angle ($+1000\mu$rad), and the crystal is oriented with a tilt angle of -1030μrad with respect to the impinging particle direction, which in principle should correspond to an orientation where the volume reflection is the dominant effect. As expected from the theory presented in section 2.3.2.3, three different regions are clearly visible:

1. An amorphous region, for $b < \sim 8\mu$m, where the average kick θ_k given by the crystal is zero.
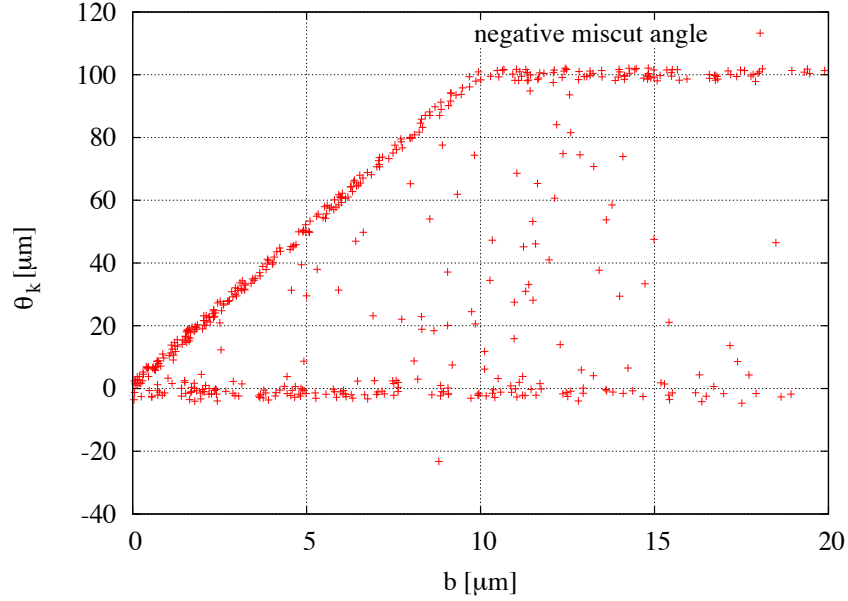
Figure 3.8: Crystal kick versus impact coordinate in the collimator reference system, for a crystal with negative miscut angle.

2. A channeling region, for $b \approx 8\mu$m, where the channeling kick θ_k is equal to the total channeling kick minus the misalignment of the crystal ($\theta_k = 100\mu$rad $- 30\mu$rad $= 70\mu$rad). Even if the acceptance of the channeling region is limited ($< 1\mu$m), in regimes of low diffusion and given the fact that the amorphous and volume reflection kicks are too low to extract the particles, this effect can be dominant.

3. A volume reflection region, for $b \gtrsim 8\mu$m, with an average kick of $\theta_k = -1.4\theta_c \approx -3\mu$rad, as expected.

Figure 3.8 corresponds to a negative miscut angle (-1000μrad), and the crystal is oriented with a tilt angle of $+1000\mu$rad with respected to the impinging particles direction in order to compensate the miscut angle. As expected from the theory presented in section 2.3.2.4, two different regions are clearly visible:

1. A reduced channeling region, for $b < b_c$. The expected critical value for the reduced impact parameter is of $\widetilde{b}_c = l \cdot \tan(\theta_{mc}) \simeq (10^{-2} \cdot 10^{-3})$m $= 10\mu$m, that is approximately the value of b_c in the picture[3].

---

[3]Obviously, if the particle hits perpendicularly with respect to the entrance face of the crystal, the reduced crystal reference frame and the crystal reference frame are the same. For small beam divergences, it is then natural that $b \approx \widetilde{b}$.

2. A full kick-channeling region, for $b > b_c$, with the design channeling angle of 100μrad.

Please notice that the presence of particles receiving a kick smaller than the one expected for channeling is due to the fact that the channeling process is not 100% efficient, and amorphous and dechanneling contribution are not negligible even for a perfect channeling orientation.

3.1.3 Impacting beam studies with a dedicated routine

As already commented in paragraph 3.1.1.1, the initial particle distribution on a primary collimator has a great impact on the results of the `SixTrack` simulations. An example of a possible edge effect for crystals is shown in paragraph 3.1.2.3, where the kick given by a crystal with large miscut angle depends on the particle impact parameter. It can be intuitively understood that also for standard amorphous collimators the edge effects are important [46]: the lower the impact parameter, the larger the probability for the particle to exit the collimator without being absorbed. A way to have a realistic impact parameter could be to generate an initial halo that does not touch the primary collimator and then let it diffuse with a realistic emittance growth. This kind of simulation, if performed with `SixTrack`, would require an excessively long computational time. In order to have a fast way to check the expected halo particle distribution on the primary collimator, a fast c-code has been developed, giving the first impact distribution as a function of the average kick received by the particle at each turn or of the expected emittance growth rate.
In this paragraph we describe the assumptions and logic of the code. The results for the LHC will be presented in section 6.4.1.

In the routine only one dimension of the transverse halo is simulated (for simplicity, we call it the x direction), while the longitudinal emittance growth is neglected. The machine is linear and the betatron and syncrotron phase advance of the particle at the turn T are:

$$\varphi_b(T) = \varphi_b(T-1) + 2\pi \cdot Q_x \tag{3.4}$$

$$\varphi_s(T) = \varphi_s(T-1) + 2\pi \cdot Q_s \tag{3.5}$$

where $\varphi_b(T-1)$and$\varphi_s(T-1)$ are, respectively, the betatron and synchrotron phase of the particle at the $T-1$ turn, Q_x is the transverse betatron tune and Q_s is the synchrotron betatron tune. The detuning with amplitude is not considered.
The position and the divergence of the particle are given by the standard linear equations:

$$x(T) = n_b \ \sigma_x \cos\varphi_b(T) + D_x \ n_s \ \sigma_p \cos\varphi_s(T) \tag{3.6}$$

$$x'(T) = -\sqrt{\frac{\varepsilon_{rms}}{\beta}} n_b \left(\alpha \cos\varphi_b(T) + \sin\varphi_b(T)\right) + D'_x \ n_s \ \sigma_p \cos\varphi_s(T) \tag{3.7}$$

where

- n_b and n_s are the amplitudes of betatron and synchroton oscillation in σ_x and σ_p units

- ε_{rms} is the nominal 1 σ_x emittance

- α and β are the horizontal Twiss parameters at the crystal location

- D, D' are the dispersion and its derivative at the same location.

The dependence of optical parameters from energy is neglected. The model is therefore a very first approximation, but as shown later it can provide us with an evaluation of the expected impact parameters on the primary collimator.
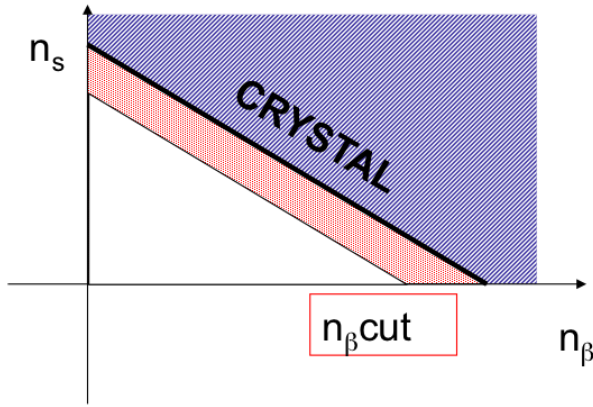
Figure 3.9: Amplitude space n_s, n_b. The crystal edge defined by equation 3.10 is shown. The initial space occupied by the particles as generated by the code is indicated in red.

The initial transverse positions and angles are distributed according to a Gaussian distribution, and the same distribution is applied for the longitudinal variables energy and time. As already noted in previous works [9], in the amplitude space n_b, n_s the crystal edge defines a line

$$n_b \cdot \sigma_x + \mid D \mid \ n_s \ \sigma_p = x_{cry} \tag{3.8}$$

where x_{cry} is the aperture of the crystal. The initial distribution of the particles is cut in order to satisfy the condition:

$$n_b \cdot \sigma_x + \mid D \mid \ n_s \ \sigma_p < x_{cry} \tag{3.9}$$

that means that no particle can hit the crystal if its betatron and/or synchrotron amplitude does not increase. In order to further optimize the code, a lower betatron cut n_{bCUT} can be imposed, so that:

$$n_b \cdot \sigma_x + \mid D \mid \ n_s \ \sigma_p > n_{bCUT} \cdot \sigma_x \tag{3.10}$$

The initial distribution in the amplitude space is shown in red in picture 3.9.

At each turn a random kick k is applied to each particle, thus increasing the betatron amplitude and shifting the betatron phase. The new betatron amplitude n_{b1} and the betatron phase shift $\Delta\varphi_b$ are calculated with the equations 2.23 and 2.24, that we repeat here for convenience:

$$n_{b1} = \sqrt{n_{b0}^2 + k^2 \cdot \frac{\beta}{\varepsilon_{rms}}}$$
$$\Delta\varphi_b = \arctan\left(\frac{k^2 \cdot \sqrt{\frac{\beta}{\varepsilon_{rms}}}}{n_{b0}}\right)$$

Since the kick is purely transversal, the synchrotron phase and amplitude are not affected. The kick is applied at the crystal location, but in fact it is representative of the natural emittance growth of the beam, and does not depend on the crystal.

After the kick, the routine continues tracking the particle and, at each turn, it checks if the transverse coordinate of the particle is larger than the crystal aperture: in that case the particle coordinates n_b, φ_b, n_s, φ_s are saved in the output file and the particle is no longer tracked.

The code accepts, as an input, either the rms kick received by the particle at each turn, or the expected emittance growth value. Depending on the machine we are studying, one or another may be more suited.

- When artificial beam heating devices are used to increase the transverse emittance value, it is easier to directly use the rms kick given to the particle. An example of a beam heating device is a transverse beam damper, used in the experiment RD22 [61] to artificially increase the impact parameter on the crystal[4], or the Tevatron electron lens [62], which is used for abort gap cleaning.

- If the natural diffusion is the only emittance growth source, it is easier to use the expected emittance growth. This is the case of the LHC: at the moment, an heating device is not foreseen[5]. The emittance growth calculation used for the LHC case is discussed in paragraph 6.4.1.

The equivalence between rms kick and emittance growth rate is quite straightforward. Let's assume a kick distribution with variance $< k^2 >$. Taking into account the statistical definition of emittance [63], the beam rms emittance increase is [61]

$$\frac{\Delta\varepsilon_{rms}}{sec} = \frac{1}{2}\beta < k^2 > \nu_{rev} \tag{3.11}$$

where ν_{rev} is the particle revolution frequency. For a Gaussian distribution $< k^2 >= \sigma_k^2$.

---

[4]The same procedure was foreseen to be used for UA9, even if in most of the experimental runs the damper was switched off, since the natural diffusion was already much higher than expected (see paragraph 5.2.1).

[5]There are studies about implementing an hollow electron lens, which should increase the betatron amplitude of the particle with $n_b > 3\sigma_x$ [6].

3.2 Experimental tools

3.2.1 Beam loss maps along the ring

Particle losses can prevent the machine from its normal operation or even damage the machine components, especially in machines with superconducting magnets, which are particularly sensitive to even small amounts of energy deposition. It is therefore important to be able to provide realistic estimations of the expected beam losses along the ring. For doing this, the full simulation package already described (paragraph 3.1.1) is generally employed. The code has been fully benchmarked [14] with beam tests in 2004. The beam tests were performed in the SPS with a LHC phase 1 prototype collimator.
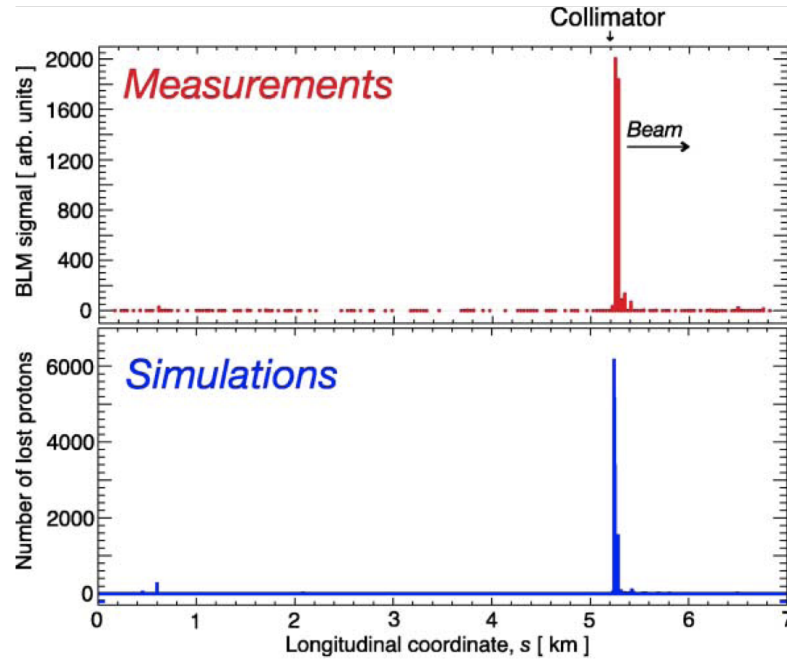
Figure 3.10: Measured and simulated SPS Beam Loss responses, full ring. From [14].

Figure 3.10 and 3.11 show the results of Beam Loss Monitor (BLM) measurements in the SPS and the cross-checking with beam loss simulations (from [14]). A longitudinal shift between simulated and measured data is observed. This is an expected feature, since for the simulations only the inelastic impacts by the primary beam are considered, while the BLMs detect mainly the showers generated by the inelastic interactions in the elements.

Given the good agreement found during the benchmark of the simulation tools,
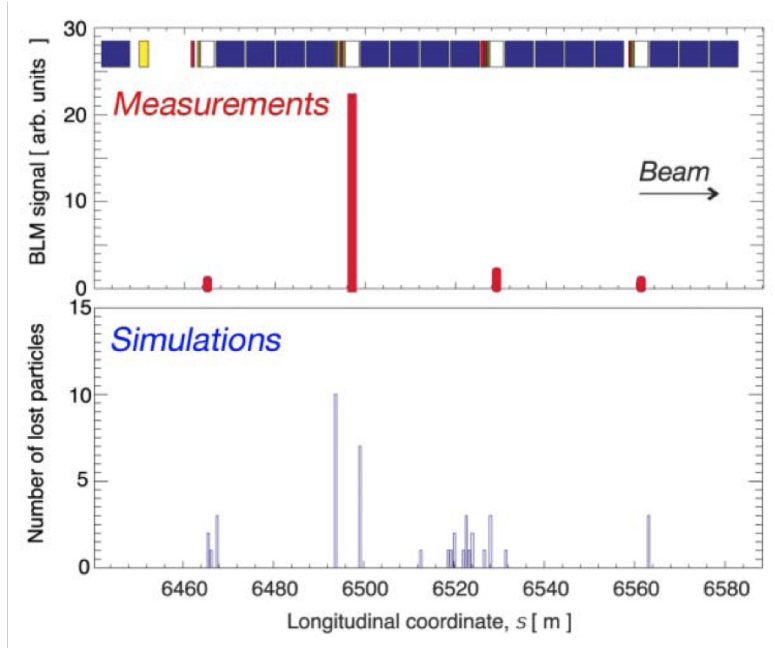
Figure 3.11: Measured and simulated SPS Beam Loss responses, for elements down-stream the collimator (about 1.2 Km downstream). From [14].

one can rely on our code to predict the beam loss variation both in case of standard and crystal collimation systems. A large discrepancy between the simulation and the loss maps could be due to the far too simplified crystal model in our routine. Edge, geometrical and/or impurity effects that were considered as secondary effects, could play an important role in circular machines.

3.2.2   Collimator scan method

A single particle impinging on the crystal face interacts with the crystalline structure and receives a kick which is characteristic of the interaction type. As already seen in section 1.3, the probabilities associated to the different interactions depend on the beam (mass, velocity, transverse momentum) and on the crystal (material, geometry, defects, orientation) characteristics: we refer to these probabilities as "single passage" efficiencies, and they are among the main outcomes of extraction-line experiments like H8-RD22 [11]. Therefore it is possible to measure analogous efficiencies also in circular machines: two different methods for measuring multi-turn efficiencies have already been presented in Section 1.3.2. A third way, developed during this thesis work, is the collimator scan: a powerful and innovative method used to experimentally evaluate the bending angle and the crystal channeling effi-

ciency in experiments. This paragraph describes the collimator scan technique and compare two different applications of the method, as it was implemented in the Tevatron for the T980 experiment ("multi-turn like" collimator scan) and in the SPS for the UA9 experiment ("single-passage like" collimator scan). In the next paragraphs we describe which fitting functions are used to find the channeling peak center and population (paragraph 3.2.2.1), and how to deduce the channeling angle (paragraph 3.2.2.2) and the channeling efficiency (paragraph 3.2.2.4)

A collimator scan consists in measuring the distribution of particles downstream the crystal by gradually moving the collimator jaw toward the beam edge, up to a minimum normalized aperture equal to the crystal one, thus generating a shower of secondary particles. The generated particle shower is measured by one or more detectors downstream the collimator (which can be Beam Loss Monitors -BLM - or other detectors like, for example, scintillators as in the Tevatron case). The detector signal is assumed to be proportional to the number of inelastic interactions at the collimator, i.e. to the number of particle intercepted by the collimator jaw: the signal is therefore proportional to the integrated beam profile at the collimator position.

It is worth noticing that the hypothesis of direct proportionality between the number of inelastic interactions at the collimator and the detected downstream shower is a strong assumption, that should be validated by dedicated simulations. Further discussion on this subject can be found in Section 4.3.2.3.
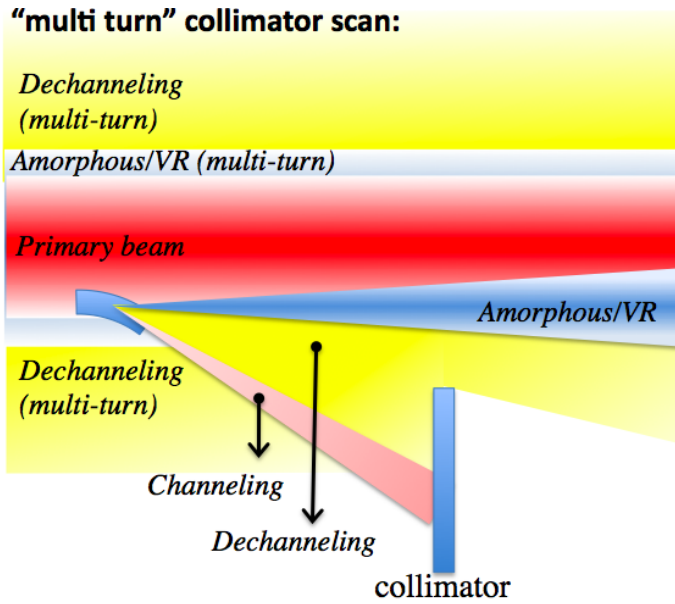
Figure 3.12: Principles of multi-turn probability measurements in a circular machine.

The collimator scan method was used in two different configurations:

- "multi-passage" collimator scan (Figure 3.12). In this case the only two components of the collimation system are the crystal (the closest element to the

beam) and the movable collimator. When inserting the collimator, it intercepts both a fraction of the particles directly scattered by the crystal, and some of the particles which are not lost at the first turn and come back to the collimator location. However a limited oscillation amplitude can fit the mechanical aperture of the machine, and therefore a limit kick exists over which the scattered particles cannot come back to the collimator location.
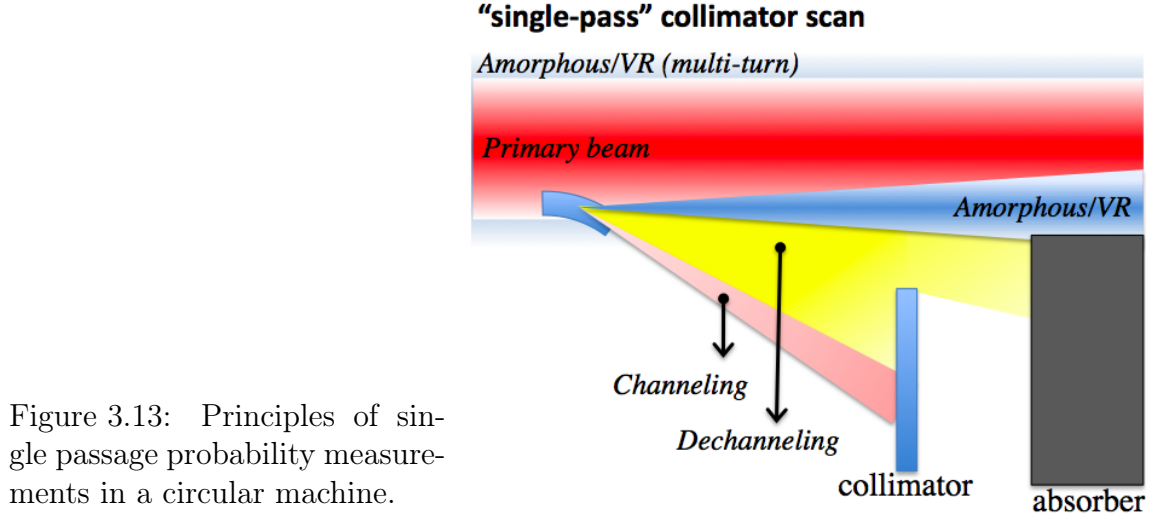
Figure 3.13: Principles of single passage probability measurements in a circular machine.

- "single-passage like" collimator scan (Figure 3.13). In this case the collimation system is composed by three elements, the crystal, the movable collimator, and an absorber whose normalized aperture is equal (or slightly larger) than the crystal one. In this configuration the absorber artificially sets a tight aperture limitation downstream: in first approximation the collimator intercepts only particles directly scattered by the crystal. However it will be demonstrated in Section 3.2.2.2 that a minimum outwards kick θ_k^{abs} exists for which the particle can escape the absorber. The associated normalized aperture a_{multi} defines the limit of the multi turn halo: for apertures smaller than a_{multi} the collimator intercepts both particles directly scattered by the crystal and particles escaped by the collimation system and come back at the collimator location with higher amplitude.

3.2.2.1   Collimator scan fitting functions for the channeling orientation

Once the crystal angular position is fixed, the structure of the secondary halo generated by the different processes in the crystal is stable and defined only by the cross sections of the different processes. By studying the fraction of beam intercepted by the collimator jaw for different jaw positions, it is possible to analyze the secondary halo. In particular, in case of channeling orientation, the losses are expected to increase in coincidence with the position of channeled beam. In this section the

functions used to fit the data for collimator scans in channeling positions are presented.

It is important to stress that the approximations presented in this section describe the halo for a purely single-passage regime i.e. when the particles scattered by the crystal cannot escape the collimation system. Even for a single passage collimator scan, the single passage assumption is valid only beyond the aperture associated to the multi turn behavior (see Section 3.2.2.3). In case of multi turn collimator scan, the fitting functions can be applied only if the crystal kicks are large enough for the particles to be surely lost in the machine mechanical aperture. However, for the experimental data analyzed in this thesis, it was always possible to fit at least the channeling peak, thus getting the relative population and the center of the channeled beam.
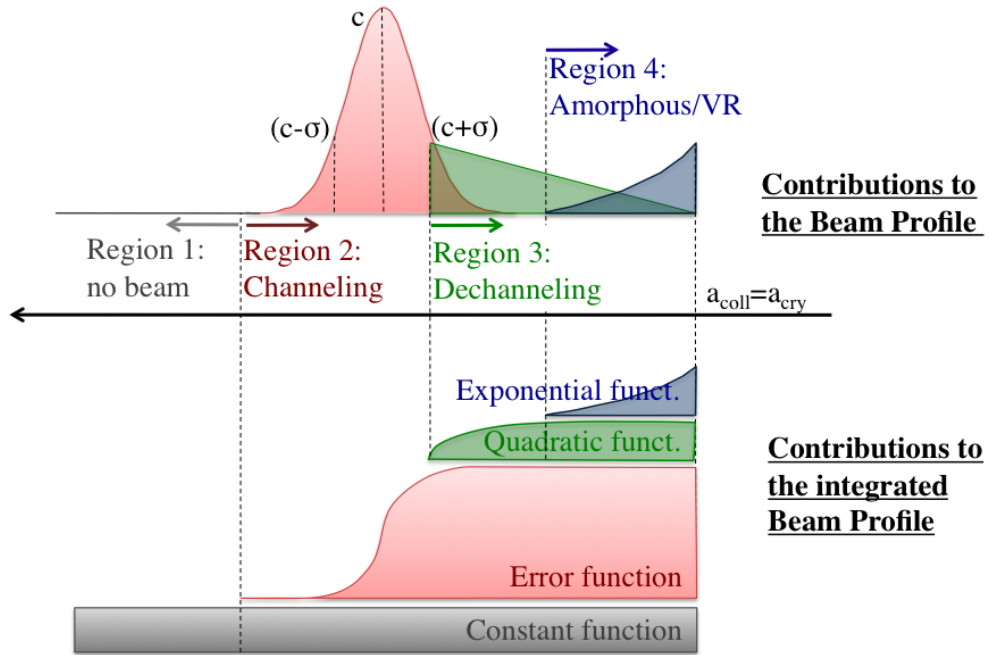
Figure 3.14: A conceptual sketch of the approximations made to fit the experimental curves

When the crystal is oriented in channeling mode, four different regions, each one associated to a different crystal regime, are expected (see the conceptual sketch in Figure 3.14):

1. A first external region where the signal detected by the monitor is zero. A constant signal is detected for the experimental data (baseline value k): this

is background noise, and it has been subtracted for all the measurements.

2. A second region where the losses increase abruptly. The signal corresponds to the channeled beam, whose profile should be Gaussian. The contribution to the integrated beam profile is fitted with an error function

$$f_1(x) = A \cdot \frac{1}{\sigma\sqrt{2\pi}} \int_0^x e^{-\frac{(t-c)^2}{2\sigma^2}} dt \qquad (3.12)$$

where A is the total area of the Gaussian, c its center and σ its standard deviation. The parameter A is then proportional to the total number of channeled particles. As explained in Section 3.2.2.2, the measure of the displacement c is related to the channeling kick θ_{chan}, while the parameter A is related to the single passage channeling efficiency in multi turn mode, as discussed in Section 3.2.2.4.

3. A third quasi-plateau region where the signal from the detector increases with a much lower rate. This is interpreted as the contribution from the dechanneling effect. The dechanneling probability increases with the crossed length, and it is assumed that the dechanneling probability is linear with the length (and therefore to the angular kick given by the dechanneling process). In case of integrated measurements like the collimator scan, a linear probability results in a quadratic signal:
$$f_{02}(x) = m\,x^2 + n\,x + q \qquad (3.13)$$
Since the maximum of the dechanneling contribution should be in zero ($n = 0$), and the dechanneling gives a contribution only for angles smaller than the channeling angle ($f_{02}(c + \sigma) = 0$), we obtain:

$$f_2(x) = m \cdot x^2 - (m \cdot (c + \sigma)^2) \qquad (3.14)$$

The equation $f_1(x) + f_2(x)$ has been used to fit the data in this region.

4. A last region, where the detector signal increases again with at higher rate. The contribution to losses in this region could come from amorphous scattering and volume reflection (whose probability is not zero even in channeling mode. We fitted this last contribution with an exponential function:

$$f_3(x) = B \cdot e^{(l \cdot x)} + D \qquad (3.15)$$

The equation $f_1(x) + f_2(x) + f_3(x)$ has been used to fit the data in this region.

3.2.2.2   Equivalent crystal kick and channeling angle computation

In this section we describe in detail which assumptions we made and which calculations are needed to calculate, for each collimator position, the equivalent crystal

kick, and therefore to deduce the channeling kick θ_{ch} from the measured channeled beam center c at the collimator location.

We assume on-momentum particles hitting the edge of the crystal at their maximum betatron extension:

$$\begin{pmatrix} x_0 \\ x'_0 \end{pmatrix}_{cry} = \begin{pmatrix} x_{cry} \\ -\frac{\alpha_{cry}}{\beta_{cry}} x_{cry} \end{pmatrix} \tag{3.16}$$

where x_{cry} is the aperture of the crystal and α_{cry}, β_{cry} are the twiss parameters at the crystal location. After a kick θ_k from the crystal, the coordinates at the crystal are:

$$\begin{pmatrix} x_1 \\ x'_1 \end{pmatrix}_{cry} = \begin{pmatrix} x_{cry} \\ -\frac{\alpha_{cry}}{\beta_{cry}} x_{cry} + \theta_k \end{pmatrix} \tag{3.17}$$

One can calculate the transverse coordinate $x(s_{coll})$ at the collimator location applying the standard transformation matrix M

$$M = \begin{pmatrix} \sqrt{\frac{\beta_{coll}}{\beta_{cry}}} (\cos\Delta\phi + \alpha_{cry}\sin\Delta\phi) & \sqrt{\beta_{cry}\beta_{coll}}\sin\Delta\phi \\ \frac{(1+\alpha_{coll}\alpha_{cry})\sin\Delta\phi + (\alpha_{coll}-\alpha_{cry})\cos\Delta\phi}{\sqrt{\beta_{cry}\beta_{coll}}} & \sqrt{\frac{\beta_{cry}}{\beta_{coll}}}\cos\Delta\phi - \alpha_{coll}\sin\Delta\phi \end{pmatrix} \tag{3.18}$$

where α_{coll}, β_{coll} are the twiss parameters at the collimator and $\Delta\phi$ is the phase advance between the crystal and the collimator. The transverse position $x(s_{coll})$ associated to a kick θ_k is then:

$$x(s_{coll}) = \sqrt{\frac{\beta_{coll}}{\beta_{cry}}} x_{cry} \cos(\Delta\phi) + \theta_k \cdot \sqrt{\beta_{cry}\beta_{coll}}\sin(\Delta\phi) \tag{3.19}$$

or, correspondingly, the kick θ_k associated to a transverse position $x(s_{coll})$ is:

$$\theta_k(s_{coll}) = \frac{x(s_{coll}) - \sqrt{\beta_{coll}/\beta_{cry}}\, x_{cry}\cos(\Delta\phi)}{\sqrt{\beta_{cry}\beta_{coll}}\sin(\Delta\phi)} \tag{3.20}$$

By calculating the equivalent kick associated to the center of the channeling peak c, one then obtains the channeling angle $\theta_{chan} = \theta_k(c)$.

3.2.2.3 Collimator scan limitations: multi turn limit and minimum detectable kick.

As seen Equation 3.20 transforms the collimator-position coordinates in the equivalent crystal kick space. For large enough collimator openings the transformation is bijective, i.e. to each transverse position corresponds one and only one possible kick at the crystal location. There is however a limit normalized aperture a_{multi} which
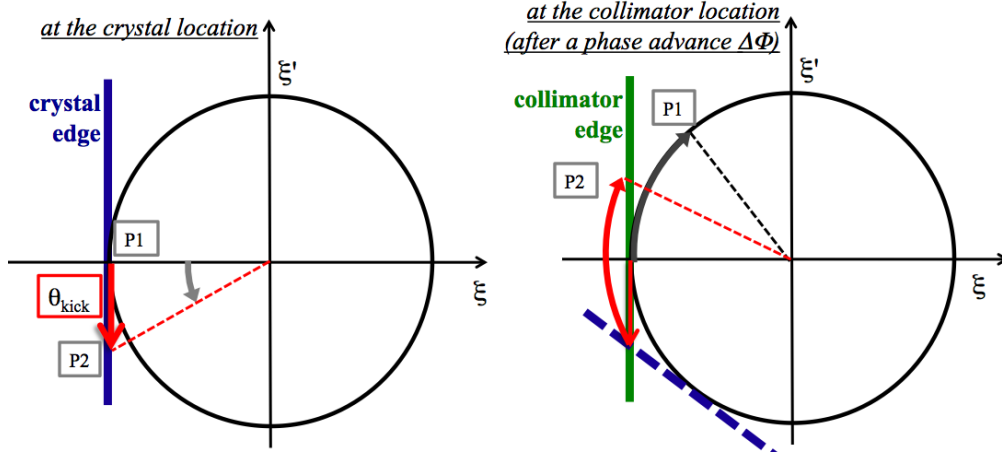
Figure 3.15: Let's consider two particles, P1 and P2, grazing the crystal surface. The particle P1 does not receive any kick by the crystal, while P2 does: this is shown in the normalized phase space, figure on the left. At the collimator (or absorber location) the particle P1 cannot be collected because of the change in phase. It is necessary a minimum kick θ_{kick}^{min} for the particle P2 to be intercepted by the collimator (or absorber) aperture, even if it is set at the same normalized aperture of the crystal (figure on the right).

sets the boundary between single passage and multi turn, and it is deduced in the following.

The presence of an absorber downstream the collimator in "single passage" collimator scan aims at reproducing a single-passage dynamics, however also in this case it always exists a maximum kick θ_{kick}^{abs} that a particle grazing the crystal can receive without being intercepted by the absorber. The kick θ_{kick}^{abs} obviously depends on the absorber normalized aperture, and its value is always larger than zero, even if the absorber has the same normalized aperture as the crystal one a_{cry} (see Figure 3.15). Given the Twiss functions at the crystal and at the absorber, the crystal and absorber transverse positions (x_{cry} and x_{abs}) and the phase advance difference $\Delta\phi_{abs}$ between the two elements, the value of θ_{kick}^{abs} can be found using equation 3.20:

$$\theta_{kick}^{abs} = \frac{x_{abs} - \sqrt{\beta_{abs}/\beta_{cry}}\, x_{cry} \cos(\Delta\phi_{abs})}{\sqrt{\beta_{cry}\beta_{abs}}\, \sin(\Delta\phi_{abs})} \tag{3.21}$$

The associated normalized amplitude a_{multi} is then:

$$a_{multi} = \sqrt{a_{cry}^2 + \sqrt{\frac{\beta_{cry}}{\varepsilon_x}}(\theta_{kick}^{abs})^2} \tag{3.22}$$

Therefore, for apertures smaller than a_{multi}, it cannot be determined if a particles at aperture was directly scattered by the crystal or performed multiple turns before being collected at the collimator, i.e. the particle position does not carry an unambiguous information on the kick received at the crystal location. For this reason, for collimator normalized positions smaller than a_{multi}, it has no meaning to apply the fitting functions illustrated in Section 3.2.2.1.

Another fundamental limitation for the collimator scan technique is the minimum detectable kick θ_k^{coll}: as we have already commented for the absorber, also for the collimator a crystal kick larger than zero is necessary to be collected at the collimator location even with the minimum collimator aperture[6] (see Figure 3.15). Using again equation 3.20, the kick θ_k^{coll} associated to the beam envelope (defined by the crystal normalized aperture a_{cry}) is then:

$$\theta_k^{coll} = \frac{\sqrt{\beta_{coll}/\beta_{cry}}\, x_{cry}(1 - \cos \Delta\phi)}{\sqrt{\beta_{cry}\beta_{coll}}\sin \Delta\phi} \tag{3.23}$$

where $\beta_{cry}, \beta_{coll}$ are the betatron functions at the crystal and collimator locations and $\Delta\phi$ is the phase advance between the two elements. This means that the collimator is intrinsically "blind" to any particle which is directly scattered by the crystal with a kick smaller than θ_k^{coll}. These particles, which at their first turn would escape the collimation system even when the collimator has the same normalized aperture at the crystal, have anyway a maximum betatron amplitude that is larger than the collimator one: they can either get lost in the machine aperture or they can be collected at the collimator location in the following turns.

3.2.2.4   Channeling efficiency computation and comparison with simulations

We assumed that the detector signal is proportional to the number of particles impacting on the collimator jaw. Using the fitting functions described in paragraph 3.2.2.1 we can evaluate the contribution of each crystal process to the measured detector signal. A normalization value is now required to calculate the probability for a certain interaction to happen. The normalization value that is measured is, in a collimator scan case, the signal associated to the total number of primary particles interacting with the crystal, and therefore the calculated probability corresponds to the multi turn efficiency (see definition in Section 1.3.2). This paragraph describes the calculation of the normalization value, the efficiency computation and the comparison with the simulations.

---

[6] i.e. when the collimator has the same normalized aperture as the crystal ($x_{coll} = \sqrt{\beta_{coll}/\beta_{cry}}\, x_{cry}$)

In order to calculate the multi turn channeling efficiency (see Section 1.3.2), it is convenient to transform the detector signal q_d in the efficiency space, defined as:

$$\frac{N_{coll}(x_{coll})}{N_{cry}} \tag{3.24}$$

where N_{coll} is the number of protons with inelastic interaction at the collimator as function of the position collimator aperture x_{coll} and N_{cry} is the number of primary protons having at least one interaction with the crystal.

We assume that the detector signal q_d downstream of the collimator is proportional to the number of inelastic interactions at the collimator N_{coll}. We write it as:

$$q_d(x_{coll}) = F \cdot N_{coll}(x_{coll}) + k \tag{3.25}$$

where F is the proportionality factor and k is an offset of the data. It is assumed that both F and k are independent on the collimator position. The baseline value k can be evaluated when the collimator jaw is retracted. On the contrary, the proportionality factor F is in principle unknown. However, when the normalized aperture of the collimator n_{coll} is even to the normalized aperture of the crystal n_{cry}, one expects that the collimator intercepts the whole flux of primary particles that is impacting on the crystal:

$$\lim_{|x_{coll}| \to (n_{cry}\sigma_x^{coll})+} N_{coll}(x_{coll}) = N_{cry} \tag{3.26}$$

However a certain leakage rate of the collimation system is foreseen, due to particles that interact with the crystal and are not lost at the collimator. For this reason an additional proportionality factor $l < 1$ is added (leakage factor), such that:

$$\lim_{|x_{coll}| \to (n_{cry}\sigma_x^{coll})+} N_{coll}(x_{coll}) = (1 - l) \cdot N_{cry} \tag{3.27}$$

The leakage factor l is usually obtained by simulations. Keeping in mind equation 3.25, one gets the signal q_{d0} detected by the detector when the normalized collimator aperture is approaching the crystal one:

$$q_{d0} = \lim_{|x_{coll}| \to (n_{cry}\sigma_x^{coll})+} q_d(x_{coll}) = F \cdot (1 - l) \cdot N_{cry} + k \tag{3.28}$$

Therefore one can express the desired quantity N_{coll}/N_{cry} in function of the detector losses:

$$\left(\frac{N_{coll}(x_{coll})}{N_{cry}}\right)^{experimental} = \frac{1/F \cdot (q_d(x_{coll}) - k)}{1/(F \cdot (1 - l)) \cdot (q_{d0} - k)} \tag{3.29}$$

Thanks to the fitting functions described in 3.2.2.1 , one can evaluate what is the contribution of the different crystal effects to the total measured detector signal. In particular, the factor A in equation 3.12 is the detector signal which is proportional to

the total number of particles in the channeled beam. The efficiency of the channeling process N_{chan}/N_{cry} is then:

$$\left(\frac{N_{chan}}{N_{cry}}\right)^{experimental} = \frac{(A-k)}{1/(1-l)\cdot(q_{d0}-k)} \tag{3.30}$$

In the case of the SPS collimator scan simulations were also performed, aiming at the comparison of experimental and simulation results. Since both $N_{coll}(x_{coll})$, N_{cry} and N_{chan} are known simulation outcomes, so that

$$\left(\frac{N_{coll}}{N_{cry}}\right)^{simulation} \quad \text{is a known quantity} \tag{3.31}$$

and the comparison with the experimental results is straightforward.

Chapter 4

Tevatron

In this chapter the results of the crystal collimation experimental program at Tevatron T980 are presented and commented. The T980 is a crystal collimation experiment where an o-shaped crystal is intended to deflect the primary halo to a downstream collimator. Different detectors were available to study the losses in the experimental region, i.e. a pin diode at the crystal location, a telescopic system of scintillators and a ionization chamber downstream the collimator. The detector signals are analyzed in details and the results are presented, including the estimation of channeling efficiency and channeling kicks for different crystal orientations. The dependency of channeling efficiency and channeling kicks is studied and successfully explained by considering effect of the large miscut angle of the crystal.

4.1   Machine description

The Tevatron [64, 65] is the main circular accelerator at the Fermi National Accelerator Laboratory in Batavia, Illinois (US). A chain of accelerators produces and accelerates protons and antiprotons up to 150 GeV before injecting them into the 6.4 km long Tevatron ring (Figure 4.1). The protons and antiprotons travel in the Tevatron in opposite directions, in one single beam pipe, while being accelerated to a maximum energy of almost 1 TeV (980 GeV). The beams collide at the centers of the 5000-ton CDF and DZero detectors located inside the Tevatron tunnel.
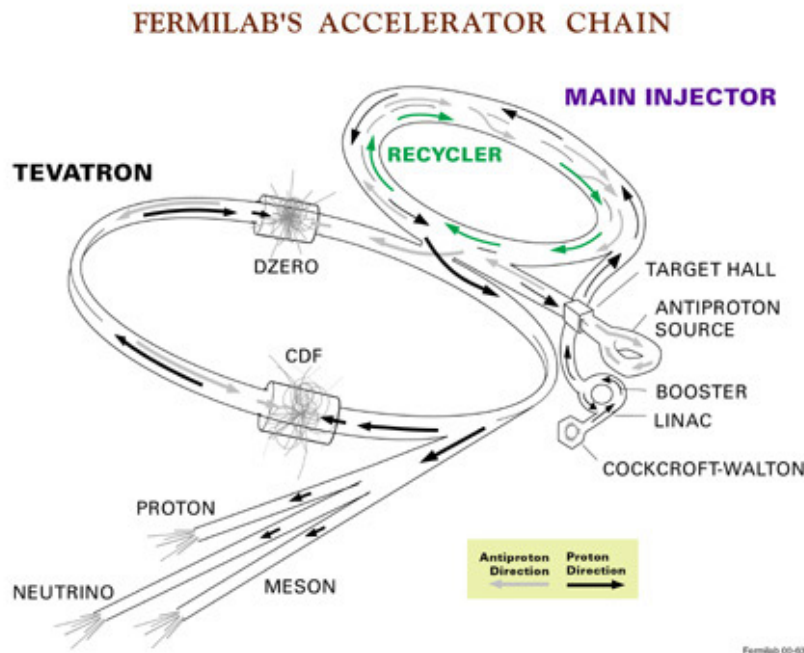
Figure 4.1: Scheme of the tevatron accelerator chain, from [64].

4.2   The Tevatron collimation system

The Tevatron collimation system is a standard two-stage system [66]: a 5 mm W primary collimator is used to scatter the beam halo, thus increasing the amplitude of the betatron oscillation and thereby increasing the impact parameter on the secondary collimators. The scattered particles are then stopped by 1.5 m long stainless steel secondary collimators. A sketch of the layout of the collimators along the machine is presented in Figure 4.2. Both the proton and the antiproton collimators have a single jaw. Moreover the collimators are L-shaped, therefore working for
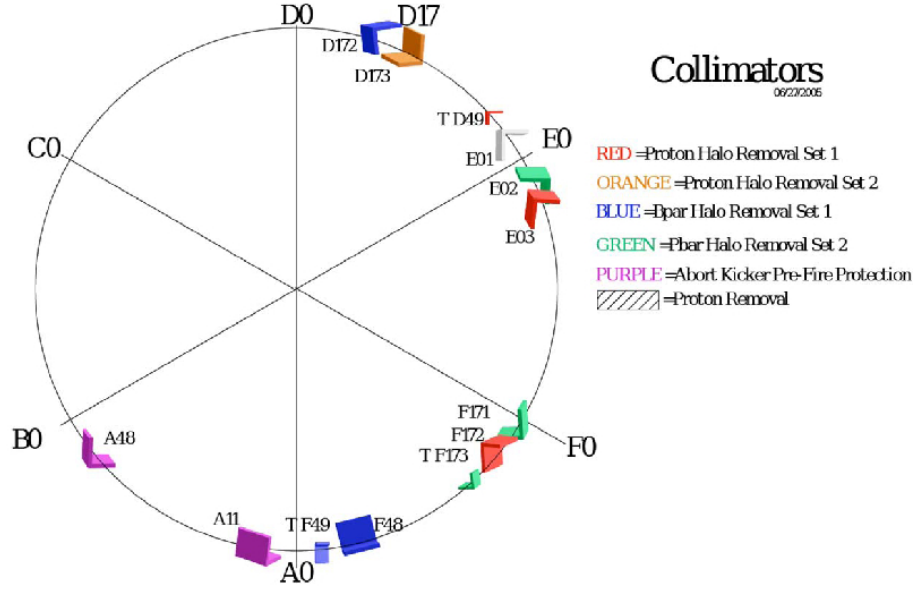
Figure 4.2: Sketch of the collimation standard collimation system in tevatron. The proton circle in clockwise direction, while the antiprotons in anti-clockwise direction. From [64].

horizontal and vertical halo at the same time.

In order to enhance the cleaning efficiency of the standard collimation system, a crystal has been inserted and tested as primary collimator for the proton beam. It is claimed in [67] that measurements at the Tevatron in 2005 showed that using a 5 mm silicon crystal to deflect the proton beam halo onto a secondary collimator improves the system performance by reducing the machine impedance, beam losses in the collider detectors and irradiation to the superconducting magnets, all in agreement with simulations. The studies presented in this chapter are focused on establishing a systematic method to analyze the data and understanding of some unexpected features observed during the measurements of the current crystal experiment in Tevatron (T-980).

4.2.1 T-980: Experimental setup, detectors and insertion region optics

The straight E0 section, where the T-980 experiment is located, is dedicated to collimation. In Figure 4.3 the insertion layouts in case of standard and crystal proton collimation are presented. During the standard runs of the machine a W
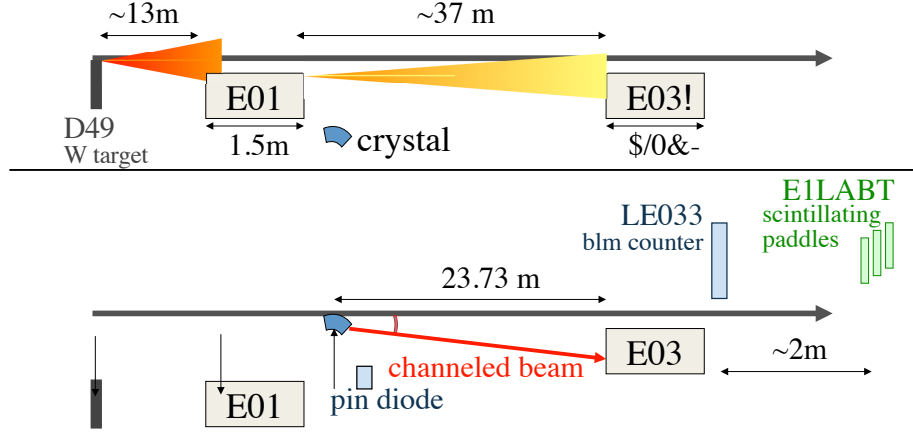
Figure 4.3: Experimental layout for standard and crystal collimation in the E0 insertion.

target (D49) is used as a primary collimator, to spread the halo particles along the downstream collimation insertion. Two secondary collimators (E01 and E03) are respectively 13 and 50 m downstream the target, in order to intercept and absorb the secondary halo. An additional proton collimator (F172) at a high horizontal dispersion location is used for momentum cleaning: the F172 collimator is about 1.3 km downstream the scraper location, in the F17 straight region.

Table 4.1: Characteristics for the crystal used in the T-980 experiment.

material	Si
length	5 mm
curvature radius	12.2 m
bending angle θ_b	410 μrad
miscut angle θ_{mis}	1.6 mrad
critical angle (straight) $\theta_{c0}(980)$GeV	6.8 μrad
critical angle (bent) $\theta_c(980)$GeV	5.5 μrad

For the T980 experiment a Si O-shaped crystal (details see Table 4.1) has been installed in the E0 insertion, at a distance $\Delta l =$23.7 m upstream the E03 collimator. The crystal is mounted on a goniometer that allows to control its angular position within 2 μrad, for a maximum range of 8 mrad. The angular position is measured both by the direct reading of the goniometer motor and by an independent optical system, which has an higher accuracy (about 0.3 μrad). The stability of the angular
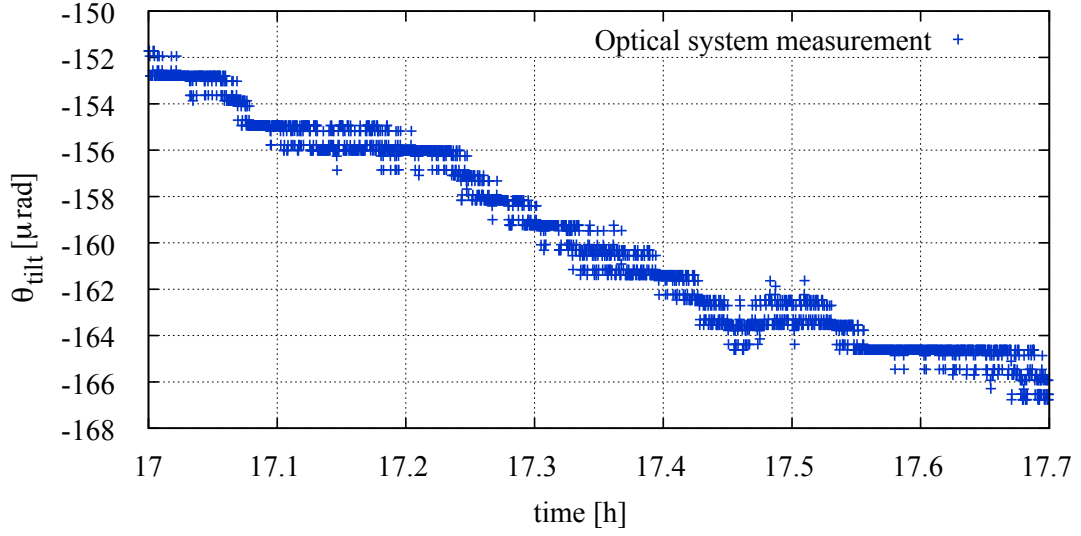
Figure 4.4: Angular position of the crystal versus time, during a crystal collimator experiment. The measurement was taken on December the 10th, 2008 between 17:00 and 17:42. During this time interval the crystal was not moved.

position over a typical collimator scan (which takes about 5 minutes) is of the order of $\pm 1 \mu$rad. A longer time interval is shown in Figure 4.4, where an angular drift of about 13 μrad in 42 minutes is registered by the optical system. It is clear that the tight alignment requirements which are required for channeling position are not met yet.

During the standard measurements the crystal aperture is set to about $3\sigma_x$, all horizontal and vertical collimators are completely retracted except for the horizontal collimator E03 and for the kicker pre-fire collimators, whose apertures are left unchanged for security reasons. The F172 horizontal jaw has also been used in one of the experimental runs in order to catch the off momentum particles scattered by the crystal.

Beam loss measurements rely on three detectors:

1. LE0PIN: A pin diode[68] about 25 cm downstream the crystal, at about 45 degrees to the beam: the signal is proportional to the total number of inelastic interactions at the crystal.

2. LE033: A beam loss monitor (ionization chamber type) about 2 m downstream of E03, clamped to the beam pipe at the beam height. The signal is proportional to the number of secondary particles generated at the collimator jaw, i.e. to the total number of inelastic interactions at the collimator.

3. A telescopic system of scintillating paddles, about 2 m downstream of E03, about 1 m over the beam height. The angle of the telescopic system is aligned with the E03 collimator. The paddles are gated in time and can discriminate the losses synchronized with the abort gap beam (E1LABT) from the losses synchronized with the bunched beam (E1LBNC). It is worth noticing that, while all the abort gap particles are outside the RF bucket, the particles synchronized with the bunched beam are a mixture of DC and bunched beam.

The scintillating paddles work in the same way and detect the same kind of particles as the ionization chambers, but differ in sensitivity and time resolution. The ionization chambers are sensitive to only large numbers of particles and the amplifiers have long rise times (microseconds). The scintillators on the other hand are sensitive to single particles and have very fast signals (rise time 2 nanoseconds).[69, 70]

Table 4.2: Values of the horizontal optical functions at the crystal and at the collimator locations, relative to the beginning of the element (with respect to the beam direction). The phase advance is to be considered with respect to the crystal. The beam rms size (σ_x) and divergence (σ'_x) have been calculated for a typical horizontal emittance of $3 \cdot 10^{-9}$m rad.

element	s [m]	β_x [m]	α_x	D_x [m]	D'_x	$\Delta\phi_x$ [2π]	σ_x [mm]	σ'_x [μrad]
crystal	3139.20	66.33	-0.47	1.94	0.012	0.0	0.45	7.43
E03 collimator	3163.02	99.15	-0.91	2.23	0.012	0.05	0.55	7.44
F172 collimator	4405.72	80.64	1.64	6.08	-0.12	3.86	0.49	11.71

The values of the main optical functions and the phase advance relative to the crystal and the collimator location are summarized in Table 4.2. In Figures 4.5 and 4.6 the horizontal beta function and the dispersion function in the E0 insertion are shown. The crystal and the collimator location are indicated in the pictures. It is worth noticing that both elements are at high positive dispersion locations. This feature makes the two elements particularly sensitive to losses of the unbunched beam, which is characterized by large negative values of δp/p. The expected δp/p for the Tevatron unbunched beam is about $-3\sigma_p/$p, where $\sigma_p/p = 0.14 \cdot 10^{-3}$ is the rms energy spread of the beam.
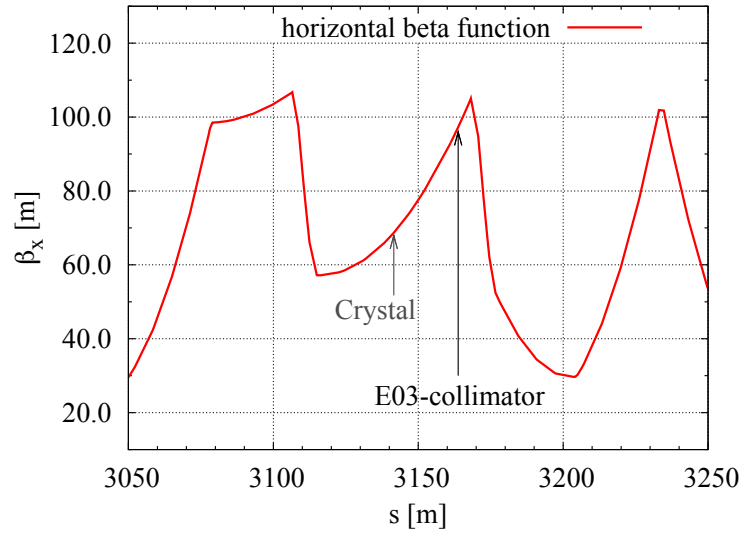
Figure 4.5: Horizontal β-function in the region where the experiment is inserted
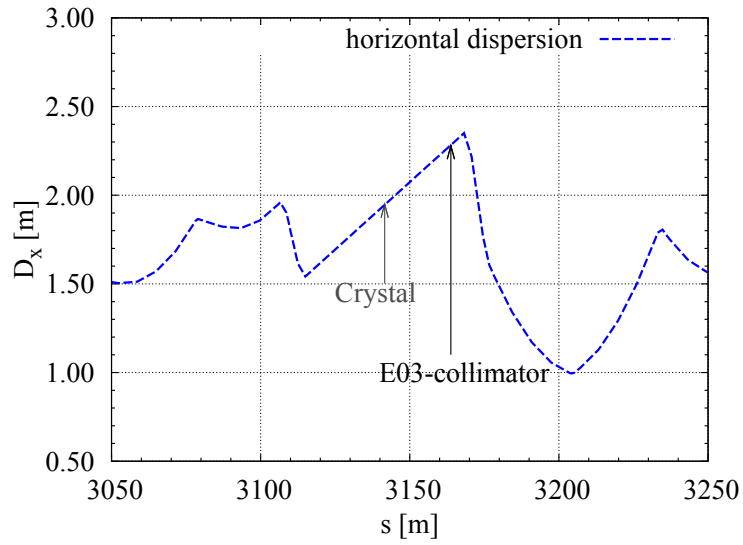
Figure 4.6: Horizontal dispersion function in the E0 region.

4.3   Experimental results

In this section the experimental results, which were obtained during October-December 2008, are presented. The experimental runs which have been analyzed and the main activities performed are listed in Table 4.3.

Table 4.3: Crystal experimental runs which have been analyzed and whose results are discussed in this chapter. The main outcomes of the experimental runs are listed.

Date	Activities
October, 29th 2008	Angular and first E03 collimator scans with crystal in main channeling and in amorphous position.
November, 20th 2008	Angular scan. E03 collimator scans with crystal for different angular orientations in the channeling region.
December 12th 2008	Angular scan. E03 collimator scans with crystal for different angular orientations in the channeling region. F17 collimator scan to intercept the off momentum particles.

During a crystal experimental run, the first priority is to identify the crystal angular orientation corresponding to the channeling region: this is done by means of angular scan, whose technique and results are described in section 4.3.1. Once the channeling region is determined, the collimator scans are performed to analyze the features of the channeled beam: the results are presented in section 4.3.2.

4.3.1   Angular scan

In this section we introduce the angular scan technique, and present the experimental results. At the first the expected features of the angular scan and the expected detector responses are listed, later some representative measurements are presented and the differences between the expected and the observed features are commented.

An angular scan consists in gradually varying the orientation of the crystal with respect to the beam axis, searching for the channeling and volume reflection region. The crystal transverse position is kept constant, and the collimator stays retracted by several σ_x (few millimeters) with respect to the crystal normalized aperture. According to theory, in correspondence to the channeling orientation, the number of inelastic interactions at the crystal should decrease while the losses at the collimator downstream should increase. Therefore the expected detector responses are:

- Pin diode "LE0PIN": The losses are expected to decrease at the channeling peak because of the reduction of inelastic interactions at the crystal. According to past simulations for the same crystal [?] a plateau region with a reduced number of inelastic interactions, associated to the volume reflection effect, should extend for about 410 μrad(equal to the bending angle) after the center of the channeling peak.

- Beam loss monitor "LE033" / scintillating paddles "E1LABT" and "E1LBNC": The losses are expected to increase at the channeling peak, since the crystal kick should direct most of the particles directly onto the collimator jaw.

The channelling peak is expected to have a Gaussian shape, and a width of about twice the crystal critical angle: $2\theta_c \approx 11$ μrad (see theory in section 1.2.2.1). Since the angular divergence is not zero, a correction factor must be considered for off momentum particles: the problem has been treated in section 2.3.1, with the grazing function formalism, and the expected additional half width is only of about 1.3 μrad (see Table 2.1). The total channeling peak width during an angular scan should consequently be about 13.6 μrad.
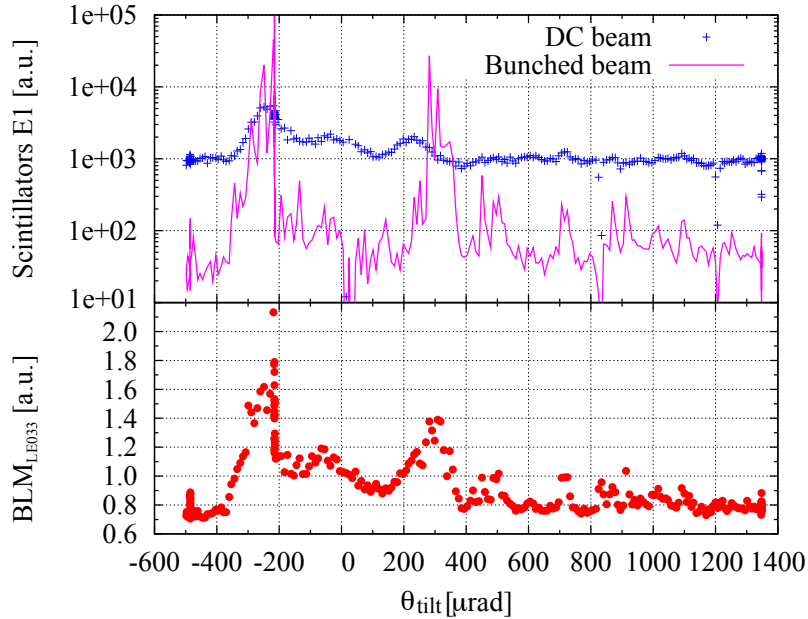
Figure 4.7: Losses detected by the BLM downstream the collimator (LE033), and by the scintillating paddles, time gated for bunched and unbunched beam.

The signals measured during the angular scans do not reproduce the expected features. Here an almost 2 mrad wide angular scan is selected, which can be considered representative of the entire set of angular scans performed. The data were taken

on November the 20th, 2008, between 16:18 and 16:23 (Chicago time). During the selected angular scan the crystal normalized aperture was about $n_{cry} = -3\sigma_x$ and the E03 collimator was retracted by 3 mm (about $5.5\sigma_x$) with respect to the crystal normalized aperture. The horizontal transverse emittance ε_x was of $3 \cdot 10^{-9}$m rad. In Figure 4.7 the beam loss monitor signal (red curve) and the scintillating paddles signals (blue curve for the abort gap beam, purple for the bunched beam) versus the crystal orientation θ_{tilt} are compared. The three signals clearly reproduce the same structure:

   - The losses start to increase at $\theta_{tilt} \simeq -360 \pm 10$ μrad for all the detectors, they reach a maximum at $\theta_{tilt} \simeq -250$ μrad and then slightly decrease.

   - There seems to be a plateau region, at least for the off momentum particles, for orientations $-250 < \theta_{tilt} < 0$ μrad.

   - A second peak (reproducible in all the angular scan performed) is between $+250$ μrad and $+300$ μrad.

The collimator scan investigations presented in Section 4.3.2.3 confirm that the main peak is associated to channeling effect, and that in coincidence with its maximum (i.e. ~ 100 μrad after the beginning of the peak) we also get the maximum channeling efficiency (see Table 4.6). On the contrary, the collimator scans performed for crystal orientations corresponding to the secondary peak did not reveal any different feature from the scans in amorphous orientation.

In Figure 4.8 the signal from the pin diode is shown for the same angular scan. Contrary to the expectations, there is no decrease of the signal in correspondence to the channeling peak. A moderate reduction of the signal is measured between about -200 and 250 μrad. At $\theta_{tilt} \simeq 300$ μrad, exactly as for the other detectors, a peak of the losses is registered.

In Figure 4.9 the beam loss monitor signal is compared to the total signal detected by the scintillating paddles (bunched beam plus abort gap beam), and the two signals, as expected, are proportional.

In summary, the unpredicted features observed during the angular scans are:

   - A narrow channeling peak has not been found. The measured peak has a width of about 150 μrad, i.e. ten times larger than expected. It will be demonstrated in section 4.3.2.5 that this behavior is compatible with the large value of miscut angle of the crystal.

   - The pin diode signal does not decrease at the channeling peak. A possible explanation could be the large amorphous layer associated to the channeling position, which is caused by the miscut angle, as commented in section 4.3.2.5.
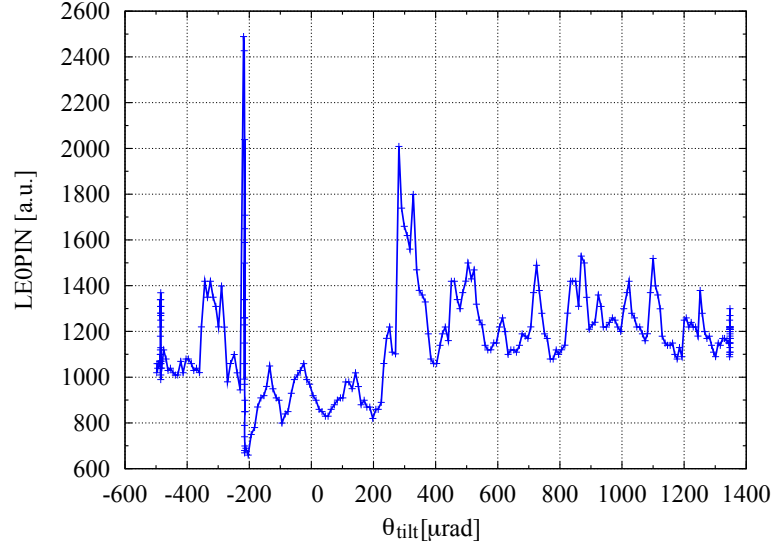
Figure 4.8: Losses detected by the PIN diode downstream the crystal (LE033) versus crystal orientation.
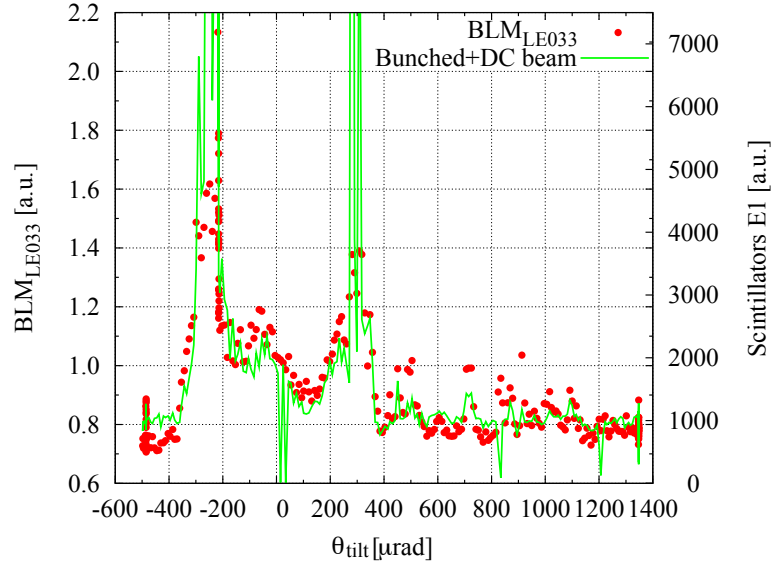
Figure 4.9: Losses detected by the BLM downstream the collimator (LE033), and zoom of the total losses detected by the scintillating paddles (sum of bunched and unbunched beam).

- A second peak, reproducible in all the measurements, is observed. Investigation of this second peak via collimator scan, not presented here, did not show any feature different from the angular scan in case of amorphous material.

4.3.2 Collimator scans

During a collimator scan the collimator jaw downstream the crystal is slowly inserted, from a totally retracted position, up to the beam edge, defined by the crystal normalized aperture (see section 3.2.2.4 for details). The crystal orientation is kept constant. The losses downstream the collimator are detected by the beam loss monitor LE033, by the scintillating paddles gated with the bunched beam (E1LBNC) and with the abort gap (E1LABT). In particular, in the case of channeling orientation, the signals of both detectors are expected to increase when the collimator jaw reaches the channeled beam position (see a complete description in section 3.2.2.1)

In sections 4.3.2.1 and 4.3.2.2 it is described how the data is analyzed, passing from the raw collimator scan data (losses versus collimator position) to efficiency curves (percentage of particles lost in the collimator vs crystal equivalent kick). Section 4.3.2.3 presents the results of the whole set of collimator scans performed and the presumed incongruences which apparently arise from the collimator scan analysis, e.g. the channeling kick value that is much smaller than expected. Possible causes are suggested and investigated in details in the next sections (4.3.2.4 and 4.3.2.5).

4.3.2.1 Normalized curves: baseline and normalization values

As explained in details in Section 3.2.2.4, for channeling efficiency calculations it is convenient to normalize the collimator scan data as described in equation 3.30 (that we repeat here for convenience):

$$\left(\frac{N_{coll}(x_{coll})}{N_{cry}}\right)^{experimental} = \frac{(q_d - k_o)}{(1/(1-l)) \cdot (q_{d0} - k_o)}$$

where $N_{coll}(x_{coll})$ are the number of particles hitting the collimator jaw when the collimator is set at an aperture x_{coll}, N_{cry} are the particles impacting on the crystal at least once, q_d is the signal detected by the detector , q_{d0} is the detector signal when the normalized collimator aperture is approaching the crystal one, k_o is an offset of the data and the proportionality factor l is the leakage factor of the system, i.e. the relative number of particles which leaks from the collimation system and and lost elsewhere. If the loss data are fit with an error function (as described in section 3.2.2.1), then the measured channeling efficiency η_{ch} is:

$$\eta_{ch}^{experimental} = (1-l) \cdot \frac{(A - k_o)}{(q_{d0} - k_o)} \tag{4.1}$$

where A is the maximum value of the error function fit.

It is important to remember that the equation 3.30 is valid only for the assumption of linear proportion between the particles hitting the collimator N_{coll} and the particles seen by the detector q_d. The factors q_{d0} and k_o are experimentally determined, while l is usually taken from the simulations. Since the simulations were not available in the Tevatron case, it seemed reasonable to use the value of 0.95 which was obtained for SPS simulations (a relative error of $\pm 5\%$ was assigned). This section presents the different element configurations which would lead to different q_{d0} and k_o values and we justify our specific choice.
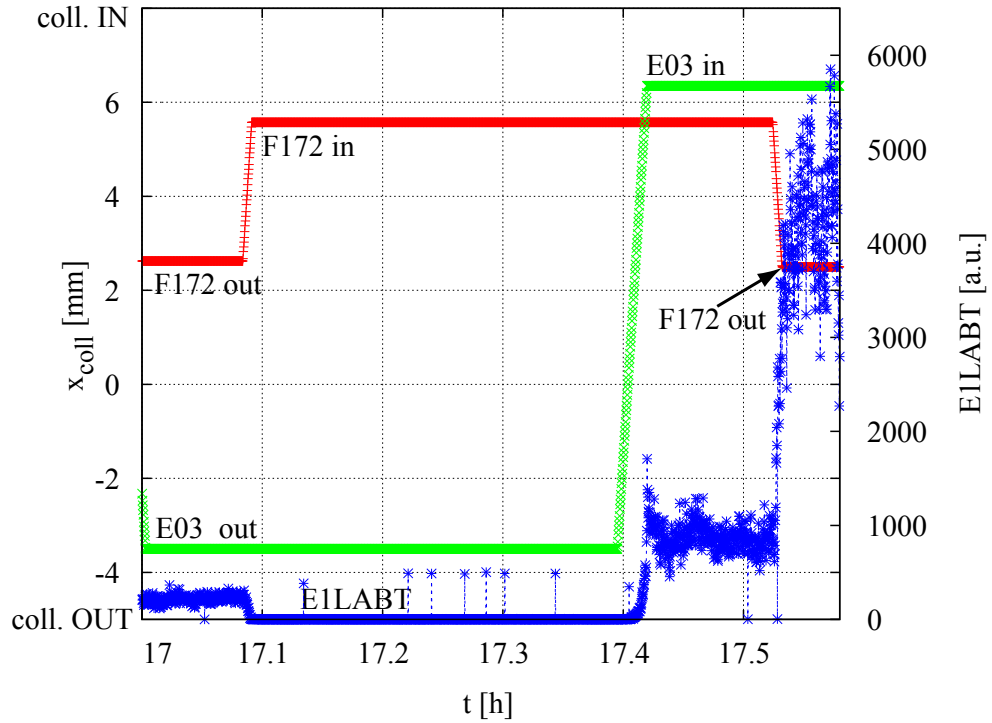
Figure 4.10: E1LABT losses versus time, with the crystal inserted. The signal variation for different configurations of the collimators is shown. The data refers to measurements performed on December the 10th, 2008.

The data presented in this section refer to the experimental run of December the 10th, the only one where measurements with the collimator F172 have been done. An example of the losses detected by the scintillating paddles (E1LABT signal) for different configurations of the E03 and F172 collimators is given in Figure 4.10.

The values must not be taken as an absolute reference, because they depend on the intensity of the stored beam and on the beam lifetime. They can however

provide a useful guideline to scale the effect of various processes.

Normalization value

For the estimation of the normalization values q_{d0}, two different configurations, for the three signals, have been considered:

1. The crystal is inserted (i.e. is positioned at about $3\sigma_x$ from the beam center) and the collimator E03 is aligned to the crystal normalized aperture.

2. The crystal is inserted and both the collimator E03 and F172 normalized apertures are equal to the crystal one.

The detector signals in the two cases, i.e. the possible normalization value q_{d0}, are listed in table 4.4. Being the E1LBNC signal (scintillating paddles gated with the bunched beam) signal to noise ratio too low, for the analyzed collimator scans only the BLM data (signal LE033) and the scintillating paddles gated with the abort gap data (signal E1LABT) are considered.

Table 4.4: Average normalization values q_{d0} used during the collimator scan data analysis. The data refers to measurements performed on December the 10th, 2008.

detector	LE033 [V]	E1LABT [Hz]	E1LBNC [Hz]
1. E03 collimator and crystal in, F172 collimator out	1.7±0.1	4200±700	up to 10^5
2. E03 collimator, F172 collimator and crystal in	1.35±0.1	890±150	up to 10^5

Since the F172 collimator was not used during the collimator scans presented in the next sections, the normalization values used for efficiency calculations correspond to the case 1 in table 4.4.

Nevertheless it is worth noting how most of the losses disappear when the F172 collimator is inserted with a normalized aperture equal to the E03 collimator (case 2 in table 4.4), since most of the off momentum particles are directly stopped by the F172 collimator, which is the one at the highest dispersion location. As expected, most of the particles in the abort gap interact with the F172 jaw, and the E1LABT drops to about 22% of its previous value, while the decrease for the LE033 signal is much lower, and it stabilizes to about the 80% of its previous value. The high

percentage of off momentum particles is compatible with the fact that all the measurements were performed at the end of the beam store.

Baseline value

The offset value k_o for the three detectors is listed in table 4.5, in four different configurations:

1. The readings of the detectors when there is no beam is perfectly zero, showing that there is no intrinsic offset in the signals and the detector signals cannot be ascribed to the residual radiation of the beam line elements.

2. The readings of the detectors when both the crystal and the E03 collimator are completely retracted (about -20 mm) is compatible with zero, showing that in retracted position the elements receive negligible radiation.

3. With the crystal inserted, and keeping the collimator about 9 mm (i.e. about $15\sigma_x$) retracted with respect to the crystal normalized aperture, the readings of the detectors are sensibly different from zero. For the E1LABT the losses are still low if compared with the maximum normalization values listed in table 4.4 (about 0.6%). On the contrary, the LE033 signal is already at the 23% of its maximum value.

   The discrepancy between the scintillator and the BLM behavior can be explained by the different positioning of the two detectors. While the BLM is

Table 4.5: Different possible offset values for different collimator configurations. The F172 collimator is out unless specified differently. The data refers to measurements performed on December the 10th, 2008.

detector	LE033 [V]	E1LABT [Hz]	E1LBNC [Hz]
1. no beam	0	0	0
2. crystal and E03 collimator totally retracted (about -20 mm)	$(2\pm 0.5)10^{-3}$	0	1±1
3. *E03 collimator retracted, crystal in*	*0.4±0.1*	*225±50*	*20±10 (spikes up to 2·10³)*
4. E03 collimator retracted, crystal in and F172 collimator in	0.08±0.05	1.5±1 (spikes up to 500)	2±2 (spikes up to 50)

"on plane" with the beam and the crystal (horizontal positioning, beam height), the scintillators are "off plane" (vertical orientation, covering only large scattering angle) and their telescopic system aims at measuring particles coming directly from the E03 collimator.

Consequently it is reasonable to assume that the losses detected by the scintillators are always related to inelastic interactions at the collimator jaw (apart from rare coincidence events generated by background particles [69]), while the losses recorded by the BLM are probably generated by other sources (e.g. direct scattering from the crystal). This topic is further discussed in the next section, leading to the conclusion that the scintillator measurements are more suitable for channeling efficiency calculations. See the details in Section 4.3.2.3.

4. When considering the reduction in losses for both detectors when the F172 collimator is inserted, it is indisputable that most of the losses seems to be correlated to off momentum particles (last case presented in table 4.5).

4.3.2.2 Equivalent kick

It can be convenient to plot the loss data versus the equivalent crystal kick (as described in section 3.2.2.2), instead of versus the collimator position. The equivalent crystal kick θ_k is calculated starting from equation 3.20 that, in terms of the measured values, becomes:

$$\theta_k = \frac{(x_{coll}^M - x_{coll0}^M) + \sqrt{\varepsilon_x^M \beta_{coll}}\; n_{cry} - \sqrt{\varepsilon_x^M \beta_{coll}}\; n_{cry} \cos(\Delta\phi)}{\sqrt{\beta_{cry}\beta_{coll}}\; \sin(\Delta\phi)} \qquad (4.2)$$

where x_{coll}^M is the absolute position of the collimator, x_{coll0}^M is the absolute position of the collimator when having the same normalized aperture as the crystal, ε_x^M is the horizontal emittance as measured during the run by a wire scanner downstream the crystal. Since the beam center at the collimator and crystal position is unknown, from the loss intensity and the past experience a normalized aperture of $n_{cry} = 3 \pm 1$ has been estimated. The optical function values ($\beta_{coll}, \beta_{coll}, \Delta\phi$) are the ones specified in table 4.2, from the Tevatron optics database [71]. A relative error of 5% has been assigned to these variables.

With this transformation it is straightforward to calculate the crystal channeling kick by fitting the data with an error function, as described in section 3.2.2.1. In this case the measured channeling angle θ_{ch} is simply:

$$\theta_{ch} = \frac{(x_{coll-CH}^M - x_{coll0}^M) + \sqrt{\varepsilon_x^M \beta_{coll}}\; n_{cry} - \sqrt{\varepsilon_x^M \beta_{coll}}\; n_{cry} \cos(\Delta\phi)}{\sqrt{\beta_{cry}\beta_{coll}}\; \sin(\Delta\phi)} \qquad (4.3)$$

where $x_{coll-CH}^M$ is the center of the error function which fits the loss data.

4.3.2.3 Collimator scan results

Different collimator scans have been performed, corresponding to different angular orientations of the crystal, all within the measured channeling region, i.e. with a crystal angular orientation θ_{tilt} between about -360 and +50 μrad (as discussed in section 4.3.1, see Figure 4.7). In this section the channeling efficiency results and the channeling angle computation are discussed: at first the normalized losses for different detectors are compared, concluding that the scintillator data is more appropriate for channeling efficiency calculation. Afterwards the results for efficiency and for channeling angle are given for all the performed collimator scans. Some unexpected features arising from the data analysis are commented at the end of this section.
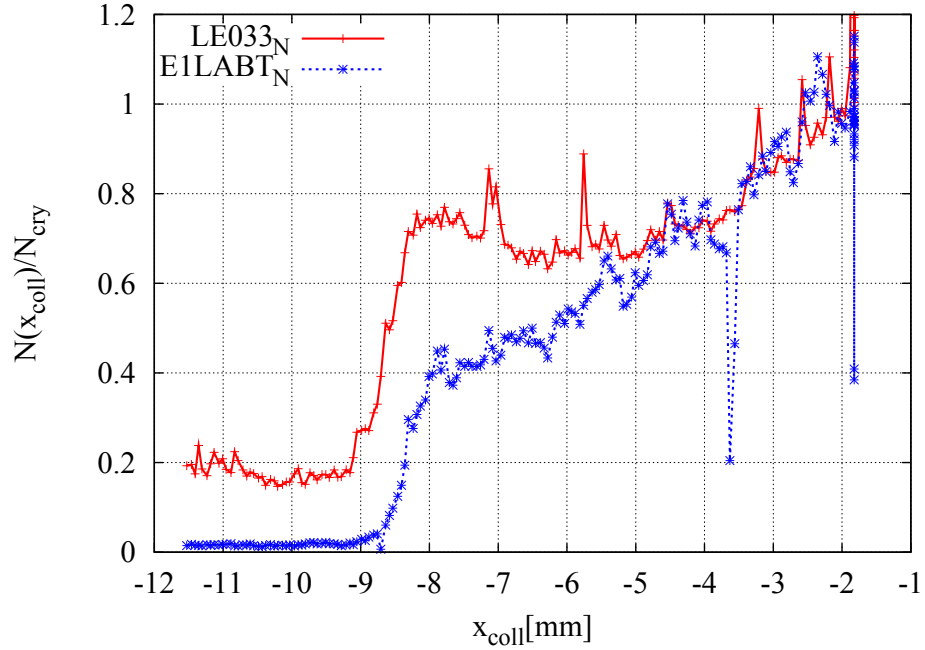
Figure 4.11: Normalized detector signals versus collimator position, for the E1LABT (Red curve) and the LE033 signal (Green curve)

A representative example collimator scan result is shown in Figure 4.11 for the normalized E1LABT (Blue curve) and the LE033 signal (Red curve). The data were taken on November the 20th, 2008, between 15:21 and 15:27 (Chicago time). The crystal angular orientation with respect to the beginning of channeling peak ($\theta_{tilt} = -360$ μrad) for this collimator scan was θ_{tilt0}=123 μrad , close to the center of the channeling peak (see Figure 4.7).

The efficiency data have been normalized as described in section 4.3.2.1, with normalization values $q_{d0} = 1.6$ and $q_{d0} = 9000$ for LE033 and E1LABT respectively. In order to take into account all the particles hitting the detectors, we set the offset value k_o to zero for both curves. The normalized sets of data are indicated with LE033$_N$ and E1LABT$_N$, with obvious notation.

The two normalized curves exhibits some differences:

- For $x_{coll} < -9.2$ mm, in first approximation the two signals do not depend on the collimator position, since no beam is expected to hit the collimator directly. However, while the E1LABT$_N$ value (about 0.6% of its maximum) is consistent with this hypothesis, the LE033$_N$ is already at about 23% of its maximum value (as already commented in section 4.3.2.1).

- Both the curves have an abrupt rise in correspondence to the collimator position -9 mm$< x_{coll} < -7.5$ mm , but afterwards their trends become sensibly different. For the LE033 signal the maximum is followed by a decrease of the signal of about 15% up to $x_{coll} = -6$ mm, then the signal grows again with a linear trend. On the other hand, for the E1LABT signal, for $x_{coll} > -7.5$ mm the signal constantly grows with a linear trend.

In order to get a realistic interpretation of the observed behavior, it is necessary to consider the different positions of the two detectors: the scintillators and the BLM. Even if they are sensitive to the same kind of radiation, their positions expose them to particles associated to different processes. While the scintillators, far from the beam pipe and in vertical position, can only detect showers generated at the E03 collimator jaw, the BLM can also detect showers directly generated by the crystal or by the collimator edge. This makes the LE033 signal particularly sensitive to edge effects in the collimator, as shown in Figure 4.12.
 If one believes the E1LABT to be purely proportional to the secondary emitted particles, and independent of any other radiation source, it is then possible to highlight these "impure" effects (direct scattering from crystal, edge effects) by subtracting the E1LABT$_N$ curve from the LE033$_N$ one.
The result is shown in Figure 4.13, where the normalized curves are plotted versus the collimator position. The blue curve corresponds to the difference between the green curve (LE033$_N$) and the red one (E1LABT$_N$) . Three regions can be identified:

- Region 1: the BLM measures about the 20% of its maximum value, while almost nothing is detected by the scintillators. The signal does not depend on the collimator position x_{coll}, for position up to x_{coll}=-9.2 mm. This region corresponds to the case 1 in picture 4.12.

- Region 2: the signals of both detectors increase, but with different rate. Their difference reaches a maximum at the position x_{coll}=-8.5 mm, i.e. 1 mm after
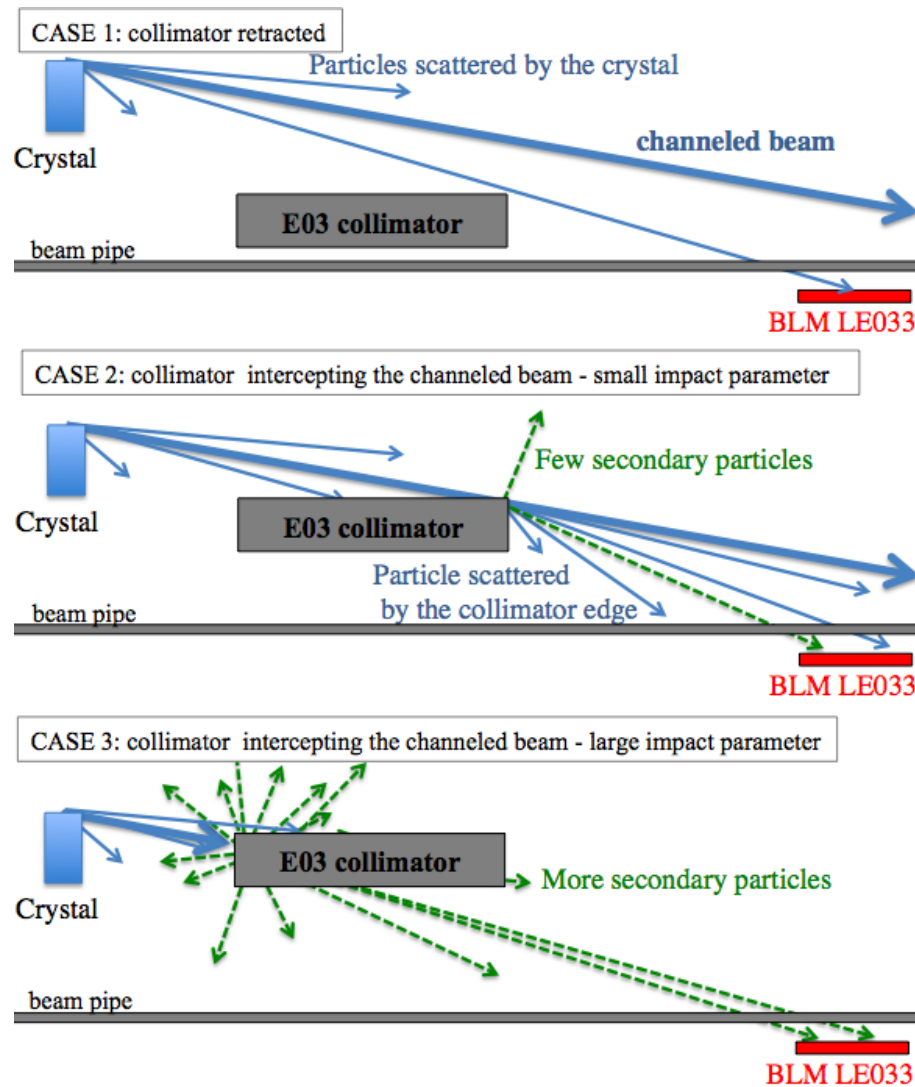
Figure 4.12: Pictorial view of the different processes that the detectors are exposed to. The BLM can detect a series of "dirty" effects, like a certain number of particles directly scattered by the crystal or by the collimator edge. The scintillators, on the other way, are sensitive only to secondary emitted particles (in green in the Figure).
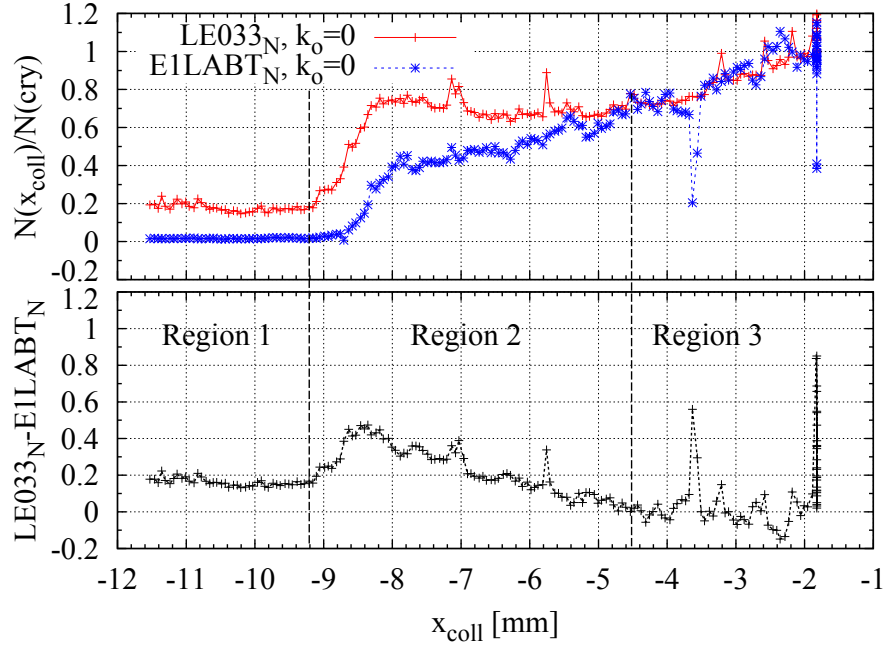
Figure 4.13: Normalized detector signals versus collimator position, for the E1LABT and the LE033 signal, and the difference between the two signals (in black).

the collimator begins to intercept the channeled beam. In further inserting the E03 collimator, the edge effect gradually decreases, up to a point (x_{coll}=-4.5 mm) where the two normalized curves (LE033$_N$ and E1LABT$_N$) have he same value. This region corresponds to the case 2 in picture 4.12.

- Region 3: the BLM and the scintillator give comparable signals, and their difference is compatible with zero. This region corresponds to the case 3 in picture 4.12, where only secondary emitted particles are detected by both detectors.

It can be then concluded that, due to its position, the E1LABT signal is more suitable for calculating the channeling efficiency $\left(\frac{N_{coll}(x_{coll})}{N_{cry}}\right)$, while both signals can be used to evaluate the channeling kick.

The edge effects, however, can play a role for the efficiency calculation even when using the E1LABT signal. As a matter of fact, for a configuration beam-collimator like the one illustrated in Figure 4.12, for the same number of particles impacting on the jaw, the number of secondary emitted particles is larger for larger impact parameters [?]. One cannot conclude whether the signal detected in the intermediate region between the channeled beam and the primary beam envelope is associated to an effective population of particles in this region, or rather an effect of the lager impact parameter that increases the E1LABT signal. The exact relationship be-

tween the E1LABT signal and the quantity $N_{coll}(x_{coll})$ could be calculated only via dedicated simulations studying the evolution of the radiation field at the scintillators location versus the position of the collimator. Since it was not possible to run the appropriate simulations during this thesis, we used the linear approximation already described in section 3.2.2.4.

It is therefore important to consider that the number of particles impacting at the collimator at the channeled position could be underestimated.
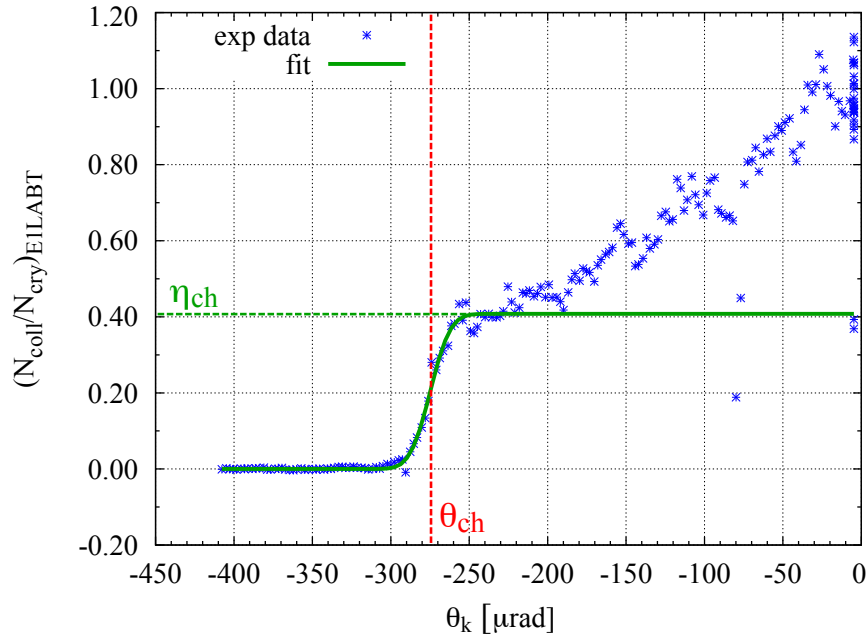
Figure 4.14: Losses detected by scintillating paddles, synchronized with the abort gap, versus the equivalent kick. Center: -275 μrad, sigma:10.1 μrad, efficiency 41%.

An example of "efficiency curve" (i.e. normalized losses versus equivalent kick curve) is given in Figure 4.14, for the E1LABT detector (data already presented in Figure 4.11). Once the efficiency curves are obtained, it is straightforward to calculate both the minimum channeling efficiency η_{ch} and the channeling kick θ_{ch}, as shown in Figure 4.14.

The results for the entire set of collimator scans are summarized in Table 4.6, where the first column θ_{tilt0} refers to the tilt angle with respect to the beginning of the channeling peak, i.e.

$$\theta_{tilt0} = \theta_{tilt} - \theta_{tiltB} \tag{4.4}$$

θ_{tilt} is the crystal orientation as read by the optical system and $\theta_{tiltB} = -360 \pm 10$

μrad is the beginning of the channeling peak as deduced by the angular scan (as discussed in section 4.3.1). The channeling angle θ_{ch} and its rms width σ_{ch} are listed for each case, and calculated both using the BLM and the scintillator data. On the contrary, for the reasons already discussed in this section, the channeling efficiency η_{ch} has been calculated using only the scintillator data.

Table 4.6: Measured equivalent kick and minimum channeling efficiency for collimator scans with different crystal orientations, where the tilt is to be considered from the beginning of the channeling peak.

θ_{tilt0} [μrad]	$\theta_{chLE033}$ [μrad]	$\sigma_{chLE033}$ [μrad]	$\theta_{chE1LABT}$ [μrad]	$\sigma_{chE1LABT}$ [μrad]	η_{ch}
65	338±21	15 ± 1	319±21	21 ± 1	0.12±0.02
73	324±21	19 ± 2	316±21	15 ± 2	0.21±0.04
91	311±21	16 ± 1	288±20	27 ± 3	0.58±0.11
97	311±21	13 ± 1	298±20	15 ± 1	0.60±0.11
102	297±20	12 ± 1	280±20	16 ± 1	0.57±0.11
105	304±20	15±1	283±20	21 ± 1	0.61±0.11
117	289±20	17 ± 1	275±19	16 ± 2	0.58±0.11
123	287±20	10 ± 3	275±19	14 ± 1	0.41±0.08
123	283±20	7 ± 3	274±19	9 ± 1	0.38±0.07
127.5	273±19	14 ± 1	259±19	16 ± 1	0.29±0.06
160	271±19	14 ± 1	256±20	12 ± 1	0.27±0.05
208	229±18	29 ± 6	209±17	30 ± 3	0.17±0.03

The errors are calculated starting from equation 4.1 (for η_{ch}) and from equation 4.2 (for $\theta_{chE1LABT}$ and $\theta_{chLE033}$) using the standard error propagation for independent variables x_i:

$$\delta(f(x_i)) = \sqrt{\sum \left(\frac{\partial f}{\partial x_i} \delta(x_i) \right)^2} \tag{4.5}$$

where the errors associated to the measured variables are listed in table 4.7. On top of that, an error of 5% was assigned to the optics variables $\beta_{coll}, \beta_{coll}$ and $\Delta\phi$ (compatible with small variations of the optics) and large uncertainty (33%) has been assigned to the crystal normalized aperture value n_{cry} (equation 4.2). The uncertainty on the proportionality factor l in equation 4.1 was set to 5%.

Some unexpected features, common to all set of data, can be noticed:

- Channeled beam are observed for a large range of orientations, as already expected from the angular scan data.

Table 4.7: Errors assumed on the measured quantities which are used for the error evaluation on the channeling kick and on the channeling efficiency.

channeling kick		
x_i	error	
$x^M_{coll-CH}$	$\delta(x^M_{coll-CH})/x^M_{coll-CH} = 0.01$	fit parameters slightly vary with the chose of the fitting interval
x^M_{coll0}	$\delta(x^M_{coll0}) = 250\ \mu$m	uncertainty on the beam envelope position, as evaluated from measurements
ε^M_x	$\delta(\varepsilon^M_x)/\varepsilon^M_x = 0.2$	assumed uncertainty on the wire scanner measurement
channeling efficiency		
x_i	error	
A	$\delta(A)/A = 0.02$	fit parameters slightly vary with the chose of the fitting interval
k_0	$\delta(k_0)) = 15$	rms spread of the signal
q_{d0}	$\delta(q_{d0}))/q_{d0} = 0.16$	rms spread of the signal

- The measured channeling angle is always smaller than the expected channeling angle (expected θ_{ch}=410 μrad), and decreases linearly with the crystal tilt. This behavior can be explained by considering the effect of the large positive miscut angle. A detailed description of the miscut angle effects is given in section 2.3.2. We evaluate the expected miscut angle effects for Tevatron in section 4.3.2.5.

- The channeling angle calculated for the abort gap beam is always smaller than the angle calculated for the total beam. The average difference is $\Delta k = 16 \pm 5$ μrad. This is probably because the equivalent kick computation is done by considering on-momentum particles. We evaluate the influence of off momentum particles in section 4.3.2.4.

- The channeling efficiency varies with the crystal tilt, and follows almost the same trend as the losses at the collimator registered during an angular scan (see Figure 4.15).
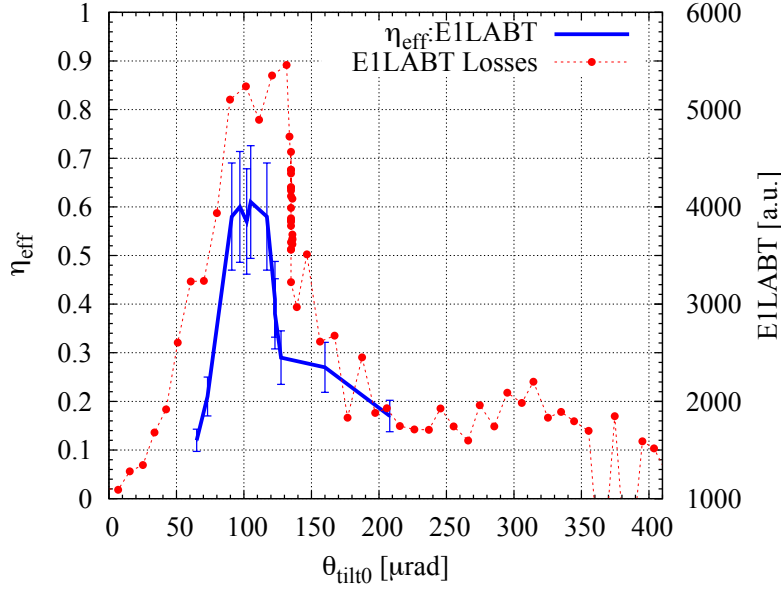
Figure 4.15: Channeling efficiency versus crystal tilt, calculated for E1LABT (abort gap) data. On the secondary vertical axis, for comparison, the E1LABT losses during an angular scan.

4.3.2.4   Off momentum particle displacement at the collimator

In this section the impact of off momentum particles in the equivalent kick calculation is studied. The method presented in section 3.2.2.2 is generalized and a correction factor for the off momentum particles constituting the abort gap beam (DC beam) is estimated.

A particle with relative momentum offset δ with respect to the nominal energy, if grazing the crystal surface, has a betatron amplitude and angle:

$$x_\beta = x_{cry} - \eta_{cry}\,\delta \tag{4.6}$$

$$x'_\beta = -\frac{\alpha_{cry}}{\beta_{cry}}\left(x_{cry} - \eta'_{cry}\,\delta\right) \tag{4.7}$$

where η_{cry} and η'_{cry} are, respectively, the dispersion and $\eta' = \frac{d\eta}{ds}$ at the crystal location. If one considers a momentum offset of $\delta = -3\sigma_p/p$ (with $\sigma_p/p = 0.14 \cdot 10^{-3}$ rms momentum offset for the Tevatron), i.e. roughly the maximum value of the momentum offset for the particles on the separatrix of the RF bucket, the impacting angle differs from the on-momentum impacting angle by about 1.6μrad. This angle is much smaller than the acceptance for channeling, which is about twice the critical angle for the crystal $2\theta_c = 13$ μrad. Therefore, as already commented, on-momentum and off-momentum particles can be channeled at the same time, thus

receiving all the same kick k.

Decoupling the betatron from dispersive motion, the off momentum particle coordinates after a kick k can be written as:

$$
\begin{pmatrix} x_{\beta 1} \\ x'_{\beta 1} \\ \delta p/p \end{pmatrix}_{cry} = \begin{pmatrix} x_{cry} - \eta_{cry}\,\delta \\ -\frac{\alpha_{cry}}{\beta_{cry}}\left(x_{cry} - \eta_{cry}\,\delta\right) + k \\ \delta \end{pmatrix} \tag{4.8}
$$

The transformation matrix to propagate the coordinates from the crystal to the collimator location is:

$$
M = \begin{pmatrix} \sqrt{\frac{\beta_{coll}}{\beta_{cry}}}\left(\cos\Delta\phi + \alpha_{cry}\sin\Delta\phi\right) & \sqrt{\beta_{cry}\beta_{coll}}\sin\Delta\phi & \eta_{coll} \\ \frac{(1+\alpha_{coll}\alpha_{cry})\sin\Delta\phi+(\alpha_{coll}-\alpha_{cry})\cos\Delta\phi}{\sqrt{\beta_{cry}\beta_{coll}}} & \sqrt{\frac{\beta_{cry}}{\beta_{coll}}}\cos\Delta\phi - \alpha_{coll}\sin\Delta\phi & \eta'_{coll} \\ 0 & 0 & 1 \end{pmatrix}
$$
$$\tag{4.9}$$

Using the input particle specified in equation 4.8, and remembering that in general $x(s) = x_\beta(s) + \eta(s)\cdot\delta$, we obtain that the transverse coordinate for an off momentum particle at the collimator location is:

$$
x(s_{coll}) = \sqrt{\frac{\beta_{coll}}{\beta_{cry}}}(x_{cry} - \eta_{cry}\,\delta)\cos(\Delta\phi) + k\sqrt{\beta_{cry}\beta_{coll}}\sin(\Delta\phi) + \eta_{coll}\,\delta \tag{4.10}
$$

The general formula for the equivalent kick is therefore:

$$
k = \frac{x(s_{coll}) - \sqrt{\beta_{coll}/\beta_{cry}}\,(x_{cry})\cos(\Delta\phi) + \left(\sqrt{\beta_{coll}/\beta_{cry}}\,\eta_{cry}\cos(\Delta\phi) - \eta_{coll}\right)\delta}{\sqrt{\beta_{cry}\beta_{coll}}\sin(\Delta\phi)} \tag{4.11}
$$

that has to be compared to the equation 3.20 for on-momentum particles. This means that, with the method described in section 3.2.2.2, we underestimate the observed equivalent kick by a quantity Δk which depends on the value of $\delta p/p$.

$$
\Delta k(\delta) = \frac{\left(\sqrt{\beta_{coll}/\beta_{cry}}\,\eta_{cry}\cos(\Delta\phi) - \eta_{coll}\right)\delta}{\sqrt{\beta_{cry}\beta_{coll}}\sin(\Delta\phi)} \tag{4.12}
$$

The value of Δk associated to a momentum offset of $\delta p/p = -3\sigma_p/p$ is 12 μrad. This value is compatible with the angular shift found when comparing the total beam and abort gap beam data, that is $\Delta k_{exp} = 16 \pm 5$ μrad (see Table 4.6).

4.3.2.5 Miscut angle effects

This section compares the measured channeling peaks with the angular kicks with a large miscut angle, as for the considered crystal. One sees how the miscut angle

successfully explains the large channeling peak, the reduced channeling kick and the dependence of the latter on the crystal tilt.

As explained in section 2.3.2, in the presence of a large positive miscut angle the channelling process is possible for every tilt of the crystal between zero and the bending angle: this would explain why the channeling effect (and therefore the channeling peak) is not limited to a narrow region as expected in a perfect crystal, but covers almost all the 410 μrad of bending angle of the crystal. Reminding that the tilt is defined to be zero when the incoming particles are aligned with the entrance face of the crystal, in our case the zero tilt is considered to be the beginning of channeling peak as detected in the angular scan (i.e. $\theta_{tiltB} = -360 \pm 10$ μrad).
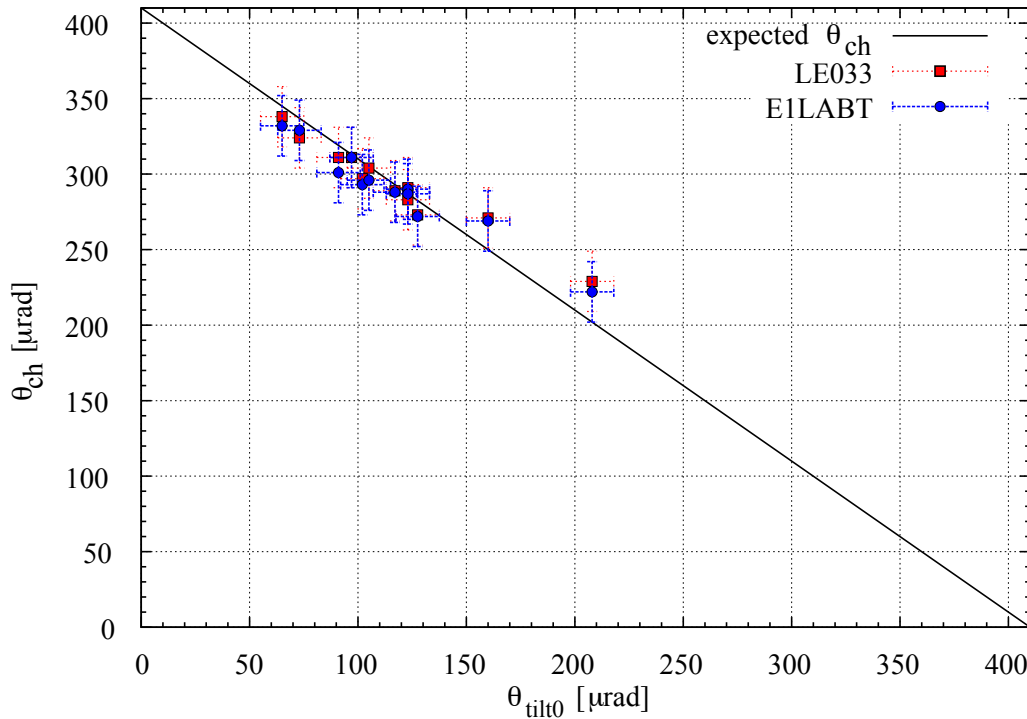
Figure 4.16: Expected and measured channeling kicks versus the crystal tilt. The E1LABT data are corrected by considering off-momentum particles of -3σ_p/p, as discussed in section 4.3.2.4.

Moreover, the miscut angle effect explains why the measured channeling kicks are always much smaller than the expected one. When the tilt is zero, the angle is expected to be the full channeling kick (θ_b =410 μrad), but if the tilt is larger than zero, then the expected channeling kick is defined by equation A.3, that is repeated

here for convenience:

$$\theta_{ch}(\theta) = \frac{\theta_b}{l_{cry}} \cdot (l_{cry} - s(\theta)) = \theta_b - \theta_{tilt}$$

The measured channeling kicks are plotted in Figure 4.16 and compared with the expected linear trend. The values for the E1LABT detector are corrected with the Δk factor for off momentum particles, as calculated in section 4.3.2.4. The uncertainty on the crystal orientation θ_{tilt0} is of about 10 μrad, due to the uncertainty of the crystal orientation at the beginning of the channeling peak.
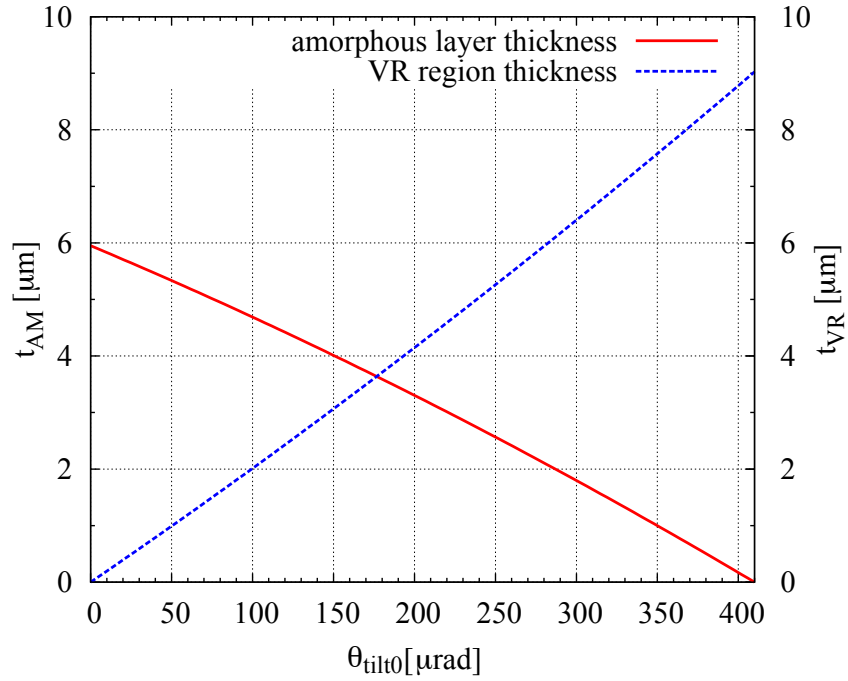
Figure 4.17: Amorphous and volume reflection layer thickness versus crystal tilt.

As already discussed in section 2.3.2, an effective amorphous layer, whose thickness depends on the crystal tilt, is associated to the miscut angle. Its thickness is defined by equation A.5, that is repeated here for convenience:

$$x_{am} = (l_{cry} - \frac{\theta_{tilt}}{\theta_b} \cdot l_{cry}) \cdot \cos{(\pi/2 - \theta_{mc} + \theta_b/2 - \theta_{tilt}/2)}$$

while the volume reflection region thickness is described by equation A.5:

$$x_{VR} = \left(\frac{\theta_{tilt}}{\theta_b} \cdot l_{cry}\right) \cdot \cos{(\pi/2 - \theta_{mc} - \theta_{tilt}/2)}$$

The two functions are plotted in Figure 4.17 for the Tevatron experiment. As expected, the amorphous layer is maximum (about 6 μm) and the volume reflection region is zero when the crystal tilt is zero: this could explain why the pin diode measurements do not see any decrease in signal (see picture 4.8). While rotating the crystal, the amorphous layer thickness decreases (thus explaining the increase in efficiency), and the volume reflection region increases, thus becoming more and more efficient. The volume reflection seems to become the main effect and gradually cover the channeling effect after about 120 μrad: for this reason, probably, the channeling efficiency decreases. Over a tilt of 200 μrad, the channeling seems to be totally covered by the volume reflection effect: the channeled beam is not detected anymore in collimator scans, and a plateau is measured by the detectors downstream the collimator in angular scans.

4.4   Conclusions

The T980 experiment helped to address and focus on critical aspects of using a crystal collimator, such as the effect of a miscut angle and the effect of dealing with off momentum particles.

A deep analysis of the experimental data and a systematic study on the detector behavior allowed to develop a reproducible method to measure the channeling kick and the channeling efficiency using the collimator scan data.

The measured channeling kick varies with the crystal orientation with respect to the beam, reaching a maximum measured value of 360 μrad, to be compared with the expected channeling angle of 410 μrad. The theory of the miscut angle effect, developed on purpose for understanding the T980 results, successfully explains the reduced measured channeling kicks.

Assuming a linear relationship between detector signal and number of halo particles impacting on the jaw, channeling efficiency values between 10% and 60% have been measured. Dedicated simulations are needed to clarify the relation between particles interacting with the collimator jaw and number of particles impacting on the different detectors: different impact positions and angles could be an important parameter in secondary emitted particle production. A better evaluation of this quantity is necessary to refine the channeling efficiency estimation given in this chapter.

Chapter 5

SPS

The UA9 experiment is designed to verify the usability and the possible advantages of the use of crystal for collimation purposes in circular machine. In previous experiments the results about collimation efficiency advantages were not clear (T980 experiment [15]) or not even encouraging (like in the case of RHIC [32, **?**], where an increase of the losses at the detector were observed with the crystal in channeling).

In UA9 two new-generation crystals (with declared negligible miscut and amorphous layer) were inserted in the SPS and used as primary elements in a two stage collimation system. The losses were recorded both locally (using a set of dedicated detectors) and in the rest of the ring (using the beam loss monitors installed on each of the SPS quadrupole).

In this Chapter the main results of the beam tests are presented. A full set of simulations have been performed, and the results are compared with the experimental ones.

5.1 The SPS

The Super Proton Synchrotron (SPS) [72] is the second largest machine in CERN's accelerator complex. The machine has a circumference of about 7 km, and it is divided in six sector, each one composed by 18 F0D0 cells plus a long straight section (LSS1-6) of about 130 m each.
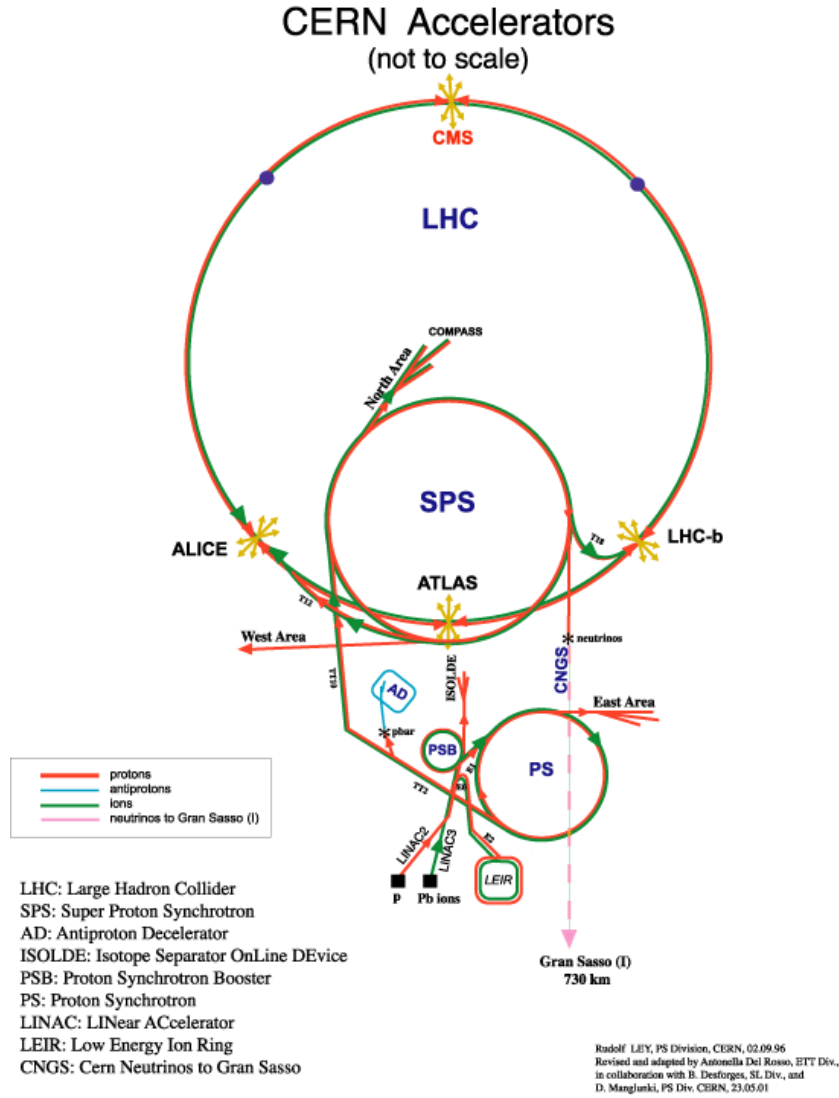
Figure 5.1: LHC accelerator complex. From [72]

The SPS, which was commissioned in 1976 with an energy of 400 GeV, has been used in the past to accelerate protons, antiprotons, electron and positrons. Between 1981 and 1984 it was used as proton-antiproton collider, leading to the

discovery of W and Z bosons. Nowadays it is used for a number of fixed target experiments (e.g. COMPASS), for sending neutrinos to the Gran Sasso laboratories (CNGS experiment) and as last injector before the Large Hadron Collider (LHC). As an injector it receives 26 GeV protons from the Proton Synchrotron (PS), accelerates them to 450 GeV and then deliveries them to the LHC through the TI2 and TI8 transfer lines[73].

5.2 UA9 experiment

The UA9 experiment [16, 74] is a crystal channeling experiment, which took place in the SPS in summer 2009, aiming at verifying the usability of a well characterized crystal for collimation purposes in a high energy circulating proton machine. A bent crystal is inserted in the halo of the circulating beam, and its effect is studied for different angular orientations. In the next sections the experimental layout (section 5.2.1), the operational procedures before measurements (section 5.2.2) and the experimental results (section 5.3) are presented.

5.2.1 Layout and instrumentation

The UA9 experiment is mounted in the straight section 5 (LSS5) of the SPS. A sketch of the layout is shown in Figure 5.2.
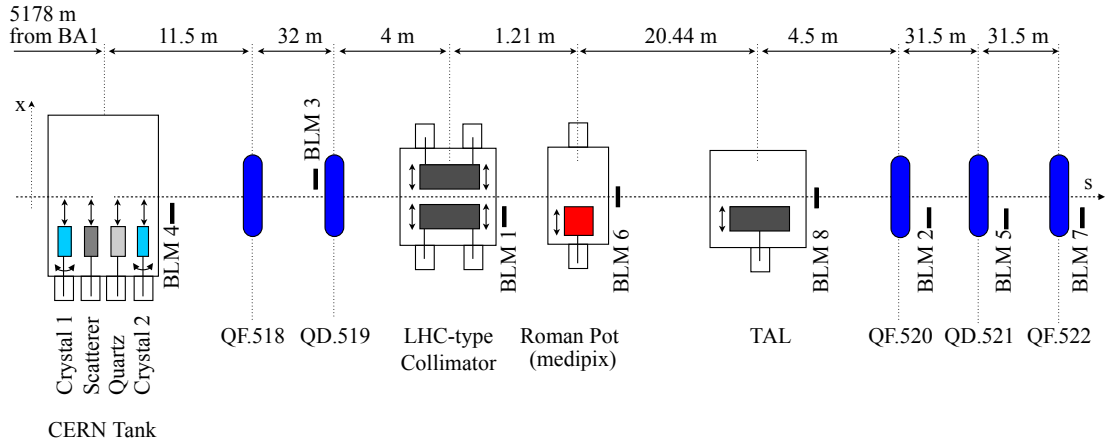
Figure 5.2: Layout of the UA9 experiment.

Two crystals have been installed in a tank positioned at the beginning of LSS5, at a longitudinal distance of 2.85 m between them. Both crystals are made of Si but they have been produced using different fabrication techniques: Crystal 1 is a

strip crystal, while Crystal 2 is a quasi-mosaic crystal [38, 37]. Their nominal total bending angles are θ_{bend}=170 μrad for Crystal 1 and θ_{bend}=150 μrad for Crystal 2. They are mounted in horizontal configuration, on the inward side of the SPS circumference, and their orientation is such that the channeled beam is directed inwards the SPS circumference. It is possible to control independently both their transverse horizontal direction and their angular tilt, since they are mounted on two different goniometers. Unfortunately the operation of the goniometers was complicated because of a large mechanical play and, therefore, a the reproducibility of the angular position was poor. As a representative example, in Figure 5.3 the angular settings (as passed to the motors) and the actual angular position (as read by the LVDT sensors) are compared. In different experimental runs it was impossible to reproduce the same angular position with an accuracy better than ± 100 μrad. The LVDT signal is used for angular position measurement in the following.
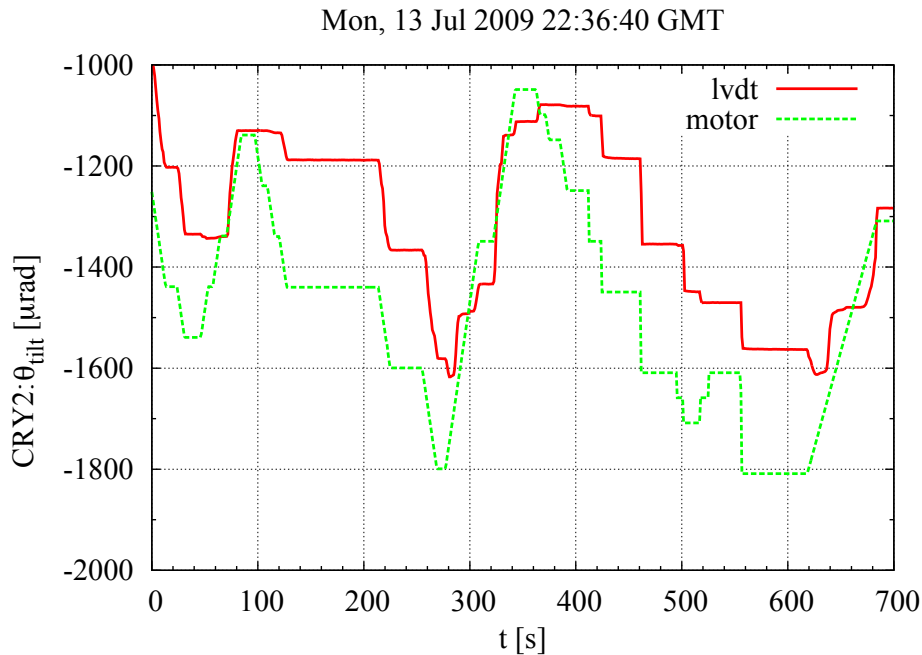
Figure 5.3: Crystal 2, angular position. Motor settings and LVDT readings.

An LHC-prototype secondary collimator (1 m of carbon fiber composite), already present in the LSS5 section, is located about 40 m downstream the first crystal. The collimator is a 1 m long CFC LHC-type collimator, and it is intended to shape the beam, be the reference for the alignment of all the elements (see section 5.2.2) and perform collimator scans (see section 5.3.2).
A Roman Pot is installed in between the crystal and the absorber, and in the Roman Pot a Si pixel detector (Medipix [75, 76], see description in section 5.3.3) has been positioned in order to measure the position and intensity of the channeled beam.

A 60 cm long tungsten absorber (TAL), located 64 m downstream the crystal, is foreseen to intercept the channeled beam.

A full set of dedicated detectors (including scintillators, quartz detectors, ionization chambers, secondary emission chambers) has been installed in the experimental region. In this thesis only the 8 LHC-type beam loss monitors installed in proximity of the crystal, of the collimator and of the absorber (see Figure 5.2 for the layout) are considered, and the Medipix detector.

Together with these detectors, the readings from the 216 BLMs already installed in the machine (one per quadrupole) are used to measure a detailed map of the losses along the whole ring, far from the crystal position.
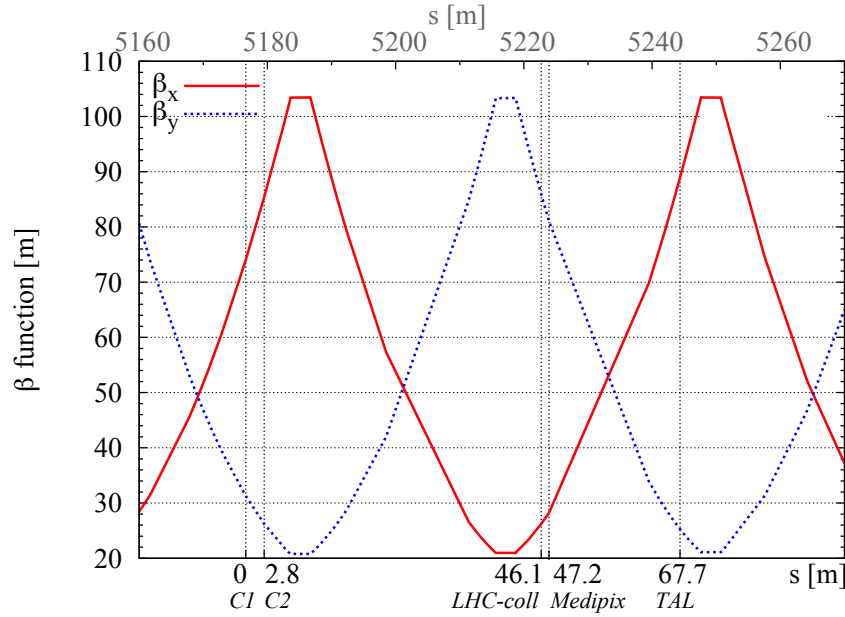
Figure 5.4: Horizontal and vertical β-functions in the UA9 experimental region.

For the optics calculation MADX [77] was used. To analyze the experimental data, and calculate quantities like the crystal equivalent kicks, the results from a MAD simulation using the thick optics was used. In Figure 5.4 an overview of the β-function in the experimental region is presented: it can be noted that the crystals are close to a maximum of the horizontal beta function, and so it is the TAL absorber. Being the SPS FODO cell with a 90 degrees phase advance, this means that the phase advance between the crystal and the absorber is of almost 90 degrees. The exact values of the optical functions at the important elements are shown in Table 5.1.

For the tracking simulations presented in section 5.4, however, a thin optics is required, i.e. the thick elements are approximated by one or more infinitely short mag-

netic lenses: 5 slices per thick element were used, and the sextupoles were switched off. The resulting optical function values are listed in Table 5.2.

Table 5.1: Values of the horizontal optical functions at different elements, thick optics approximation. The longitudinal position s and the horizontal phase advance $\Delta\phi_x$ are expressed with respect to the longitudinal coordinate (5176.6 from BA1) and the phase (39.17π from BA1) of Crystal 1.

element	s	β_x	α_x	D_x	D_x'	ϕ_x
	[m]	[m]	[-]	[m]	[-]	[-]
Crystal 1	0	74.1	-1.89	-0.77	-0.020	0
Crystal 2	2.9	85.4	-2.06	-0.83	-0.020	0.01π
collimator	46.1	26.2	-0.78	-0.20	0.010	0.35π
Medipix	47.3	28.2	-0.86	-0.19	0.010	0.36π
TAL	67.8	88.9	-2.11	0.002	0.010	0.49π

Table 5.2: Values of the horizontal optical functions at the different elements, thin optics approximation. The longitudinal position s and the horizontal phase advance $\Delta\phi_x$ are expressed with respect to the longitudinal coordinate (5176.6 from BA1) and the phase (39.29π from BA1) of Crystal 1.

element	s	β_x	α_x	D_x	D_x'	ϕ_x
	[m]	[m]		[m]		[2π]
crystal 1	0	73.99	-1.89	-0.70	-0.018	0π
crystal 2	2.87	85.32	-2.06	-0.75	-0.018	0.01π
collimator	45.14	24.79	-0.73	-0.19	0.009	0.34π
Medipix	47.27	28.16	-0.86	-0.18	0.009	0.37π
TAL	67.71	88.88	-2.11	0.003	0.009	0.50π

5.2.2   Operation: Beam Based alignment procedure

The first operation to be performed in a crystal experiment is to measure the position of one element with respect to the beam, and then to align all the other elements with respect to this device. The LHC-prototype collimator has been used for this purpose. Together with an emittance measurement, and relying on the optics values specified in Table 5.1, this procedure enables to calculate the distance of all the elements from the beam center.

The procedure, called "Beam Based alignment" [78], is described here:

- *Centering of the collimator:*
  The two jaws are slowly inserted, with gradually reduced step sizes, toward the beam center. In order to keep the collimator gap centered, comparable losses must be observed for the same inward movements on both sides. The BLMs readings downstream the collimators (BLM 1 and BLM 6) were used for the alignment.
  After that the left jaw of the collimator is brought to a totally retracted position (about -30 mm from the beam center), as required by the experimental settings.

  Knowing the absolute positions of right and left jaw, the beam orbit position x_{orb} in the collimator reference frame is inferred. The absolute aperture x_{coll} and normalized aperture $a_{coll} = \frac{x_{coll}}{\sqrt{\varepsilon_x \beta_x^{coll}}}$ of the collimator can be calculated, using the horizontal emittance measured value ε_x and the beta function at the collimator β_x^{coll}.

- *TAL alignment and final positioning*:
  The TAL is slowly inserted up to a normalized aperture a_{tal} which is even to the collimator one a_{coll}. As soon as it reaches the collimator normalized aperture (and therefore the edge of the primary halo) a spike of losses is registered by the BLM immediately downstream the TAL (BLM 8). At this point the TAL is retracted of about $1\sigma_x$, to its final experimental settings. This is done in order to be sure that it cannot intercept primary particles.

- *Crystal alignment*:
  The crystal is inserted up to a normalized aperture a_{cry} which is even to the collimator one: $a_{cry} = a_{coll}$. A few additional motor steps are performed in order to ensure that the crystal is the limiting aperture of the collimation system. For this operation the BLM immediately downstream the crystal (BLM 4) are used.

The system is ready for angular and collimator scans.

5.3 Experimental results

During the summer 2009 SPS machine time was dedicated to the UA9 experiment. A list of the dates and the main activities can be found in Table 5.3.

In this section the main experimental results of the summer 2009 are discussed. The results of the angular scans (section 5.3.1), and the results of the collimator

Table 5.3: Main collimation activities performed during the UA9 experimental runs in Summer 2009.

Date	Activities
June 30th, 2009	Crystal 1: angular scan and collimator scans in different orientations (channeling, amorphous, volume reflection).
July 13th, 2009	Crystal 1 and Crystal 2: angular scans.
September 22nd, 2009	Crystal 1 and Crystal 2: angular scan and collimator scans in different orientations.
November 4th, 2009	Crystal 1: Medipix data.

scans (section 5.3.2) are compared with the Medipix detector data (section 5.3.3). The loss maps along the ring are briefly commented in the last section (5.3.4).

Both the collimator scan and the loss map data will be compared with the simulations results in the section dedicated to simulations (section 5.4).

5.3.1   Angular scans

In this section the angular scans for both Crystal 1 and Crystal 2 are presented. The showers generated at the crystal location are measured with a beam loss monitor while the crystal orientation is changed progressively. From theory (see section 1.2.1) it is expected that the channeling peak is associated with a decrease of the inelastic interactions at the crystal, and therefore a decrease of the signal registered by a downstream detector. For this purpose the BLM4 was used (see Figure 5.2), immediately downstream the tank containing the crystals.

In Figure 5.5 a Crystal 1 angular scan is presented. In the analyzed range (of almost 8 mrad) multiple regions associated to a strong decrease of inelastic interactions can be observed. This is compatible with the existence of multiple channeling peaks, i.e. to channeling processes associated to different sets of crystal planes. The presence of channeling from skew planes is the first evidence that the crystal is almost aligned for axial channeling (see section 1.2.4 and section 1.4). This observation will be confirmed by the investigation of the channeling peak performed with the Medipix (see section 5.3.3). As shown in Figure 5.5, the most intense channeling peak among the detected ones, is for a crystal orientation $\theta_{tilt} \simeq -2000$ μrad. In the following this peak is considered as the main one..
For Crystal 2 only one channeling peak has been observed, as expected when the crystal is correctly oriented for planar channeling.
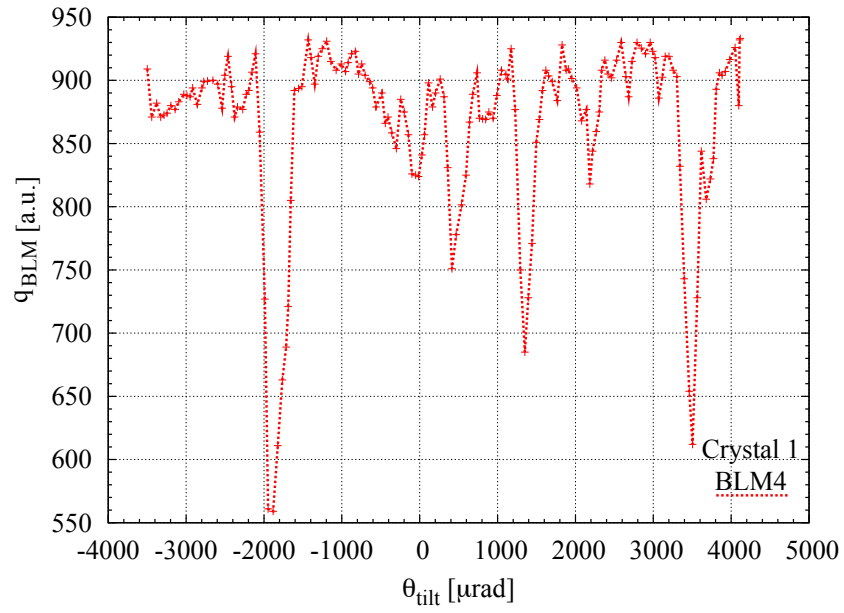
Figure 5.5: Wide angular scan for Crystal 1, taken on September 22nd, 00:36:25 GMT.
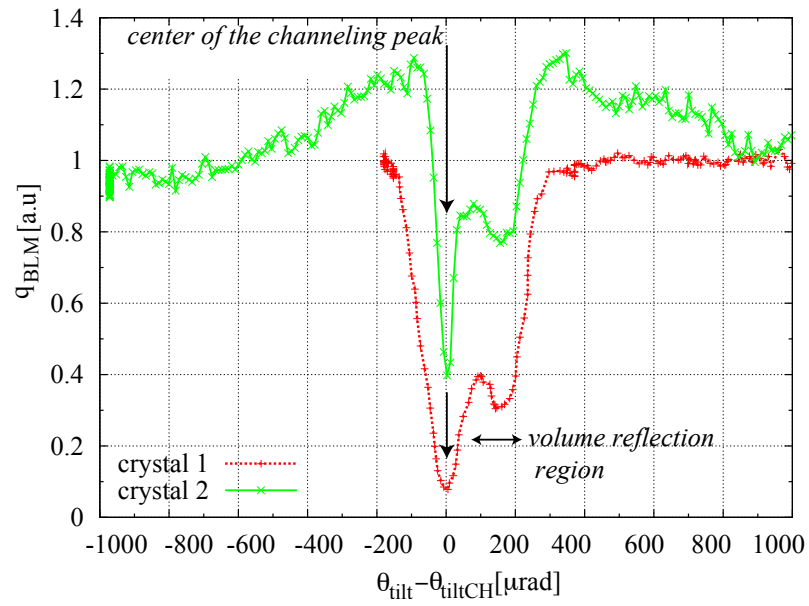
Figure 5.6: Refined angular scans for Crystal 1 and Crystal 2, taken on July 13th 2009.

Once the channeling peak(s) are identified, a slower, more refined angular scans can be performed in the regions of interest. In Figure 5.6 slow angular scans are shown for both Crystal 1 (main channeling peak) and Crystal 2: in the plot the BLM4 signal is normalized and the angular orientation is rescaled. This means that:

- *BLM signal normalization*: the offset signal measured by the BLM4 when both crystals are retracted is subtracted to the raw data. The data are then divided with respect to the value of the losses in amorphous position.

- *Angle rescaling*: The variable $\tilde{\theta}_{tilt}$ is defined as $\tilde{\theta}_{tilt} = \theta_{tilt} - \theta_{tiltCH}$, where θ_{tilt} is the crystal orientation and θ_{tiltCH} is the tilt associated to the middle of the channeling peak. In this way the minimum of the channeling peak is at $\tilde{\theta}_{tilt} = 0$ for both crystals.

For both curves the channeling peak and the volume reflection region are clearly visible. It is interesting to notice how, for Crystal 2, the losses increase in the region immediately before and after the coherent interaction region, reaching a maximum of about 27% more than in the far-away amorphous region: this behavior has not been explained yet.

Three important parameters can be deduced by the angular scan analysis:

- the angular acceptance of the channeling process σ_{chAcc}

- the total bending angle of the crystal θ_b

- the reduction of inelastic loss rates at the crystal when in channeling position, with respect to amorphous position $\dot{I}_{cry}(ch)/\dot{I}_{cry}(am)$

The results are presented in the following.

Angular acceptance of the channeling process

To estimate the channeling acceptance σ_{chAcc}, a Gaussian fit was applied to the channeling peak:

$$G(\theta_{tilt}) = A \cdot \exp\left(\frac{-\tilde{\theta}_{tilt}^2}{2(\sigma_{chAcc}/2)^2}\right) + c \tag{5.1}$$

where A, c are fitting parameters and σ_{chAcc} is twice the rms width of the Gaussian, i.e. the full angular acceptance of the channeling process. For Crystal 1 one gets $\sigma_{chAcc} = 130 \pm 3$ μrad and $\sigma_{chAcc} = 50 \pm 3$ μrad for Crystal 2. Since the critical angle θ_c for Si crystals at the considered energy is of about 19 μrad, and the angular spread $\Delta\theta_{rf}$ calculated for grazing particles (see section 2.3.1) is about 1.3 μrad, the single-pass channeling acceptance is of about $1.4 \cdot \theta_c + 2 \cdot \Delta\theta_{rf} = 29$ μrad. For both crystals the measured acceptance values are higher than expected. For the Crystal

2 case, the discrepancy can be justified by the multi-turn process (see section 5.3.1). This is not the case for Crystal 1: here the σ_{chExp} value obtained is more than four times the expected one. Investigations with the Medipix detector (see section 5.3.3) show that this width is caused by the overlap of different channeling peaks from different skew planes.

Total bending angle

The total bending angle should be equal to the angular extension between the center of the channeling peak and the maximum at the end of the volume reflection region. The experimental value are $\theta_b = 155 \pm 10$ μrad for Crystal 1 and $\theta_b^{exp} = 161 \pm 10$ μrad for Crystal 2. This is expected to be also the nominal channeling angle.

Reduction of inelastic interaction rate

The reduction of inelastic interaction rate at the crystal, when in channeling orientation, is closely connected to the single pass channeling efficiency $\eta_{chann}^{s.p.}$ in multi turn environment defined in section 1.3.2. The BLM4 losses, in the following, are considered proportional to the inelastic interaction rate at the crystal $\dot{I}_{cry}$. Calling $q_{BLM4}(ch)$ and $q_{BLM4}(am)$, respectively, the BLM4 signal in channeling and in amorphous orientation, the efficiency is:

$$\eta_{ch}^{s.p.} = \frac{q_{BLM4}(am) - q_{BLM4}(ch)}{q_{BLM4}(am)} = 1 - \frac{q_{BLM4}(ch)}{q_{BLM4}(am)} \tag{5.2}$$

That means a maximum single pass channeling efficiency (in multi turn mode) of 90% for Crystal 1, and between 60% and 70% for Crystal 2 (depending on the value we chose for $q_{BLM4}(am)$). The inelastic interaction rate reduction, defined as $\frac{q_{BLM4}(am)}{q_{BLM4}(ch)}$, is then a factor 10 for Crystal 1 and a factor 2.5-3 for Crystal 2.

Table 5.4: Angular acceptance, bending angle and loss reduction factor of the channeling process as measured during the angular scans.

	σ_{chAcc} [μrad]	θ_b [μrad]	$\frac{q_{BLM4}(ch)}{q_{BLM4}(am)}$ [-]
Crystal 1	130 ± 3	155 ± 10	10
Crystal 2	50 ± 3	161 ± 10	2.5-3

A summary of the results obtained by the angular scan analysis is presented in Table 5.4.

5.3.2   Collimator scans

The collimator scan technique allows us to analyze the halo generated by the crystal with the use of a movable collimator. As already described in sections 3.2.2.2 and 3.2.2.4, the losses downstream the collimator are detected for different collimator positions, and from these losses the efficiency curves (i.e. relative losses at the collimation location versus equivalent crystal kick) are obtained.
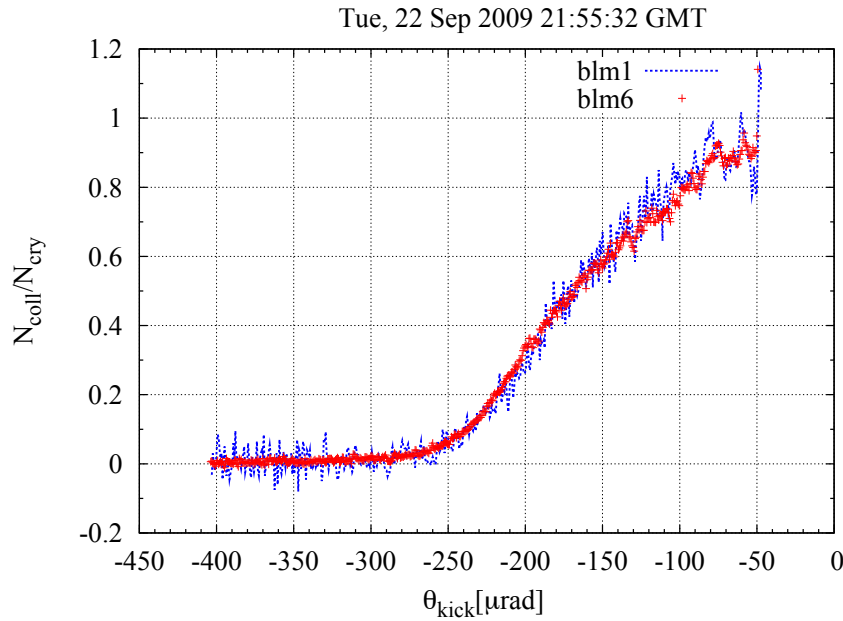
Figure 5.7: Comparison of the normalized losses for BLM1 and BLM6, versus the equivalent crystal kick.

For detecting the secondary particles generated in the collimator it is possible to use both the BLM1 and BLM6. The two normalized signals of the detectors are compared in Figure 5.7, for a collimator scan performed on September 2009, 22nd at 21:55 GMT. The two sets of data almost completely overlap, but the BLM6 has a better signal to noise ratio, and was therefore chosen for the collimator scan data analysis.

In the next sections the main features and results of collimator scans are presented. First the limitations and uncertainties, which can affect the collimator scan technique, are explained (section 5.3.2.1 and section 5.3.2.2). In section 5.3.2.3 and 5.3.2.3 the results are discussed, respectively for Crystal 1 and for Crystal 2.

5.3.2.1   Collimator scan limitations: minimum detectable kicks

The presence of a W absorber (TAL) downstream the movable collimator should guarantee a single passage type collimator scan, i.e. to each collimator position should correspond one (and only one) equivalent kick at the crystal (see section 3.2.2). This should enable to univocally determine the secondary halo structure by looking at the number of inelastic interactions at the collimator. However there are limitations to this technique, which in the case of UA9 layout are particularly important:

- There is a limit collimator aperture over which the single pass assumption is valid: the multi-turn normalized aperture a_{multi}. This defines the limit of the single turn vs the multi turn halo, and depends on the normalized apertures of the crystal and of the collimator: for collimator normalized apertures smaller than a_{multi} it is impossible to determine if the particles hitting the collimator jaw are directly scattered from the crystal or have performed multiple turns before interacting with the collimator.

- Even if the collimator reaches the same normalized aperture at the crystal, there is a minimum crystal kick which is needed to get, in a single passage, to the collimator jaw. The collimator equivalent crystal kick θ_{kick}^{coll} sets the minimum detectable kick in the single passage.

In the following the typical values of these two quantities in the UA9 experiment are discussed.

Multi-turn normalized aperture

As discussed in section 3.2.2.3, a minimum kick is necessary for the particle to be directly deviated on the TAL jaw. For small enough kicks, however, a particle would not be stopped by the TAL, and could come back in the following turns with a different phase, and possibly larger transverse excursion. The maximum amplitude a_{multi} that an "escaped" particle can reach is described by equation 3.20, that is repeated here for convenience:

$$a_{multi} = \sqrt{a_{cry}^2 + \sqrt{\frac{\beta_{cry}}{\varepsilon_x}(\theta_{kick}^{TAL})^2}}$$

A clear effect of the multi turn nature of the halo detected at normalized apertures $a < a_{multi}$ is shown in Figure 5.8, where the data for two collimator scans in the same conditions: the blue data are associated to an inward movement of the collimator (i.e. toward the primary halo), while the red data have been taken while the collimator was moving outward. The two sets of data overlap for large collimator apertures, but at the multi turn normalized aperture a_{multi} the signal associated
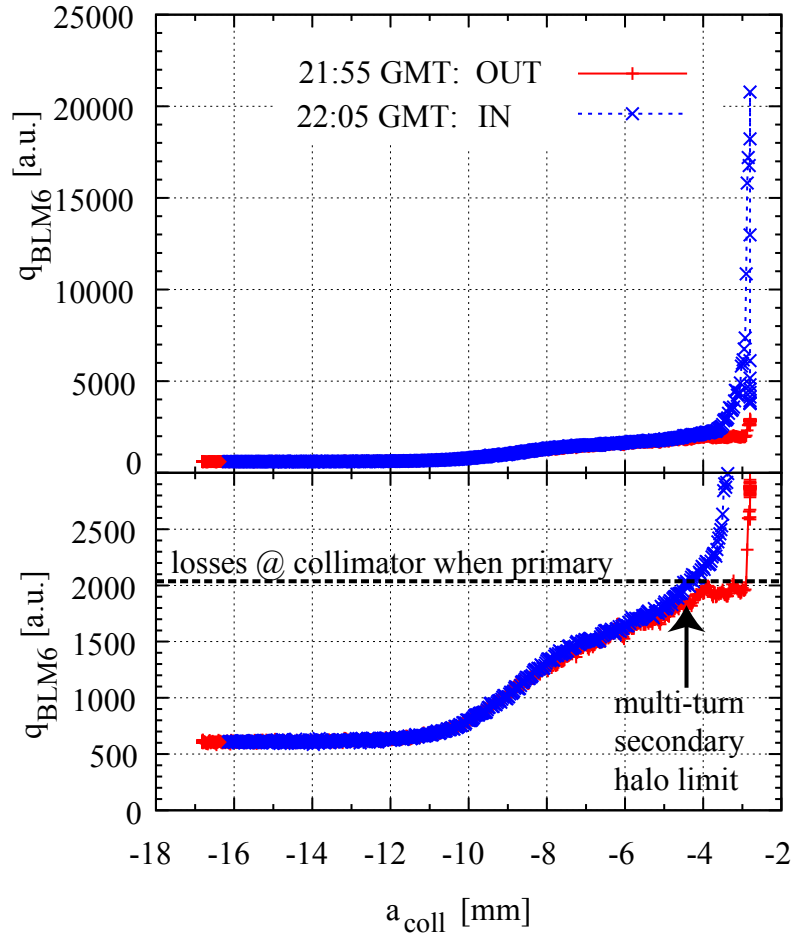
Figure 5.8: BLM6 signal versus collimator transverse position. The plot on the bottom is a zoom of the top one, to show the differences between collimator scan in and out. The Losses when the collimator is in stable conditions are about 2010 μrad.

to the "inward" movement becomes much higher that the "outward" one. This is because the multi turn halo accumulates while the collimator is retracted, and the collimator cuts it when moving inward. For this reason the collimator scans analyzed in the next sections are always done with the outwards movement of the collimator jaw.

It can be convenient calculating the multi turn normalized aperture in terms of equivalent crystal kicks. Using equation 3.22 we can define the associated angle θ_k^{multi}:

$$\theta_k^{multi} = \frac{a_{multi}\sqrt{\varepsilon_x} - a_{cry}\sqrt{\varepsilon_x}\cos(\Delta\phi)}{\sqrt{\beta_{cry}}\sin(\Delta\phi)} \tag{5.3}$$

It is worth remembering that θ_k^{multi} sets the limit of the multi-turn secondary halo, and therefore the validity of the fitting functions described in section 3.2.2.1.

Collimator equivalent crystal kick

As discussed in section 3.2.2.3, a minimum kick (θ_{kick}^{COLL}) is necessary to get to the collimator jaw in one single passage even if the collimator reaches the same normalized aperture as the crystal: the system is therefore blind for all the particles which receive a kick lower than θ_{kick}^{COLL} (which can be collected only in multi-turn mode). The kick θ_{kick}^{COLL} associated to the beam envelope at the collimator location can be found using equation 3.20, that becomes:

$$\theta_{kick}^{COLL} = \frac{\sqrt{\beta_{coll}/\beta_{cry}}\, x_{cry}(1 - \cos\Delta\phi)}{\sqrt{\beta_{cry}\beta_{coll}}\sin\Delta\phi} \tag{5.4}$$

where, $\Delta\phi$ is now the phase advance between the collimator and the crystal. While this value was very low in the case of Tevatron (about 3 μrad), for UA9 experiments the θ_{kick}^{COLL} had typical values up to ≈ 66 μrad. The protons that are not detected, are either lost during the same turn elsewhere in the SPS or come back and can receive another crystal-induced deflection (multi-turn process).

In summary, two fundamental limitations to the collimators scan technique are:

- it is impossible to determine the single passage probabilities associated to kicks smaller than the multi turn secondary halo limit θ_k^{multi}.

- it is impossible to detect, at their first turn, particles which have received a kick smaller than θ_{kick}^{COLL}.

From simulations it is assumed that about 5% of the particles which receives non-detectable kicks ($\theta < \theta_{kick}^{COLL}$ are then lost in the machine aperture. On this assumption the collimator scan data are normalized and the channeling efficiency is

calculated. If the population of the particles receiving a small kick is lower than predicted, the efficiency estimation would be scaled down proportionally. It is worth noticing that the same limitations apply to any kind of the detector, e.g. the Medipix, which could be used to analyze the scattered beam.

5.3.2.2   Collimator scan: uncertainties in the efficiency calculations

In the previous section some intrinsic limitations of the collimator scan technique, concerning the minimum detectable angles and the multi turn limit, have been presented. In this section the main sources of error when evaluating the efficiency starting from the beam loss monitor data are investigated.

As already discussed in section 3.2.2.4, an estimation of the channeling efficiency via collimator scans requires the knowledge of the baseline offset value k_o and of the normalization value N_{cry}:

- *Offset value k_o:*
  Contrary to what was found for the Tevatron case (see section 4.3.2.1) the same offset of the BLM readings is present both when there is no beam and when the LHC collimator is retracted and the crystal is primary, and it is therefore assumed as baseline of the measurement. The uncertainty on the offset value is of about 2%.
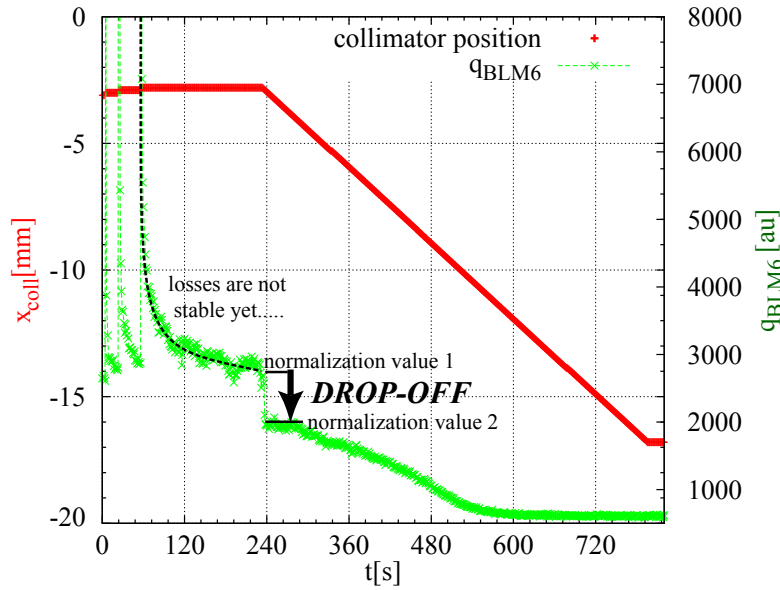
Figure 5.9: Drop-off of the losses detected by BLM6 at the beginning of a collimator scanThe possible normalization values for the losses are shown. Crystal 1, data taken on Tue, 22 Sep 2009 21:51:40 GMT
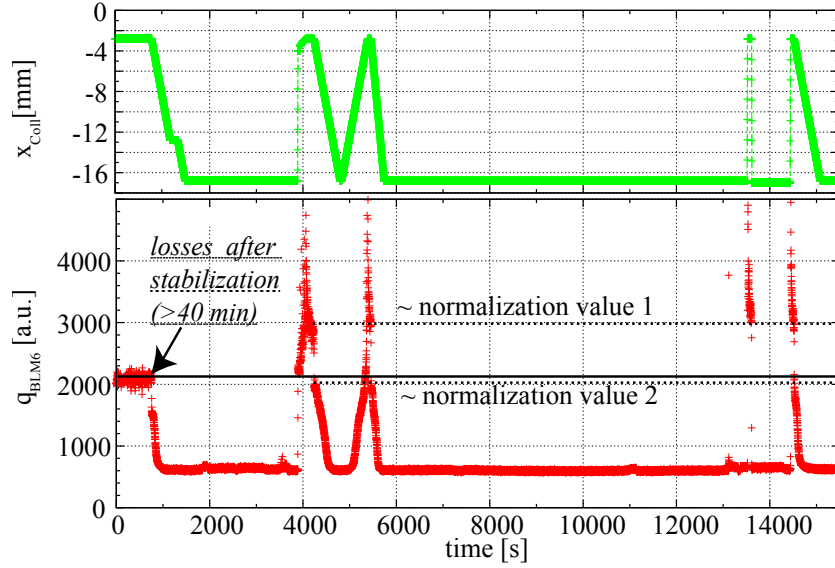
Figure 5.10: BLM6 signal vs time for a series of collimator scans. The possible normalization values for the losses are shown, together with the value of the stabilized losses after the alignment procedure. Crystal 1, Tue, 22 Sep 2009 21:51:40 GMT

- *Normalization value N_{cry}*:
  Whenever possible, the normalization value is associated to the signal of the BLM when the collimator is primary, and the losses are stable (normalization value after stabilization). If not possible, two different choices can be made: the value of the BLM signal immediately before (normalization value 1) or after (normalization value 2) the beginning of the collimator jaw retraction. The two normalization values, that in principle should be equal, are found to differ of up to 30% one from another [1] (see an example in Figure 5.9). It is therefore necessary to understand which normalization value is more meaningful: since in general the normalization value 2 differs no more than 5% from the normalization value after stabilization (see an example in Figure 5.10), the normalization value 2 is used, and an uncertainty of 5% is assumed.

A further uncertainty in the channeling efficiency estimation arises from the presence of particles at very large amplitudes (>3 standard deviations from the calculated channeling center), thus generating large tails that are not correctly fit by an error function.

This could be due to large unexpected tails of channeling distribution (i.e. the assumption of Gaussian channeled beam is wrong) or a different process that is not

---

[1]This is because, when inserting a collimator, a certain amount of time is needed for the losses to stabilize. This has been previously observed in the SPS for the standard collimation system [79]. Relaxation times of the order of 20 minutes have been found in past experiments.
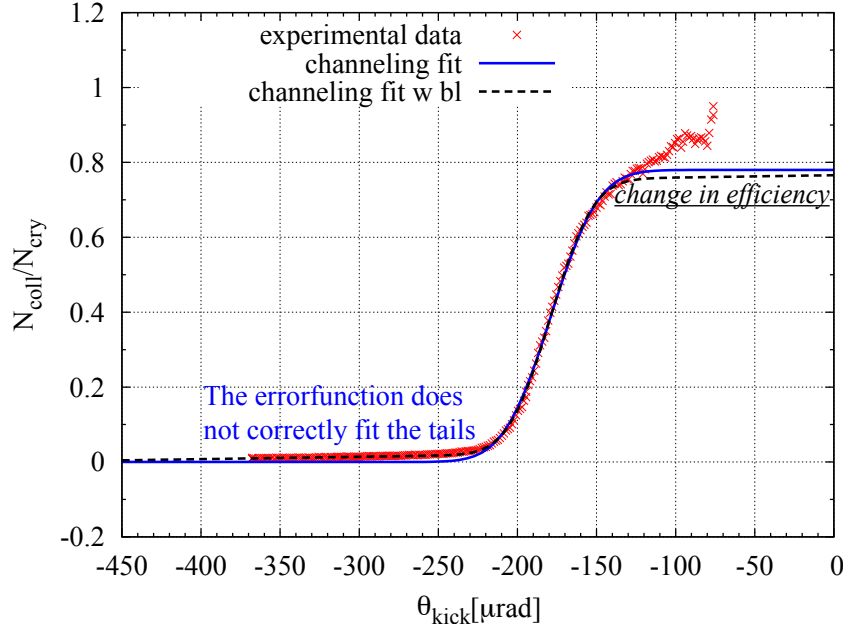
Figure 5.11: Error function fit with and without baseline, for a collimator scan of Crystal 2. Measurement taken on Wed, 23 Sep 2009 05:19:44 GMT

clear yet (e.g. scattering from the sample holder). Adding a linear trend to the error function fit (Figure 5.11) allows a better fit, and in general does not affect the channeling kick estimation, but slightly decreases the estimated channeling width and the channeling efficiency value. In the following both fits are always considered.

5.3.2.3 Crystal 1 collimator scan results

The angular scan for Crystal 1 revealed multiple channeling peaks (see Figure 5.5), and among them a main peak has been identified (at $\theta_{tilt} \approx -2000 \ \mu$rad). The halo structure generated by the crystal in channeling orientation has been investigated using the collimator scan technique for different channeling peaks. A list of all the collimator scans performed can be found in Table 5.5.

Two examples of collimator scan (C1.1 and C1.2 collimator scan) for the main channeling peak are shown in Figures 5.12 and 5.13. For each Figure, on the top plot the normalized BLM6 signal is presented versus the crystal equivalent kick. The same data are smoothed and a numerical derivative is computed in attempt of reconstructing the beam profile at the collimator location: the curve, whose total area is normalized to 1, is shown in the bottom plot.

The main channeling peak has been analyzed three different times, in two MDs (1st July and 22nd September 2009). A comparison between all the secondary halo

Figure 5.12: Normalized BLM6 losses versus crystal kick (top) and reconstructed secondary halo distribution (bottom), for scan C1.1.
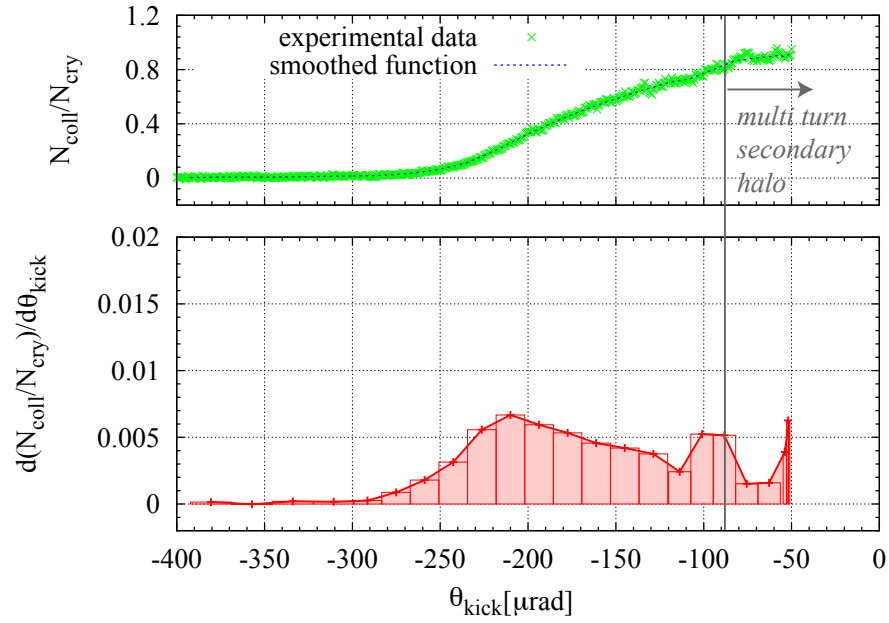
Figure 5.13: Normalized BLM6 losses versus crystal kick (top) and reconstructed secondary halo distribution (bottom), for scan C1.2.

Table 5.5: List of the collimator scans for Crystal 1

scan n.	MD date	θ_{tilt} [μrad]	ε_x [m·rad]	n_{cry} [σ_x]	θ_{kick}^{COLL} [μrad]	θ_k^{multi} [μrad]
C1.1	01 Jul 2009 03:23:20 GMT	≈ -2000 (main chan.)	$14 \cdot 10^{-9}$	-3.1	-26	-56
C1.2	22 Sep 2009 21:35:00 GMT	≈ -2000 (main chan.)	$35 \cdot 10^{-9}$	-3.1	-41	-89
C1.3	22 Sep 2009 22:15:20 GMT	≈ -2000 (main chan.)	$35 \cdot 10^{-9}$	-3.1	-41	-89
C1.4	01 Jul 2009 03:36:40 GMT	$\approx +1400$ (skew chan.)	$14 \cdot 10^{-9}$	-3.1	-26	-56
C1.5	01 Jul 2009 04:34:50 GMT	≈ -5000 (skew chan.)	$14 \cdot 10^{-9}$	-3.1	-26	-56
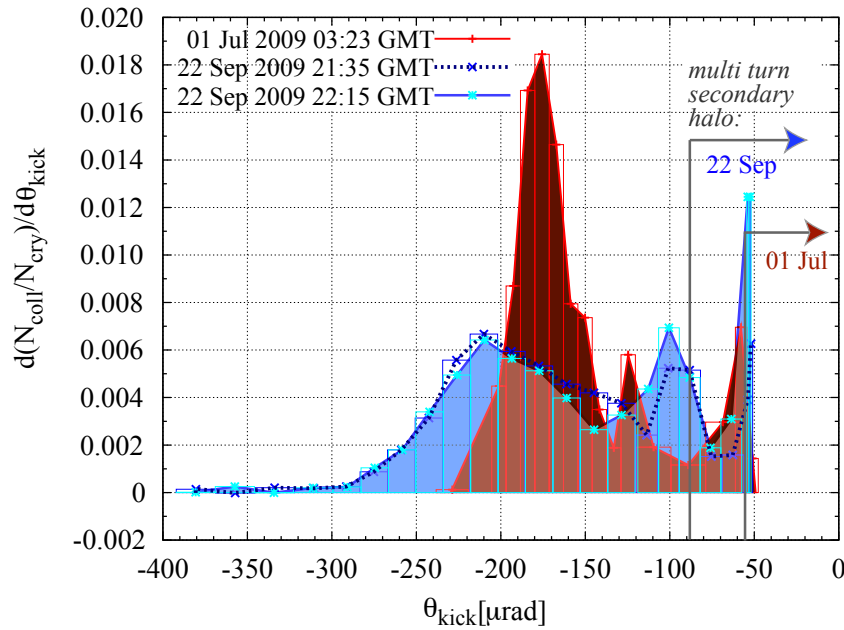
Figure 5.14: Reconstructed secondary halo distribution (bottom) for three different scans of Crystal 1. All the orientations are within the main channeling peak.

distributions measured within the main channeling peak is shown in Figure 5.5. It is worth noticing that, while the C1.2 and C1.3 distributions almost overlap, the curve relative to the C1.1 scan presents a fairly different distribution, both concerning the

peak of the channeled beam and its width. While it is sure that for the scans C1.2 and C1.3 the crystal orientation is the same (the scans were performed one after the other, without changing the crystal orientation in the meantime), unfortunately the poor reproducibility of the goniometer does not allow to reconstruct the relative change in crystal orientation between the C1.1 scan and the C1.2-C1.3 ones. Investigations with the Medipix detector, presented in section 5.3.3, confirms that the spread in results, both for the channeling kick θ_{chan} and for its width σ_{ch}, is consistent with the channeled beam shape when slightly changing the crystal orientation still within the main channeling peak.
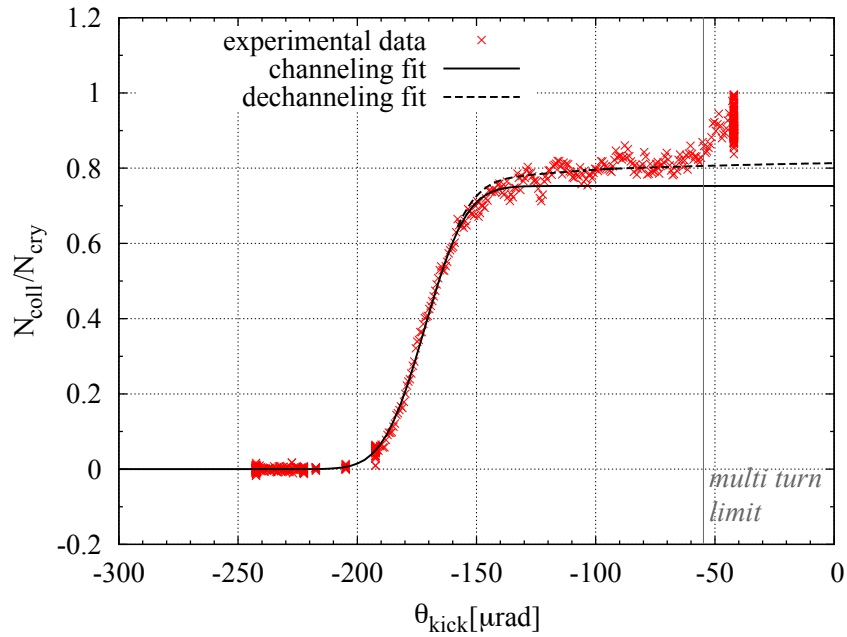
Figure 5.15: Channeling and dechanneling fitting functions, applied to the collimator scan C1.1. The fitting functions, described in 3.2.2.1, permit to calculate the efficiency associated to the different processes.

In order to calculate the efficiencies associated to the different processes, the fit functions described in section 3.2.2.1 were applied to the collimator scan data. An example is shown in Figure 5.15, were the channeling and dechanneling fit are applied to the C1.1 collimator scan data. Being the multi turn limit $\theta_k^{multi} = 56$ μrad, the amorphous region could not be observed and fitted. However the probability associated to the dechanneling process has been estimated to be $5 \pm 1\%$.

For the other collimator scans, where the multi-turn kick is even higher (about 100 μrad), only the channeling fit has been applied, which allowed to calculate the channeled beam center, width and its population (or, equivalently, the channeling

efficiency).

Table 5.6: List of the collimator scan results for Crystal 1

scan n.	no baseline			with baseline		
	θ_{chan} [μrad]	σ_{ch} [μrad]	η_{chan} [%]	θ_{chan} [μrad]	σ_{ch} [μrad]	η_{chan} [%]
C1.1	173±1	17±1	75±4	172±1	16±1	73±4
C1.2	199±1	40±1	65±3	201±1	35±1	59±3
C1.3	198±1	42±1	64±3	202±1	35±1	56±3
C1.4	153±1	16±1	33±2	147±1	152±1	12±3
C1.5	155±4	19±3	20±2	153±1	9±1	14±1

A summary of the channeling kick and width evaluation is presented in table 5.6. The error on the efficiency calculation is dominated by the uncertainty on the normalization value, which, as discussed in section 5.3.2.2, is of the order of 5%.

5.3.2.4 Crystal 2 collimator scan results

As already discussed in section 5.3.1, Crystal 2 presents, as expected, only one channeling peak. An angular scan was performed in the middle of the channeling peak to measure the channeled beam features (displacement, width) and to reconstruct the halo beam profile. The details of the collimator scan can be found in Table 5.7. The scan result and the reconstructed beam distribution are shown in Figure 5.16.

Table 5.7: List of the collimator scans for Crystal 2

	date	θ_{tilt} [μrad]	ε_x [m·rad]	n_{cry} [σ_x]	θ_{kick}^{COLL} [μrad]	θ_{kick}^{multi} [μrad]
C2.1	23 Sep 2009 05:19:44 GMT	−1525	31.3·10^{-9}	-6.0	-66	-100

As specified in section 3.2.2.1, the channeling angle and width have been evaluated by an error function fit of the collimator scan data. The measured channeling kick value is about 165 μrad, and the channeled beam width is about 20-21 μrad(see table 5.8). The measure channeled beam width is in good agreement with the expected theoretical value (about the critical angle $\theta_c = 19$ μrad). The channeling efficiency
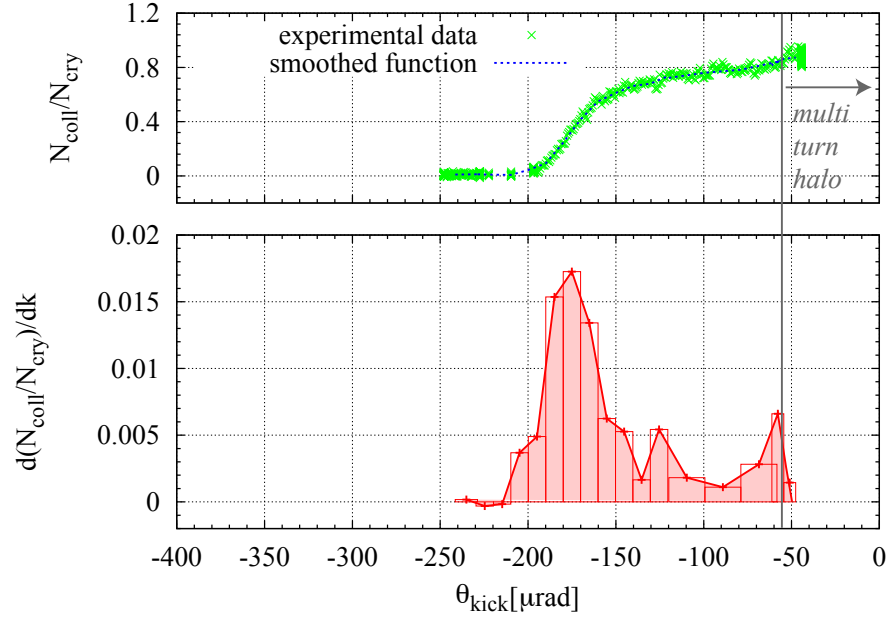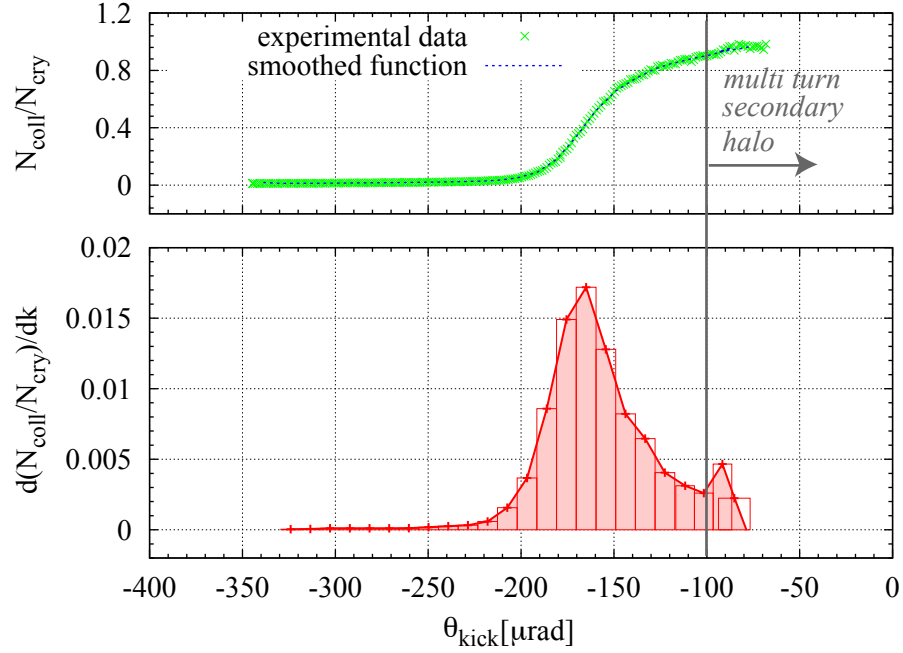
Figure 5.16: Normalized BLM6 losses versus crystal kick (top) and reconstructed secondary halo distribution (bottom), for scan C2.1

Table 5.8: List of the collimator scan results for Crystal 2

scan n.	no baseline			with baseline		
	θ_{chan} [μrad]	σ_{ch} [μrad]	η_{chan} [%]	θ_{chan} [μrad]	σ_{ch} [μrad]	η_{chan} [%]
C2.1	165±1	21±1	85±5	164±1	20±1	77±4

value goes from the 77% (with with baseline) to 85% (fit without baseline). As already commented for Crystal 1, the uncertainty on the efficiency calculation (about 5%) is dominated by the uncertainty on the normalization value.

5.3.3   Medipix data

The Medipix detector [76, 75] used in the UA9 experiment is formed by 256×256 square pixels. Each 55 μm-wide pixel counts up to 11,810 particles, and the minimum time separation required for two events to be detected by a pixel is 1μs. For UA9 the acquisition time is set to 1 s, afterwards about 2 s are needed for the data readout, i.e. the actual acquisition frequency is about 3 s.

The Medipix was positioned in a Roman Pot about 1.2 m downstream the LHC-type collimator (see Figure 5.2), on the right side with respect to the beam direction, and in horizontal orientation. The transverse position of the Roman Pot could be adjusted, thus allowing a beam based alignment of the Medipix sensor and therefore knowing its exact distance from the beam center.

This section presents the results of the analysis of the channeled beam of Crystal 1, in different orientations. The data have been taken on the 4th November 2009, between 15:20 and 15:40 GMT, and analyzed with a software specifically developed at CERN for this purpose[80]. Several screenshots of the analysis software are shown in Figure 5.17, to give a pictorial view of the changes in the channeled beam shape with the crystal orientation. Each screenshot is divided in four frames:

- frame on the top-left: image of the channeled beam as detected by the sensor. The color scale is normalized to the maximum pixel reading.

- frame on the top-right: integrated horizontal beam profile. The vertical scale is normalized to the maximum value calculated. This is in principle should correspond to the beam profile obtained by the numerical derivative of the collimator scans data (see, for example, Figures 5.13 and 5.16). The peak of this curve is fitted with a Gaussian, and its center and rms are used to compute the channeling kick θ_{ch} and the channeled beam width σ_{ch}.

- frame on bottom-left: vertical section of the Medipix data, corresponding to the horizontal position of the channeled beam center. The vertical scale is normalized to the maximum pixel reading.

- frame on bottom-right: horizontal section of the Medipix data, corresponding to the vertical position of the channeled beam center. The vertical scale is normalized to the maximum pixel reading.

A slow angular scan of the main channeling peak is considered, from -1730 to -1982 μrad (starting from the volume reflection and moving toward the amorphous region): in this range 11 different orientations were analyzed. The total measured angular acceptance of the channeling process is larger than 200 μrad, in good agreement with the rms acceptance $\sigma_{chAcc} = 130\mu$rad measured with the BLM4 during the angular scan (see section 5.5).

For each orientation we calculated the channeling peak displacement from the sensor edge and its rms width (Gaussian fit). Thanks to the relative alignment with the collimator, it was possible to calculate the absolute position of the sensor with respect to the center of the beam, and hence the absolute position of the channeled beam center. The equivalent crystal kick was finally calculated with equation 3.20, with the optics parameters relative to the roman pot position. The results are shown in Figure 5.18
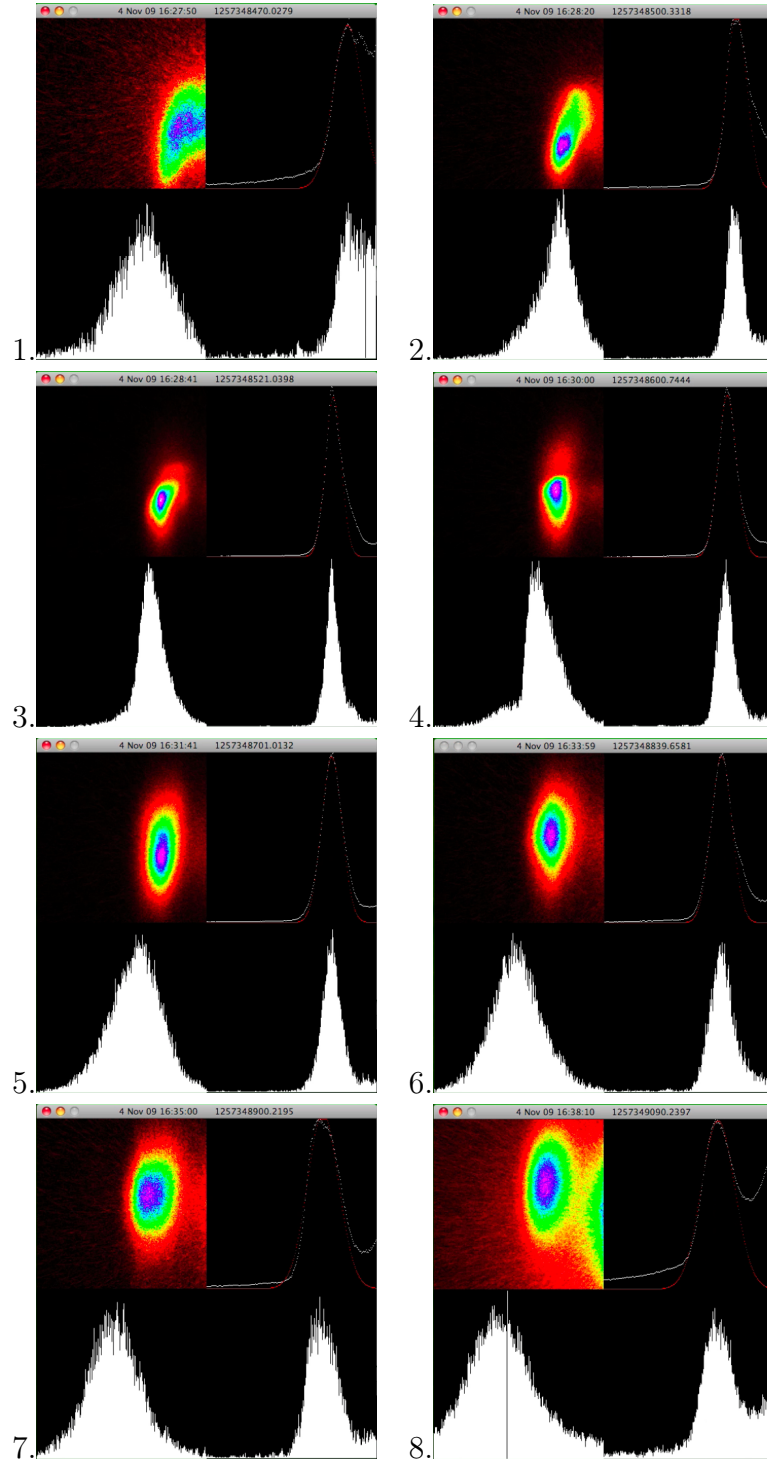
Figure 5.17: Channeled beam image by the Medipix detector, for different crystal orientations: 1. -1737 μrad,2. -1769 μrad, 3. -1795 μrad, 4. -1810 μrad, 5. -1836 μrad, 6. -1883 μrad, 7. -1907 μrad, 8. -1961 μrad. For the detailed description of the different frames see the text.
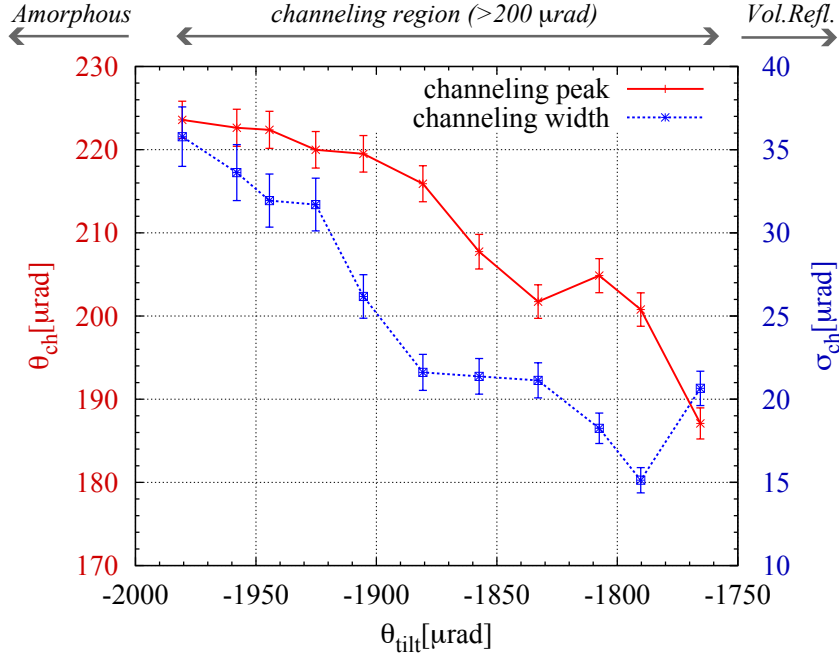
Figure 5.18: Channeling kick and rms width of the channeled beam for different orientations of Crystal 1, as measured using the Medipix data.

The channeling kicks and rms widths change almost linearly with the crystal orientation:

- Channeling angle from 224 to 187 μrad, while moving from the amorphous orientation toward the volume reflection region. Variation of almost 40 μrad. The kick values detected by the Medipix seems to be always higher than the values measured via collimator scans. A systematic error on the measurement could be due to an imprecision on the beam based alignment procedure, or, equivalently, on a movement of the closed orbit[2].

- Channeling width between 32 to 15 μrad, while moving toward the volume reflection region. Larger channeling width values are generally associated to larger channeling kicks.

The variations of the channeled beam profile and position (see Figure 5.17), both in vertical and horizontal direction, are consistent with the hypothesis of partial alignment of the crystal with respect to the axial channeling. The spread observed for the channeling parameters with the Medipix data is consistent with the results obtained with the collimator scans.

---

[2]The beam movement hypothesis is compatible with the highly unstable losses which were recorded during the whole experimental run on November the 4th.

5.3.4 Beam loss maps

An important test for understanding the improvement in collimation efficiency is to measure the change in far away losses when using the crystal in different configurations. It was unfortunately difficult to see any reproducible effect of crystal on beam loss maps around the SPS ring, probably for a limit of sensitivity of the BLMs. The only successful attempt was done on August 11, when the crystal was driven into the core of the SPS beam and its angular orientation was changed from amorphous to channeling, and back again. The analyzed BLMs data were taken in a time interval of about 7 min, between 17:10 and 17:17 (local time). This section gives an overview on the results of the analysis (Analysis by S. Redaelli [81]).
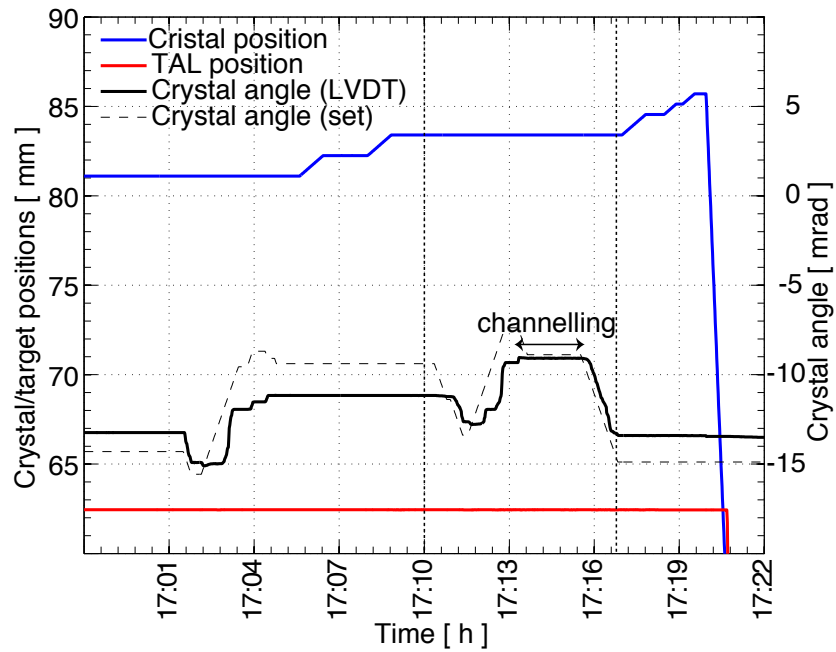
Figure 5.19: Positions of crystal, TAL and crystal orientation vs time. From [81].

In Figure 5.19 the transverse position of the TAL and the Crystal, together with the crystal orientation, are shown, and the time interval of interest is indicated. In Figures 5.20, 5.21 and 5.22 the BLM readings are presented respectively for the straight insertions 2, 5 and 6: each column corresponds to a different BLM, and different colors correspond to different time intervals. For some of the BLMs an exponential decay is visible - interrupted by a region where the losses decrease, in time with the channeling orientation of the crystal. The exponential decay is associated to the movement inward of the crystal [79], which is expected to generate losses with long decay times. The BLMs whose readings are totally flat were either

saturated or not detecting any loss, showing large zero-offset value for some of them, also with negative values. The real offset values for the BLMs remain unknown; to estimate the efficiency gain a zero offset value was assumed.
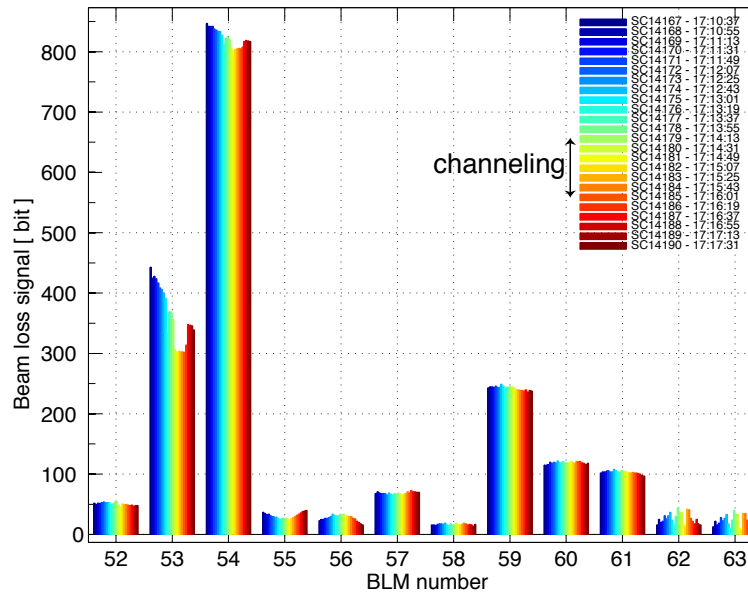
Figure 5.20: Losses in Long straight section 2 (LSS2), between 17:10:37 and 17:17:31 (local time). From [81].

The highest reduction in losses is found, as expected, just downstream the crystal position (see Figure 5.21, BLM n. 163, 7 m downstream the crystal), in the straight section 5. The loss reduction is of about 53%, or, equivalently, an increase in local cleaning efficiency (see section 2.2.3) of 2.11. This is however not relevant for collimation purposes. For the regions far downstream of the crystal three BLM present a strong variation in losses:

- BLM 53 (magnet "QFA.21610", distance from the crystal 3398 m): factor 1.16 ± 0.01

- BLM 54 (magnet "QFA.21710", distance from the crystal 3400 m): factor 1.03 ± 0.01

- BLM 201 (magnet "QF.62010", distance from the Crystal 1223 m): factor 1.29 ± 0.05

It must be stressed that no correction for eventual BLM offsets was applied. All other BLMs showed no significant change in loss reading.
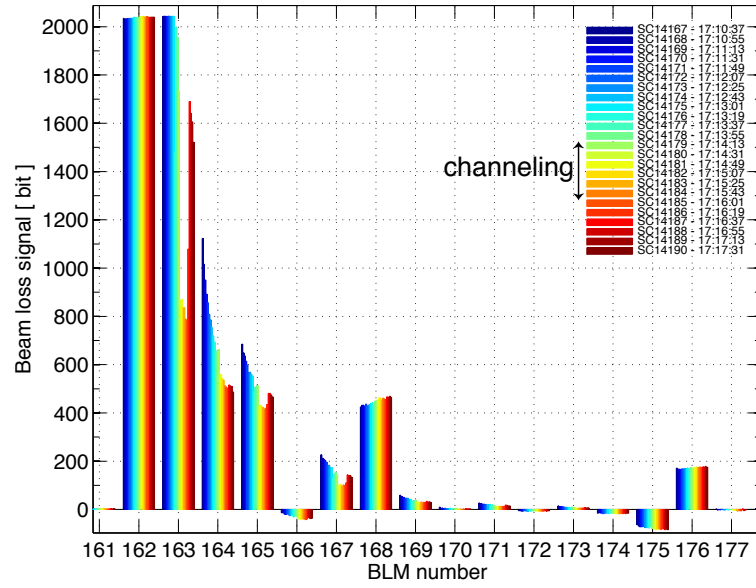
Figure 5.21: Losses in Long straight section 5 (LSS5), between 17:10:37 and 17:17:31 (local time). From [81].
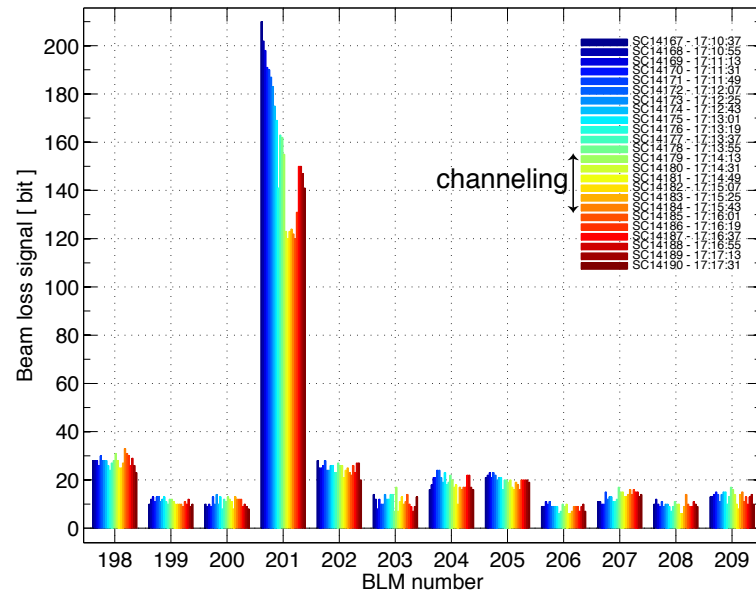
Figure 5.22: Losses in Long straight section 6 (LSS6), between 17:10:37 and 17:17:31 (local time). From [81].

5.4 SixTrack simulations

The three main experimental outcomes for the UA9 experiments analyzed so far are:

1. Angular scans: by moving the crystal orientation and detecting the losses downstream the crystal, the difference between the nuclear interaction rate in amorphous and channeling orientation is found. The channeling angular acceptance and total bending angle are also evaluated (Section 5.3.1).

2. Collimator scan: by gradually moving the collimator toward the beam edge, the channeled beam profile can be reconstructed: the channeling efficiency, average kick and width are therefore evaluated (Section 5.3.2).

3. Far away losses: by using the SPS BLMs, the reduction in far away losses can be registered, and therefore the relative loss reduction of channeling mode with respect to amorphous (Section 5.3.4).

The Sixtrack code has been used to simulate all the experimental outcomes. In particular two different sets of measurements have been done:

- Low-statistic simulations (6400 particles, 500 turns) for reproducing angular and collimator scans. The results are presented and compared with experimental data in Sections 5.4.1 and 5.4.2.

- High statistics simulations (1.6 million particles, 750 turns) for simulating the losses along the ring. The results are compared with the experimental data, see the discussion in Section5.4.3

For the three cases a 1 mm long Si crystal, 111 orientation with curvature radius of 6.67 m (i.e. a channeling angle of 150 μrad) is used. It is worth noticing that value differs from the nominal value for Crystal 1, that is 170 μrad, because the simulations have been set before knowing the precise crystal features. The crystal transverse directions are typical dimensions for a strip crystal, i.e. a width of 500 μm and a height of 50 mm. If not specified differently, the simulation settings (element positions and emittance) matches the experimental ones. In the next sections the comparison between the simulation and the experimental results are presented, while an analysis of the possible causes for the found discrepancies is given in Section 5.5.

5.4.1   Angular scans

As suggested from the multiple peaks detected during the angular scan data (see Figure 5.5), and verified by the Medipix investigations (Section 5.3.3), the Crystal 1 is in quasi-axial position. This means that different skew planes are crossed before reaching the main channeling direction: this situation cannot be simulated by our code at the moment. For this reason only the Crystal 2 angular scan has been simulated, and the comparison between experimental data and simulation outcomes is

shown in Figure 5.23. All the data are normalized as explained in Section 5.3.1.
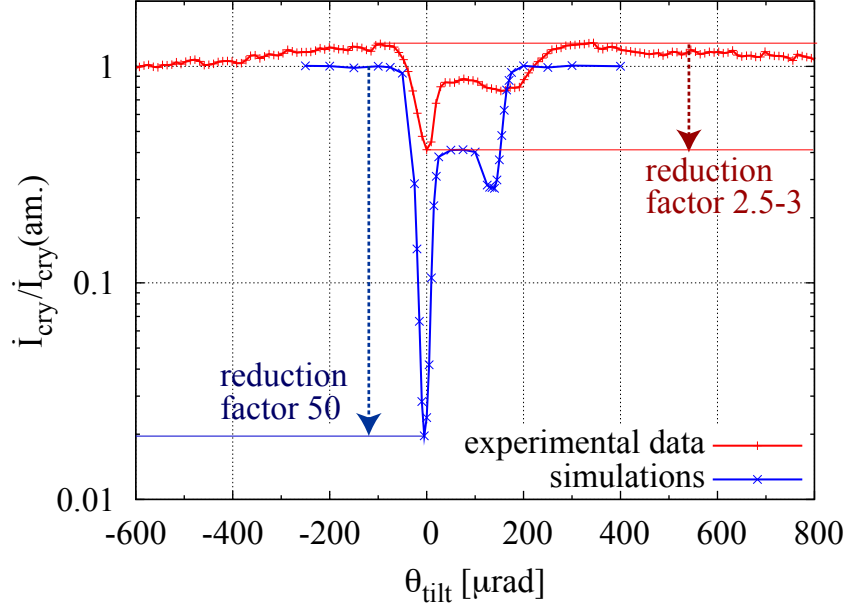
Figure 5.23: Angular scan for Crystal 2: comparison between simulation and measurements.

As for the experimental data, three important parameters are deduced from the simulated angular scan:

- The channeling acceptance. The simulation value is $\sigma_{chAcc} = 52$ μrad, in good agreement with the experimental value $\sigma_{chAcc} = 50$ μrad. However both values are higher than the theoretically expected value (29 μrad) for the single-pass experiments. This is a known effect of the multi turn dynamics, that increases the angular divergence of the impinging beam, therefore widening the channeling angular acceptance.

- The total bending angle θ_b. In case of simulations $\theta_b^{sim} = 145 \pm 5$ μrad, while for the experimental data $\theta_b^{exp} = 161 \pm 10$ μrad. The higher measured bending angle agrees with the channeling angle measured during the collimator scan C2.1, $\theta_c = 164 \pm 1$ μrad (see Section 5.3.2.4). The total bending angle measured for Crystal 1 is $\theta_b = 155 \pm 10$ μrad.

- Single-pass efficiency in multi-turn environment. In the simulated case, the signal reduction in channeling is about a factor 50, to be compared with the factor 2.5-3 got by experimental data. The reduction factor measured for Crystal 1 is approximately a factor 10.

5.4.2   Collimator scans

Three different collimator scans have been simulated, both for Crystal 1 and for Crystal 2. For each case a set of simulations with different apertures of the collimator right jaw (the left jaw is kept retracted as in the experimental condition) was performed, and the number of particles which had inelastic interactions in the collimator jaw was considered. In this Section the comparison between simulations and experiment is presented.

Table 5.9: Emittance and transverse aperture settings used for collimator scan simulations

	simulated coll. scan	ε_x [m·rad]	n_{cry} [σ_x]	n_{COLL} [σ_x]	n_{TAL} [σ_x]
S1.1	C1.1	$14 \cdot 10^{-9}$	-3.14	-17→-3.1	-4.97
S1.2	C1.2	$35 \cdot 10^{-9}$	-3.11	-14→-3.1	-5.26
S2.1	C2.1	$31.3 \cdot 10^{-9}$	-6.03	-16→-6	-7.05

The simulation details, together with the indication of the corresponding collimator scan, are specified in Table 5.9.

The simulation results were analyzed as the experimental ones, and the obtained halo distributions - as seen by the collimator jaws - are compared in Figure 5.24.

It is interesting to notice that the three curves in Figure 5.24 almost overlap, despite the different emittances, the different normalized apertures of the elements and even the 2-meters longitudinal displacement between Crystal 1 and Crystal 2. The distributions show a clear channeled beam: a Gaussian fit gives a center 150 μrad and an rms of 13 μrad for the three cases. Both values are in perfect agreement with the theoretically expected values, i.e. the set channeling angle and the expected rms ($0.7 \cdot \theta_c = 12.95$ μrad). It must be stressed that only the case of perfectly on momentum halo has been simulated: if considering the angular spread of off momentum particles, and keeping the grazing assumption (see Section 2.3.1), the rms width is expected to increase to a value of 16.5 μrad.

The comparison between the simulation and the experimental results are shown in Figure 5.25, 5.26 and 5.27.
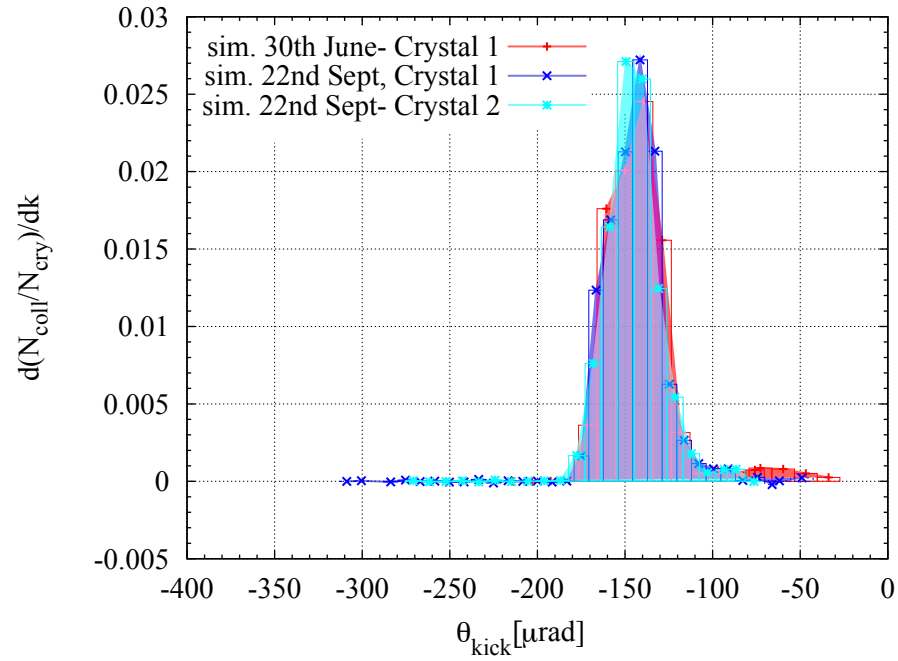
Figure 5.24: Secondary halo distribution as measured by the collimator for the simulation cases specified in the text.
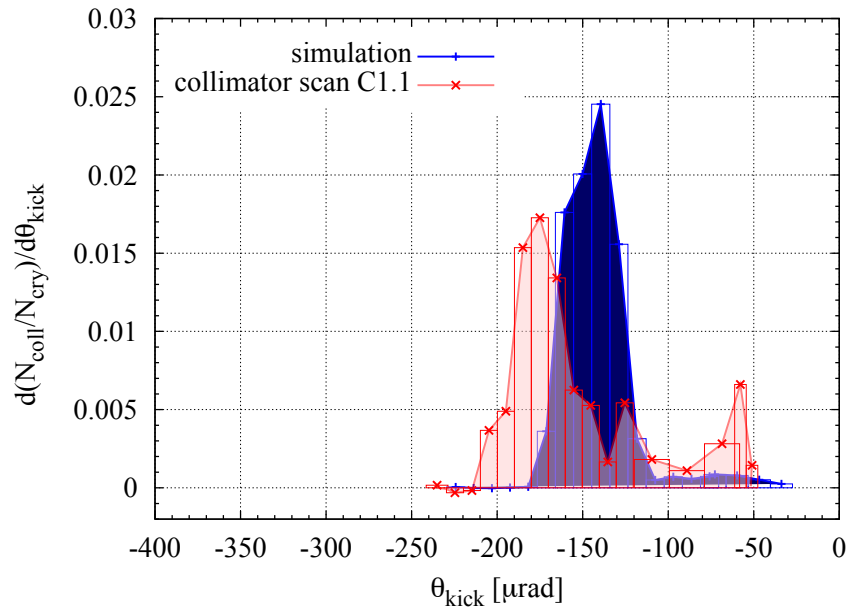
Figure 5.25: Secondary halo distribution as measured by the collimator scan for the case C1.1, compared with the results of the simulation S1.1.
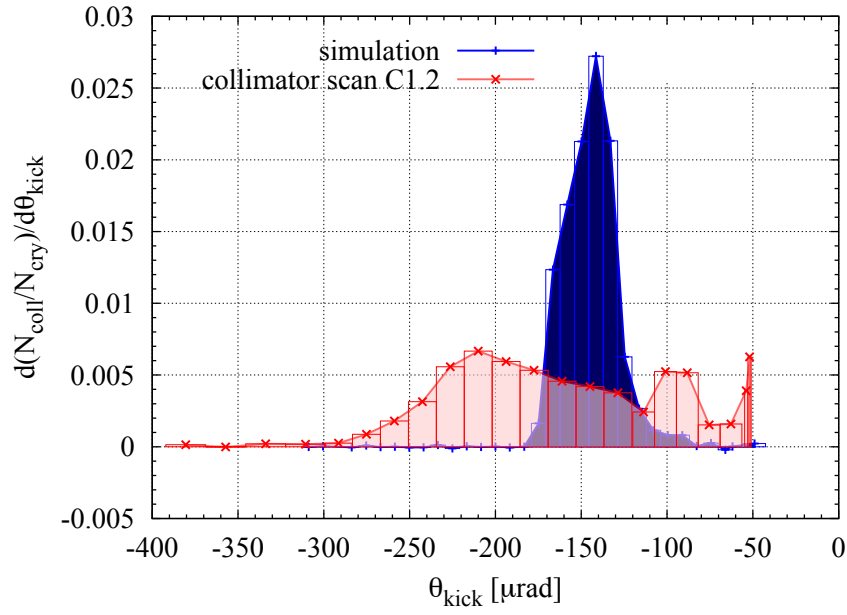
Figure 5.26: Secondary halo distribution as measured by the collimator scan for the case C1.2, compared with the results of the simulation S1.2.
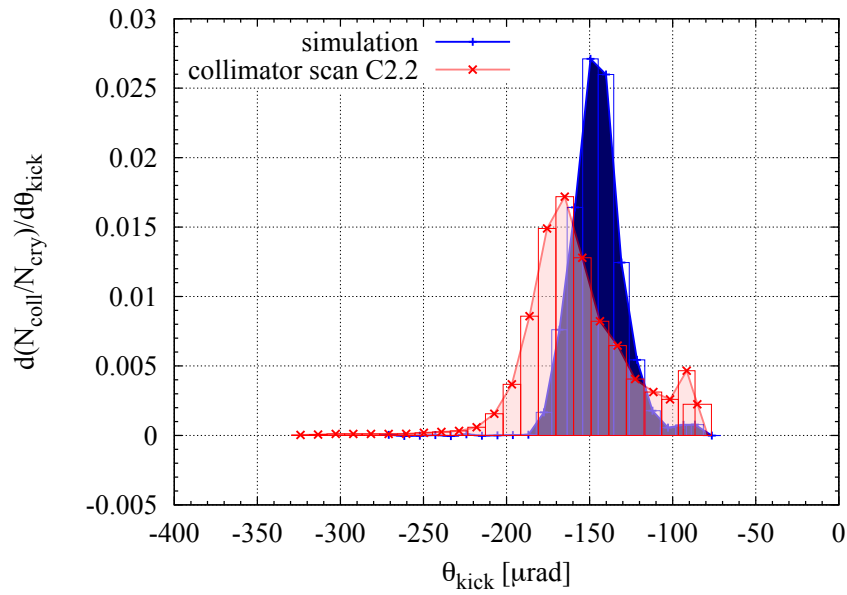
Figure 5.27: Secondary halo distribution as measured by the collimator scan for the case C2.1, compared with the results of the simulation S2.1.

Table 5.10: List of the collimator scan results: simulations and measurements are compared. For the channeling angle θ_{kick} the nominal value has been used.

scan n.	$\theta_{ch}^{meas}/\theta_{ch}^{nominal}$ [-]	$\sigma_{ch}^{meas}/\sigma_{chan}^{sim}$ [-]	$\eta_{chan}^{meas}/\eta_{chan}^{sim}$ [-]
C1.1	1.01	1.3	0.82
C1.2	1.15	3.07	0.71
C2.1	1.10	1.62	0.92

The comparison between the measured and the experimental results is summarized in Table 5.10. For the three cases, the measured rms widths of the channeled peak are systematically larger than the simulated one, while the measured efficiency is smaller. For the bending angle the comparison is made with the nominal values. The experimental result for collimator scan C1.1 agrees with the expected values, while it is larger for the other cases.

5.4.3   Beam Loss Maps

The main feature of our simulation tool is the possibility to evaluate the local inefficiency of the collimation system by comparing the tracks of the particles with a detailed aperture model (see Section 3.1.1.2). The local cleaning inefficiency η is defined by equation 2.32, that is repeated here for convenience:

$$\eta = \frac{N_{abs}(dl)}{N_{Tot} \cdot dl}$$

with N_{abs} the number of particles hitting the aperture in the longitudinal interval dl over the total number of particles absorbed by the collimation system N_{Tot}, normalized over the length dl. The picture of the local cleaning inefficiency versus the longitudinal coordinate s is called loss map. A set of simulations with different crystal orientations has been performed to understand how the loss maps along the SPS are supposed to vary. In this section the loss map results are presented and compared with the experimental results.

The simulation layout is the one already shown in Figure 5.2, but the crystal is positioned in the middle of the tank and there is a second roman pot 15.6 m downstream the first one: these differences are due to the fact that, when the simulation campaign has been launched, the experimental layout had been not finalized yet. The crystal used for our simulations is a Si crystal, 111 orientation. The length is 1 mm and the curvature radius is 6.67, that means a channeling angle of 150 μrad.

Its transverse directions are typical dimensions for a strip crystal, i.e. a width of 500 μm and a height of 50 mm.

Table 5.11: Equivalent thickness in Cu for the different RP regions. The value for the detector region can vary depending on the number of Si detectors inserted in the RP.

RP region	transverse dimension	equivalent Cu thickness
Detector	$b > 650\mu$m	664-882μm
Dead	150μm $< b < 650\mu$m	370 μm
Border	$0 < b < 150\mu$m	1.16 cm

The roman pots are multi layered objects both in longitudinal and in vertical direction. We used an equivalent thickness in Cu, rescaling with the nuclear interaction length, to represent each RP transverse layer (edge, dead region, detector region). For each layer we got a different equivalent thickness, as summarized in table 5.11. Since our code does not foresee multi-layer elements in the transverse direction, we choose to use a Cu thickness of 750μm, representative of the detector region.

Table 5.12: Settings for beam loss maps simulations

	simulated	ε_x [m·rad]	n_{cry} [σ_x]	n_{RP1} [σ_x]	n_{RP2} [σ_x]	n_{TAL} [σ_x]
S.LM	Beam loss maps	$11.7 \cdot 10^{-9}$	-6.0	-7.0	-7.0	-6.83

The aperture settings of the different elements are listed in Table 5.12. Scans of 35 different crystal orientations between -400 and +250 μrad were made.

The loss maps for amorphous and channeling case are presented in Figures 5.28 and 5.29. Outside of the experimental region, in both cases we can recognize three peaks in far away losses, at 1712 m, 4036 m and 6499 m. Two of the BLMs which detected the highest change in losses were close to this coordinates (1669 and 6402 m), showing that our simulations can locate the regions which get more losses.
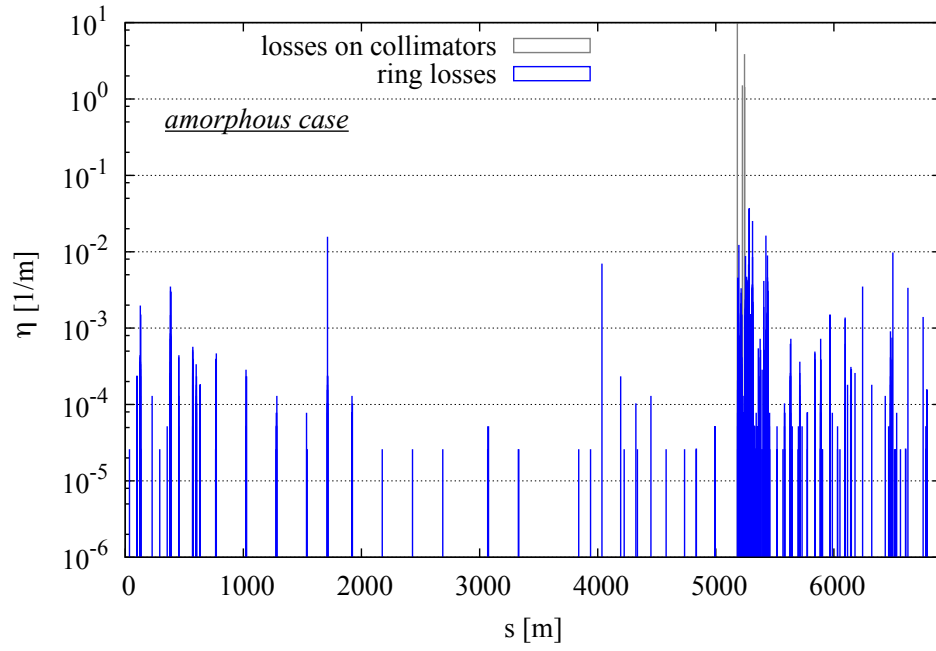
Figure 5.28: Beam loss map in the SPS, when using the crystal in amorphous orientation.
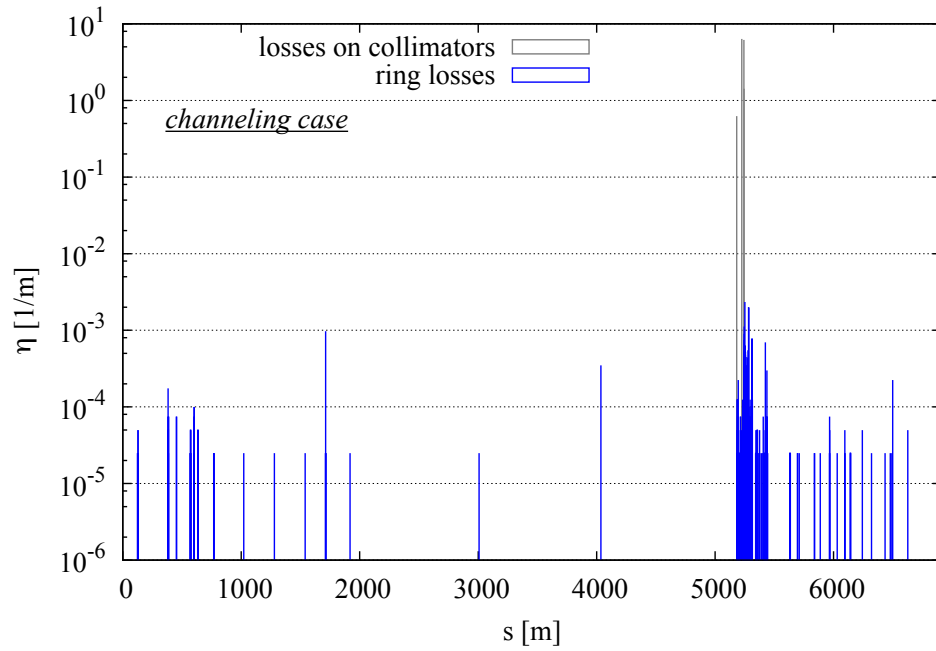
Figure 5.29: Beam loss map in the SPS, when using the crystal in channeling orientation.

Figure 5.30: Maximum of the local cleaning inefficiency for local (within 500 m downstream the crystal) and far away losses (in the rest of the ring) for different crystal orientations. Case of perfect crystal.

The maximum of local cleaning inefficiency versus crystal orientation is shown in Figure 5.30. The ring has been divided in two regions: the first 300 meters downstream the crystal (local losses) and the rest of the machine (far away losses). As shown in the plot, the predicted reduction for maximum cleaning inefficiency goes up to a factor 17 ± 2 for local losses, and a factor 16 ± 3 for far away losses. These estimations should be compared with the experimental data from the BLMs (section 5.3.4), where the maximum measured loss reduction factor is of about 2 for local losses, and a factor of 1.3 for far away losses, i.e. ten times smaller than predicted by simulations.

5.5 Discrepancies between experiment and simulation: possible causes

Comparing the experimental results with the simulated cases, it was found that the crystal performances are generally worse than expected, i.e.:

- From angular scan, a reduction in nuclear interactions rate at the crystal of a factor 20 is expected - the experimentally measured values are a factor 10 (for Crystal 1) and a factor 2.5-3 (for Crystal 2).

- From collimator scan simulations, a channeling efficiency of 92% is expected, to be compared with a wide rage of efficiencies obtained (from 64 to 85%). The channeled beam features are also different: channeling angles higher than the nominal angles are found, and the measured beam widths are also slightly higher than expected.

- From the Beam loss maps, a loss reduction factor of 16 in far away losses is predicted by simulations, but the maximum measured value was about 1.3.

To understand these discrepancies, the simulation settings must be considered. Since a perfect crystal in perfect channeling orientation is considered both for collimator scan and beam loss map simulations, the experimental results could indicate that:

- the crystal is not "perfect", i.e. the channeling probabilities in the edge of the crystal are, for some reason (e.g. amorphous layer, higher degree of impurities, cracks...), lower than expected.

- the orientation is not "perfect", i.e. we are not measuring the distribution associated to the optimal channeling orientation.

Or, more realistically, a mixture of both conditions. Both hypothesis can help in justifying different experimental results. A reduced edge efficiency could account for the angular scan results, the measured far away loss reduction and the channeled beam width and population, but the only way to get a channeled kick larger than expected is a misalignment of the crystal[3]. On the other hand, a simple misalignment could not justify the angular scan results. Given the poor control on the available goniometers (see Figure 5.3), a small misalignment is possible: its effect, however, is investigated elsewhere [82]. In this section more details are given about the possible influence of a reduced channeling efficiency on the crystal edge: this has been obtained in our simulations by adding an amorphous layer.

Amorphous layer thicknesses (λ_{am}) between 50 nm and 0.5 mm were added to the crystal model (see Section 3.1.2.2 for details). It should be stressed that these studies are meaningful only if we rescale the amorphous layer thickness with the initial impact parameter of the particles on the entrance face of the crystal (b). In our case the characteristic impact parameter is of about 18 μm (typical length resulting from an exponential fit of the data).

The effect on the collimator scan simulations is presented in Figure 5.31, while in Table 5.13 the fitting parameters and the channeling probabilities for the different λ_{am} are summarized. It is interesting to notice how values of amorphous layer of up to 50% of the impact parameter value seem to have little effect on the multi-turn channeling efficiency. A slight decrease (about 4%) in efficiency can be observed

---

[3]Always in the case that the expected value is correct, i.e. the crystal bending angle is still the one measured before the experiment in the crystal characterization.
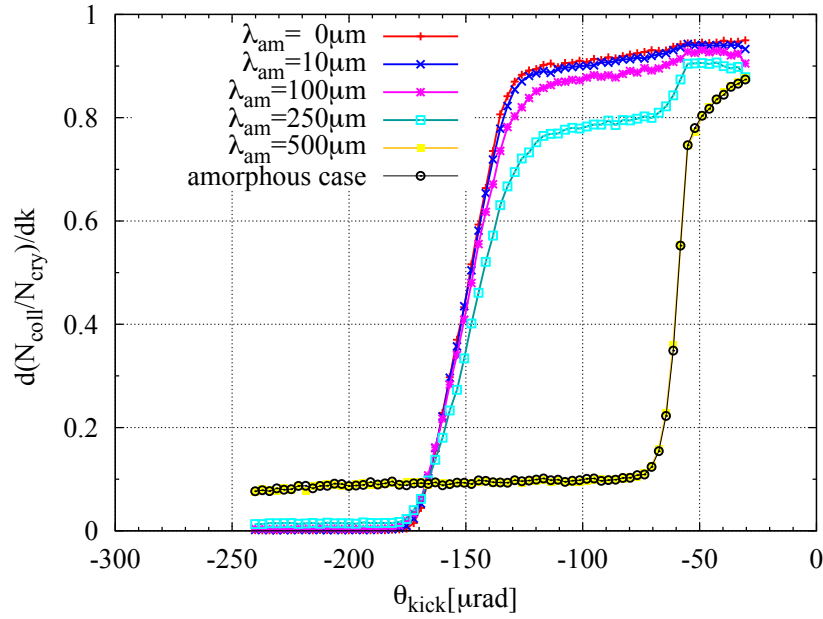
Figure 5.31: Efficiency curves for the simulation S1.1, with different amorphous layer thicknesses.

Table 5.13: Displacement c, rms σ_c and relative population of the channeled beam at the collimator location, as calculated fitting the collimator scan data, for different thicknesses of the amorphous layer.

λ_{am} [μm]	λ_{am}/b [-]	θ_{ch} [μrad]	σ_{ch} [σ_x]	η_{ch} [%]
0	0	-150 ± 0.5	13.2 ± 0.3	92 ± 1.4
1	0.05	-150 ± 0.5	13.1 ± 0.3	91 ± 1.4
10	0.5	-150 ± 0.4	13.6 ± 0.2	91 ± 1.2
100	5	-150 ± 0.5	14.2 ± 0.02	87 ± 1
250	14	-148 ± 0.5	15.4 ± 0.5	77 ± 1.4
500	28	no visible channeling effect		
scan C1.1	?	172 ± 1	16 ± 1	73 ± 4

for values of $\lambda_{am} = 5b$, while a strong effect (decrease of about 15%) is observed for $\lambda_{am} = 14b$. When $\lambda_{am} = 28b$, the channeling effect is no efficient anymore. An amorphous layer between 100 and 250 μrad can reproduce the best efficiency values found for the two crystals: in particular a value of 250 μm fits almost perfectly both the channeled beam population and width of the collimator scan C1.1.
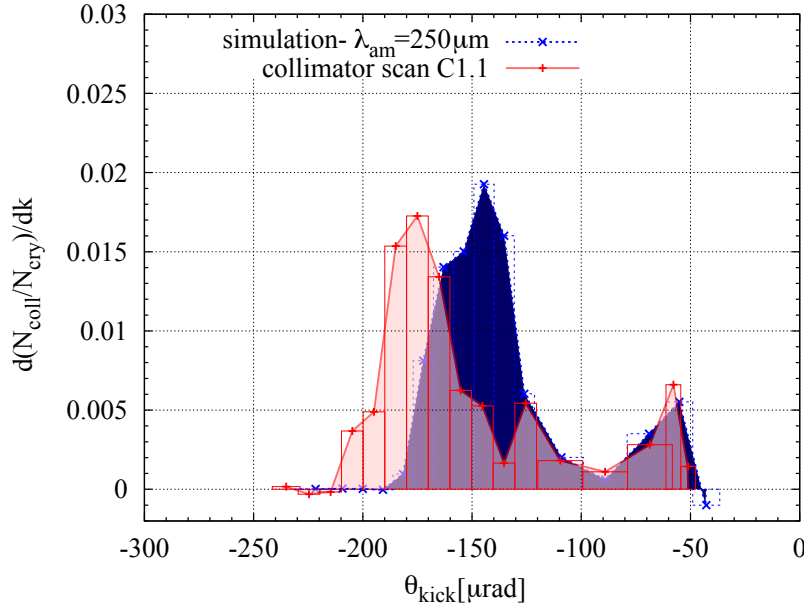
Figure 5.32: Secondary halo distribution as measured by the collimator scan for the case C1.1, compared with the results of the simulation S1.1 with an amorphous layer of 250 μm.

The comparison between the beam profile measured by the collimator scan C1.1 and the corresponding simulation results, including an amorphous layer of 250 μm, is shown in Figure 5.32. The simulations well reproduce both the channeling peak (width and population) and the intermediate region. The different average kick is compatible with the different simulation settings.

Investigations of the influence of amorphous layer on loss maps have been performed as well. Once again different amorphous layer thicknesses, between 500 nm and 1 mm, have been considered, and the typical initial impact parameter of the particles at the crystal is of about 18 μm. The perfect channeling orientation was simulated, as described in Section 5.4.3. In Figure 5.33 the maximum of the local cleaning inefficiency both for local and far away losses is shown for different amorphous layer.

As it was found for collimator scan simulations, an amorphous layer of 500 μm give results that cannot be distinguished by the pure amorphous case. In particular the loss reduction factor with respect to the amorphous case for a thickness of 250 μm is of 1.75 ± 0.20 for local losses, and 1.86 ± 0.22 for far away losses, to be compared with the experimental values (2 for local losses, 1.3 for far away losses). Even though the agreement is not perfect, the results are much closer to the experimental values than the one obtained for the perfect crystal (17 for local losses, 16 for far away losses).
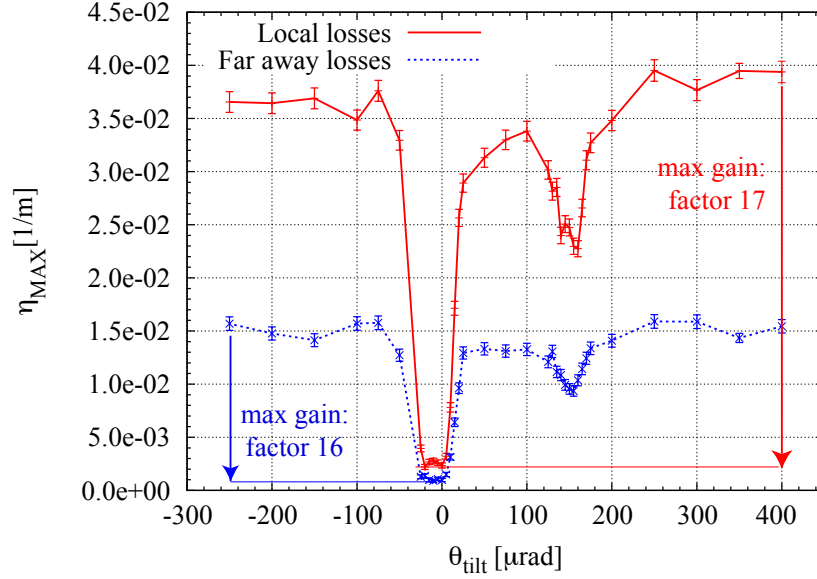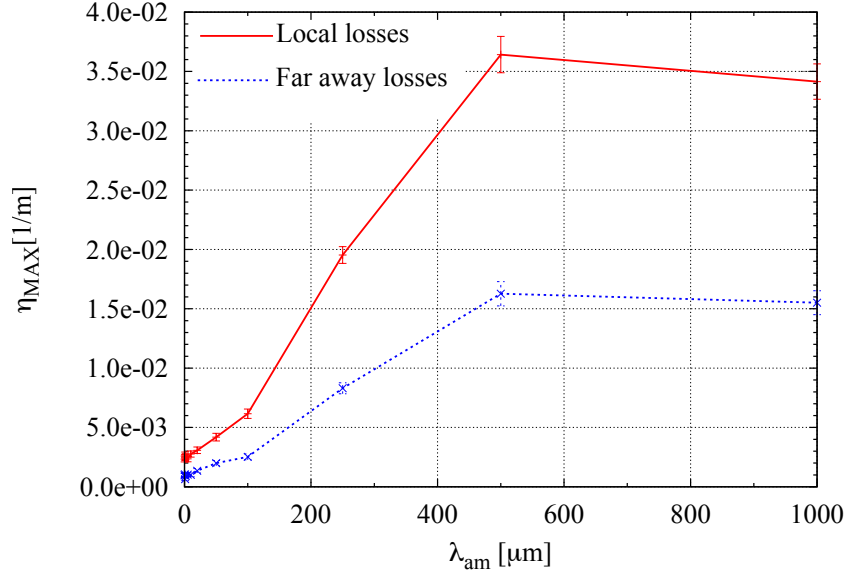
Figure 5.33: Maximum of the local cleaning inefficiency for local (within 500 m downstream the crystal) and far away losses (in the rest of the ring) for different amorphous layer thicknesses, in case of perfect crystal.

It was shown that simulations with an amorphous layer of 250 μm can account for most of the features observed in the experimental results: this is considered a strong evidence of the fact that the channeling efficiency at the crystal edge is smaller than the one considered in our simulations.

5.6   Conclusions

The main results of the UA9 experiment have been presented. The experiment consisted in deviating the SPS circulating beam halo with a bent crystal in different operational modes: two Si crystals, fabricated with different techniques, have been tested so far. A set of BLM detectors, combined with the collimator scan technique, enabled a direct measurement of the multi turn channeling efficiency: for the two considered crystals we obtained efficiencies between 57 to 85%. The lower values are associated to non optimal crystal orientations. Using the same procedure the channeled beam parameters (center and width) have been calculated, and the results are in good agreement with the images of the channeled beam registered by the Medipix detector.

A full set of simulations have been performed in an attempt to reproduce and understand the collimator scan results. In case of simulations for a perfect crystal,

the experimental channeling efficiencies do not reach more than the 70% of the values predicted by the simulation. However it was possible to reproduce most of the features of the experimental results by adding, in the crystal model used for simulations, a 250 μm thick amorphous layer (to be compared with an rms impact of 18 μm).

Regarding the far-away losses, it was unfortunately difficult to get a clean measurement of the loss variations when using the crystals in different operational modes. Unfortunately the experimental value is affected by the limited resolution of the SPS beam loss monitors: a precise calibration should be performed to get a better evaluation. However, in the hypothesis of a negligible offset value of the considered BLMs, the maximum measured loss reduction in channeling mode was about a factor of 1.3 for far away losses, while the simulations for a perfect crystal predicted a factor of 16. More realistic vales can be obtained by adding, again, an amorphous layer to the crystal surface exposed to the beam: when simulating a thickness of 250 μm, a loss reduction factor of 1.86 ± 0.22 is obtained.

Chapter 6

LHC

In this chapter a possible implementation of a crystal-enhanced collimation system is evaluated for the LHC. Simulation studies were performed with the same state-of the art tracking codes as used for the design of the conventional LHC collimation system. The numerical models are described and predictions for the local and global cleaning efficiency with a crystal-based LHC collimation system are presented for the nominal 7 TeV energy. Open issues and further work towards a crystal collimation design for the LHC are discussed.

6.1   The machine

The LHC is the main accelerator and collider at the CERN laboratories, Geneva. It is a 27 km long ring, located in an underground tunnel which crosses through France and Switzerland, where two beams circulate in opposite directions. It can accelerate both protons and lead ions. Eight curved regions (main arcs), alternated with eight straight regions (insertion regions), constitute the accelerator layout (see Figure 6.1).
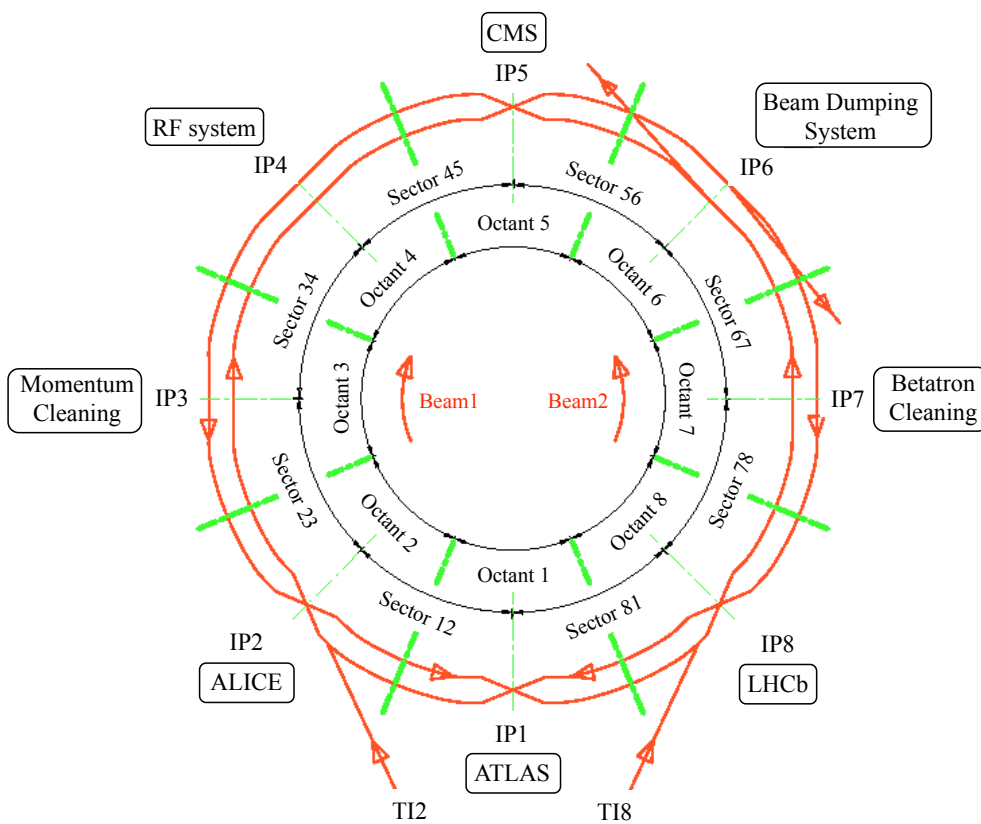
Figure 6.1: The 27 km LHC ring, which lays underground over the territories of France and Switzerland. From [83].

In the main arcs superconducting dipoles and quadrupoles are used to steer the beams and keep them focused. The 15-m long superconducting dipoles fill about 2/3 of the total accelerator length, and they are designed to operate with a central field of about 8.3 T. The superconducting elements are constantly kept at the superfluid helium temperature (1.9 K), and the temperature margin, e.g. the maximum temperature increase that the superconducting material can sustain without

losing its superconducting capabilities, is about 1.5 K. Any release of energy, causing a temperature raise over the temperature margin, would provoke a quench, i.e. a transition between the superconducting and resistive state. The maximum energy per volume unit that could be deposited in a superconducting magnet is called the quench limit, and it generally depends on the material, operational parameters of the superconductor (magnetic field, temperature, electric current) and cooling power. The quench limit value and its implications for the LHC collimation system are discussed in the next section.

In the straight sections the experimental regions and the utility insertions are located. The main experiments, placed at the four interaction points (IPs) of the accelerator, are: ATLAS (IP1), ALICE (IP2), CMS (IP5) and LHCb (IP8).

The two large experiments, ATLAS and CMS, are based on general-purpose detectors and they are designed to investigate the largest range of physics possible, including the search for the Higgs boson and particles that could make up dark matter.

The two medium-size experiments, ALICE and LHCb, have specialized detectors: LHCb investigates the slight differences between matter and antimatter by studying a type of particle called the 'beauty quark', or 'b quark', while ALICE is specially designed to be used during Lead ion runs, to study a state of matter known as quark gluon plasma, which is believed to have existed soon after the Big Bang

The remaining straight insertion regions (IRs) are dedicated to RF cavities (IR4), the beam dump (IR6) and collimation (IR3 and IR7). More details about the LHC collimation system will be given in the next section.

6.2 Importance of the LHC collimation system: cleaning, machine protection and background reduction

With its actual center-of-mass energy of 7.0 TeV, the LHC is nowadays the most powerful accelerator in the world. During the next 2 years it is foreseen to run the LHC with a collision energy of 7 TeV (3.5 TeV per beam); after that, a long shutdown will be required to overcome the present limitations and reach the LHC's design collision energy of 14 TeV.

In nominal conditions there will be 2808 bunches per beam with $1.15 \cdot 10^{11}$ protons per bunch. The energy stored in the circulating beam (up to 360 MJ per beam [2]) makes it very powerful and highly destructive.

The expected loss rates are shown in Table 6.1. The total power loss corresponding to the most critical case (collision energy, beam lifetime of 0.2 h) reaches almost

Table 6.1: Specified maximum loss rates for safe operation of the machine.

	Total time [s]	beam lifetime [h]	Rate Losses [p/s]	Lost power [W]
Injection (450 GeV)	continuous	1.0	$0.8 \cdot 10^{11}$	$6 \cdot 10^3$
	10	0.1	$8.6 \cdot 10^{11}$	$60 \cdot 10^3$
Collision (7 TeV)	continuous	1.0	$0.8 \cdot 10^{11}$	$90 \cdot 10^3$
	10	0.2	$4.3 \cdot 10^{11}$	$480 \cdot 10^3$

500 kW for a maximum of 10 s. The collimation system is designed to stand such a power.

Obviously a fraction of particles could be lost in the superconducting elements. One has to make sure that the power associated to the losses in the magnets are lower than the cooling capacity of the cryogenic system. Extensive theoretical and experimental studies [7, 8] were performed to evaluate the maximum sustainable power load (quench limit) for the main LHC superconducting magnets. A comprehensive summary of the results can be found in [9]. For the studies carried out in this thesis, as usually done for standard collimation studies, the case of continuous heat deposit is assumed: the estimated quench limits in this assumption are listed in Table 6.2.

Table 6.2: Magnet quench limit associated to continuous losses. See [7] for a complete description.

	Quench limit [mW/cm^3]	Quench limit [p/s/m]
Injection (450 GeV)	10	$7.0 \cdot 10^8$
Collision (7 Tev)	5	$7.8 \cdot 10^6$

The collimation system is designed to keep the unavoidable beam losses in the cryogenic regions lower than the quench limit, by concentrating them in dedicated collimation insertions: this is the **halo cleaning** function of the collimation system, and the main purpose of the LHC collimation system. The huge disproportion (about 8 orders of magnitude) between the expected power lost in the machine and the value of the quench limit demands for a sophisticated, highly-efficient system.

The quantity used to qualify the effectiveness of the LHC collimation system is the local cleaning inefficiency η, defined by equation 2.32 and repeated here for

convenience:

$$\eta = \frac{N_{abs}(dl)}{N_{Tot} \cdot dl}$$

i.e. the number of particles N_{abs} hitting the aperture over the length dl divided by the total number of particles absorbed by the collimation system N_{Tot} and normalized to the length. At collision, taking into account the quench limit and the assumed losses, a local cleaning inefficiency of 1.7×10^{-5} 1/m can be tolerated. A
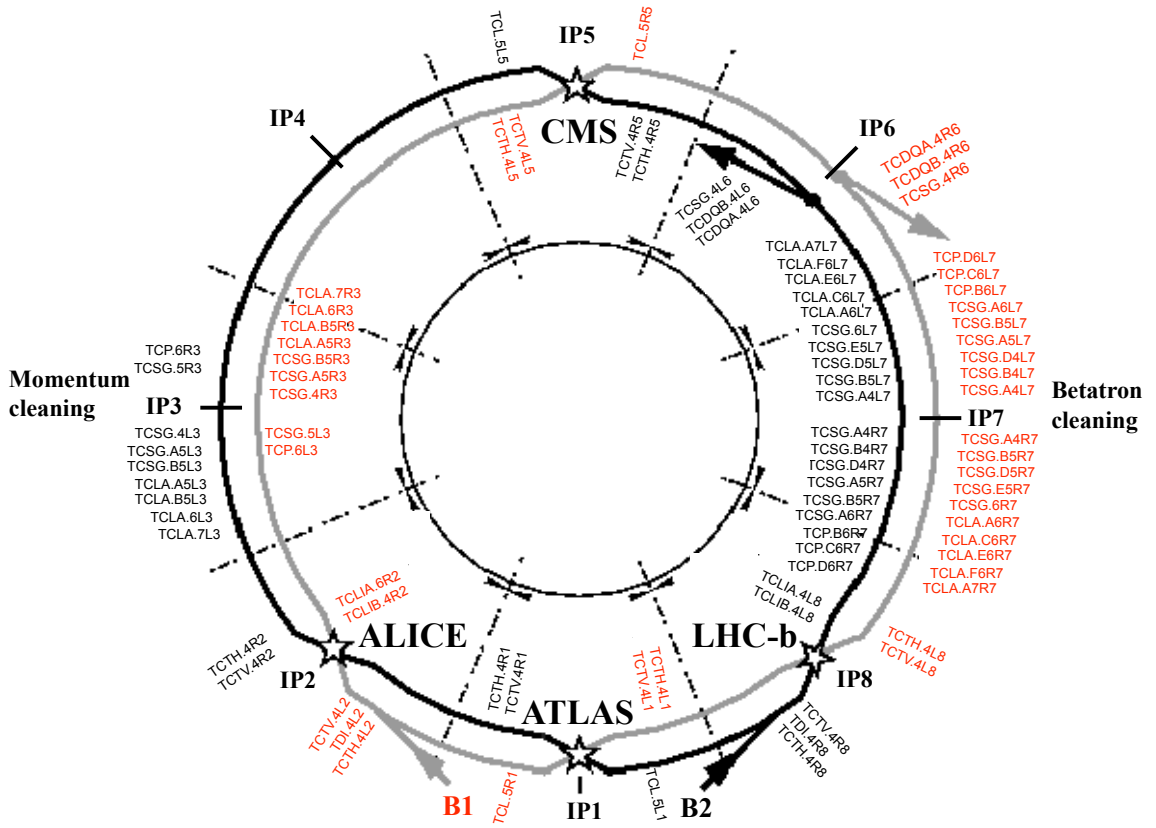
Figure 6.2: Layout of the phase 1 collimation system for the two beams (not in scale). Courtesy of C. Bracco [9].

sketch of the installed collimation system is shown in Figure 6.2. The cleaning insertions are positioned in IR3 and IR7: the first one is dedicated to momentum cleaning collimation, while IR7 is the betatron cleaning insertion (for details on collimation theory see section 2.2.2). In both regions the collimators are organized in two stages:

the 60 cm long CFC[1] primary collimators (TCP) are used to scatter the beam halo onto the 1m long CFC secondary collimators (TCS) downstream. At the very end of the insertion, W absorbers (TCLA) are set to intercept the particles which have escaped the secondary collimators (tertiary halo), immediately before the beginning of the cold region.

Apart from the halo cleaning function, the LHC collimation system is designed to provide limited **passive machine protection** in case of abnormal losses. Special protection devices, in fact, shield the most sensitive parts of the LHC against losses caused by equipment failures or wrong operation of the machine:

- Injection errors: occurring when the injection kicker magnets misfire. The TDI (injection beam stopper) and the TCLIA, TCLIB collimators are foreseen in IR2 and IR8.

- Extraction error: in the event of an asynchronous beam dump the beam can be swept over the machine aperture. Two identical, single-sided elements (TCDQA) are installed in IR6 to absorb the mis-kicked particles.

- Failures inducing multi-turn losses (e.g. RF failure, vacuum leak, mis-function of the kickers for the separation at IPs...): large part of the beam population is intercepted at the smallest aperture (i.e. the primary collimators) in few turns. This example underlines the importance of the robustness of the collimators.

A third and last task of the collimation system is also the **minimization of collimation-related background at the experiments**. Horizontal (TCTH) and vertical (TCTV) tertiary collimators are installed upstream the magnets at high beta locations (triplet magnets) at the interaction regions: the setting of the TCTs have been optimized to protect the triplets yet keeping the background as low as possible. Finally, special absorbers (TCL) located downstream of the high luminosity IPs use two pure copper jaws to catch the physic debris coming out from the interaction points during collisions

6.3   LHC collimation system: the phased approach

Depending on the loss rate and the efficiency of the collimation system, the performance of the machine could be limited. In view of the high energy of the LHC halo and the stringent constraints due to the cryogenic environment, the LHC collimation system is implemented in a phased approach. The Phase 1 relies on the robustness of the system, while the Phase 2 is intended to allow the LHC to run at its nominal settings (energy and intensity). Recent studies [9] assess a limitation of 40% of the nominal intensity for the Phase 1 of the collimation system, yet considering a

---

[1]Carbon Fiber Carbon composite

machine without imperfections such as jaw flatness tolerances, tilt errors, machine alignment errors, non ideal closed orbits. When the imperfections are taken into account the machine luminosity is further reduced to a few percent of the nominal value.

The Phase 2 collimation system is being designed to improve the efficiency by means of metallic collimators to be used during stable physics runs and adding collimators in the cryogenic region [4]. In parallel, advanced collimation studies are carried out to maximize ultimate performance of the LHC. Crystal collimation is one of these advanced options. The idea is to use the well-studied and tested crystal channeling effect in a bent crystal to increase the betatron amplitude of the halo particles, thus increasing the impact parameter on secondary collimators and possibly improving the collimation efficiency for the betatron halo.

6.4 Simulations

This section presents the results of simulations studying the feasibility and the optimum configurations for a crystal-based collimation insertion. In section 6.4.1 a study on the basic features of the particles impacting on the crystal surface, starting from the expected beam lifetime, is presented. The distribution of impact parameter and impacting angle is obtained, and used as input for the tracking studies performed with Sixtrack.

The Sixtrack simulations for the LHC, investigating the possible configurations for a crystal-based collimation insertion during stable physics runs at the LHC nominal energy (7 TeV), are described in section 6.4.2.

6.4.1 Impacting beam features

A bent crystal gives a kick to an impinging particle if certain initial conditions are fulfilled. In detail, channeling is possible only if the relative angle between the particle velocity and the crystal planes is lower than the crystal critical angle θ_c (see section 1.2.2.1). For a Si crystal with 110 orientation, the critical angle varies between about 8 μrad and 2 μrad (respectively at LHC injection and collision energy). It is therefore important to evaluate the expected divergence of the particles impacting on the crystal surface: here the collision case is studied, because it is expected to be the most critical one due to the tightest constraints on angular acceptance. Since the vertical dispersion at the crystal location is close to zero (see Table 6.5), the impact parameter spread and impact angle spread is expected to be smaller. For this reason only the horizontal case is treated. In this section the results of a simulation evaluating the first impact coordinates of the particles on the crystal are presented.

In order to have a realistic impacting particle distribution the code described in section 3.1.3 was used. The code generates a matched Gaussian tail distribution both in the transverse and longitudinal dimension, where particles receive a transverse random kick every turn (all the details can be found in Section 3.1.3).

A method to estimate a realistic kick could be to consider the effect of the different processes responsible for the emittance growth in the machine. Many processes lead to a natural increase of the emittance, such as intra beam scattering (IBS), scattering with residual gas, elastic scattering at the interaction points, diffusive phenomena (like resonance crossing or ripple in the power converters), collective effects like beam beam, space charge and instabilities (for further details please see [63, 84, 85, 86]). In addition to these processes, the natural reduction of emittance associated to the synchrotron radiation must be taken into account. In principle the contribution of each effect to the total emittance growth should be evaluated separately, but unfortunately most of them cannot be easily predicted, e.g.:

- The effect of wake fields and electron cloud depends strongly on the lattice of the machine, and can be evaluated only via dedicated simulations [87].

- The effect of the beam beam depends strongly on the particle amplitude and it is not easy to "be translated" in a single diffusion coefficient [88].

A different approach to evaluate the equivalent kick is to tune the single-turn kick in the code to match the assumed beam lifetime (i.e. a beam lifetime of 0.2 h, see section 6.2). The beam lifetime condition is satisfied when:

$$N^{part}(0.2h) = \frac{1}{e} \cdot N^{part}(0) \tag{6.1}$$

where $N^{part}(t)$ is the number of particles in the accelerator at the time t. Assuming, in very first approximation, that the particle losses are equally generated by the horizontal and the vertical kicks we expect that at the time t=0.2 h:

$$N_x^{lost}(t = 0.2h) = \frac{1}{2}N^{lost}(t = 0.2h) = \frac{1}{2}\left(1 - \frac{1}{e}\right) \tag{6.2}$$

where $N_x^{lost}(t)$ the number of lost particles in the horizontal plane and $N^{lost}(t)$ is the total number of lost particles. It follows that the condition on the beam lifetime, for the single x plane (illustrated in Figure 6.3), becomes:

$$N^{part}(t = 0.2h) = (1 - N_x^{lost}) \cdot N^{part}(t = 0) \simeq 0.68\, N^{part}(t = 0) \tag{6.3}$$

For a Gaussian distribution, and considering only the horizontal plane, equation 6.3 becomes:

$$N_0 \int_{x=-x_{lim}}^{x=x_{lim}} \frac{1}{\sqrt{2\pi}\sigma_x(0.2h)} e^{\frac{x^2}{2\sigma_x^2(0.2h)}} = 0.68 \cdot N_0 \int_{x=-x_{lim}}^{x=x_{lim}} \frac{1}{\sqrt{2\pi}\sigma_x(0)} e^{\frac{x^2}{2\sigma_x^2(0)}} \tag{6.4}$$
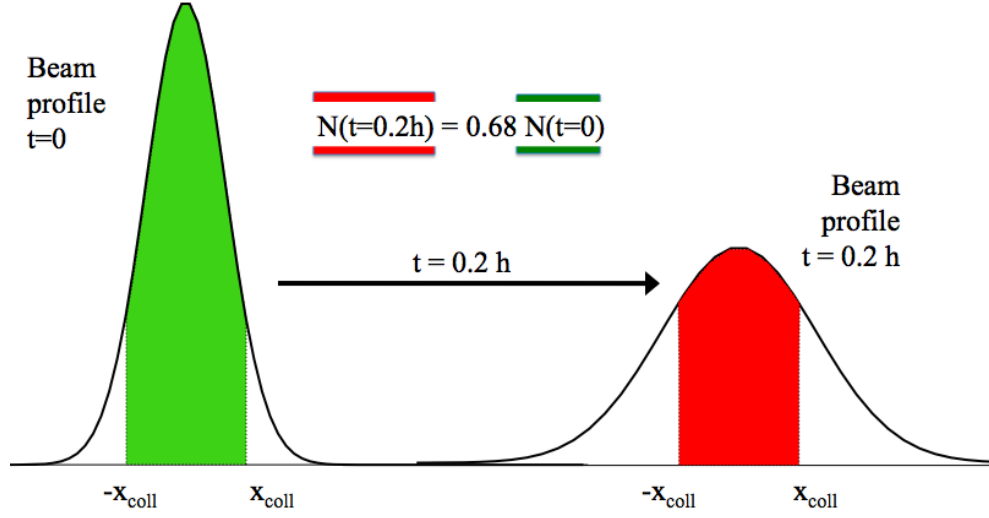
Figure 6.3: Beam lifetime condition for the horizontal plane: the total number of particle circulating in the machine must be reduced to 68% of its initial number after a time equal to the selected beam lifetime.

where $N_0 = N^{part}(0)$ is the initial number of particles, x_{lim} is the half aperture limitation in the machine, $\sigma_x(t)$ is the horizontal dimension of the beam at the time t. The initial rms beam dimension is $\sigma_x(0) = \sqrt{\varepsilon_{x0}\beta_x}$ where β_x is the value of the horizontal beta function at the point where the kick is applied and ε_{x0} is the initial horizontal emittance (the usual value $5 \ 10^{-10}$m $\cdot$ rad [1] is considered).

A one turn matrix code was used to simulate the beam population variation over a large turn number for different rms kicks given to the particles at each turn. The code starts from a matched Gaussian particle distribution fitting the machine aperture, and gives a random kick to each particle every turn: if the particle touches the aperture bottleneck (in our case corresponding with the crystal aperture), it is considered lost and removed from the tracking. The particle initial distribution and all the details about the code can be found in Section 3.1.3. Ten different scenarios were simulated, tracking, for each case, a gaussian distribution of 1000 particles for about 8 million turns (=0.2h) and varying the rms kick from 0.5 nrad to 15 nrad. The kick was applied, for convenience, at the crystal longitudinal location, where $\beta_x = 137.62$ m. It was found that an rms kick of 3 nrad satisfies equation 6.3. Considering the equation linking an rms kick with an average emittance growth after one turn:

$$\Delta\varepsilon = \frac{1}{2} \cdot \beta_x < k >^2 \tag{6.5}$$

Using the LHC revolution frequency (11245 Hz) one gets an emittance growth rate of $7 \cdot 10^{-12}$ m rad/s in the horizontal plane.
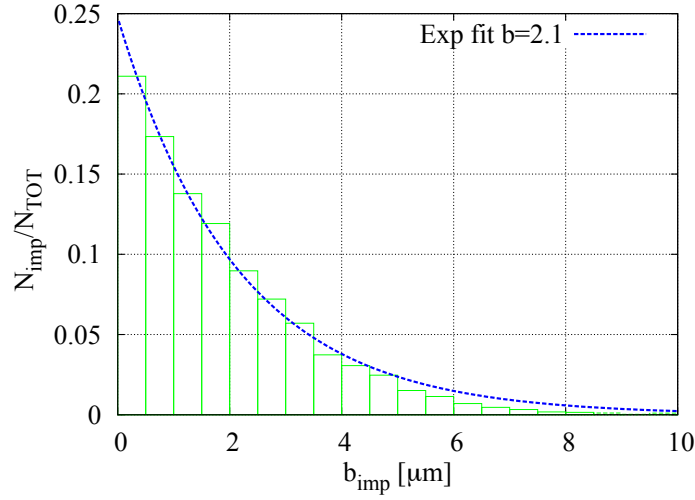
Figure 6.4: Impact parameter distribution on the crystal as simulated assuming a beam lifetime of 0.2h

The distribution of the first impact parameters obtained by the simulations is shown in Figure 6.4. The simulated data have been fitted with an exponential function, with a decay length of 2.1 μm: the simulations presented in section 6.4.2 have been tuned to obtain similar first impact parameters.
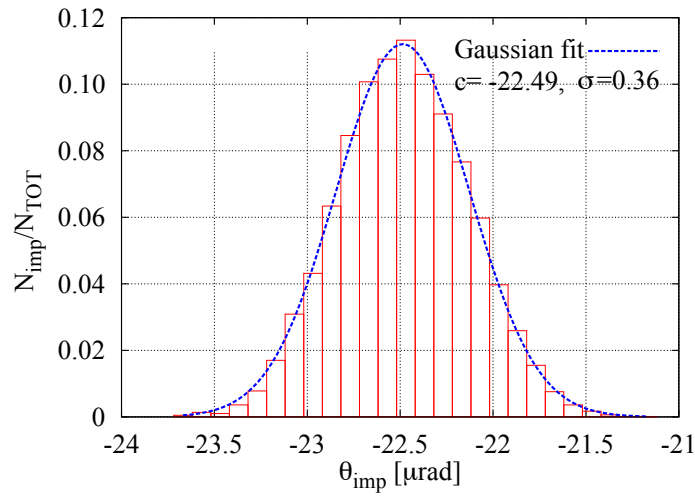
Figure 6.5: Impacting angle distribution on the crystal as simulated assuming a beam lifetime of 0.2h

The angular distribution of the impacting particles is presented in Figure 6.5 for the horizontal case, and a Gaussian fit is applied. The mean angle[2] in the Gaussian fit is $\theta_{imp0} = -22.5$ μrad, with an rms $\sigma_{\theta-imp}$ =0.4 μrad. The channeling acceptance is, for the collision case, about 3.5 μrad. Particles with an angular deviation within $\pm 4\sigma_{\theta-imp}$ from the average are still suitable for channeling, i.e. less than 0.01% of the incoming particles are expected to be incompatible with the channeling process. Given single-passage channeling probabilities of the order of 50-60% [23], the angular distribution is not expected to be a limiting factor, assuming that a good alignment can be achieved.

6.4.2   `SixTrack` simulations

Being the energy stored in the halo 8 orders of magnitude larger than the quench limit, the local losses around the ring must be evaluated very precisely. It is not only necessary to evaluate the escape rate of particles from the collimation system, but it is also critical to understand how losses are distributed along the machine. To run detailed simulations, the software package described in section 3.1.1 is used, and the losses are evaluated along the ring with a longitudinal precision of 10 cm. In this sections we present the results of the tracking simulation, aiming at verifying and evaluating the possible implementation of a crystal in the standard LHC collimation system.

In section 6.4.2.1 all the details about the physical inputs are given, with a particular attention to the description of the collimation insertion where the crystal is mounted, the corresponding beam optics, and the crystal characteristics. The results of the simulations are then presented in section 6.4.2.2 for different crystal bending angles (θ_b), and an optimal bending angle is proposed. The correction to be applied to the simulation results as inferred from the SPS experimental data are detailed in section (6.5).

6.4.2.1   `SixTrack` inputs: optics and collimator database

The simulated case corresponds to the 7 TeV collision optics for beam 1, with the full Phase 1 collimation system plus a crystal installed in the slot of the Phase 4 collimator TCP.A6L7.B1(s coordinate 19795 m from IP1), space presently available at the beginning of the IR7 insertion, next to the primary collimators. The complete

---

[2]The expected angle for on momentum particles just grazing the crystal surface is:

$$n_{cry} \cdot \alpha_x \sqrt{\frac{\varepsilon_x}{\beta_x}} = -22.2 \ \mu\text{rad} \tag{6.6}$$

where $n_{cry} = 6$ is the crystal normalized half aperture (in σ_x units), ε_x is the beam horizontal emittance and α_x, β_x are the twiss parameters at the crystal location: β_x =137.6 m, α_x =1.94.

list of the elements in IR7, with their longitudinal position, material, length and
azimuthal angle (θ_{tilt} in Figure B.1, section 3.1.1.1) can be found in Table 6.3. The
aperture settings for the IR7 elements both for the crystal option and the standard
Phase 1 system [9] are summarized in Table 6.4.

Table 6.3: List of collimators in IR7 and their setting for the simulations

s [m]	name	material	lenght [m]	angle [rad]
19789.18	TCP.D6L7.B1	CFC	0.6	1.571
19791.18	TCP.C6L7.B1	CFC	0.6	0.000
19793.18	TCP.B6L7.B1	CFC	0.6	2.215
19795.18	CRY.A6L7.B1	CRY-Si	$0.0005 \rightarrow 0.01$	0.000/1.571
19832.68	TCSG.A6L7.B1	CFC	1	2.463
19891.91	TCSG.B5L7.B1	CFC	1	2.504
19895.91	TCSG.A5L7.B1	CFC	1	0.710
19917.24	TCSG.D4L7.B1	CFC	1	1.571
19987.16	TCSG.B4L7.B1	CFC	1	0.000
19991.16	TCSG.A4L7.B1	CFC	1	2.349
19995.16	TCSG.A4R7.B1	CFC	1	0.808
20086.42	TCSG.B5R7.B1	CFC	1	2.470
20102.42	TCSG.D5R7.B1	CFC	1	0.897
20106.42	TCSG.E5R7.B1	CFC	1	2.277
20141.02	TCSG.6R7.B1	CFC	1	0.009
20148.09	TCLA.A6R7.B1	W	1	1.571
20178.96	TCLA.B6R7.B1	W	1	0.000
20212.51	TCLA.C6R7.B1	W	1	1.571
20214.51	TCLA.D6R7.B1	W	1	0.000
20231.86	TCLA.A7R7.B1	W	1	0.000

The crystal analyzed is a Si crystal with orientation 110, curvature radius of 50
m and no amorphous layer. Different lengths were scanned, in order to explore a
range of bending angles between 10 and 200 μrad. The values of the main optical
functions at the crystal location are listed in Table 6.5. The horizontal and vertical
beta functions and the phase advance in the IR7 insertion are shown, respectively,
in Figure 6.6 and Figure 6.7.

A perfect machine with the sextupoles switched off was considered. The initial
beam has no energy spread and its average impact parameter on the crystal front
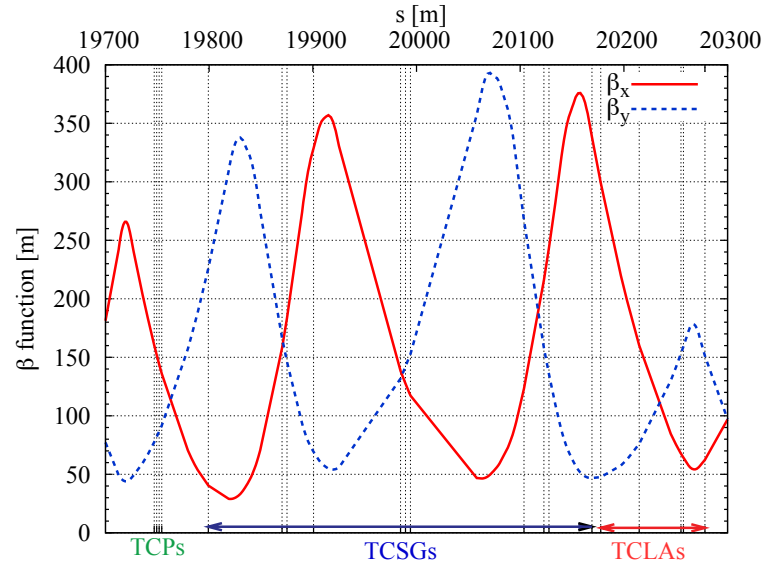
Figure 6.6: Horizontal and vertical beta function versus longitudinal coordinate in IR7 insertion.
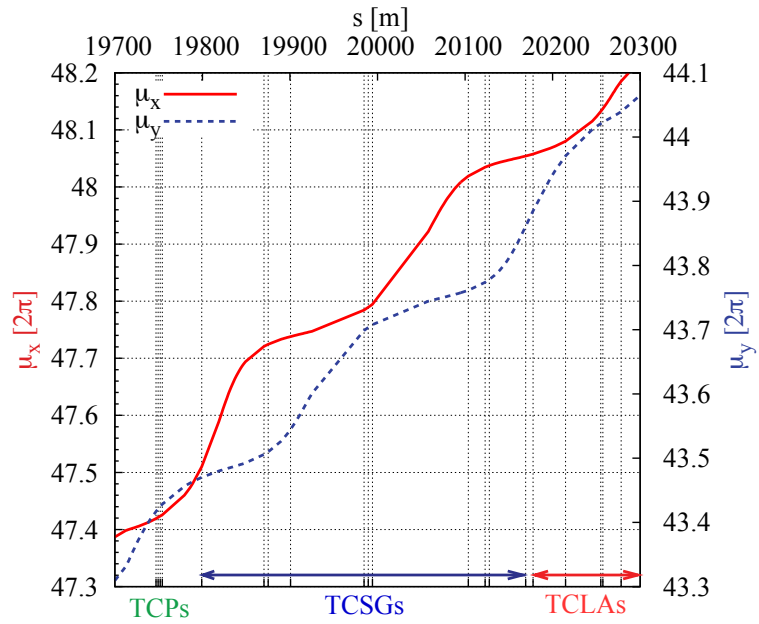
Figure 6.7: Horizontal and vertical phase advance versus longitudinal coordinate in IR7 insertion.

Table 6.4: Aperture settings for the IR7 elements.

element		Half aperture [σ]	
		crystal	Phase 1
CFC primary collimators	(TCP)	6.2	6.0
crystal collimator	(CRY)	6.0	-
secondary collimator	(TCSG)	7.0	7.0
W absorbers	(TCLA)	10.0	10.0

Table 6.5: Values of the horizontal and vertical optical functions at the crystal location, rms beam size σ and beam divergence at 1 σ.

	β [m]	α [-]	D [m]	1σ [μm]	$1\sigma'$ [μrad]
x direction	137.62	1.94	0.59	262	3.7
y direction	90.65	-1.25	0.002	213	2.9

face is $\sim 1\mu$m, in accordance with the studies presented in section 6.4.1.

Since the planar channeling provides a kick in one transverse direction, while acting as a drift in the other direction, the horizontal and vertical halo were studied indipendently, with a purely horizontal channeling kick applied for the horizontal halo, and a purely vertical one for the vertical halo. Each simulation has been performed by tracking 8 million particles for 500 turns. The results are compared with those for the standard Phase 1 system, having the same optics and same initial conditions.

6.4.2.2   Simulation results: beam loss maps and crystal bending angle optimization

In order to understand how losses are distributed along the machine, the local cleaning inefficiency is evaluated with a 10 cm binning along the 27 km ring, as described in section 3.1.1. The plot of the local cleaning inefficiency versus the longitudinal position is usually called loss map. In this section the loss maps in case of crystal and standard collimation system are compared, and an optimization of the bending angle for the crystal collimation option is presented.

Examples of loss maps for the horizontal case, without and with crystal collimation, are presented respectively in pictures 6.8 and 6.9 for the IR7-dispersion
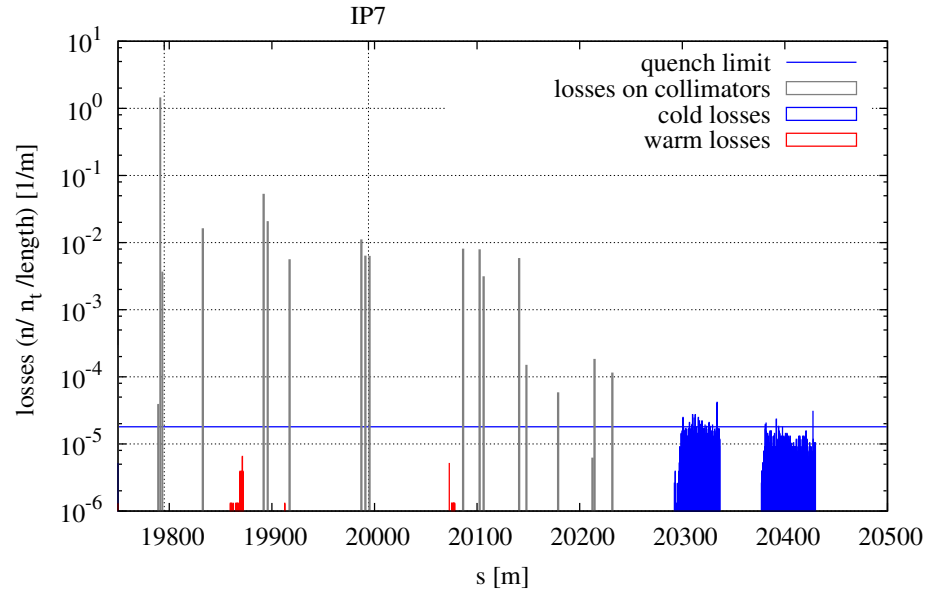
Figure 6.8: Loss map in case of standard collimation, horizontal halo, Phase 1. Zoom in the IR7 and dispersion suppression region, for perfect setup.
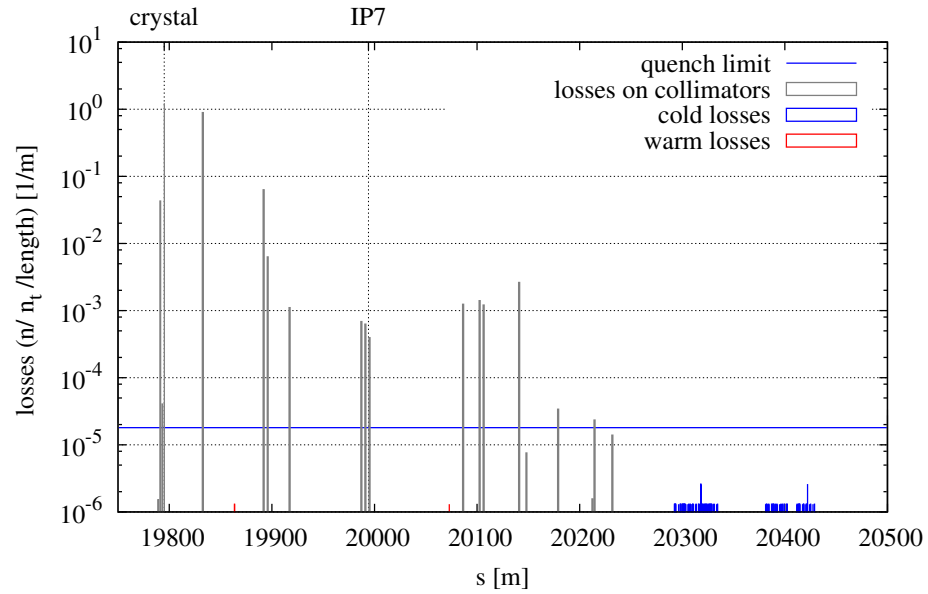
Figure 6.9: Loss map in case of crystal collimation, 40 μrad, channeling alignment, horizontal orientation. Zoom in the IR7 and dispersion suppression region, for perfect setup.

suppressor region: losses outside of this region are negligible. The vertical case is analogous. Figure 6.9 refers to the crystal option, with a crystal in perfect channeling position, bending angle of 40 μrad, which shows a massive decrease for cold losses: the cleaning inefficiency peak values, in the two cases, go from $4.2 \cdot 10^{-5}$ to $2.6 \cdot 10^{-6}$, showing about a factor 15 improvement. Figures 6.10 and 6.11 show the dependence of the local cleaning inefficiency peak value from the crystal orientation in the cold region, together with the maximum power load released in the IR7 warm insertion, along a length of 10 cm.
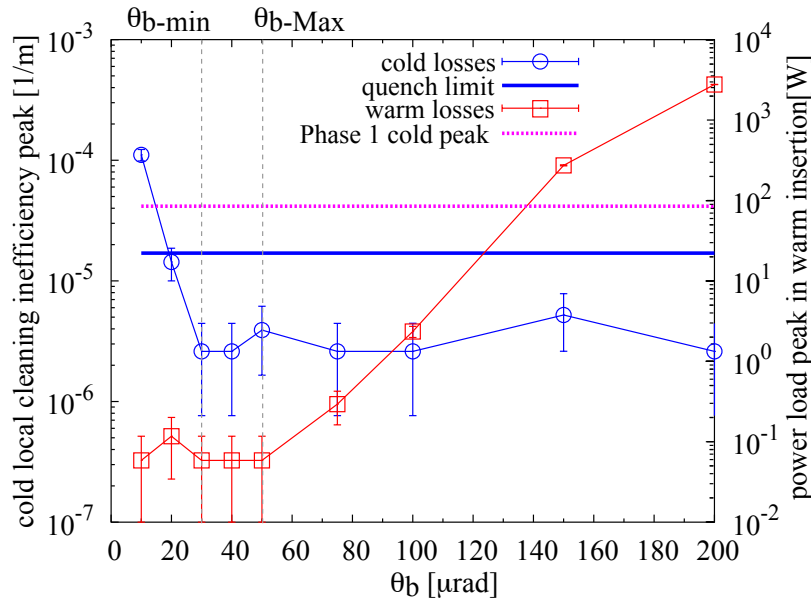
Figure 6.10: Maximum local cleaning inefficiency for different bending angles. The crystal is perfectly aligned in channeling position, horizontal case.

It is interesting to notice how these two variables naturally define an optimal range for the crystal bending angle:

1. For channeling kicks beyond a critical value θ_{b-min} the maximum local inefficiency in cold regions does not improve; this defines the minimum bending angle for maximum cleaning inefficiency.

2. For channeling kicks up to a critical value θ_{b-Max} the loss peak in the warm insertion is stable, while it increases for large values; this defines the maximum bending angle for minimum radiation load to warm elements.

The angles θ_{b-min} and θ_{b-Max} (whose values are listed in Table 6.6) define the range of optimal bending angles.
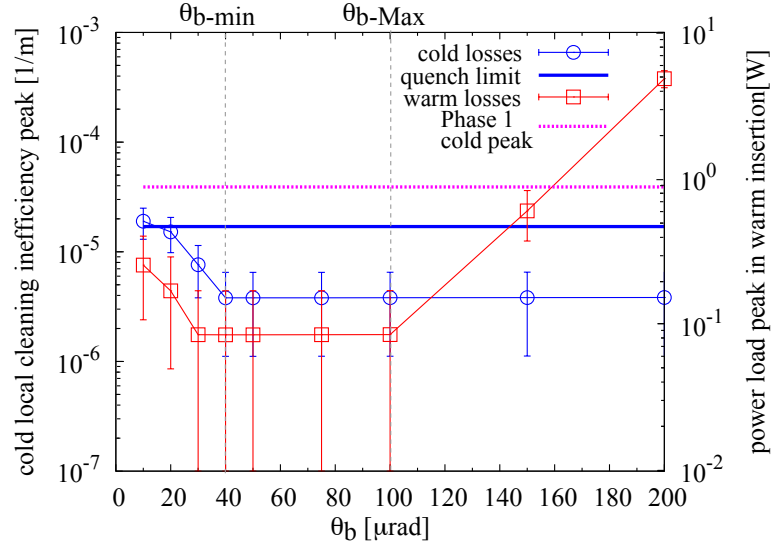
Figure 6.11: Maximum local cleaning inefficiency for different bending angles. The crystal is perfectly aligned in channeling position, vertical case.

Table 6.6: Range for an optimal bending angle.

case	θ_{b-min} [μrad]	θ_{b-Max} [μrad]
horizontal	30	50
vertical	40	100

It is important to remember that the simulation results do no take into account the showers generated in the collimators; it is assumed that, for inelastic interactions, all the energy associated to the particle is absorbed at the interaction location. This assumption, while it is a good approximation in case of metallic collimators, cannot be considered realistic for our graphite collimators. Even if a proton crosses the whole length of the collimator, the average lost energy is about 0.5 percent of the impacting one [?]; the rest is dispersed in showers. It is therefore important to understand how the inelastic losses redistribute on collimators of the IR7 insertion for the different scenarios. In Table 6.7 the collimator where the highest losses are concentrated are listed, with the relative number of inelastic interactions and the average impact parameter depending on the bending angle.

It is found that, in 6 out of 7 cases within the optimal channeling range, the largest part of the primary halo is stopped at the first secondary collimator (TCSG.A6L7.B1).

Table 6.7: Number of inelastic interactions on the highest loaded secondary collimator versus the bending angle θ_b. The name, longitudinal position and average impact parameter are also shown.

$\theta_\mathbf{b}$ [μrad]	name	position [m]	$\frac{\mathbf{N_{abs}}}{\mathbf{N_{tot}}}$	b [mm]
	horizontal case			
010	TCSG.6R7.B1	345.84	0.912	4.024
020	TCSG.B5R7.B1	291.24	0.388	0.016
030	TCSG.B5L7.B1	96.73	0.907	1.005
040	TCSG.A6L7.B1	37.50	0.893	0.066
050	TCSG.A6L7.B1	37.50	0.889	0.352
075	TCSG.A6L7.B1	37.50	0.895	1.065
100	TCSG.A6L7.B1	37.50	0.893	1.773
150	TCSG.A6L7.B1	37.50	0.886	3.171
200	TCSG.A6L7.B1	37.50	0.880	4.552
	vertical case			
010	TCSG.D4L7.B1	122.06	0.777	0.081
020	TCSG.A6L7.B1	37.50	0.783	0.021
030	TCSG.A6L7.B1	37.50	0.909	0.245
040	TCSG.A6L7.B1	37.50	0.907	0.475
050	TCSG.A6L7.B1	37.50	0.906	0.703
075	TCSG.A6L7.B1	37.50	0.903	1.267
100	TCSG.A6L7.B1	37.50	0.900	1.825
150	TCSG.A6L7.B1	37.50	0.893	2.922
200	TCSG.A6L7.B1	37.50	0.887	4.003

The rate of inelastic interactions is about 90%, and decreases for larger bending angles (while the warm losses increase). This means that the main shower source is shifted downstream by at least 37.5 m with respect to the Phase 1 system, where collimators which sustain the highest number of hits are the primary ones. A detailed evaluation of the energy deposition must be done with the use of dedicated programs, in order to check that the downstream equipment (quadrupole, electronics in the UJ76 insertions, ...) is not affected. It is also highly likely that the CFC collimator must be replaced by a dedicated halo dump. Checks remain to be done for injection and ramp energies.

6.5 Impact of experimental tests on simulation predictions

The LHC simulations for a crystal-based collimation system promise a consistent increase of cleaning efficiency (a factor of 15) for far away losses. However the simulation predictions should always be verified by experimental data: it has been presented that, for SPS, analogous simulations were predicting an improvement factor of about 16 for the channesling case, while the BLMs measurements did not detect an improvement factor better than 1.3 (Section 5.3.4). In this section we present a short summary of the experimental results presented in this thesis, which represent, so far, the state of the art of the crystal collimation experiments.

Two experiments, inserted in circular machines, have been considered: the UA9 (in the SPS) and T980 (Tevatron). The important results for collimation purposes are the crystal channeling efficiency in multi-turn mode and the achievable reduction in losses along the ring. These experimental results are here commented and compared, when possible, to the simulations.

The efficiency, average kick and rms angular spread of the channeling process were measured using the collimator scan technique: a summary of the results can be found in Table 6.8.

Table 6.8: Equivalent kick θ_{ch}, rms angular spread σ_{ch} and multi-turn channeling efficiency η_{ch} for measured and simulated collimator scans.

Experiment (Crystal)	θ_{ch}^{exp} [μrad]	σ_{ch}^{exp} [μrad]	η_{ch}^{exp} [%]	θ_{ch}^{sim} [μrad]	σ_{ch}^{sim} [μrad]	η_{ch}^{sim} [%]
T980	304±20	15±1	0.61±0.11	-	-	-
UA9:						
Crystal1	173±1	17±1	75±4	150	13	92
	199±1	40±1	65±3	150	13	92
	198±1	42±1	64±3	150	13	92
Crystal2	165±1	21±1	85±5	150	13	92

For the T980 experiment only the best efficiency result has been listed in Table 6.8: varying crystal orientations, a wide spread in results (both efficiency, rms spread and average kick) have been measured. The measured angular dependence has been explained as an effect of the large crystal miscut angle: once an orientation is fixed, the results present a good reproducibility.

On the other hand, in the same Table all the results for the UA9 experiments are included : some hypothesis have been advanced to account for the wide spread found in the experimental results and for the differences with the simulations, but, given the limited reproducibility of the goniometers, an experimental confirmation is not available yet. At the moment one can only state that the best channeling multi turn efficiency ever measured in $85 \pm 5\%$ for Crystal 2 (UA9 experiment), to be compared with a 92% efficiency predicted by simulations. It is important to remember that, with the collimator scan, a minimum detectable kick θ_{kick}^{COLL} exists: our efficiency calculation is based on the assumption that only 5% of the particles receiving kicks $\theta < \theta_{kick}^{COLL}$ are lost in the machine aperture (value taken from simulations). If the actual population of particles receiving a small angular deflection is higher than expected, then the number of lost particle would increase and the measured efficiency would proportionally be scaled down.

Regarding far-away losses, unfortunately only one measurement is available. This has been performed in the SPS, with the Crystal 1, by inserting the crystal deep into the primary halo and switching fast from amorphous to channeling orientation. A maximum loss reduction of a factor 1.3 has been measured outside of the experimental insertion, while a factor 16 was expected by the simulations.

The experimental results of UA9, both regarding the multi turn efficiency and the far away losses, could be reproduced by adding an amorphous layer of 250 μm to the "perfect crystal" model. If this results are really depending on the crystal quality (as simulations seem to suggest), the LHC predictions should be equally rescaled of about a factor 10, and an improvement factor of maximum 1.5-2 could be expected. Further and more precise measurements in the SPS next summer (2010) are expected to validate the presented data and prove (or disprove) the hypothesis here discussed.

6.6   Conclusions

One of the limiting factor for crystal collimation are the tight alignment requirements, together with the fact that, in a location where the twiss parameter α is different from zero, the divergence of the beam halo changes during the energy ramp (see [5] for details). This makes the use of a crystal possible only during stable physics runs. It follows that the crystal must be a complement and not a replacement of the existent collimation system, which in principle should be able to take over in case of crystal misalignment/misfunctioning. A crystal collimation solution for the LHC has been worked out, showing that, according to simulations, a perfect crystal in channeling mode can increase the cleaning efficiency by about a factor of 10-15 with respect to the standard Phase 1 collimation system. This solution is compatible with the present layout in IR7. On the contrary, simulations of crystals

in volume reflection mode did not show any improvement.

Optimal bending angles have been found for horizontal and vertical cleaning. Fundamental problems (like the heat load in the secondary collimator which is directly hit by the channeled beam) have not been addressed. The main particle shower source is shifted by about 40 m downstream.

In the light of the experimental result analysis, it is clear that the performance predicted by simulation are still to be proven, and that the predicted improvement factor could be scaled down even by a factor 10. Further experimental results are expected, in summer 2010, to give a better insight on the possible crystal performances.

Conclusions

This PHD thesis aims at giving a first performance evaluation of a possible crystal-enhanced collimation system for the Large Hadron Collider (LHC, CERN, Geneva, Switzerland) by analytical, experimental and simulation investigations.

At first, analytical studies of a crystal inserted in a circular machine has been performed. Since in approximation of zero diffusion rate the particles just "graze" the primary collimator surface, two correlated effects have been treated:

- the angular distribution of grazing particles and its comparison with the crystal channeling acceptance. For assessing the role of synchrotron motion on the expected angular spread a new optical function, g, has been introduced [12] and used to qualify possible crystal collimator locations.

- the spatial distribution of the grazing particles, which makes the edge effect (such as amorphous layer or miscut angle) extremely relevant. The consequences of a large miscut angle has been studied in details for the first time.

New tools have also been established for simulations and experimental measurements. On the simulation side, a code describing the crystal has been introduced in the "state-of-the-art" tracking code currently used at CERN for collimation studies. The crystal code was adapted and further developed to include the edge effects: amorphous layer and miscut angle. A separate, simplified routine was written to give a first estimation of the initial spatial and angular particle distribution on the crystal surface, when using realistic diffusion values. The results were used as an input for the tracking code.

On the experimental side, an innovative method has been developed to calculate the multi-turn channeling efficiency, i.e. the ratio of channeled particles with respect to the total number of particles in the primary beam halo. The method consists in gradually cutting the secondary halo particles with a collimator jaw downstream the crystal, and detecting the generated loss rates. For large enough kicks, it allows the reconstruction of the profile of the particles directly scattered by the crystal. The method is however limited:

- Since the phase advance is larger than zero between crystal and collimator, a kick larger than zero is necessary for being collected at the collimator location

at the first turn after the interaction with the crystal. This is true even when the collimator normalized aperture is the same as the crystal one. For "small enough" kicks the particles can be detected only in multi-turn mode.

- The data normalization relies on the assumption that the collimator is capable of collecting, in multi turn mode, all the particles deviated by the crystal. In reality a fraction of the particles receiving a "small enough" kick can be lost in the machine aperture: a leakage factor is therefore expected (we use a 5% value, as predicted by simulations). If, for some reason (amorphous layer, miscut angle, increase dechanneling population, etc...) the "small angle" particle population is higher than expected, the obtained efficiency must be scaled down proportionally.

The collimator scan method has been applied, as main tool for calculating multi-turn channeling efficiency, in two crystal collimation experiments: the T980 (at Tevatron, winter 2008-2009) and the UA9 (at SPS, summer 2009). Efficiency values between 10% and 60% (for the T980 experiment) and between 56% and 85% (for the UA9 experiment) have been found, to be compared with the 92% efficiency predicted by simulations (only for the UA9 experiment). The efficiency results are not the only discrepancy with the simulation results: also the measured channeling angles and rms widths are different from the expected values. These features were successfully explained, in the T980 case, by the large miscut angle value of the "old" crystal installed in the Tevatron [15]. On the other hand, two new generation crystals produced with advanced manufacturing techniques were installed in the SPS: in this case the differences with simulations could be explained by the misalignment of the crystal [82] and/or by reduced channeling efficiency at the crystal edge. In this thesis, the second the reduced channeling efficiency has been investigated, and the observed features of the UA9 collimator scans could be reproduced by adding, to the perfect crystal model, an amorphous layer of 250 μrad.

Another important results for collimation studies is the reduction in far-away losses when using the crystal in channeling mode. This could be measured only once in the SPS, and a maximum measured reduction of a factor 1.3 was found, while the simulations were predicting a factor 16. Once again, realistic value could be obtained by adding an amorphous layer to the perfect simulated crystal.

The SPS experimental results and the cross-check with dedicated simulations are the foundations of a critical prediction for the LHC. In this thesis a first optimized crystal collimation layout for the LHC was worked out. According to simulations, a factor 15 decrease in far away losses (cold regions) is expected for an optimized crystal-based collimation system, in comparison with the Phase 1 collimation system. However the experimental results in SPS demonstrated that the simulation of a perfect crystal could not realistically reproduce the experimental data: if we

base our expectations on the SPS experiment, the improvement factor of 15 could be lowered to a value not higher than 1.5-2, which is not as beneficial as expected or required for the phase 2 of the LHC collimation system. Moreover the performed simulations should be finalized by secondary showers calculation, to understand how the inelastic losses redistribute on collimators of the IR7 insertion for the different scenarios, and by mechanical calculations to verify that the lost power in secondary collimators can be safely managed.

Further work is needed to better understand the feasibility of a crystal-based collimation system in the LHC. First of all, a clear, reproducible measurements of the multi turn channeling efficiency and of far-away loss reduction are necessary to corroborate our simulations and validate our predictions for the LHC. New experiments in the SPS will follow in summer 2010 for this purpose.

Moreover, some technical limitation must still be overcome. Given the tight angular acceptance constraints, it was seen that a good goniometer is essential for the success of a crystal collimation experiment. While the Tevatron goniometer allowed to precisely orient the crystal (a control within 2 μrad was achieved), the UA9 experiment suffered from the poor instrument reproducibility. It is important to stress that, not even in the Tevatron experiment, the required angular stability over long time intervals have been achieved. Considering that the channeling angular acceptance scales with $1/\sqrt{E}$, where E is the beam energy, this could be an important technological problem for applications at the LHC energies, where the crystal orientation should be realistically kept within 1-2 μrad for a time comparable with the beam lifetime (e.g. many hours).

At last, a conceptual proposal for improving the collimator scan method in future experiments can be made: in order to minimize the angle for which the collimator is "blind", a telescopic system could be implemented:

- a first collimator should be positioned at large beta location and optimal phase advance with respect to the channeling kick , to optimize the available resolution of particle distribution for large kicks;

- a second collimator, close to 180 degrees phase shift, should be used to collect the fraction of secondary halo receiving crystal kicks "small enough" to escape the first collimator.

In this way, the normalization of the collimator scan data would be checked, and the efficiency values would be more reliable.

Appendix A

The miscut angle theory

In this section the influence of a positive miscut angle on the particle-crystal interaction is analyzed. It will be demonstrated that the channeling mode is not limited to a specific particle-crystal orientation, but it is possible to have channeling in an angular range which correspond to the bending angle of the crystal. The dependency of channeling angle on crystal orientation is deduced.

In the following we consider a crystal with length l_{cry}, bending angle θ_b and positive miscut angle θ_{mc}. As shown in Figure A.1, with the coordinate s_{cry} we refer to the curvilinear coordinate which follows the lateral face of the crystal, while the direction perpendicular to the entrance face is t. The relative angle between the direction t and the particle direction is called θ. With $\theta_{pl}(s_{cry})$ we indicate the angle between the direction t and the crystalline planes. At the entrance face of the crystal, by definition, we have that $\theta_{pl}(0) = \theta_{mc}$, while at the exit face $\theta_{pl}(l_{cry}) = \theta_b + \theta_{mc}$.

Table A.1: A summary of the symbols which are used in this section.

|	
l_{cry}	crystal length
s_{cry}	curvilinear coordinate which follows the lateral face of the crystal
s_0	s_{cry} coordinate of the first impact point
t	direction perpendicular to the entrance face
θ_b	crystal bending angle
θ_{mc}	crystal miscut angle
θ	angle between the direction t and the beam direction
$\theta_{pl}(s_{cry})$	angle between the direction t and the crystalline planes at the coordinate s_{cry}
$\delta\theta_{imp}(s_{cry})$	angle between the crystalline planes and the beam direction at the coordinate s_{cry}; $\delta\theta_{imp}(s_{cry}) = \theta - \theta_{pl}(s_{cry})$
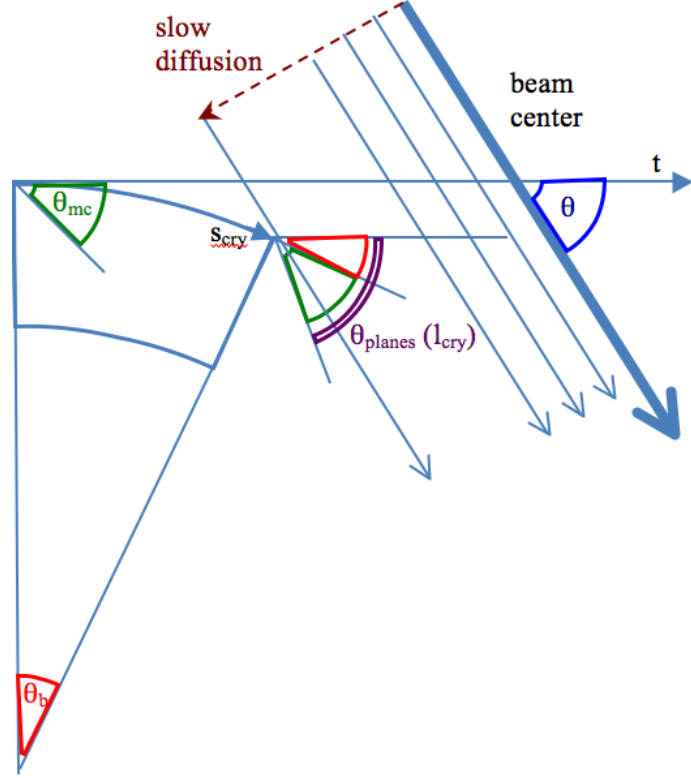
Figure A.1:   Zero   divergence
beam impacting on the crystal
surface.   The bending angle θ_b,
the miscut angle θ_{mc} and the im-
pacting angle θ are shown.

Assuming a zero divergence beam in zero-limit diffusion regime implies that
the particles would always hit first the point of the crystal which is closer to the
beam center. With s_0 we indicate the s_{cry} coordinate of the first impact point.
The angle between the crystalline planes and the incoming particles at s_0 is named
$\delta\theta_{imp}(s_0) = \theta - \theta_{pl}(s_0)$.

A summary of the symbols which are used in this section is given, for conve-
nience, in Table A.

In the following different particle orientations are considered, and the effect of
the miscut angle is derived. We first consider two limit cases, i.e. when the particles
are aligned with the crystalline planes at $s_{cry} = 0$ and $s_{cry} = l_{cry}$, the intermediate
cases are then deduced.

Limit case 1: $\theta = \theta_{mc}$

At first we consider the case when $\theta = \theta_{mc}$, i.e. when the particle velocity is
aligned with the planes at the entrance face of the crystal ($s_{cry} = 0$). This is the
orientation that is needed in order to recover the channeling alignment at the en-
trance face of the crystal, as already discussed in the previous section (see Figure

2.10, case 3).

Figure A.2: Positive miscut angle, beam aligned with the crystaline planes at the entrance face of the crystal. In the illustrated case $\theta_b > \theta_{mc}$.

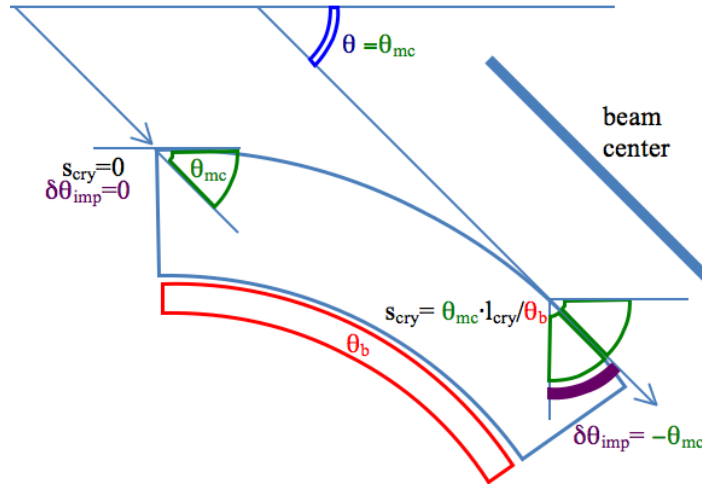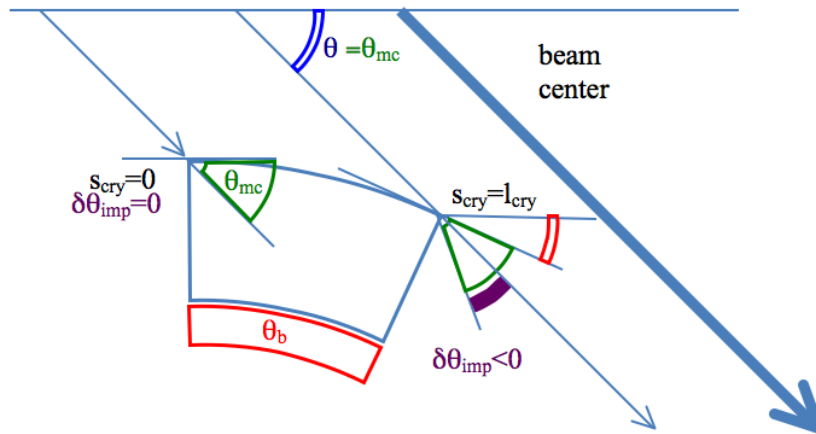
Figure A.3: Positive miscut angle, beam aligned with the crystaline planes at the entrance face of the crystal. In the illustrated case $\theta_b < \theta_{mc}$.

For calculating the first impact point s_0 and the corresponding relative alignment between the crystalline planes and the incoming particles $\delta\theta_{imp}(s_0)$, two cases must be distinguished:

- if the bending angle θ_b is larger than the miscut angle θ_{mc}, the first impact point corresponds to the tangency point $(s_0 = \theta_{mc} \cdot \frac{l_{cry}}{\theta_b})$. In this case the angle between the particle velocity and the crystal planes is $\delta\theta_{imp}(s_0) = \theta - \theta_{pl}(s_0) = \theta - 2\theta_{mc} = -\theta_{mc}$. This case is shown in Figure A.2.

- if the bending angle θ_b is smaller than the miscut angle θ_{mc}, the tangency point is outside of the crystal: in this case the particle simply hits the end of the crystal, that is $s_0 = l_{cry}$. Since $\theta_{pl}(s_0) = \theta_b + \theta_{mc}$, the relative angle between the particles and the crystal planes at the impact point is equal to $\delta\theta_{imp}(l_{cry}) = \theta - \theta_{pl}(l_{cry}) = -\theta_b$. This case is shown in Figure A.3.

In both cases, if the absolute value of $\delta\theta_{imp}(s_0)$ is larger than the half channeling acceptance angle (about the critical angle of the crystal θ_c), so the particles cannot channel in the point where they impact first. In order to channel the particles must overcome the layer where they are misaligned with the crystal planes, and where the interaction are amorphous-like. The thickness of such amorphous layer will be calculated when considering the more general case (see equation A.5).

Limit case 2: $\theta = \theta_{mc} + \theta_b$

Let's consider the other limit case, i.e. when the particles are aligned with the crystal planes at $s = l_{cry}$, that means $\theta = \theta_{pl}(l_{cry}) = \theta_{mc} + \theta_b$. The situation is illustrated in Figure A.4.
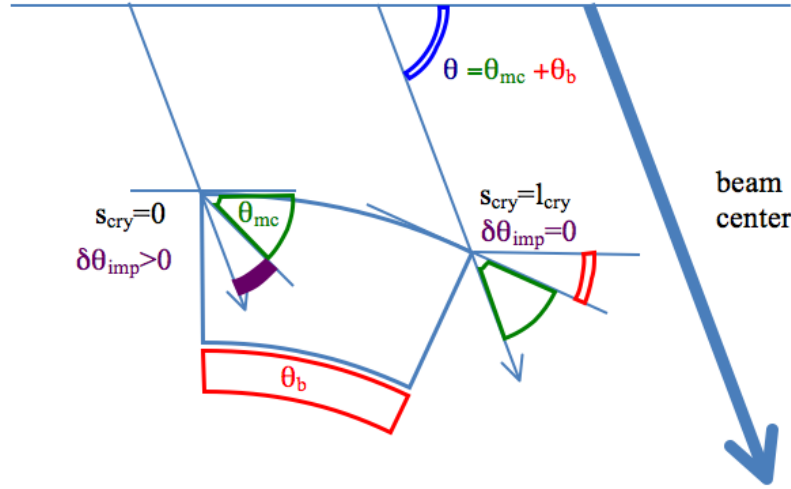

Figure A.4: Positive miscut angle, beam aligned with the crystaline planes at the end of the crystal. In the illustrated case $\theta_b < \theta_{mc}$.

In this case the first region of the crystal which is seen by the particles is always its end, i.e. $s_0 = l_{cry}$, and therefore $\theta_{pl}(l_{cry}) = 0$: the particles are, in principle,

aligned for channeling. However, since the remaining length of the crystal is zero, the channeling angle is zero as well.
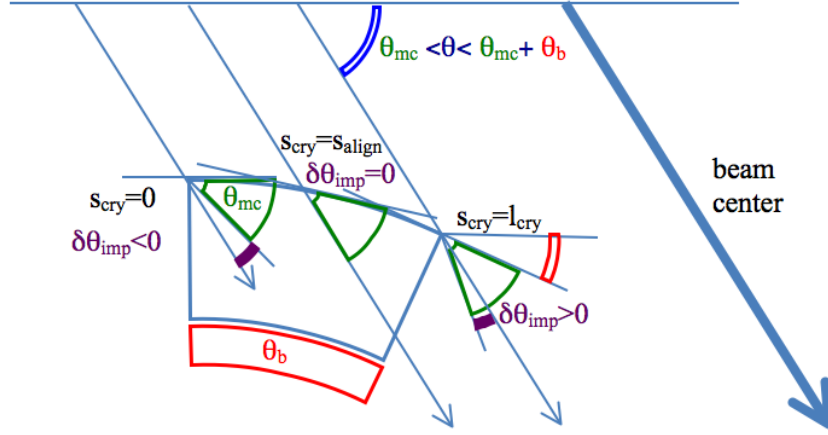

Figure A.5: Relative alignment $\delta\theta_{imp}$ in case of $0 < \theta_{tilt} < \theta_b$, for the case $\theta_b < \theta$.

General case: $\theta_{mc} < \theta < \theta_{mc} + \theta_b$

We have analyzed the two limit cases: particles aligned at the beginning ($\theta = \theta_{mc}$) or at the end of the crystal ($\theta = \theta_{mc} + \theta_b$). Now the more general case is treated, i.e. an impacting angle $\theta = \theta_{mc} + \theta_{tilt}$, with $0 < \theta_{tilt} < \theta_b$ (see Figure A.5). The first impact point is, in this case:

- if $\theta_b > \theta$, the first impact point is $s_0 = \theta \cdot \frac{l_{cry}}{\theta_b}$. In this case $\delta\theta_{imp}(s_0) = -\theta_{mc}$, by definition of miscut angle.

- if $\theta_b < \theta$ the particle first hits the end of the crystal ($s_0 = l_{cry}$). In this case $\delta\theta_{imp} = \theta - \theta_{pl}(s_0) = \theta_{tilt} - \theta_b$.

In both cases there is a negative misalignment $\delta\theta_{imp}(s_0)$ at the impact point s_0. On the other hand, at the entrance face, there would be a positive misalignment $\delta\theta_{imp}(0) = \theta - \theta_{mc} = \theta_{tilt}$. Being the physical function $\delta\theta_{imp}(s_{cry})$ continuous, in between the entrance face ($s_{cry} = 0$) and the first impact point s_0 of the crystal there must be a point s_{align} where $\delta\theta_{imp}(s_{align}) = 0$ (i.e. the particles are aligned with the crystal planes). The coordinate s_{align} depends on the incoming angle (θ), and with some trigonometry it can be derived its value:

$$s_{align}(\theta) = \frac{\theta_{tilt}}{\theta_b} \cdot l_{cry} = \frac{(\theta - \theta_{mc})}{\theta_b} \cdot l_{cry} \qquad (A.1)$$

It is true that the channeling angular acceptance $2\theta_c$ is a finite quantity larger than zero. The particles can therefore channel not only at the single point s_{align}, but in the whole region where $\delta\theta_{imp}$ is smaller than the critical angle θ_c. In terms of the curvilinear coordinate s_{cry}, the particle will channel in a region whose width Δs is:

$$\Delta s = s_{al}(\theta + \theta_c) - s_{al}(\theta - \theta_c) = \frac{2\theta_{crit}}{\theta_b} \cdot l_{cry} \tag{A.2}$$

and the thickness of this region in the direction perpendicular to the particle velocity (i.e. the thickness of the impact parameter) is $\Delta s \cdot \sin\theta_{mis}$.

It was demonstrated that, if the particle can reach the appropriate region in the crystal, it can channel. However the channeling kick given by the crystal is smaller than the nominal kick θ_b, because the crossed crystal length won't be the total length l_{cry} but a reduced length $l_{cry} - s_{align}$, where s_{align} depends on θ. The effective average channeling kick is:

$$\theta_{chan}(\theta) = \frac{\theta_b}{l_{cry}} \cdot (l_{cry} - s_{align}(\theta)) = \theta_b - \theta_{tilt} \tag{A.3}$$
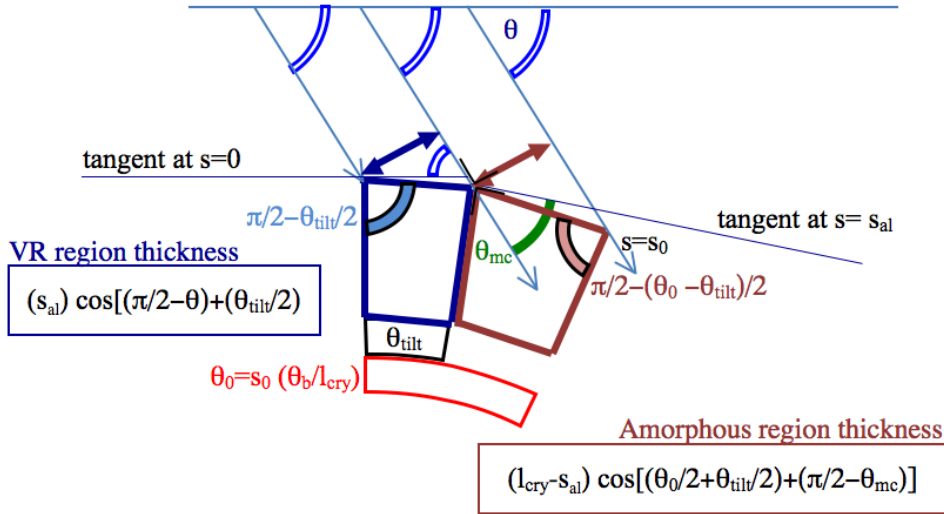
Figure A.6: Approximation used to calculate the thickness of the volume reflection and the amorphous regions.

The interactions between particles and crystal outside the channeling region depends on the impacting point. If a particle hits the crystal between the channeling region and the end of the crystal ($s_0 < s_{cry} < l_{cry}$), where $\delta\theta_{imp} > 0$, then its orientation is such to have an amorphous-like interaction; on the other hand, if the impacting point is between the channeling region and the entrance face of the crystal

$(0 < s_{cry} < s_0)$, the relative orientation $\delta\theta_{imp}$ is negative and therefore associated to the volume reflection process. In order to evaluate the thicknesses of the amorphous and volume reflection region, again a bit of trigonometry is needed. Using the straight-pieces approximation of the crystal in Figure A.6 the amorphous and volume reflection layer thicknesses are found to be:

$$x_{am} = (s_0 - s_{al}(\theta)) \cdot \sin\left(\theta_{mc} - \theta_0/2 + \theta_{tilt}/2\right) \tag{A.4}$$

$$x_{VR} = s_{al}(\theta) \cdot \sin\left(\theta - \theta_{tilt}/2\right) \tag{A.5}$$

where θ_0 is the angle associated to the first impact point s_0, e.g. $\theta_0 = s_0 \cdot (\theta_b/l_{cry})$.

Appendix B

The collimator database

In this appendix we give a detailed description of the format of the collimator database file, and of the modifications introduced for describing a crystal collimator.
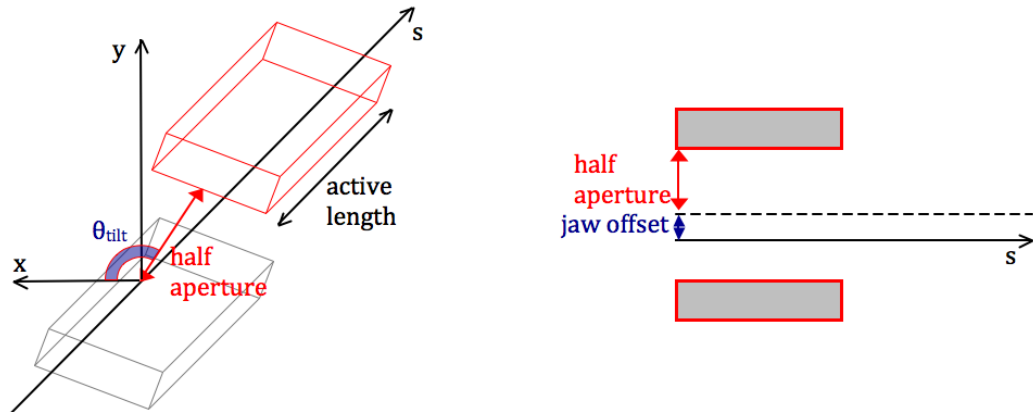
Figure B.1: Sketch of the collimator where the main characteristics, specified in the database, are indicated.

For an amorphous collimator, the specified parameters are:

1-2 Collimator name (which should match with the name specified in the *fort.2* file)

3 Half aperture in sigma units (red arrow in Figure B.1).

4 Jaw material. The scattering routine of `SixTrack` allows to treat graphite, copper, tungsten, aluminum, beryllium and lead. The case of vacuum (simple drift) and black absorber can be treated as well.

5   Jaw active length [m] (Figure B.1).

6   Azimuthal angle [rad] of collimator jaws (θ_{tilt} in Figure B.1).

7   Transverse collimator gap offset [m] (Figure B.1).

8-9 Design horizontal and vertical β-function [m] at the collimator location.

where the bold number corresponds to the line number in each collimator entry.

For crystal collimators, the code has been adapted to read the additional data which are needed to characterize them:

1-2   Crystal collimator name (which should match with the name specified in the *fort.2* file)

3   Normalized aperture in sigma units.

4   Crystal material. The crystal routine of `SixTrack` allows to treat Silicon, Tungsten, Carbon or Germanium crystals.

5   Crystal total length [m], considered as the length of the curved surface of the crystal.

6   Azimuthal angle rad of crystal (θ_{tilt} in picture 3.3/1). For the moment only purely horizontal or vertical crystal are treated in the code ($\theta_{tilt} = 0$ or $\theta_{tilt} = \pi/2$ respectively).

7   Transverse collimator gap offset [m].

8   Bending radius [m].

9-10 Transverse x-z dimension [m] (see picture 3.3/2).

11   Thickness of the amorphous layer at the crystal edge [m].

12   Orientation of the crystal planes for silicon crystals (integer, can be 1 for the Si 110, or 2 for the Si 111). This parameter is ineffective in case of non-Si crystals.

11   Crystal tilt [rad] (cry$_{tilt}$ in picture 3.3).

12   Miscut angle [rad] (see paragraph 3.1.2.3 for a complete description)

13-14 Design horizontal and vertical β-function [m] at the collimator location

Appendix C

Skew orientation for standard and crystal collimators

In this appendix we define how the aperture for a skew collimator is found, and why implementing a skew crystal collimator would require a new degree of freedom in the crystal holder.

For a standard collimator the azimuthal angle θ_{tilt} is defined as the angle between the horizontal axis x and the line perpendicular to the jaw faces, in clockwise direction (see picture C.1).
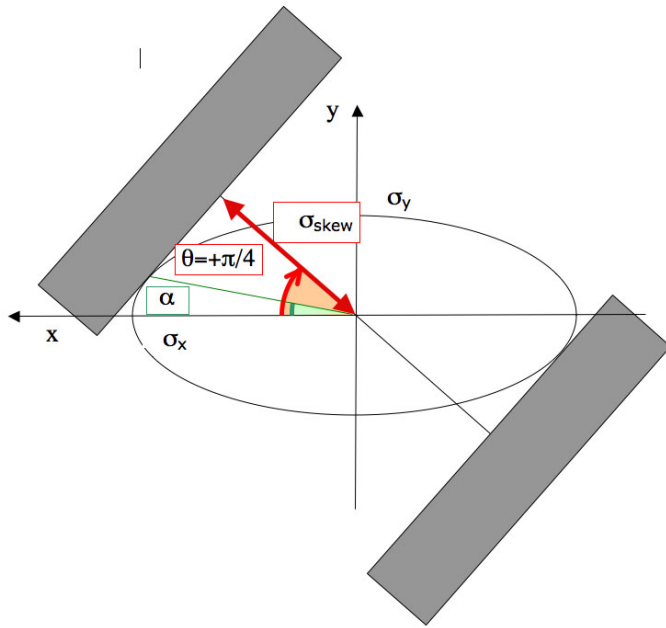
Figure C.1: Sketch of a skew collimator. In this picture an hypothetic azimuthal angle of $\theta_{tilt} = \pi/4$ is chosen. It is clear from the image that the angle α which corresponds to the tangency point is different from $\pi/4$, and depends on the shape of the beam ellipse.

In the transverse space x-y, the equation of 1-σ ellipse in the x$-$y plane is:

$$\frac{x^2}{\sigma_x^2} + \frac{y^2}{\sigma_y^2} = 1 \tag{C.1}$$

where $\sigma_{x,y}$ are, respectively, the rms dimensions of the beam in the x,y plane, and in general $\sigma_x \neq \sigma_y$. Here the collimator jaw is represented by a line:

$$y = -\frac{1}{\tan \theta_{tilt}} \cdot x + q \tag{C.2}$$

where the parameter q is not yet defined. A collimator oriented with an angle θ_{tilt} is tangent at the 1σ ellipse in the point (x_0, y_0) with, in general, $\alpha = \frac{y_0}{x_0} \neq \theta_{tilt}$. For calculating (x_0, y_0), the system of equations C.1 and C.2 must be solved:

$$\begin{cases} \frac{x^2}{\sigma_x^2} + \frac{y^2}{\sigma_y^2} = 1 \\ y(x) = -\frac{1}{\tan \theta_{tilt}} \cdot x + q \end{cases} \tag{C.3}$$

and tangency condition ($\Delta = 0$) must be imposed. The value of q is then deduced:

$$q = \pm\sqrt{\sigma_y^2 + \sigma_x^2 \cdot \frac{1}{\tan^2 \theta_{tilt}}} \tag{C.4}$$

The half gap of the collimator is called σ_{skew} in the code (see Figure C.1), and it can be found by solving the system:

$$\begin{cases} y(x) = -\frac{1}{\tan \theta_{tilt}} \cdot x + \sqrt{\sigma_y^2 - \sigma_x^2 \cdot \frac{1}{\tan \theta_{tilt}}} \\ y(x) = \tan \theta_{tilt} \cdot x \end{cases} \tag{C.5}$$

where the second equation refers to the line perpendicular to the collimator jaw, and passing from the origin. The solution (x_1, y_1) of the system is

$$(x_1, y_1) = \left(\sin \theta_{tilt} \cos \theta_{tilt} \cdot \sqrt{\sigma_y^2 - \sigma_x^2 \cdot \frac{1}{\tan \theta_{tilt}}}, \sin^2 \theta_{tilt} \cdot \sqrt{\sigma_y^2 - \sigma_x^2 \cdot \frac{1}{\tan \theta_{tilt}}} \right) \tag{C.6}$$

so the half aperture is:

$$\sigma_{skew} = \sqrt{x_1^2 + y_1^2} = \sqrt{\sigma_x^2 \cdot \cos^2 \theta_{tilt} + \sigma_y^2 \cdot \sin^2 \theta_{tilt}} \tag{C.7}$$

If we consider a crystal the situation is different. While the face of a standard collimator jaw can be considered an infinite straight line in the x-y axis, being it dimension much larger that the typical values of σ_x, σ_y, this is not necessarily true for the crystal. For strip and quasi-mosaic crystals the face is not even straight, while this assumption remains valid for o-shape crystals. This would make the calculation of the parameters α, σ_{skew} strictly dependent on the geometrical characteristics of the crystal used (see figure C.2).

Moreover, it is usually required to use the central region of the crystal, where quality of the crystal and the geometrical parameters are optimized. In order to use the crystal in its center it would be necessary to align the crystal with the ellipse in
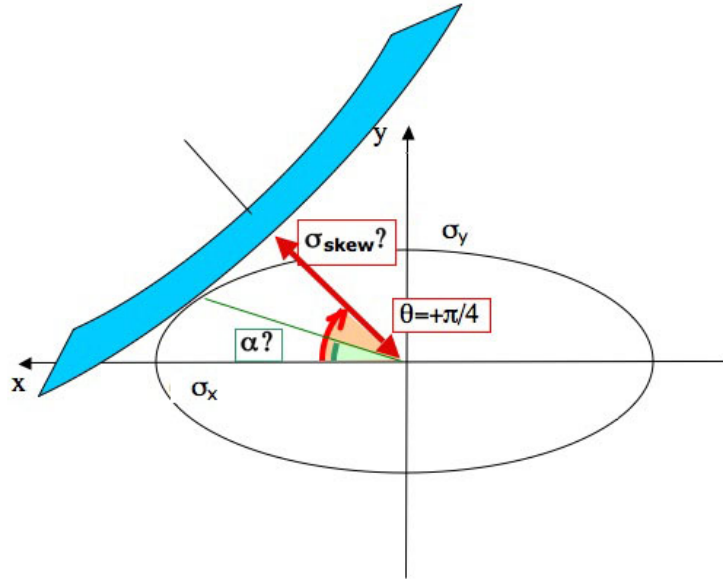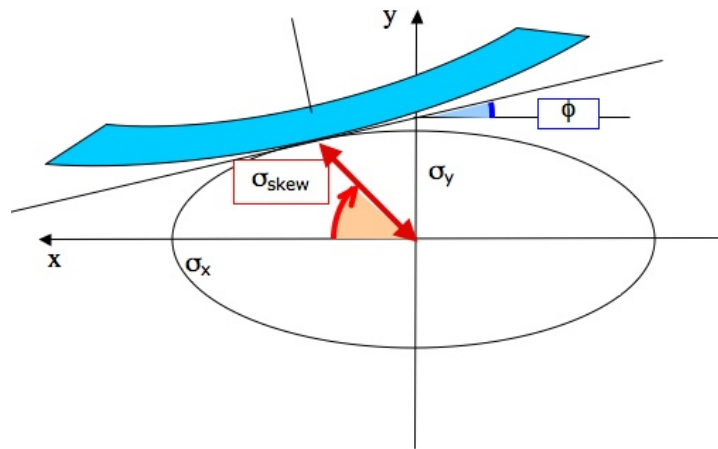
Figure C.2: Skew crystal collimator

Figure C.3: Skew crystal collimator aligned with the beam ellipse.

the x-y plane (see figure C.3). The tilt angle ϕ, defined in picture C.3, can be simply found using again the transformation describer in equations C.8. the transformation:

$$X = \frac{x}{\sigma_x} \tag{C.8}$$
$$Y = \frac{y}{\sigma_y}$$

In the X, Y reference system the ellipse becomes a circle ($X^2 + Y^2 = 1$), the line perpendicular to the the angle θ_{tilt} defines the tangency. The line passing through the origin, with azimutal angle θ_{tilt}, becomes:

$$Y_r = \frac{\sigma_y}{\sigma_x} \cdot \tan\theta_{tilt} \cdot x \tag{C.9}$$

and its tangent:

$$Y_t = -\frac{\sigma_y}{\sigma_x} \cdot \frac{1}{\tan\theta_{tilt}} \cdot X + n \tag{C.10}$$

where n is the coordinate at $Y = 0$, which is not of interest at the moment. Transforming back to the x-y coordinates:

$$y_t = -\frac{\sigma_y^2}{\sigma_x^2} \cdot \frac{1}{\tan\theta_{tilt}} \cdot x + \sigma_y \cdot n \tag{C.11}$$

The angle ϕ is therefore defined as:

$$\tan\phi = -\frac{\sigma_y^2}{\sigma_x^2} \cdot \frac{1}{\tan\theta_{tilt}} \tag{C.12}$$

The alignment with the ellipse tangent would require a new degree of freedom in the holder. In this case the aperture of the crystal collimator would be:

$$\sigma_{skew-CRY} = \frac{\sigma_x \sigma_y}{\sqrt{\sigma_y^2 \cdot \cos^2\theta_{tilt} + \sigma_x^2 \cdot \sin^2\theta_{tilt}}} \tag{C.13}$$

With the standard holders the alignment of the crystal for a skew position is not foreseen. For the moment the skew option has not been implemented in the code.

Bibliography

[1] "LHC design report." (Volume 1 Chapter 1).

[2] "LHC design report." (Volume 1 Chapter 18).

[3] R. W. Assmann, I. S. Baishev, M. Brugger, et al. "Requirements for the LHC collimation system." LHC-Project-Report-599.

[4] R. W. Assmann, G. Bellodi, J. M. Jowett, E. Métral, and T. Weiler. "Accelerator Physics Concept for Upgraded LHC Collimation Performance." Presented at Particle Accelerator Conference (PAC 09), Vancouver, BC, Canada, 4-8 May 2009.

[5] R. Assmann, S. Redaelli, and W. Scandale. "Optics Study for a Possible Crystal-based Collimation System for the LHC." Proceeding of EPAC 2006, Edinburg, Scotland.

[6] J. C. Smith, R. Assmann, V. Previtali, V. Shiltsev, and A. Valishev. "Prospects for Integrating a Hollow Electron Lens into the LHC Collimation System." Presented at Particle Accelerator Conference (PAC 09), Vancouver, BC, Canada, 4-8 May 2009.

[7] J. B. Jeanneret, D. Leroy, L. Oberli, and T. Trenkler. "Quench levels and transient beam losses in LHC magnets." CERN-LHC Project Report n.044.

[8] L. Burnod, D. Leroy, B. Szeless, B. Baudouy, and C. Meuris. "Thermal modeling of the LHC dipoles functioning in superfluid helium." Presented at 4th European Particle Accelerator Conference (EPAC 94), London, England, 27 Jun - 1 Jul 1994.

[9] C. Bracco. "Commissioning scenarios and tests for the lhc collimation system." Ph.D. thesis, École Polytechnique Fédérale de Lausanne, CERN-THESIS-2009-031.

[10] V. Biryukov, Y.A.Chesnokov, and V. Kotov. "Crystal channeling and its application at high-energy accelerators." Springer, 1997.

[11] W. Scandale, D. A. Still, A. Carnera, et al. "High-Efficiency Volume Reflection of an Ultrarelativistic Proton Beam with a Bent Silicon Crystal." *Phys. Rev. Lett.*, volume 98.

[12] S. G. Peggs and V. Previtali. "Grazing function g and collimation angular acceptance." *Phys. Rev. ST Accel. Beams*, volume 12(11):(2009) page 114001.

[13] G. Robert-Demolaize, R. Assmann, S. Redaelli, and F. Schmidt. "A new version of SixTrack with collimation and aperture interface." Presented at the 21st Particle Accelerator Conference (PAC05), Knoxville, Tennessee, USA. March 16-20, 2005.

[14] S. Redaelli, G. Arduini, R. Assmann, and G. Robert-Demolaize. "Comparison between measured and simulated beam loss patterns in the CERN SPS." CERN-LHC-Project-Report.

[15] N. V. Mokhov, G. Annala, A. Apyan, et al. "Crystal collimation studies at the tevatron (t-980)." Presented at the Particle Accelerator Conference (PAC 09), Vancouver, BC, Canada, May 2009.

[16] W. Scandale. "The UA9 Experiment at the CERN-SPS." Prepared for Particle Accelerator Conference (PAC 09), Vancouver, BC, Canada, May 2009.

[17] C. Kittel. "Introduction to solid state physics." Wiley, 2005.

[18] N. W. Ashcroft and D. N. Mermin. "Solid state physics." Thomson Learning, 1976.

[19] G. Robert-Demolaize. "Design and Performance Optimization of the LHC Collimation System." Ph.D. thesis, Université Joseph Fourier, Grenoble, CERN-THESIS-2006-069.

[20] G. Moliere. "Theorie der Streuung schneller geladener Teilchen I. Einzelstreuung am abgeschirmten Coulomb-Feld." *Z. Naturforsch.*, volume A2:(1947) page 133.

[21] Lindhard. "K. danske vidensk. selsk." Math.-Fys Meddr., 34-1, 1965.

[22] D. S. Gemmell. "Channeling and related effects in the motion of charged particles through crystals." *Rev. Mod. Phys.*, volume 46(1):(1974) pages 129–227.

[23] W. Scandale, D. A. Still, A. Carnera, et al. "High-efficiency volume reflection of an ultrarelativistic proton beam with a bent silicon crystal." *Physical Review Letters*, volume 98(15):154801.

[24] W. Scandale, A. Vomiero, S. Baricordi, et al. "High-efficiency deflection of high-energy protons through axial channeling in a bent crystal." *Physical Review Letters*, volume 101(16):164801.

[25] W. Scandale, A. Vomiero, S. Baricordi, et al. "Volume reflection dependence of 400 gev/c protons on the bent crystal curvature." *Physical Review Letters*, volume 101(23):234801.

[26] W. Scandale. "Crystal-based collimation in modern hadron colliders." Prepared for Final CARE-HHH Workshop on Scenarios for the LHC Upgrade and FAIR, Chavannes-de-Bogis, Switzerland, 24 - 25 Nov 2008, pp.154-161.

[27] W. Scandale, I. Efthymiopoulos, D. A. Still, et al. "Apparatus to study crystal channeling and volume reflection phenomena at the SPS H8 beamline." *Review of Scientific Instruments*, volume 79(2):023303.

[28] C. T. Murphy et al. "First results from bent crystal extraction at the Fermilab Tevatron." *Nucl. Instrum. Meth.*, volume B119.

[29] R. A. Carrigan, Jr. et al. "Extraction from TeV range accelerators using bent crystal channeling." *Nucl. Instrum. Meth.*, volume B90:(1994) pages 128–132.

[30] R. A. Carrigan, Jr. et al. "Beam extraction studies at 900-GeV using a channeling crystal." *Phys. Rev. ST Accel. Beams*, volume 5.

[31] R. A. Carrigan, D. Chen, G. Jackson, et al. "First observation of luminosity-driven extraction using channeling with a bent crystal." *Phys. Rev. ST Accel. Beams*, volume 1(2):(1998) page 022801.

[32] R. P. Fliller. "The Crystal collimation system of the Relativistic Heavy Ion Collider." *UMI-31-61096, Ph.D. thesis, Stony Brook University.*

[33] H. Akbari et al. "First results on proton extraction from the CERN SPS with a bent crystal." *Phys. Lett.*, volume B313:(1993) pages 491–497.

[34] K. Elsener, W. Herr, and J. Klem. "Proton and Pb ion beam extraction experiments with bent crystals at the CERN-SPS." Prepared for the International Symposium on Near Beam Physics, Batavia, IL, USA, 22-24 Sep 1997.

[35] G. Arduini et al. "On the energy dependence of proton beam extraction with a bent crystal." *Phys. Lett.*, volume B422.

[36] K. Elsener et al. "What did we learn from the extraction experiments with bent crystals at the CERN SPS?" Presented at 6th European Particle Accelerator Conference (EPAC 98), Stockholm, Sweden, 22-26 Jun 1998.

[37] V. Guidi et al. "Tailoring of silicon crystals for relativistic-particle channeling." *Nucl. Instrum. Meth.*, volume B234:(2005) pages 40–46.

[38] Y. M. Ivanov, A. A. Petrunin, and V. V. Skorobogatov. "Observation of the elastic quasi-mosaicity effect in bent silicon single crystals." *JETP Lett.*, volume 81:(2005) pages 99–101.

[39] W. Scandale, A. Vomiero, S. Baricordi, et al. "Observation of Multiple Volume Reflection of Ultrarelativistic Protons by a Sequence of Several Bent Silicon Crystals." *Physical Review Letters*, volume 102(8):084801.

[40] M. A. Maslov, N. V. Mokhov, and I. A. Yazynin. "The SSC beam scraper system." Superconducting Super Collider Lab., Dallas, TX (United States), SSCL-484, 1991.

[41] K. Wille. "The physics of particle accelerators: An introduction." Oxford, UK: Univ. Pr. (2000).

[42] D. A. Edwards and M. J. Syphers. "An Introduction to the physics of high-energy accelerators."

[43] J. B. Jeanneret. "Optics of a two-stage collimation system." *Phys. Rev. ST Accel. Beams*, volume 1(8):(1998) page 081001.

[44] C. Bracco and R. Assmann. "Chromatic LHC Optics Effects on Collimation Phase Space." CERN-ATS-2009-033.

[45] P.Bryant and E.Klein. "The design of betatron and momentum collimation systems." *CERN-SL/92-40*.

[46] M. Seidel. "The Proton collimation system of HERA." Ph.D. thesis, DESY-94-103.

[47] T. Trenkler and J.-B. Jeanneret. "The Principles of two stage betatron and momentum collimation in circular accelerators." *Part. Accel.*, volume 50:(1995) pages 287–311.

[48] A. Drees and R. Fliller. Private communication.

[49] E. Laface. Private communication.

[50] D.Still and A.Valishev. Private communication.

[51] E. Shaposhnikova, S. Fartoukh, and J.-B. Jeanneret. "LHC Abort Gap Filling by Proton Beam." Presented at 4th European Particle Accelerator Conference (EPAC 94), London, England, 27 Jun - 1 Jul 1994.

[52] F. Schmidt. "Sixtrack, user reference manual." CERN, 1994, SL/94-56.

[53] "Collimation website." http://lhc-collimation-project.web.cern.ch/lhc-collimation-project/code-tracking.htm.

[54] R. Assmann, M. Brugger, M. Hayes, et al. "Tools for predicting cleaning efficiency in the lhc." Prepared for the 20th Particle Accelerator Conference PAC03, Portland, Oregon, May 12-16 2003.

[55] T. Trenkler and J. B. Jeanneret. "K2, a software package evaluating collimation systems in circular colliders."

[56] K. Goulianos. "Diffractive Interactions of Hadrons at High-Energies." *Phys. Rept.*, volume 101:(1983) page 169.

[57] H. Bichsel, D. E. Groom, and S. R. Klein. "Passage of particles through matter (Rev.)." *Phys. Rev. B*, volume D66:(2002) page 010001.

[58] S. Redaelli, R. Assmann, and G. Robert-Demolaize. "LHC aperture and commissioning of the collimation system." Proceedings of the LHC Project Workshop "Chamonix XIV", January 2005.

[59] G. Battistoni, F. Cerutti, A. Fassò, et al. "The FLUKA code: Description and benchmarking." *AIP Conf. Proc.*, volume 896:(2007) pages 31–49.

[60] A. Ferrari, P. R. Sala, A. Fasso, and J. Ranft. "FLUKA: A multi-particle transport code (Program version 2005)." Technical note SLAC-R-773 and CERN-2005-010, October 2005.

[61] W. Herr. "Diffusion of particles induced by transverse noise and its application to crystal extraction experiments." Technical Report CERN-SL-92-53-AP, CERN, Geneva, 1992.

[62] V. Shiltsev et al. "Tevatron Electron Lenses: Design and Operation." *Phys. Rev. ST Accel. Beams*, volume 11:(2008) page 103501.

[63] D. Mohl. "Sources of emittance growth." (pp.45-69). Lesson given at CAS - CERN Accelerator School and KVI: Specialised CAS Course on Small Accelerators, Zeegse, The Netherlands.

[64] "Tevatron official website." `http://www-bdnew.fnal.gov/tevatron/`.

[65] R. R. Wilson. "The Tevatron." *Phys. Today*, volume 30N10:(1977) pages 23–30.

[66] M. Church, A. I. Drozhdin, A. Legan, N. V. Mokhov, and R. Reilly. "Tevatron run-II beam collimation system." Given at IEEE Particle Accelerator Conference (PAC 99), New York, NY, 29 Mar - 2 Apr 1999.

[67] R. A. Carrigan et al. "Channeling collimation studies at the Fermilab Tevatron." *Proc. SPIE Int. Soc. Opt. Eng.*, volume 6634:(2007) page 66340I.

[68] V. Shiltsev. "Fast PIN-diode beam loss monitors at Tevatron." *Nucl. Instrum. Meth.*, volume A411:(1998) pages 81–92.

[69] R. Tesarek. Private communication.

[70] R. Tesarek. "Instrumentation to Detect Crystal Channelling: Status and Plans." Presentation at T980 Meeting, July 2008.

[71] "Tevatron Optics Database." `http://www-bd.fnal.gov/cgi-tev/search_latt2.pl`.

[72] "SPS Presentation at AB-OP-SPS Home Page." `http://ab-dep-op-sps.web.cern.ch/ab-dep-op-sps/SPS_Presentation.htm`.

[73] "LHC design report." (Volume 3 Chapter 11).

[74] V. Previtali, R. Assmann, S. Redaelli, and I. Yazynin. "Beam loss predictions for the UA9 crystal collimation experiment." Prepared for Particle Accelerator Conference (PAC 09), Vancouver, BC, Canada, May 2009.

[75] "Medipix 2 CERN Project Homepage." `http://medipix.web.cern.ch/MEDIPIX/Medipix2/indexMPIX2.html`.

[76] E. Laface, L. Tlustos, and V. Ippolito. "Crystal Collimation efficiency measured with the Medipix detector in SPS UA9 experiment." Prepared for the International Particle Accelerator Conference IPAC10, Kyoto Japan, 23-28 May 2010.

[77] F. Schmidt, G. Iselin, and H. Grote. "Madx User Guide." `http://mad.web.cern.ch/mad/uguide.html`.

[78] T. Weiler et al. "Beam loss response measurements with a LHC prototype collimator in the SPS." Prepared for Particle Accelerator Conference (PAC 07), Albuquerque, New Mexico, 25-29 Jun 2007.

[79] S. Redaelli. "Highlights of 2008 Collimator beam tests at the SPS." Presentation LHC collimator working group, December 2008.

[80] E. Laface, L. Tlustos, and V. Ippolito. "What we can do in UA9 with Medipix." Presented at Crystal Channeling mini workshop (CC09), CERN, 9-10 November 2009.

[81] S. Redaelli. Private communication.

[82] W. Scandale et al. "First results on the SPS beam collimation with bent crystals." Draft submitted to PRL, july 2009.

[83] "Cern Document Server." `http://cdsweb.cern.ch/`.

[84] M. Lamont. "Estimates of Annual Proton Doses in the LHC." CERN, LHC Project Note 375, 2005.

[85] M. Giovannozzi. "Sources of emittance growth." Presentation at CERN Accelerator School 2005, Trieste, Italy, 2 - 14 October 2005.

[86] G. Rumolo and E. Metral. "Multi-particle effects in particle accelerators." Lessons at USPAS 2009, Vanderbilt University, Nashville, Tennessee, January 12-23, 2009.

[87] G. Rumolo and F. Zimmermann. "Electron cloud simulations: beam instabilities and wakefields." *Phys. Rev. ST Accel. Beams*, volume 5(12):(2002) page 121002.

[88] W. Herr. "Beam beam interactions." pages 379–410. Included in the proceedings of CAS - CERN Accelerator School: Intermediate Course on Accelerator Physics, Zeuthen, Germany, September 2003.